Novel Sol-gel Synthesis and Characterization of Oxide Nanopowders for Solid Oxide Fuel Cells

by

Zihua Wang

Submitted in accordance with the requirements for the degree of Doctor of Philosophy

The University of Leeds
Institute for Materials Research
School of Process, Environmental and Materials Engineering

August, 2012

Publications

1. **Zihua Wang**, Girish M. Kale, Nariman Soltanian and Mojtaba Ghadiri, "Granulated sodium alginate mediated cation-exchange process for the synthesis of NiO nanopowders," *RSC Advances*, Manuscript in preparation.
2. **Zihua Wang**, Girish M. Kale, Qingchun Yuan and Mojtaba Ghadiri, "X-ray micro-tomography of freeze dried nickel alginate beads and transformation into NiO nanopowders," *RSC Advances*, DOI: 10.1039/c2ra21171h.
3. **Zihua Wang**, Girish M. Kale and Mojtaba Ghadiri, "Novel Ion-exchange process for the preparation of Metal Oxide nanopowders from Sodium Alginate," *Journal of the American Ceramic Society*, DOI: 10.1111/j.1551-2916.2012.05366.x.
4. **Zihua Wang**, Girish M. Kale and Mojtaba Ghadiri, "Synthesis and characterization of $Ce_xGd_{1-x}O_{2-\delta}$ nanopowders employing an Alginate mediated ion-exchange process," *Chemical Engineering Journal*, 198-199, 149, 2012.
5. **Zihua Wang**, Girish M. Kale and Mojtaba Ghadiri, "Sol-gel production of $Ce_{0.8}Gd_{0.2}O_{1.9}$ nano powders using Sucrose and Pectin as organic precursors," *Journal of the American Ceramic Society*, 95, 2863, 2012.
6. **Zihua Wang**, Tim P. Comyn, Mojtaba Ghadiri and Girish M. Kale, "Maltose and Pectin assisted sol-gel production of $Ce_{0.8}Gd_{0.2}O_{1.9}$ solid electrolyte nanopowders for solid oxide fuel cells," *Journal of Materials Chemistry*, 21, 16494, 2011.

Acknowledgements

First of all I would like to thank my supervisors, Dr. Girish M. Kale and Prof. Mojtaba Ghadiri, for offering me their absolutely invaluable guidance, support and encouragement throughout my PhD study. Financial support from Institute for Materials Research, University of Leeds is greatly appreciated.

I thank Dr. Tim P. Comyn for teaching me XRD Rietveld structural refinement technique and Dr. Michael B, Ward and Mr. John Harrington for microstructure characterization using TEM and SEM. I also appreciate Dr. Qingchun Yuan for XMT characterization analysis and Dr. Adrian Cunliffe for TGA/DSC and ICP-AES analysis.

I also thank to other students and postdoctoral researchers who work in IMR and IPSE including Miss. Fangyuan Zhu, Mrs. Zhanxiang Zhao, Dr. Basit Munir, Mr. Umesh Lad, Mr. Peter Ene and Dr. Nicole Hondow.

Finally, I would like to thank my parents for their support and encouragement during my study in UK.

Abstract

In this research, three different sol-gel synthesis methods by using cost effective materials, such as sugar + pectin, sodium alginate beads or sodium alginate granules, have been investigated for nanopowders production in Solid Oxide Fuel Cells (SOFCs) application. Materials (cerium gadolinium oxide and nickel oxide) have been selected as model materials. Cerium gadolinium oxide (CGO) is one of the most important electrolyte materials in SOFC due to its high ionic conductivity at 500–800 °C, whilst nickel oxide (NiO) can be reduced into nickel in SOFC fuels (H_2 or CH_4) as catalyst in anode layer.

First of all, a novel sol-gel method has been developed for the production of high purity nanopowders of $Ce_{0.8}Gd_{0.2}O_{1.9}$ (CGO2) solid solution using maltose or sucrose as an organic chelating agent and pectin for gelation. The results of this investigation indicate that the final particle size of approximately 10 nm can be obtained after calcination of the dried gel at 500 °C for 2 hours in ambient air. Powder X-ray diffraction (XRD) shows that all samples are single phase cubic CGO powders. The mean crystallite sizes calculated from XRD analysis using Rietveld refinement method agree with the morphological features observed by transmission electron microscopy (TEM). The nominal composition of CGO2 has been found to be in excellent agreement with that determined by energy dispersive X-ray spectroscopy (EDS) and inductively coupled plasma - atomic emission spectrometry analysis (ICP-AES). The ionic conductivities of $Ce_{0.8}Gd_{0.2}O_{1.9}$ samples are measured by AC-impedance which appears reasonably well with the reference data which will qualify the use of this material for SOFC as solid electrolyte and in the fabrication of composite electrodes.

On the other hand, another novel and generic sol-gel method has been developed for the production of high purity metal oxide nanopowders using sodium alginate (Na-ALG). This has been demonstrated successfully employing NiO and CGO CGO1 ($Ce_{0.9}Gd_{0.1}O_{1.95}$) and CGO2 ($Ce_{0.8}Gd_{0.2}O_{1.9}$) as model materials in this instance. For NiO, the results of this investigation indicate that the final particle size of ~20 nm can be obtained after calcination of the predried beads at 500 °C for 3 hours in ambient air. XRD shows that the obtained samples are single phase cubic NiO powders. Furthermore, freeze dried and X-ray micro-tomography (XMT) technologies are applied to observe the inside morphology of the Ni-ALG beads. XMT

shows that nickel ions have been uniformly cross-linked in the alginate structure and remained stable after freeze drying evidenced by the bright green color of the freeze dried beads. Finally, NiO nanopowders can also be synthesized using Na-ALG granules.

Moreover, this alginate method has also been demonstrated successfully employing CGO in two composites designated as CGO1 ($Ce_{0.9}Gd_{0.1}O_{1.95}$) and CGO2 ($Ce_{0.8}Gd_{0.2}O_{1.9}$), respectively. The results indicate that the nanopowders having a final particle size of ~7 nm can be obtained after calcination of ion-exchanged alginate precursor at 500 °C for 2 hours in ambient air. The chemical structures of Na-ALG solution and CGO beads are analyzed by Fourier transform infrared spectroscopy (FTIR) which indicates that Ce^{3+}/Gd^{3+} are ion-exchanged with Na^{+} after gelation. The nominal compositions of CGO1 and CGO2 have been found to be in excellent agreement with that determined by EDS and ICP-AES. The ionic conductivities of these two samples are measured by AC-impedance which appears reasonably well with the reference data which will also qualify the use of this material for SOFC as solid electrolyte.

All of these new sol-gel methods are simple, environmentally friendly and non-toxic routes for a large scale production of high purity single phase nanopowders in a cost effective manner at significantly low temperatures.

Table of Contents

List of Tables

List of Figures

List of Abbreviations

SOFCs	Solid Oxide Fuel Cells
IT-SOFCs	Intermediate Temperature Solid Oxide Fuel Cells
NO_x	Nitrogen Oxides (x = 1, 2)
H_2O	Water
UV	Ultraviolet
FTIR	Fourier Transform Infrared Spectroscopy
TGA	Thermo-Gravimetric Analysis
DSC	Differential Scanning Calorimetric
XRD	X-ray Diffraction
HT-XRD	High Temperature X-ray Diffraction
XMT	X-ray Micro0Tomography
SEM	Scanning Electron Microscopy
TEM	Transmission Electron Microscopy
EDS	Energy-Dispersive X-ray Spectroscopy
ICP-AES	Inductively Coupled Plasma – Atomic Emission Spectroscopy
D.C.	Direct Current
A.C.	Alterative Current
wt.	weight
at.	atom
CGO	Gadolinium doped Ceria
NiO	Nickel Oxide
SP	Sucrose and Pectin
MP	Maltose and Pectin
Na-ALG	Sodium Alginate
ALG	Alginate

List of Symbols and Units

λ	Wavelength (nm)
$d_{(hkl)}$	Interplanar spacing (nm) of the plane (hkl)
a	Lattice parameter (Å)
θ	Diffraction angle (radius)
B_{iso}	Temperature factor (Å)
R_{wp}	Weight residual (%)
R_{exp}	Expected residual factor (%)
GOF	Goodness of Fit
σ	Conductivity (Siemens cm^{-1})
ΔG^0	Standard Gibbs free energy of formation (kJ mol^{-1})
R	Gas constant (8.314 J K^{-1} mol^{-1})
f	Frequency (Hz)
Z	Impedance (Ohm)
Re(Z)	Real impedance (Ohm)
Im(Z)	Imaginary impedance (Ohm)
E_a	Activation energy (J mol^{-1} or eV)
A	Cross section area (m^2)
t	Thickness (μm)
r	Radius of pellets (m)

Chapter 1 Introduction

Solid oxide fuel cells (SOFCs) have the promise to improve energy efficiency and to provide society with a clean energy producing technology. The high temperature of operation (500−1000 °C) enables the SOFC to operate with existing fossil fuels to give very efficient conversion of fuels to electricity and to be used in combined heat and power applications or efficiently coupled with gas turbines. SOFCs are quiet and non-polluting and their inherent high efficiency leads to lower greenhouse gas emissions.

In order to achieve long term performance stability and to widen the material selections, SOFC technologies are moving away from traditional temperature of 1000 °C towards intermediate or low temperatures of 500−800 °C [1, 2]. One of the ways to circumvent the problems, such as increase in electrolyte resistivity and high electrode over-potential, that prevail at intermediate and low temperature in SOFCs is to use solid electrolyte materials with high ionic conductivity and high chemical stability in oxygen potential gradient. This can be achieved by the use of gadolinium doped ceria (CGO) at intermediate or low operating temperature of SOFC [3]. On the other hand, a metal catalyst such as nickel is usually applied into anode electrodes to increase the reaction rate during operation. According to the literature review [4], the electrochemical performance of Ni based anode is significantly influenced by the starting nickel oxide (NiO) powders. This is due to the particle properties, such as average particle size and particle size distribution of NiO. Hence, to successfully obtained high purity single phase metal oxide nanopowders, such as CGO and NiO, is crucial in SOFC development.

1.1. Motivation

SOFC components produced from nanopowders have a number of advantages. The component electrolyte may exhibit a finer sintered grain structure, and therefore a higher density of grain boundaries. Nanoparticulate compacts have the ability to sinter to higher densities at much lower temperatures as a result of high surface area and exhibit high fracture toughness [5-8]. These features may contribute towards increasing the oxygen ion mobility and therefore the ionic conductivity and reducing ohmic loss in an electrochemical cell [9]. In order to obtain nano crystalline pure CGO or NiO powders, various sol-gel techniques have been explored,

including the use of ethylene glycol [10] and ammonium carbonate [11]. However, from a commercial perspective, it is important to synthesize bulk nanopowders of CGO more rapidly and efficiently in an environmentally friendly and cost effective manner.

In this study, three different sol-gel synthesis methods using media such as sugar + pectin, sodium alginate beads or sodium alginate granules, will be investigated for nanopowders production. First, a combination of maltose or sucrose and pectin will be used for as chelating and gelation agents respectively of Ce^{3+} and Gd^{3+} cations in the aqueous precursor solutions for the production of high purity CGO nanopowders. This method is very much like jam making in food industry. Maltose is a disaccharide containing two α-glucose units linked by α-glycosidic bond. This covalent bond connects two monosaccharides at the carbon C_1 (anomeric) of the first unit of glucose to carbon C_4 of the second unit of glucose [12]. Sucrose is made from one unit of α-glucose and one unit of β-fructose, and is probably one of the most abundant organic chemicals in the world. These two unit in chains are linked by a β-glycosidic bond which is a covalent bond between two monosaccharides that involves carbon C_1 (anomeric) of the glucose and carbon C_2 of the fructose [12]. Pectin is present in ripe fruits and some vegetables. It consists of a linear polysaccharide containing between 300 and 1000 monosaccharide units. Pectin is widely used in the food industry as a gelling agent [13]. It is well known that these organic materials are abundant in nature which results in low cost during production process. By using these organic materials in sol-gel production, nanopowders can be synthesized more rapidly and cost efficiently in manufacturing production scale.

Furthermore, another novel and generic sol-gel method will be developed for the production of high purity nanopowders of metal oxides and their solid state solutions using organic powders such as sodium alginate (Na-ALG) which can function as ion-exchange media. Since the ion-exchange reaction takes place immediately as sodium alginate contacts with metal solution, it will significantly reduce the gelation time compared with sugar + pectin jam making process. Hence, it is possible to increase the metal oxide production rate during manufacturing process. Alginate is an anionic polysaccharide that is naturally found in abundance in the cell walls of brown algae and it has 200–300 times more water absorbing capacity compared to its own weight. Sodium alginate dissolves readily in water, and it forms a gel if it is brought into contact with an aqueous solution of metal ions, whereby the

sodium ion in the polymer structure is replaced by the metal ion. By virtue of the gel structure, the metal ions become immobile and cannot readily get close to each other, hence the possibility of producing small nanoparticles. Moreover, the energy requirement for calcinations is partially provided by heat of combustion of the alginate. Therefore, metal oxides can be produced after calcination at a temperature range that is much lower than the conventional methods. The findings will prove that this method is simple, quick and environmental friendly which not only produces simple oxide such as NiO, CuO, CoO, ZrO_2 or Fe_2O_3, but also produces complex oxide such as $NiFe_2O_4$, $CoFe_2O_4$ and CGO for many applications in solid state electrochemistry technologies.

1.2. Thesis Organization

This thesis is separated into seven chapters including Introduction, Literature Review, Experimental Methods and Materials, Results, Discussion, Conclusion and Future Plan.

Chapter 1 Introduction, presents a short induction of SOFC, followed by the motivation of this research and the organization of this thesis is described.

Chapter 2 Literature Review, contains the types of fuel cells, component parts and working principle of SOFCs. This chapter also presents an overview of the most important materials and their principle for SOFC electrodes and electrolytes components. Moreover, a comprehensive study in sol-gel process including the history, mechanism and chemistry is also presented. A discussion of some advantages and disadvantages of the sol-gel method is included followed by the sol-gel precursors which previously used.

Chapter 3 Experimental Methods and Materials, contains three novel sol-gel synthesis methods using sugar + pectin and sodium alginate as media. Followed by the theories and operating principles of various analytical methods, such as simultaneous Thermo-Gravimetric Analysis and Differential Scanning Calorimetry (TGA/DSC), Fourier transform infrared spectroscopy (FTIR), X-ray Diffraction (XRD) with Rietveld size/strain structural refinement, High Temperature X-ray Diffraction (HT-XRD), X-ray Micro-Tomography (XMT), Scanning Electron Microscopy (SEM), Transmission Electron Microscopy (TEM), Inductively Coupled Plasma - Atomic Emission Spectrometry analysis (ICP-AES) and AC-impedance

spectroscopy, for material characterizations have been discussed in this chapter, respectively.

Chapter 4 Results and Chapter 5 Discussion, provide the details of the research works and its findings of various metal oxides. CGO2 ($Ce_{0.8}Gd_{0.2}O_{1.9}$) nanopowders obtained from sugar + pectin sol-gel routes are shown in section 4.1 and 5.1, respectively. NiO nanopowders obtained from sodium alginate sol-gel routes are discussed in section 4.2 and 5.2, respectively. Finally, CGO1 ($Ce_{0.9}Gd_{0.1}O_{1.95}$) and CGO2 ($Ce_{0.8}Gd_{0.2}O_{1.9}$) nanopowders synthesized using sodium alginate beads are written in section 4.3 and 5.3, respectively.

At the end of the thesis, Chapter 6 Conclusion gives a general conclusion of this research work, followed by Chapter 7 Future Plan, which gives some guidelines about future research directions and in the end the reference list.

Chapter 2 Literature Review

SOFC development is an attractive research area requiring knowledge from different fields of study including physics, electrochemistry and materials science. One of a major objective in SOFC development is obtaining the proper material with high performance. Recently, there has been an increasing interest in nanoparticles for SOFC components due to their ability to sinter to high density at much lower temperatures as a result of high surface area and exhibit high fracture toughness. Thus, in this chapter, a comprehensive literature review of SOFC including working mechanism, materials in each component (e.g. Ni/NiO as catalyst in anodes and CGO in electrolytes) and nanopowders synthesis methods (e.g. sol-gel) is presented.

2.1 Solid Oxide Fuel Cells (SOFCs)

Fuel cells are electrochemical devices which generate electricity, water and heat with hydrogen or a gaseous fuel (rich in hydrogen) passing from one side of the device and oxygen from the other side. The main characteristic of the fuel cell is its ability to convert chemical energy into electrical energy which is the reverse of electrolysis of water. Hence, solid oxide fuel cells have much higher efficiency than other conventional power generation technologies as shown in Table 2.1. In addition, little pollution is generated and no particulates or NO_x are emitted during this process.

Over time, different types of fuel cells have been investigated. The main parts of a fuel cell are electrolyte with two different electrodes attached on both sides. The electrolyte is a material layer that conducted the charged atoms or molecules (ions) from one side to another. The cathode, where reduction takes place and which has a higher charge level. The anode, where oxidation takes place and which normally has the lower charge level. The electrolyte and the electrodes materials identify the types of the fuel cells.

Table 2.1. Classification of different types of fuel cells [14].

Fuel Cell Type	Electrolyte	Anode Gas	Cathode Gas	Temp. (°C)	Efficiency	Application
Alkaline Fuel Cells **(AFC)**	Potassium Hydroxide	Hydrogen	Pure Oxygen	50 ~ 250	35 ~ 60%	Space Vehicles, Transport
Proton-Exchange Membrane Fuel Cells **(PEM)**	Solid Polymer	Hydrogen	Pure or Atmospheric Oxygen	50 ~ 80	50 ~ 70%	Transport, CHP[a]
Direct Methanol Fuel Cells **(DMFC)**	Solid Polymer	Methanol Solution in Water	Atmospheric Oxygen	80 ~ 200	35 ~ 40%	Small CHP[a], Transport
Phosphoric Acid Fuel Cells **(PAFC)**	Phosphoric Acid	Hydrogen	Atmospheric Oxygen	~ 200	35 ~ 50%	Medium CHP[a], Power Generation
Molten Carbonate Fuel Cells **(MCFC)**	Alkali-Carbonates	Hydrogen	Atmospheric Oxygen	~ 600	40 ~ 55%	Large CHP[a] Power Generation
Solid Oxide Fuel Cells **(SOFC)**	Ceramic Oxide	Hydrogen, Methane	Atmospheric Oxygen	500 ~ 1000	50 ~ 80%	CHP[a], Power Generation

[a]Combine Heat and Power (CHP).

Out of all these types of fuel cells, SOFCs are distinguished by high working temperature, high efficiency and their ability to generate electricity directly by hydrocarbon fuels see Table 2.1. The advantage of the SOFC is that both hydrogen (H_2) and methane (CH_4) can be used as fuel, whilst methane is not applicable in other fuel cells. Hence, many common hydrocarbon fuels, such as natural gas, diesel, gasoline, alcohol and coal gas, can be easily and safely used in SOFC. Another advantage is that the solid ceramic electrolyte and electrodes can be easily cast into any shapes for application.

SOFCs are constructed entirely from solid ceramic materials, including a solid, compact, non porous metal oxide electrolyte and two solid porous electrodes. The fuel such as H_2 is continuously supplied to the porous anode which reacted with the oxide ions (O^{2-}) from the electrolyte and released water and electrons (e^-) to the external circuit. The oxidant (O_2 or air) is fed to the cathode with supplied the oxygen ions (O^{2-}) for the electrolyte. The electrolyte conducts the ions from the cathode towards the anode layer which maintaining the overall electrical charge balance as shown in Figure 2.1.

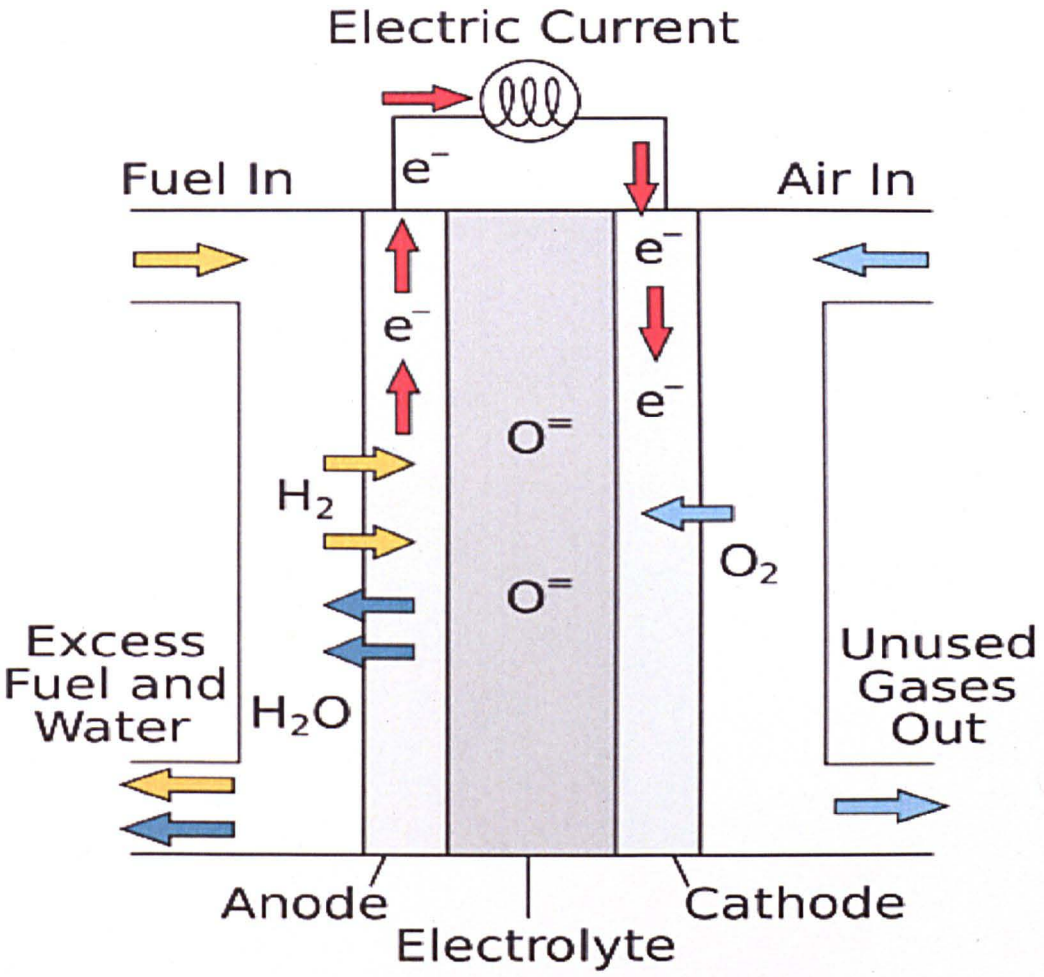

Figure 2.1. Schematic overview of a working SOFC.

The anode reaction is:

$$H_2(g) + O^{2-} \rightarrow H_2O(g) + 2e^- \quad (2.1)$$

The cathode reaction is:

$$\frac{1}{2}O_2(g) + 2e^- \rightarrow O^{2-} \quad (2.2)$$

The total reaction of SOFC is:

$$H_2 + \frac{1}{2}O_2 \rightarrow H_2O(g) + \text{electricity}\ (\Delta G = -237\ \text{kJ mol}^{-1}) \quad (2.3)$$

The cell voltage corresponds to the Gibbs free energy of the reaction via the equation $\Delta G = nF\Delta U_0$. Where n is the number of electrons involved in the reaction and F is the Faraday constant. ΔU_0 is the voltage of the cell for

thermodynamic equilibrium in the absence of a current flow. Therefore, $-\frac{237}{nF} = 1.23V$.

The working specifications of each SOFC components are highlighted below. More details will be discussed later.

Anodes:

- High electronic conductivity
- High porosity
- High strength
- Effective oxidation catalyst
- Chemical and mechanical stability
- Thermal expansion compatibility with the electrolyte and the other fuel cell components (cathode and interconnects)
- Durability
- Low fuel transport resistance
- Easy fabrication at a low cost

Electrolytes:

- Gas tightness
- High density
- High fracture toughness
- High oxygen ion conductivity
- Minimum electronic conductivity
- High strength
- Good chemical stability with respect to the electrodes
- Durability
- Thermal expansion compatibility with other components
- Easy fabrication at low cost

Cathodes:

- Good electro-catalytic activity for O_2 reduction
- Good electronic conductivity
- Stability over very wide ranges of oxygen pressure

- High strength
- Non-volatile
- Durability
- Thermal expansion compatible with the other components
- Easy fabrication at a low cost

SOFCs are produced into different shapes and configuration depending on their usage. The most employed geometries were Planar, Ring, Tubular, Monolithic and High Power Density SOFC [15], respectively.

Planar SOFCs contain 25−250 μm thick electrolyte with two electrodes (25−100 μm) on either side of the electrolyte at an operation temperature between 800 and 1000 °C. These individual cells are stacked in series by using a bipolar plate (interconnect) as shown in Figure 2.2. This interconnect is an electrical conductor and a separator plate which provided a gas barrier between the anode and cathode of two adjacent cells. The advantage of this design is that low cost fabrication methods such as screen printing and tape casting can be used.

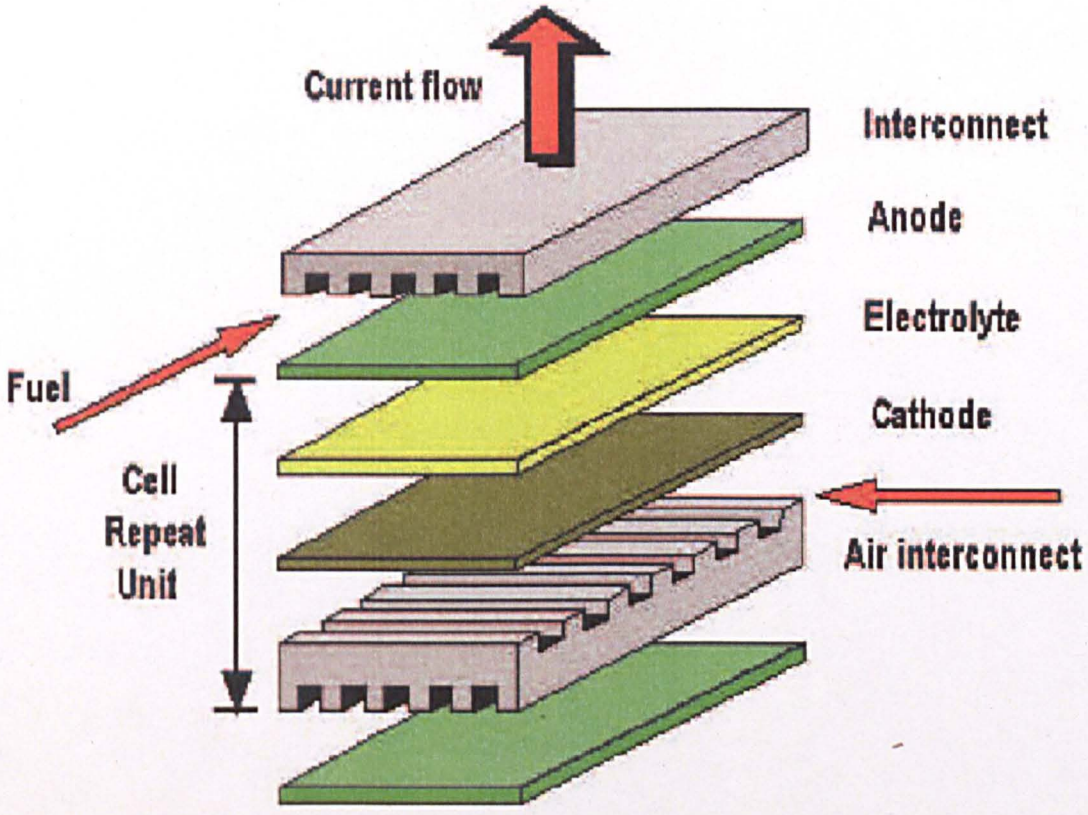

Figure 2.2. Planar SOFC design.

Similar to planar SOFC, Ring-type SOFC is designed with endplate (top) and interconnect (bottom) single cell (see Figure 2.3). The fuel is fed into the centre of a cylindrical stack consisting of layered circular cells. The reactant air is preheated whilst they pass through each interconnect gas manifold. The metal and ceramic contact joints between the electrodes and interconnects is made by LSC ($La_xSr_{1-x}CoO_\delta$) at the cathode side and a Ni gauze at the anode side. The un-reacted fuel is burnt with the un-reacted oxygen from air outside the device [15].

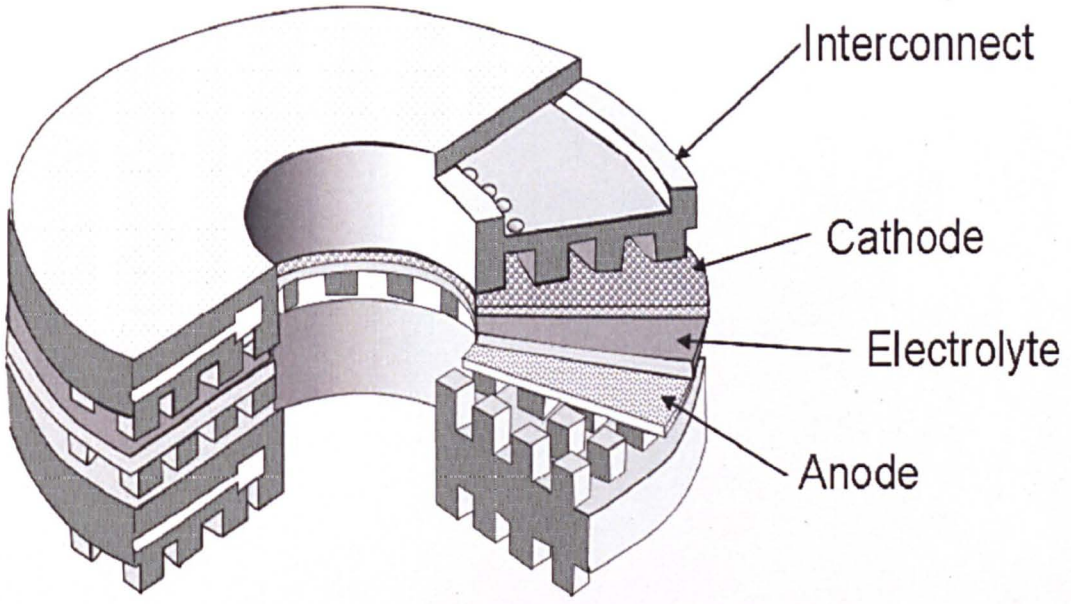

Figure 2.3. Ring-type SOFC [15].

In contrast to planar and ring-type SOFC designs, tubular geometries are developed by Siemens-Westinghouse as shown in Figure 2.4. In this design, air or fuel is passed inside the tube and the other gas is passed outside. The advantage of this geometry is that it becomes much easier to seal and separate the fuel from the air compared with the planar design. The cell operates between 900 and 1000 °C and the usual electrolyte material is YSZ.

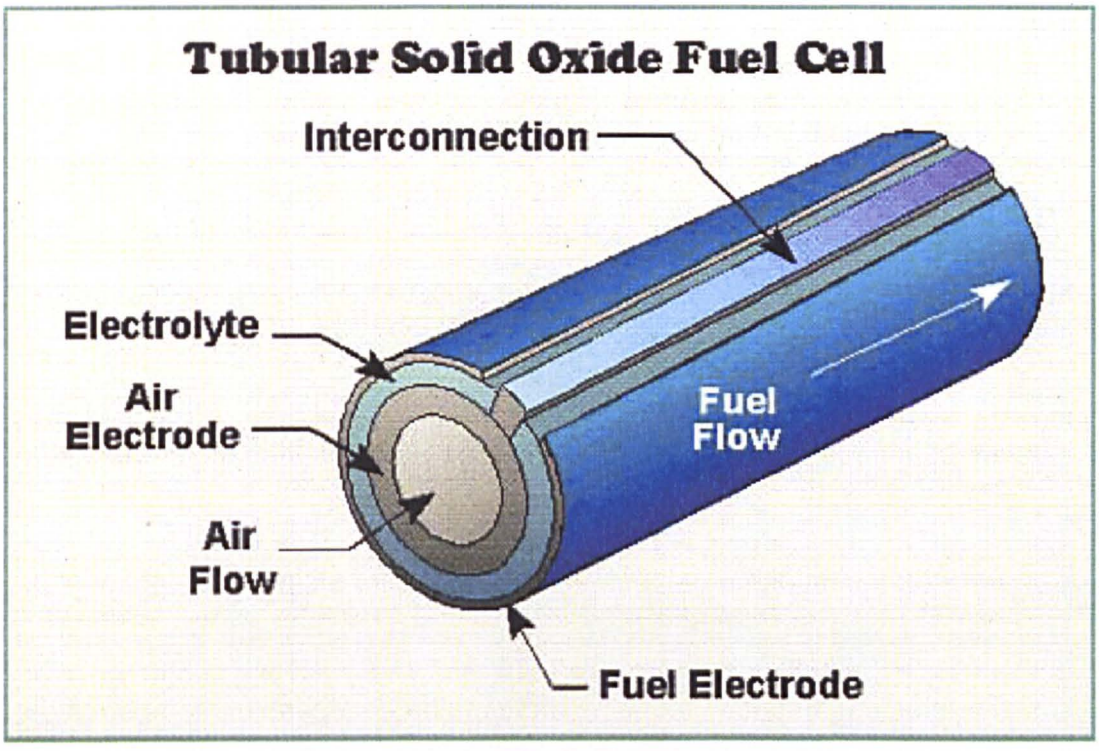

Figure 2.4. Tubular design SOFC from Siemens-Westinghouse [15].

Siemens-Westinghouse has also investigated a High Power Density SOFC design (see Figure 2.5) with a flat cathode tube with ligaments. Easy flow of air inside the tube and high packing density of cells are the main advantages for this design. Therefore, higher volumetric power densities of a stack can be achieved. The bridge within the cathode tube allows for shorter current paths, which in turns decreases the ohmic resistance of each cell and increases the power density of cell stacks [15].

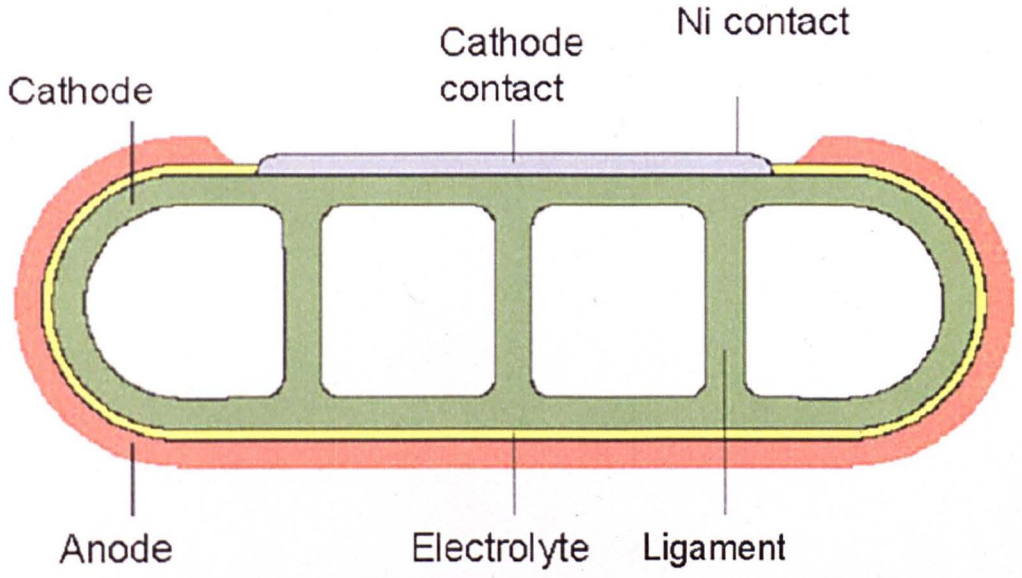

Figure 2.5. High Power Density SOFC [15].

Monolithic SOFC design (see Figure 2.6) consists of alternating anode and cathode compartments which are divided by individual electrolyte/electrode assemblies. According to laboratory tests, high efficiency, high potential of manufacturing and low costs can be achieved from this design. Another big advantage of these cells is that the co-sintering of the multiple cells in stack avoid the need for separated seals.

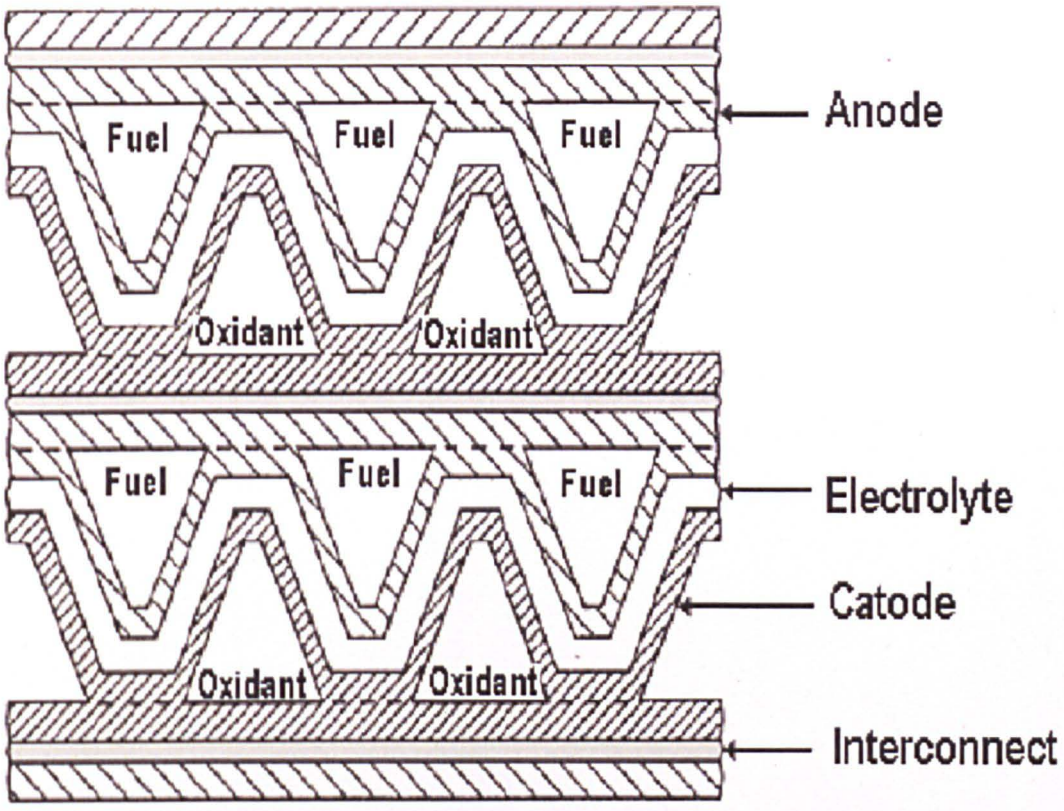

Figure 2.6. Monolithic design SOFC.

2.2 Electrolyte Materials

Electrolyte materials in SOFC require high ionic conductivity/low electronic conductivity known as Mixed Ionic Electronic Conductivity (MIEC), stability in both oxidizing and reducing environments, good mechanical properties and long-term stability. The state of art electrolyte in SOFC application is yttria stabilized zirconia (YSZ) with ideal operating temperature around 800−1000 °C. On the other hand, gadolinium or samarium doped ceria (CGO or CSO) introduces oxygen vacancies and induces ionic conductivity at low temperature region [16] due to the ionic radii of Gd^{3+} or Sm^{3+} which nearly match the ionic radius of Ce^{4+} [17, 18]. In addition, these material exhibit low electronic conductivity at low oxygen partial pressure. At 700 °C,

high conductivity close to the conductivity of YSZ at 1000 °C is observed for CGO [19, 20]. Therefore, CGO is also selected as a suitable candidate for IT-SOFC electrolyte material. Furthermore, Sr and Mg-doped lanthanum gallate ($LaGaO_3$) has attracted more and more attention as a potential candidate in SOFC electrolyte material. $La_{1-x}Sr_xGa_{1-y}Mg_yO_{3-x/2-y/2}$ (LSGM) has ionic conductivity higher than YSZ but lower than CGO. In addition, the stability of LSGM is higher compared with the one from CGO and thus, it is being suggested as electrolyte material operated at temperatures between 600−800 °C. The minimum temperature at which each of these systems can be operated depends on a combination of the ionic conductivity and a realistic assessment of a minimum electrolyte film thickness of 10 μm and a conductivity of 1×10^{-2} Scm^{-1} (corresponding to an area specific resistance of 0.1 ohms cm^{-2}), then the minimum operating temperatures are ~700 °C (YSZ), ~550 °C (CGO) and ~550 °C (LSGM) based on the data in Figure 2.7.

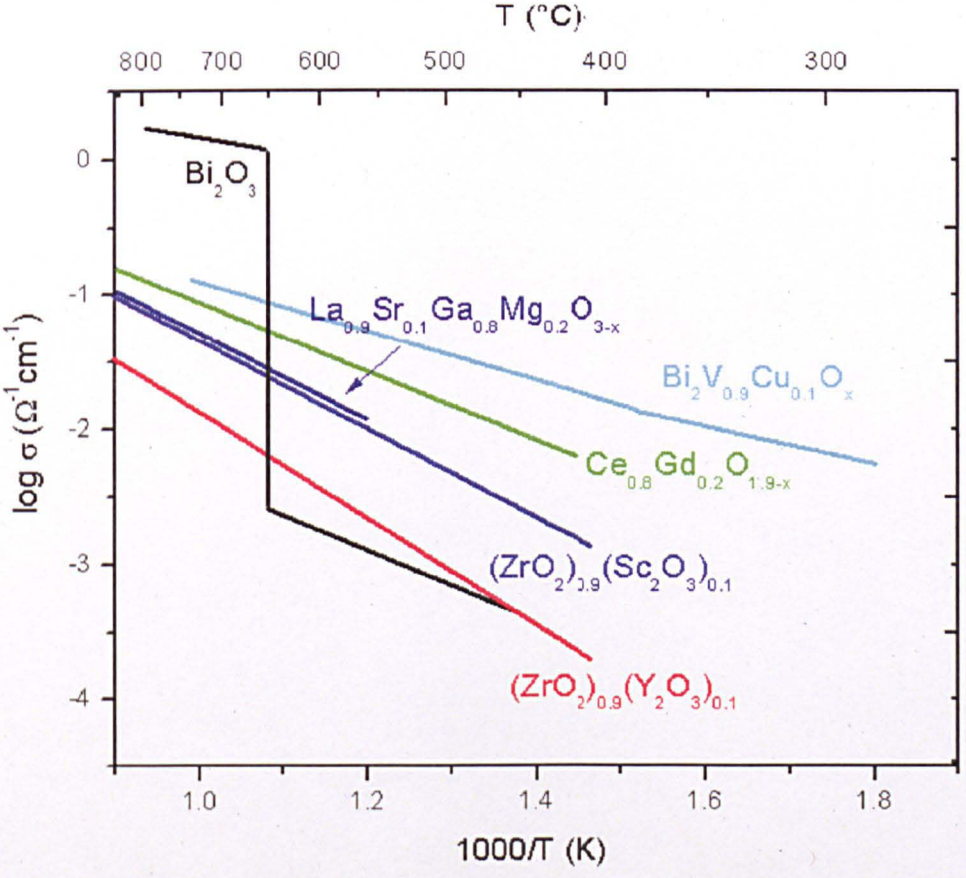

Figure 2.7. Ionic conductivity of different electrolyte materials [15].

Each electrolyte system offers advantages and disadvantages. Thus, YSZ fulfills the electrical requirements at high temperatures and has good high temperature mechanical properties. Problems occur because of its reactivity with perovskite oxide electrodes containing lanthanum at high temperature forming $La_2Zr_2O_7$ resistive layers. LSGM has higher ionic conductivity than YSZ and is more compatible with lanthanum transition-metal oxide perovskite cathodes. On the anode-electrolyte side, composite LSGM-NiO anodes are less compatible with LSGM because of the reactivity of NiO, than the corresponding composite Ni-YSZ anodes are with YSZ. Furthermore, single phase LSGM is very difficult to produce since secondary phases such as $La_4Ga_2O_9$ and $SrLaGa_3O_7$ are obtained at the grain boundaries during synthesis [21, 22]. Ceria doped with rare earth metals has received considerable attention as an alternative electrolyte and it has the highest conductivity at lower temperature of other than doped bismuth oxides when substituted with 0.1–0.2 Gd_2O_3. Doped ceria is more stable than bismuth oxides but, in reducing conditions ($pO_2 \approx 1\times10^{-19}$ atm), Ce^{4+} is reduced to Ce^{3+}. The reduction reaction results in the introduction of electronic conductivity thereby reducing the fuel cell efficiency. The width of the electrolytic domain increases as the temperature is lowered and the electronic conductivity is no longer a problem at 500 °C [23].

2.2.1. YSZ

Commercial 8 mol% yttria stabilized zirconia (8YSZ) has so far been the choice for the electrolyte, due to its high ionic conductivity (~0.1 Scm^{-1}), high stability and thermal expansion compatibility (~10.5×10^{-6} K^{-1}) with other components. However, YSZ ideal operating temperature of 800–1000 °C causes a large number of engineering problems. The main target so far has been to reduce the operating temperature whilst keeping high ionic conductivity during operation. The ionic conductivity is known to vary with preparation routes and sintering conditions due to the resultant microstructure of YSZ [24]. A number of researchers were investigating the relationship between microstructure and ionic conductivity of YSZ electrolyte with different sintering and synthesis conditions. Details of findings are described briefly below.

Gaudon *et al.* [25] concluded that the total ionic conductivity was contributed by bulk and grain boundaries of YSZ electrolyte. The bulk conductivity was related to the density of the sample, whilst the grain boundary conductivity was related to the density and grain size of the sample.

Chen *et al.* [26] studied the sintering behavior of commercial 8YSZ with a mean particle size of 50 nm under different heat treatment conditions. The author found that both sintering temperature and annealing time influenced the total ionic conductivity of 8YSZ. The best sintering temperature for 8YSZ was 1350 °C with highest ionic conductivity 0.105 Scm^{-1}. At a fixed sintering temperature 1000 °C, the total conductivity of YSZ increased with increased annealing time at maximum measurement (0.112 Scm^{-1}) after 8 hours. Mazaheri *et al.* [27] obtained high density 8YSZ compacts (> 97%) by two step sintering method [28]. The initial nanopowders were obtained by glycine nitrate process with mean particle size ~25 nm. The two step sintering conducted at first step T_1 = 1250 °C and second step T_2 = 1050 °C significantly prohibited the grain growth in the final stage of sintering without deteriorating the densification process. The grain size was decreased from 2.15 mm (for normal sintering) to 295 nm by applying two-step sintering process as shown in Figure 2.8.

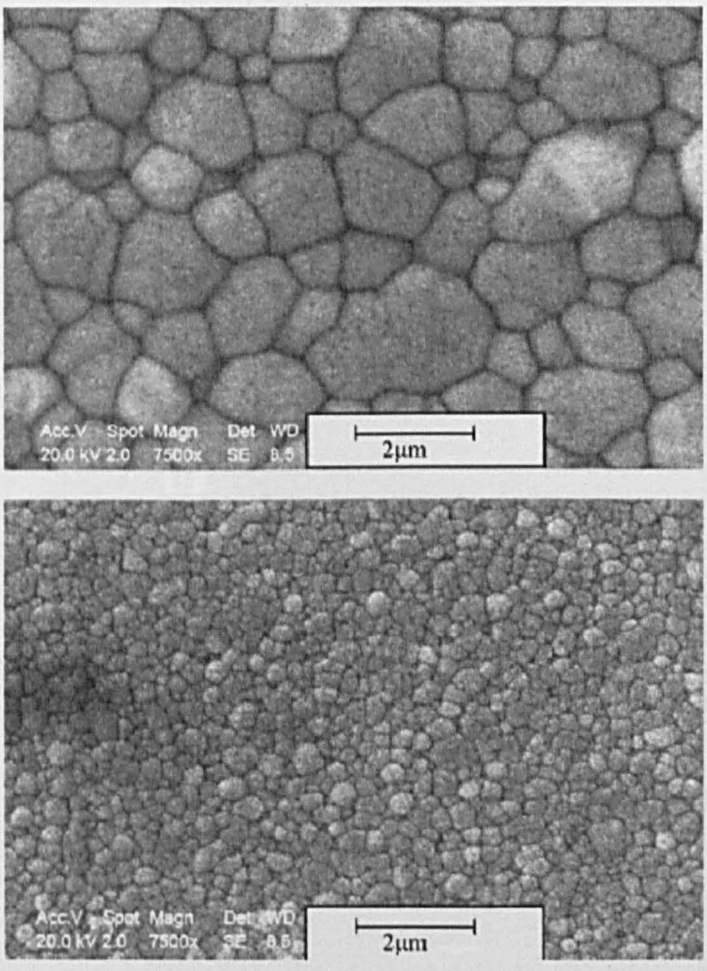

Figure 2.8. SEM micrographs of nano crystalline 8YSZ compacts sintered according to Normal Sintering (top) and Two Step Sintering (bottom) [28].

On the other hand, research was also focused on synthesis 8YSZ nano particle by different methods to reduce the calcination temperature and particle size. Suciu *et al.* [9] synthesized 8YSZ nano particles by sol-gel method with sucrose and pectin as precursors. After calcination at two different temperatures, 500 and 1000 °C, final particle size was measured as 8.3−10.3 nm and 37−58 nm (see Figure 2.9), respectively.

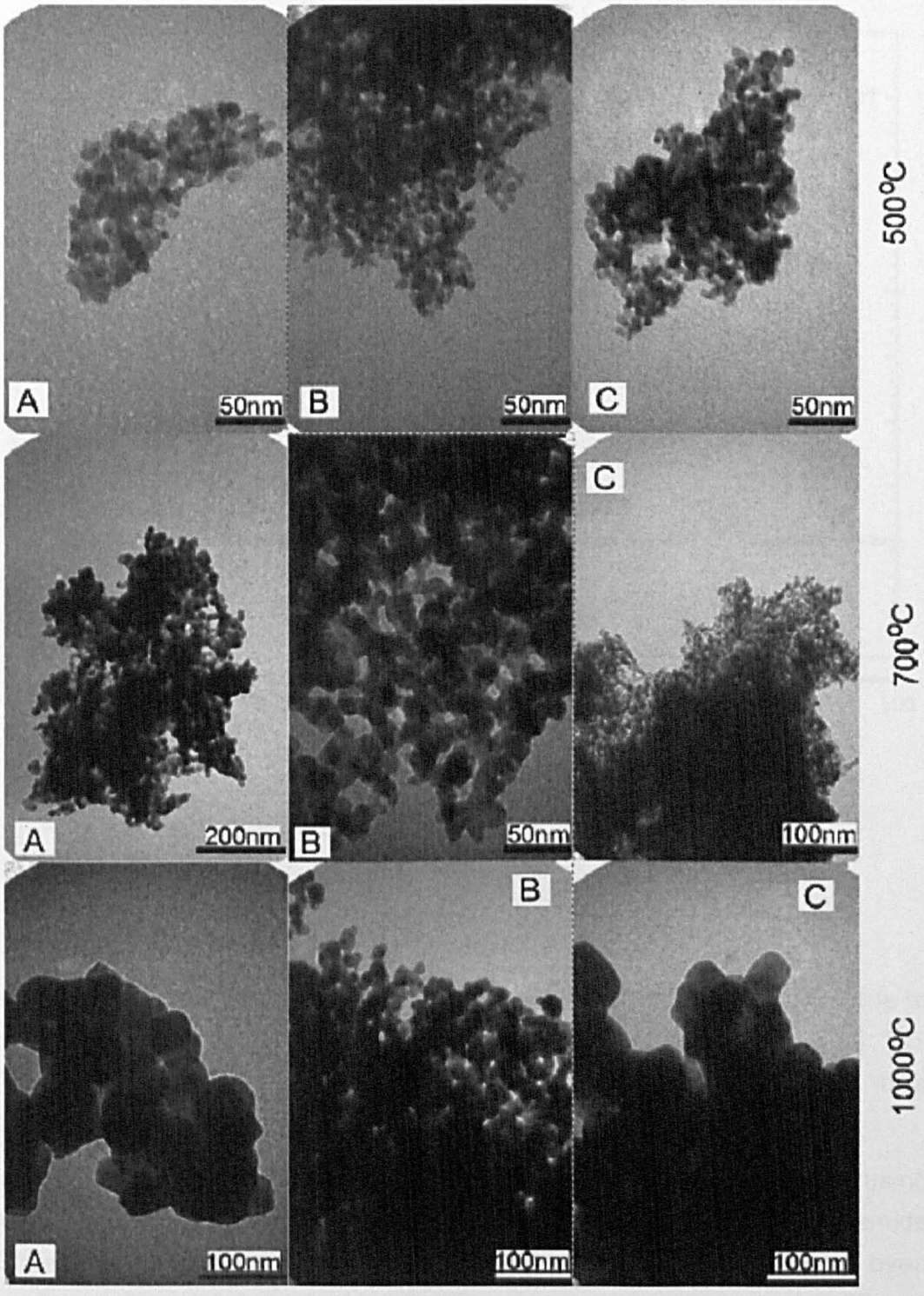

Figure 2.9. TEM images of 8YSZ calcined at 500, 700 and 1000 °C, respectively [9].

Gaudon *et al.* [25] produced nano crystallized 8YSZ by spray pyrolysis with lower sintering temperature (600 °C) compared with conventional preparation route. Tarancón *et al.* [29] also obtained 8YSZ nanopowders using polyacrylamide gel-combustion process. The mean crystal size was 9 nm calculated by XRD Rietveld refinement as shown in Figure 2.10.

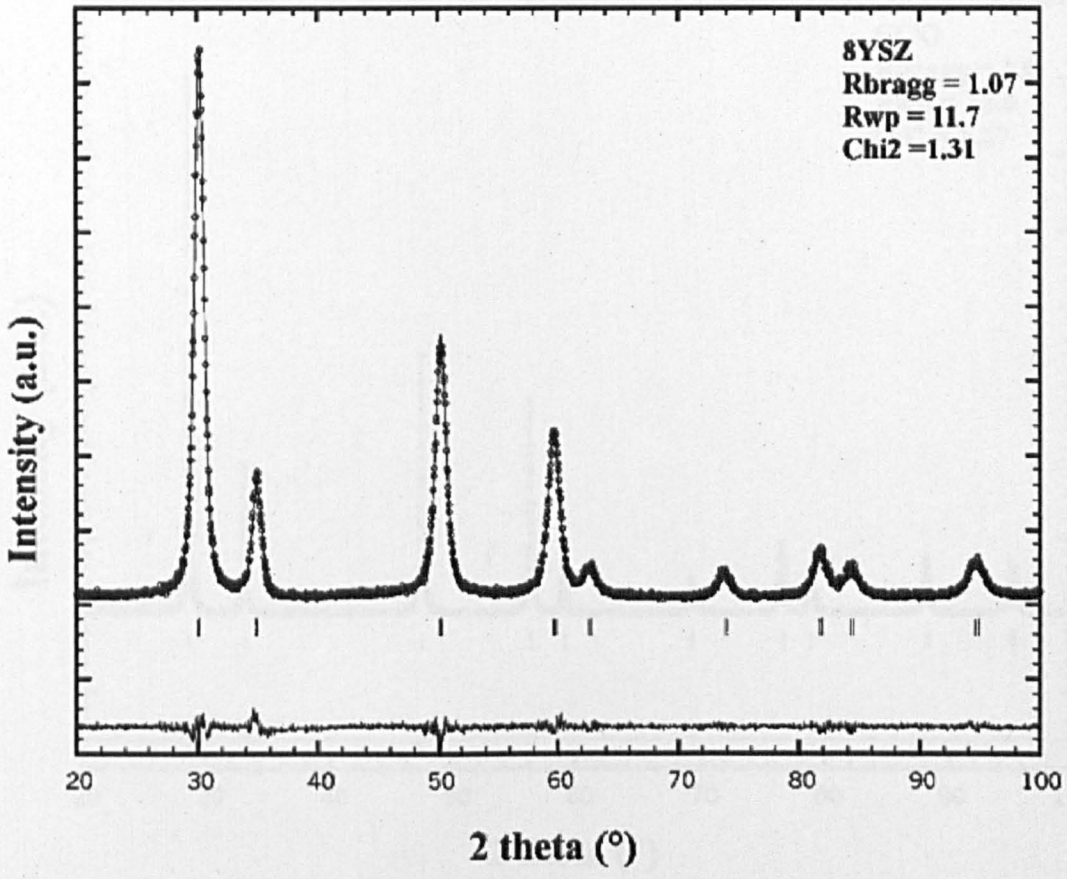

Figure 2.10. XRD Rietveld refinement pattern of 8YSZ [29].

2.2.2. CGO

Gadolinium doped ceria (CGO) was an ideal candidate for IT-SOFCs due to its high conductivity (~0.1 Scm^{-1}) at relatively low temperature (500 °C). Various methods had been applied to obtain CGO nanopowders in a relatively quick, cost effective and environmental friendly manner.

Tarancón *et al.* [29] obtained $Ce_{0.8}Gd_{0.2}O_{1.9}$ (CGO2) nanopowders using polyacrylamide gel-combustion process. An aqueous solution of acrylamide (CH_2=$CHCONH_2$) was used as a chelating agent. After microwave oven dried and thermal heat treatment, the mean crystal size was ~35 nm calculated by XRD Rietveld refinement as shown in Figure 2.11. TEM

images further confirmed the calculation from XRD Rietveld refinement. Although this sol-gel process produced single phase CGO2 nanopowders due to homogeneous distribution of Ce^{3+} and Gd^{3+} metal cations in aqueous solution, the chelating agent was relatively expensive for commercial production.

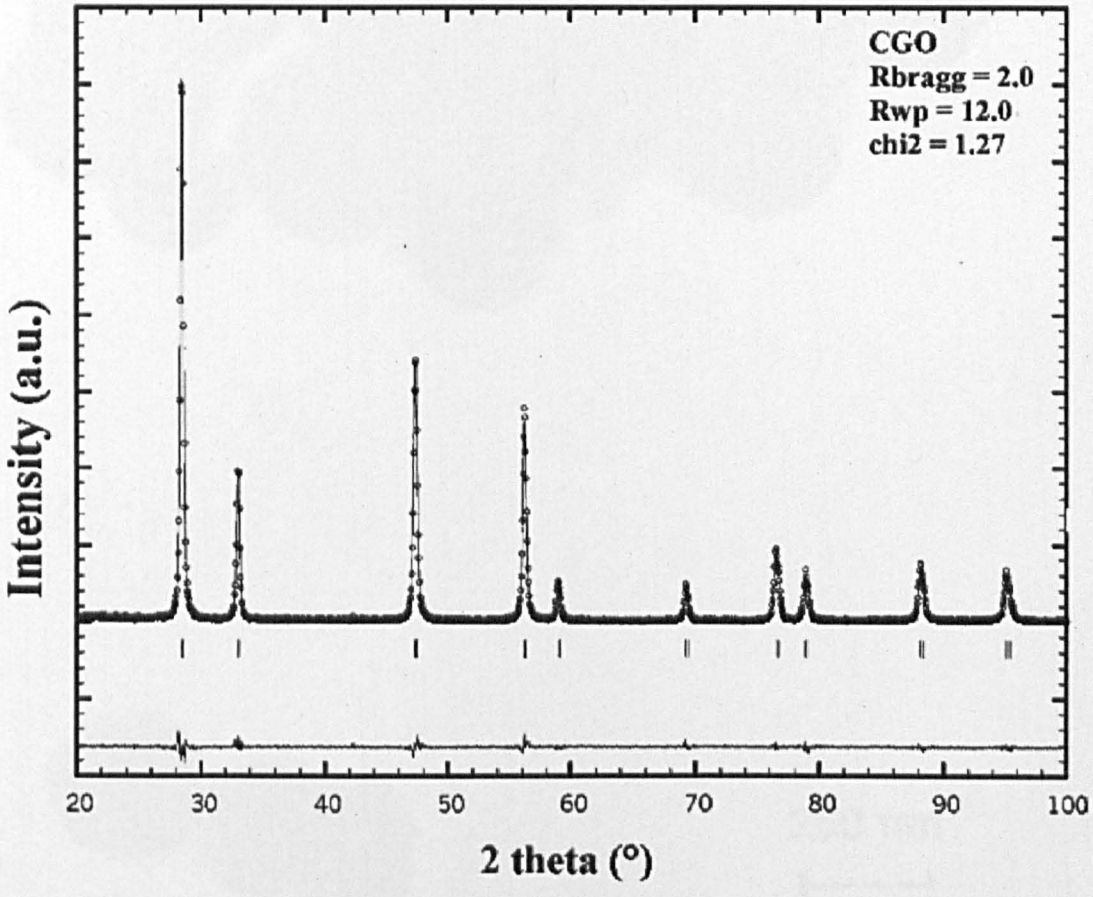

Figure 2.11. XRD Rietveld refinement pattern of CGO2 [29].

Huang *et al.* [10] synthesized $Ce_{0.9}Gd_{0.1}O_{1.95}$ (CGO1) nanopowders by conventional ceramic solid state method and sol-gel process with nitric acid and ethylene glycol. The researcher did not report the particle size obtained from conventional solid state method, but an average diameter of 250 nm (see Figure 2.12) CGO nanopowders were obtained from sol-gel method.

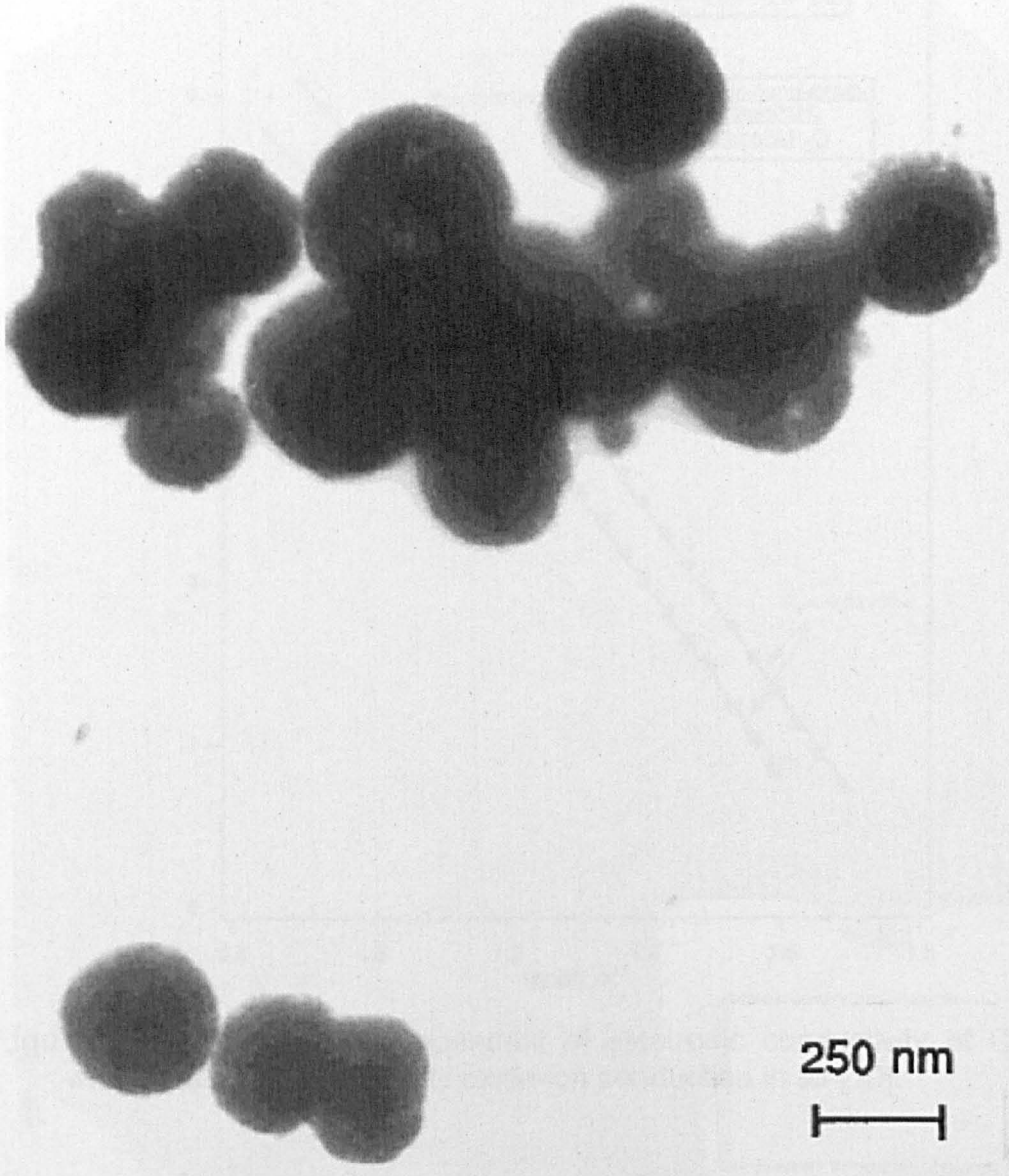

Figure 2.12. TEM picture of CGO1 particles prepared from sol–gel process and calcined at 700 °C [10].

The obtained nanopowders were pressed into pellets and sintered to 99% of the theoretical value. Five different atmospheres were chosen: air, Ar, Ar + 2% H_2, Ar + 10% H_2 and H_2 + 3% H_2O to measure the electrical conductivity of CGO1 in temperature range 320 °C≤ T ≤ 800 °C. The activation energy E_a in Ar + 10 vol.% H_2 and H_2 + 3 vol.% H_2O conditions as shown in Figure 2.13.

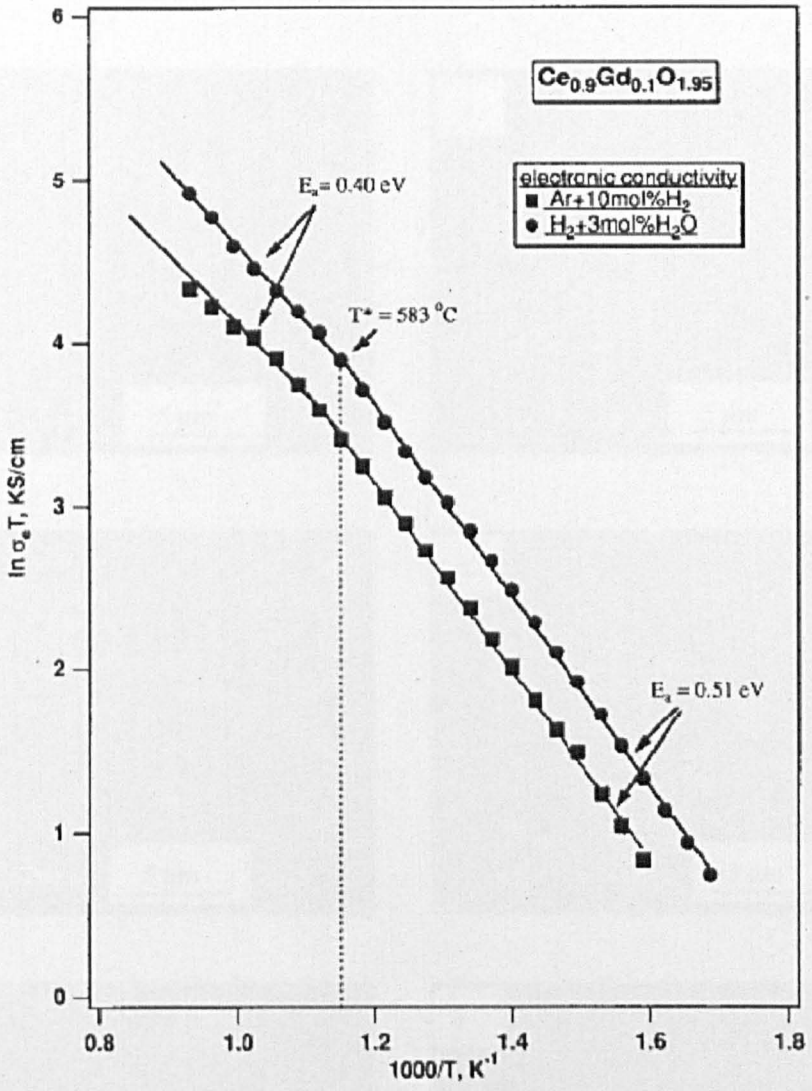

Figure 2.13. Temperature dependent of electronic conductivity of CGO1 with the assumption of only oxide-ion conduction in air [10].

Ma *et al.* [30] produced $Ce_{0.8}Gd_{0.2}O_{2-\delta}$ (CGO2) by conventional ceramic solid state method with Gd_2O_3 (mean diameter ~550 nm) and CeO_2 (mean diameter ~500 nm) as starting materials, and determined the sintering temperature to CGO2 compound. It was found that the dissolution of Gd_2O_3 in CeO_2 was completed at 1600 °C for 5 hours. The addition of Gd_2O_3 increased sintering temperature, retarded densification, and also depressed grain growth as compared with un-doped CeO_2. The sample sintered at 1550 °C for 5 hours had the highest grain boundary conductivity. The grain sizes of CGO2 after different sintering conditions were observed by SEM and shown in Figure 2.14. The activation energy E_a = 0.986, 0.920 and 0.915 eV after sintered at 1500, 1550 and 1600 °C, respectively [30]. The disadvantage of the solid state method was that large grain growth was observed during processing.

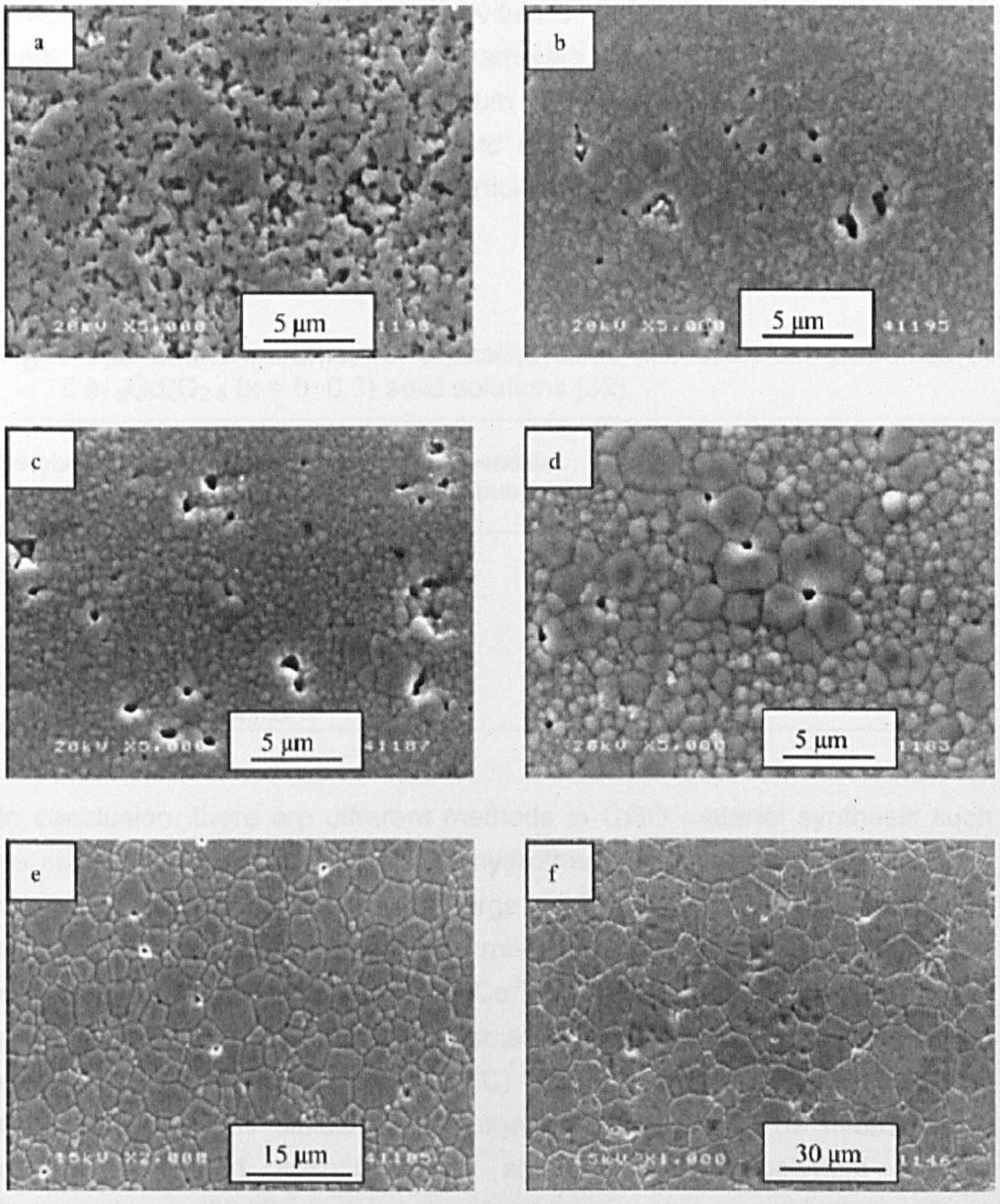

Figure 2.14. SEM of CGO2 sintered in air for 5 hrs at (a) 1300 °C, (b) 1400 °C, (c) 1500 °C, (d) 1550 °C, (e) 1600 °C and (f) 1700 °C, respectively [30].

Castillo *et al.* [31] obtained $Ce_{1-x}M_xO_{2-\delta}$ (M = Gd, Sm or Y; x = 0 ~ 0.2) nanopowders using a radio frequency inductively coupled plasma reactor. The obtained nanopowders were single phase with mean particle size ~25 nm. This synthesis method is quick, but expensive which is not suitable for commercial production.

Dikmen et al. [32] synthesized $Ce_{1-x}Gd_xO_{2-\delta}$ (x = 0–0.3) nanopowders by hydrothermal process. The conductivities of CGO of various compositions were measured in air. Different parameters were shown in Table 2.2. In these CGO composites, the maximum conductivity, $\sigma_{600\ °C} \sim 7.53 \times 10^{-3}$ Scm^{-1} with Ea = 0.58 eV, was found at x = 0.25. Although hydrothermal synthesis method produced small particles, it usually required long time heat treatment.

Table 2.2. Lattice parameters, crystallite sizes and electrical properties of $Ce_{1-x}Gd_xO_{2-\delta}$ (x = 0–0.3) solid solutions [32].

Composition x	Lattice parameter a (nm)	Aver. Crystallite size D (nm)	Conductivity $\sigma_{600\ °C}$ (Scm^{-1}) (± 5%)	Activation energy Ea (eV) (± 0.05)
0	0.54120(5)	50	1.10×10^{-5}	1.03
0.05	0.54156(2)	50	1.86×10^{-5}	1.01
0.10	0.54194(4)	46	3.31×10^{-4}	0.99
0.15	0.54225(2)	68	1.23×10^{-3}	0.97
0.20	0.54260(4)	65	5.09×10^{-3}	0.83
0.25	0.54296(6)	54	7.53×10^{-3}	0.58
0.30	0.54330(7)	41	4.99×10^{-3}	0.80

In conclusion, there are different methods in CGO material synthesis such as solid state method, sol-gel and hydrothermal synthesis. For solid state synthesis, high temperature and large crystal size are usually observed since large energy was required to merge CeO_2 and Gd_2O_3 particles. For sol-gel method, since homogenous Ce^{3+} and Gd^{3+} cations are tracked in a system, it is possible to obtained small nanopowders after calcination at relatively low temperature (~600 °C). However, the chelating agent is expensive which is difficult for commercial production. The hydrothermal synthesis method also produces small CGO nanopowders at low temperature (~200 °C), but long time heat treatment is crucial in this method. Apart from initial starting nano particles, sintering temperature and time are also important to achieve high conductivity because of the compact density, grain size and grain boundary. In IT-SOFCs application, two compositions $Ce_{0.9}Gd_{0.1}O_{1.95}$ (CGO1) and $Ce_{0.8}Gd_{0.2}O_{2-\delta}$ (CGO2) are often being chosen due to their high conductivity. Different parameters of these two compositions of CGO are summarized in Table 2.3.

Table 2.3. Different parameters of $Ce_{0.9}Gd_{0.1}O_{1.95}$ (CGO1) and $Ce_{0.8}Gd_{0.2}O_{1.9}$ (CGO2).

Materials	Synthesis Method	Calcination	Particle Size (nm)	Sintering	Grain Size (μm)	Activation Energy Ea (eV)	Ref.
CGO1	*Sol-gel (ethylene glycol)*	700 °C – 24 hrs	250	1585 °C – 6 hrs	1 ~ 5	0.40 ~0.51	[10]
	Sol-gel (ammonium carbonate)	800 °C – 2 hrs	25	1350 °C – 5 hrs	1 ~ 2	0.85	[11]
	Sol-gel (PVP)	600 °C – 2 hrs	15	1400 °C	1 ~ 5	0.49	[33]
	Hydrothermal	260 °C – 10 hrs	46	1400 °C – 4 hrs	-	0.99	[32]
CGO2	*Sol-gel (acrylamide)*	800 °C – 5 hrs	35	-	-	-	[29]
	Sol-gel (EDTA)	1000 °C – 2 hrs	250	1600 °C – 10 hrs	10 ~ 20	1	[34]
	Solid State	-	500	1600 °C – 5 hrs	10 ~ 15	0.915 ~ 0.998	[30]
	Solid State	-	-	1600 °C – 5 hrs	5 ~ 20	0.826	[35]
	Hydrothermal	260 °C – 10 hrs	65	1400 °C – 4 hrs	1 ~ 1.5	0.83	[32]

Furthermore, Leng *et al.* [3] studied an entire single cell performance made of $Ce_{0.8}Gd_{0.2}O_{1.90}$ electrolyte layer with thickness about 10 μm supported by $Ni/Ce_{0.9}Gd_{0.1}O_{1.95}$ cermet anode. The cathode layer was made of LSCF/CGO material with ~30 μm thickness. High power densities of these samples were observed with 578, 358 and 167 $mWcm^{-2}$ at 600, 550 and 500 °C, respectively. Even higher power density (625 $mWcm^{-2}$ at 600 °C) was achieved by increasing the air flow rate to about 1100 sccm.

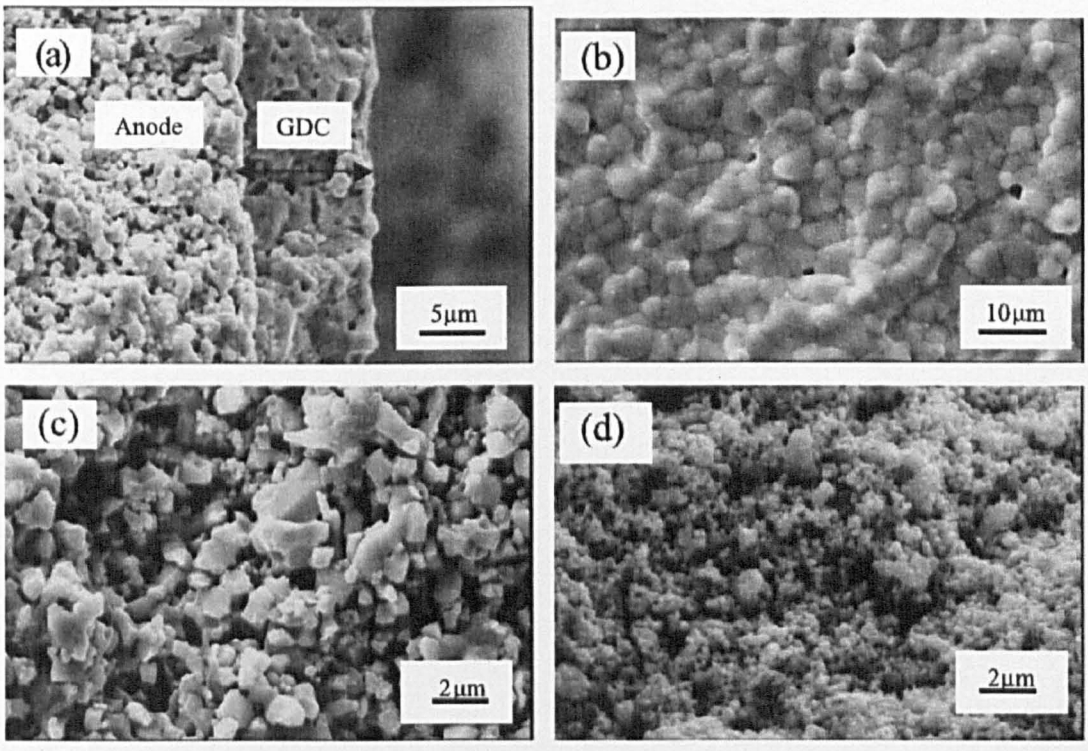

Figure 2.15. SEM of (a) cross-section of anode and electrolyte, (b) surface of electrolyte, (c) cross-section of anode, (d) cross-section of cathode [3].

Xia *et al.* [36] studied an anode supported SOFCs based on $Gd_{0.1}Ce_{0.9}O_{1.9}$ prepared using glycine-nitrate process with Ni/CGO-35 wt.% as anode and SSC/CGO-10 wt.% as cathode. The maximum power density was obtained as 145 and 400 $mWcm^{-2}$ at 500 and 600 °C, respectively. The SEM image of the cross section of a single cell is shown in Figure 2.16.

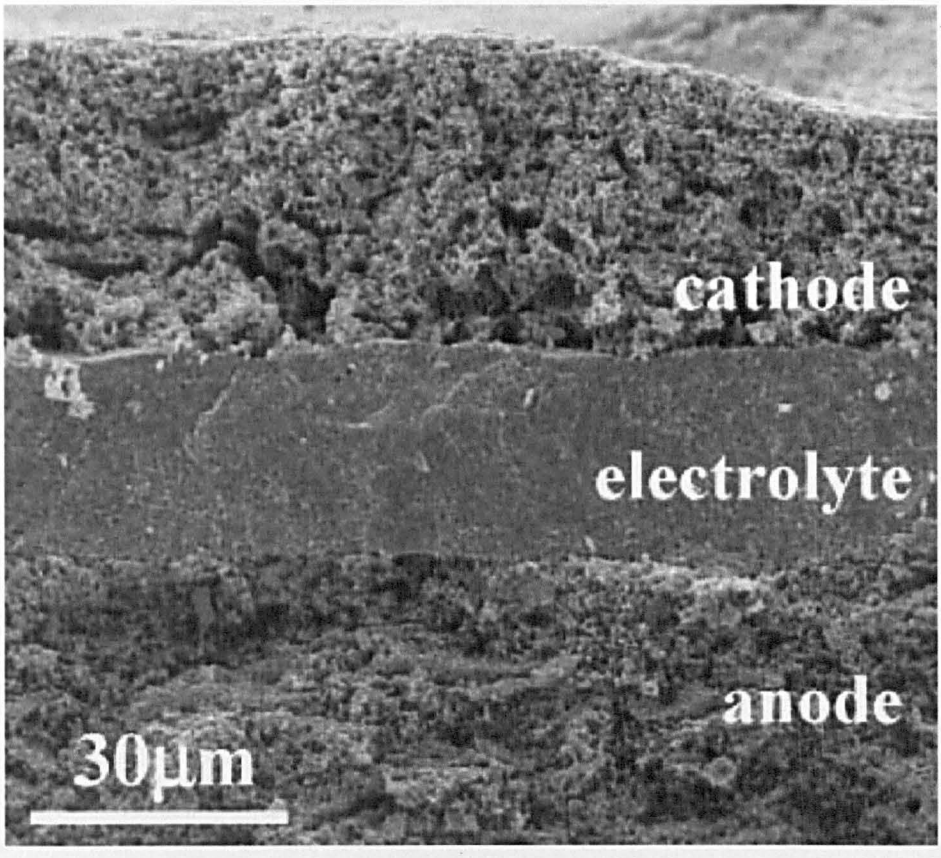

Figure 2.16. SEM cross-section of a single cell [36].

Although excellent performance was obtained from CGO, it had a relatively narrow region of oxide ion conductivity [37]. In order to minimize the instability at low oxygen partial pressures, other ceria based materials with substitution of Gd by Sm, Ca and Mg had been analysis [30, 38-41]. It is now known that the ionic conductivities of ceria based materials depended on the ionic radii of added cation and the most promising system so far was gadolinium doped ceria (CGO).

2.2.3. LSGM

A perovskite oxide, $La_{0.8}Sr_{0.2}Ga_{0.8}Mn_{0.2}O_3$ (LSGM) [42] had a comparable oxide ion conductivity (0.1 Scm^{-1}) with YSZ at intermediate temperature, 550−800 °C. Over a large range of oxygen partial pressures (1−10^{-20} atm), this material showed good chemical stability and negligible electronic conductivity [43]. Thermal expansion coefficient of this material was 17.5 × 10^{-6} K^{-1}. Over time, LSGM had been synthesized by various methods. Tarancon *et al.* [29] investigated nano crystalline LSGM by using sol-gel method. According to XRD pattern, impurity phases such as $La_2Ga_2O_9$, $LaSrGa_3O_7$, $LaSrGaO_4$ and $Sr_2Ga_2O_6$ were obtained between 800 and 1300 °C sintering temperature. (See Figure 2.17)

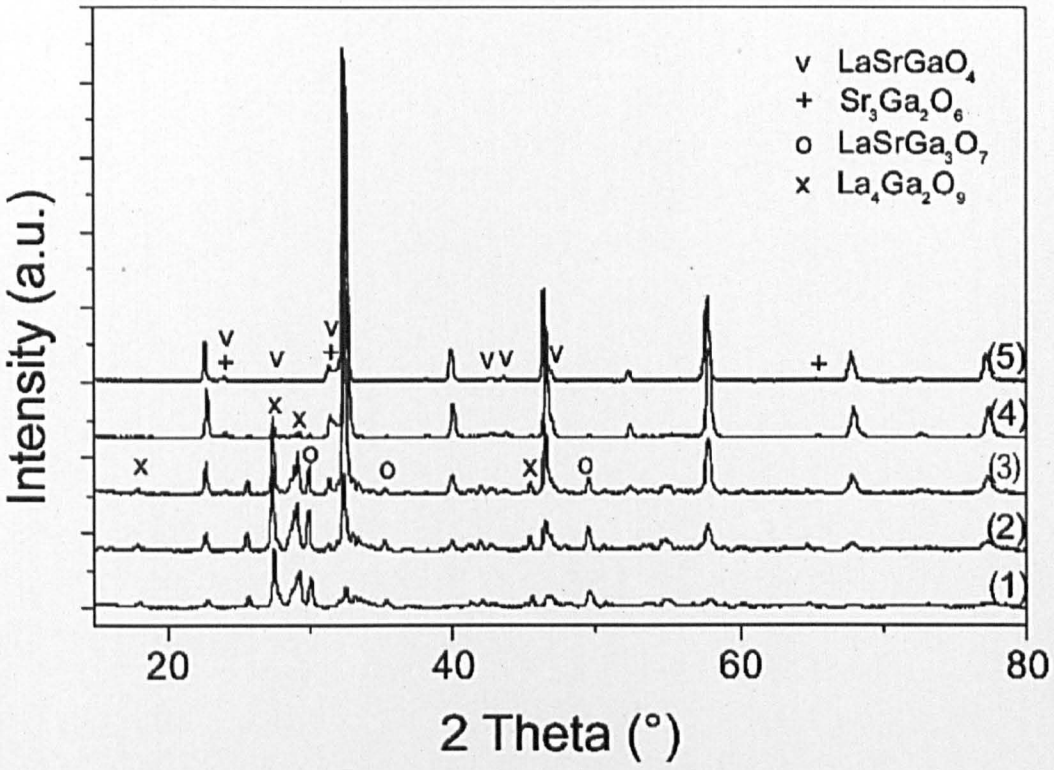

Figure 2.17. XRD patterns of LSGM sintering at (1) 800 °C, (2) 900 °C, (3) 1000 °C, (4) 1100 °C, (5) 1300 °C for 5hrs in static air condition, respectively [29].

Shi *et al.* [44] also synthesized LSGM by using glycine-nitrate combustion method. The XRD pattern indicated that main phase ($LaGaO_3$) existed in all specimens, the impurity phases decreased remarkably with increasing temperature. There were nearly no secondary phases appeared at temperature above 1400 °C. Single phase LSGM could be obtained at lower sintering temperature (~1432 °C) by glycine-nitrate combustion method compared with conventional sol-gel or solid state route. Therefore, the main disadvantages of LSGM were undesired segregation of impurities during synthesis and high calcination temperature. Extensive literature showed that single phase LSGM would be obtained with a calcination temperature up to 1500 °C, depending on the preparation routes [45-47].

2.3 Electrode Materials

Electrodes are critical components in SOFCs in that they provide the interface between the chemical energy associated with fuel oxidation and electrical power. Typically, they are complex structures that consist of a

three phase percolating composite of a metal or mixed conducting oxide, an oxide electrolyte and the pore space. The transport reaction network in such porous structures is very complex and contributions from the various processes and thereby the overall electrode performance has been studied by many groups. Several materials requirements are general to both anodes and cathodes. Both electrodes must have high electro-catalytic activity and electronic conductivity to minimize the effective resistance. The anode acts as an electro-catalyst for the oxidation of fuel components by oxide ions transported through the electrolyte and the cathode catalyzes the oxygen reduction reaction. Electrons produced or consumed by the chemical reactions at the electrode surfaces must be transported from the electrode to the external circuit. The electrodes must also be stable. Because a SOFC is cycled between room temperature and the operating temperature, the thermal expansion of the electrode must be matched to that of the electrolyte and the current collector to give stable interfaces. The electrodes must be chemically stable at the operating temperature with respect to the electrolyte and the current collector and must have stable microstructures under operating conditions with respect to both porosity and surface area [23].

2.3.1 Anode

In SOFC, metal catalyst such as Ni is usually applied into anode electrodes to increase the reaction rate during operation. An interface is generated with electrolyte, catalyst and porous electrode in order for electrons, oxygen ions and fuel gas to present in the same electrochemically active area. This area represents as Triple Phase Boundary (TPB) which extensively affects the total performance of the cell. At the anode electrolyte interface, the O^{2-} ion (coming from the electrolyte) gives up two electrons and, simultaneously, together with H_2 (from fuel, coming from the anode pores) formed water molecule. It is well known that the electrochemical reaction can only occur at the TPB. If ions from the electrolyte does not appear at the reaction area, if fuel molecules do not reach to the reaction area, or if electrons cannot be removed from the reaction area, there is no electricity contribution from the cell. Therefore, more and more studies are concentrated on the relationship between TPB and total performance of the fuel cell. A schematic diagram of TPB is shown in Figure 2.18.

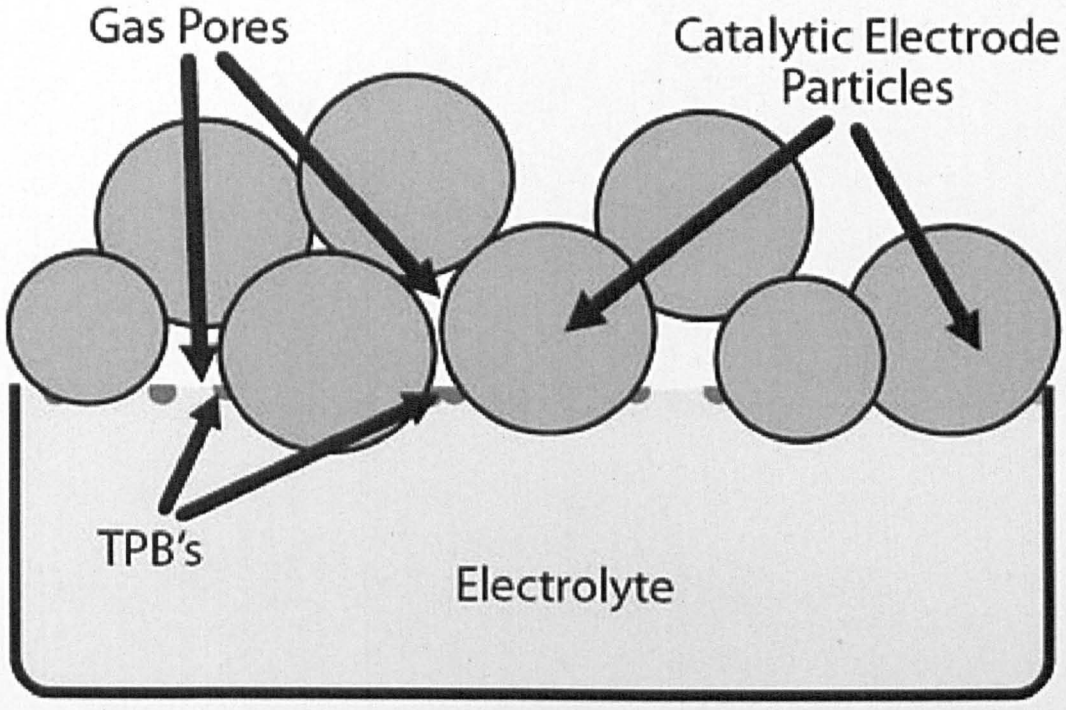

Figure 2.18. Schematic diagram of electrode/ electrolyte interface.

In order to increase the TPB area, introduction of an intermediate layer between anode and electrolyte is investigated as shown in Figure 2.18. This layer not only increases the electrochemically active area, but also reduces the mismatch in thermal expansion coefficients between anode and electrolyte. Another way is to increase the size of TPB geometrically by using nano particles during electrode and electrolyte synthesis. However, the porosity of the anode layer decreases by using smaller starting particles. Thus, careful design of the microstructure in SOFC preparation is important.

Furthermore, in order to minimize the polarization losses of H_2 oxidation reaction, anode materials should meet the basic requirements of high electronic conductivity, sufficient electro-catalytic activity, chemical stability and thermally comparable with other cell components [48]. Some anode materials are discussed below.

The state of the art anodes used with YSZ electrolytes were composites of nickel metal with YSZ as the ionic conducing component. Conventional Ni/YSZ cermet anodes were usually made by commercial NiO and YSZ powders. Mechanical mixing and ball milling were required to homogenize these powders. The mixture powders were then sintered to form dense NiO/YSZ cermet. After reduction heat treatment, usually under H_2 and N_2

gas mixture, porous Ni/YSZ electrode was obtained. Large amount of research findings [49-51] indicated that the performance of Ni/YSZ cermet anode was critically dependent on the microstructure and distribution of Ni and YSZ phases [49-51]. Therefore, the fabrication route, characteristics of starting NiO and YSZ powders and sintering behavior were crucial for Ni/YSZ anode production.

The electrochemical performance of Ni/YSZ anode was significantly influenced by the starting NiO and YSZ powders. This was due to the particle properties, such as average particle size, particle size distribution and sintering behavior of NiO and YSZ starting powders varied from different suppliers. Eight different commercial NiO powders had been evaluated by Tietz and his co-workers [4]. The average grain size after sintering varied greatly from 0.5 to 14.7 μm. (see Figure 2.19) The density difference Δd (%) of NiO powder ranged from 5.8 to 47.8% after 10 hours sintering at 1400 °C. The maximum shrinkage rate occurred at temperature range between 447 and 1400 °C. In general, high surface area corresponded to high shrinkage and low starting sintering temperature. Similar to commercial 3 and 8 mol% YSZ powders, the characteristics of starting powders also varied considerably from different suppliers. Ciacchi *et al.* [52] found that the specific surface areas of commercial 3YSZ powders change from 7.5 to 17 m^2g^{-1} and 8YSZ from 8.6 to 26 m^2g^{-1}, respectively.

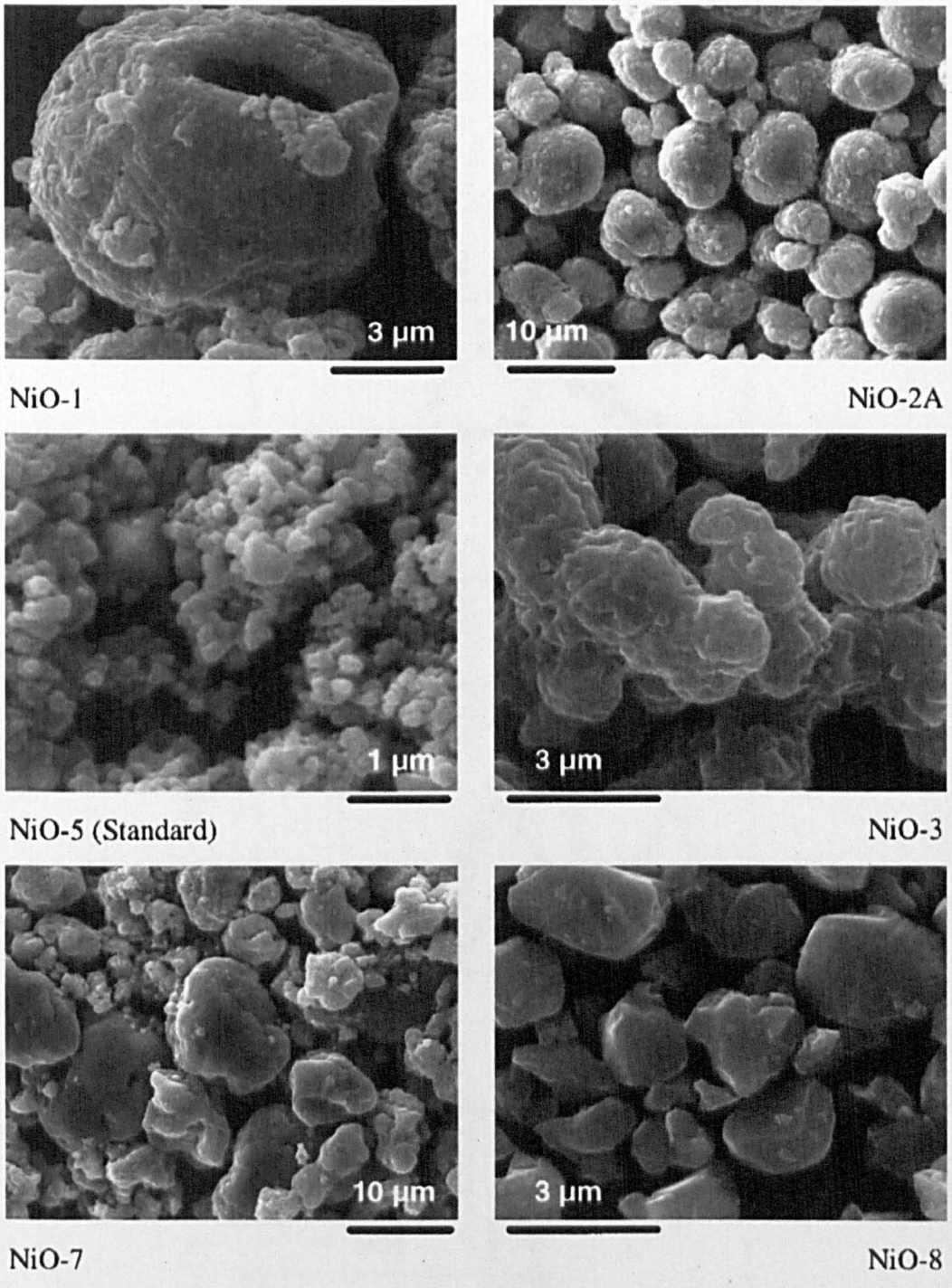

Figure 2.19. Eight different particle morphologies of NiO powders [4].

Coarsening treatment of starting powder was also important in Ni/YSZ anode preparation to control particle size distribution and shrinkage profile for high quality Ni coating. In practice, careful heat treatment of starting NiO and YSZ powders controlled the sintering profile of the cermet powder. The effect of coarsening NiO powders on the polarization performance of Ni/3YSZ anodes was studied by Jiang *et al.* [53]

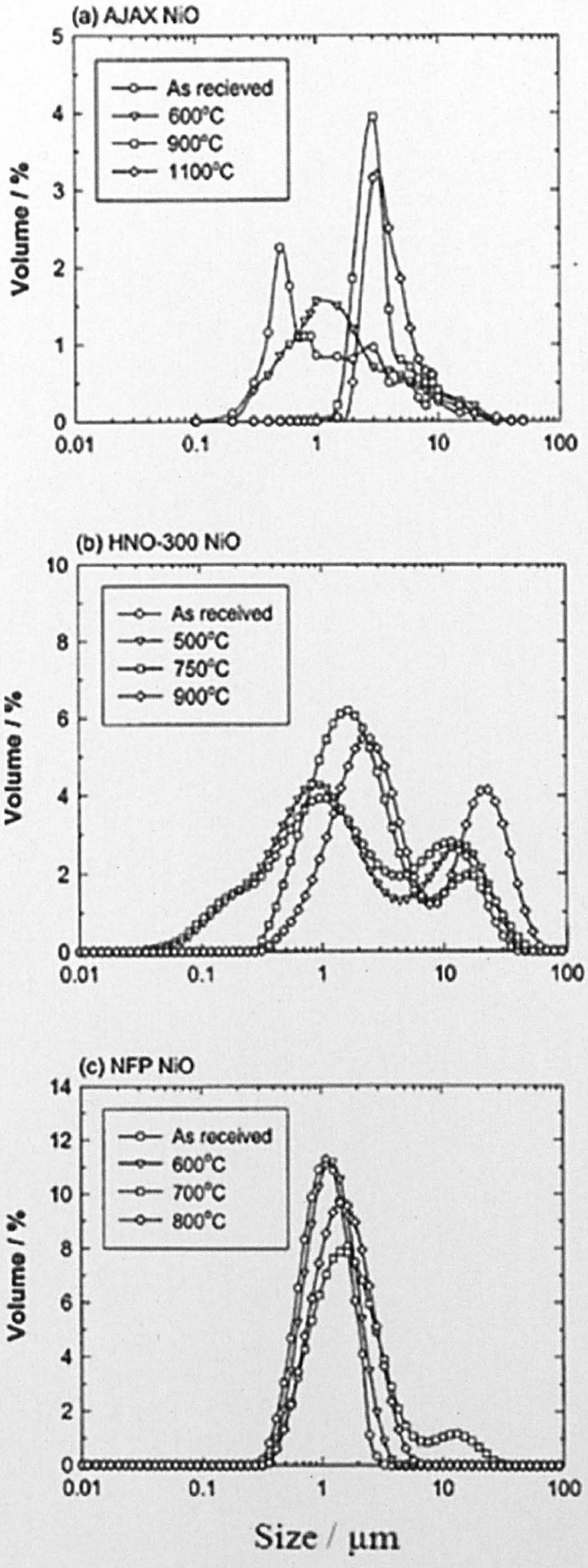

Figure 2.20. Change of particle size distribution of NiO as a function of coarsening temperature for three different commercial NiO powders (a) AJAX NiO, (b) HNO-300 NiO, (c) NFP NiO [54].

Figure 2.20 illustrated a typical particle size distribution of NiO as a function of coarsening temperatures for three commercial NiO powders. As-received AJAX NiO powders showed fine particles with broad particle size distribution. (See Figure 2.20a) Average particle size was measured as ~1 μm. At 900 °C, AJAX NiO powder dramatically changed indicated by the increased average particle size and narrowed particle size distribution. The NFP NiO powder, as shown in Figure 2.20c, had narrow particle size and normal distribution of the particle. The average particle size was increased by coarsening heat treatment. The characteristics of starting NiO powders in relation to coarsening treatment had direct effect on the electrode performance. For Ni/3YSZ cermet anodes prepared from AJAX NiO powder, the polarization losses reached minimum at coarsening temperature ~600 °C. (See Figure 2.21a) For HNO-300 NiO powder, the polarization losses remained more or less the same with coarsening temperature below 900 °C as shown in Figure 2.21b [53].

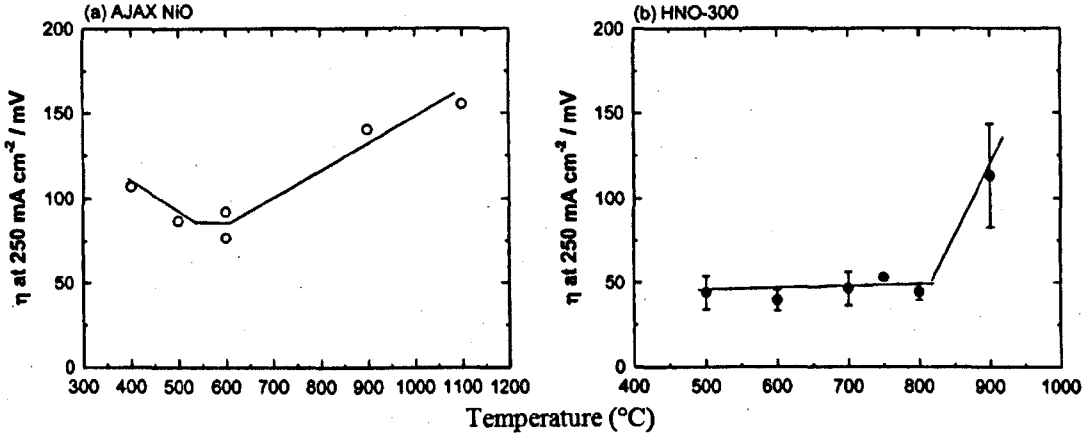

Figure 2.21. Electrode performance of Ni/3YSZ (50 vol.%) cermet anodes as a function of coarsening temperature of (a) AJAX NiO and (b) HNO-300 NiO. Over-potential was measured under a current density of 250 $mAcm^{-2}$ at 1000 °C in 97% H_2 / 3% H_2O [53].

The fundamental reason for this significant difference in heat treatment effect on Ni/YSZ cermet anode performance was related to the YSZ sintering behavior. In the case of YSZ powders, the sintering behavior was corresponded to yttria content. The figure below (Figure 2.22) indicated the change of average particle size of Tosoh 3 and 8YSZ powders and AJAX NiO with different heat treatment temperatures [55]. There was a significant grain growth observed for 8YSZ powders above 1200 °C. This indicated that the 8YSZ grain growth kinetics were much faster compared with the one

from 3YSZ and NiO powders. Matsushima *et al.* [56] studied the effect of sinterability of 8YSZ powders on the electrode performance of Ni/8YSZ cement anodes. 8YSZ had shrinkage rate of 26.8% compared with NiO powders at 15.6%. However, the sintering profile of NiO/8YSZ cermet was primarily dominated by 8YSZ phase rather than NiO phase. The maximum sintering rate for 8YSZ occurred at ~1300 °C which was similar to Jiang's data [55]. As suggested by Lange *et al.* [57], maximum sintering rate corresponded to a transition from densification kinetics to grain growth kinetics. Therefore, comparable grain growth kinetics of 8YSZ and NiO powders benefited the establishment of Ni-Ni contact in the cermet. This resulted in significant reduction in electrode ohmic resistance during coarsening cermet powder preparation.

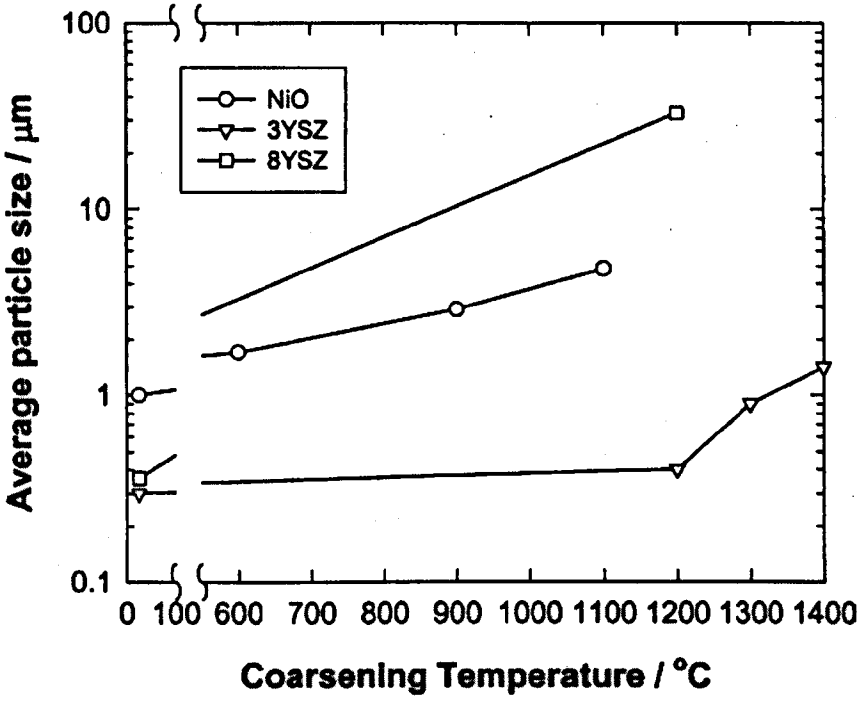

Figure 2.22. Change of the average particle size of Tosoh 3YSZ, Tosoh 8YSZ and AJAX NiO powders with coarsening temperature [55].

Sintering of Ni/YSZ cermet coating at high temperature such as 1400 °C was essential to achieve high electrode performance and low electrode ohmic loss resistance. Fukui *et al.* [58] studied the sintering behavior of Ni/YSZ cermet anodes prepared by spray pyrolysis. The researcher used NiO/8YSZ which was printed on an YSZ electrolyte with LSM as cathode on the other side. The single cell obtained by this method was operated in a condition of 97%H_2/3%H_2O for anode and air for cathode with various operating

temperatures. In this atmosphere, NiO/8YSZ was reduced to Ni/8YSZ to form anode at the first stage. The best performance of this cell was observed at about 1350 °C with lowest IR and polarization losses. SEM indicated that the Ni/YSZ anode had high homogeneous porous structure with fine YSZ and Ni grains as shown in Figure 2.23. These highly dispersed fine grains contributed to the total length of TPB, therefore high performance was obtained.

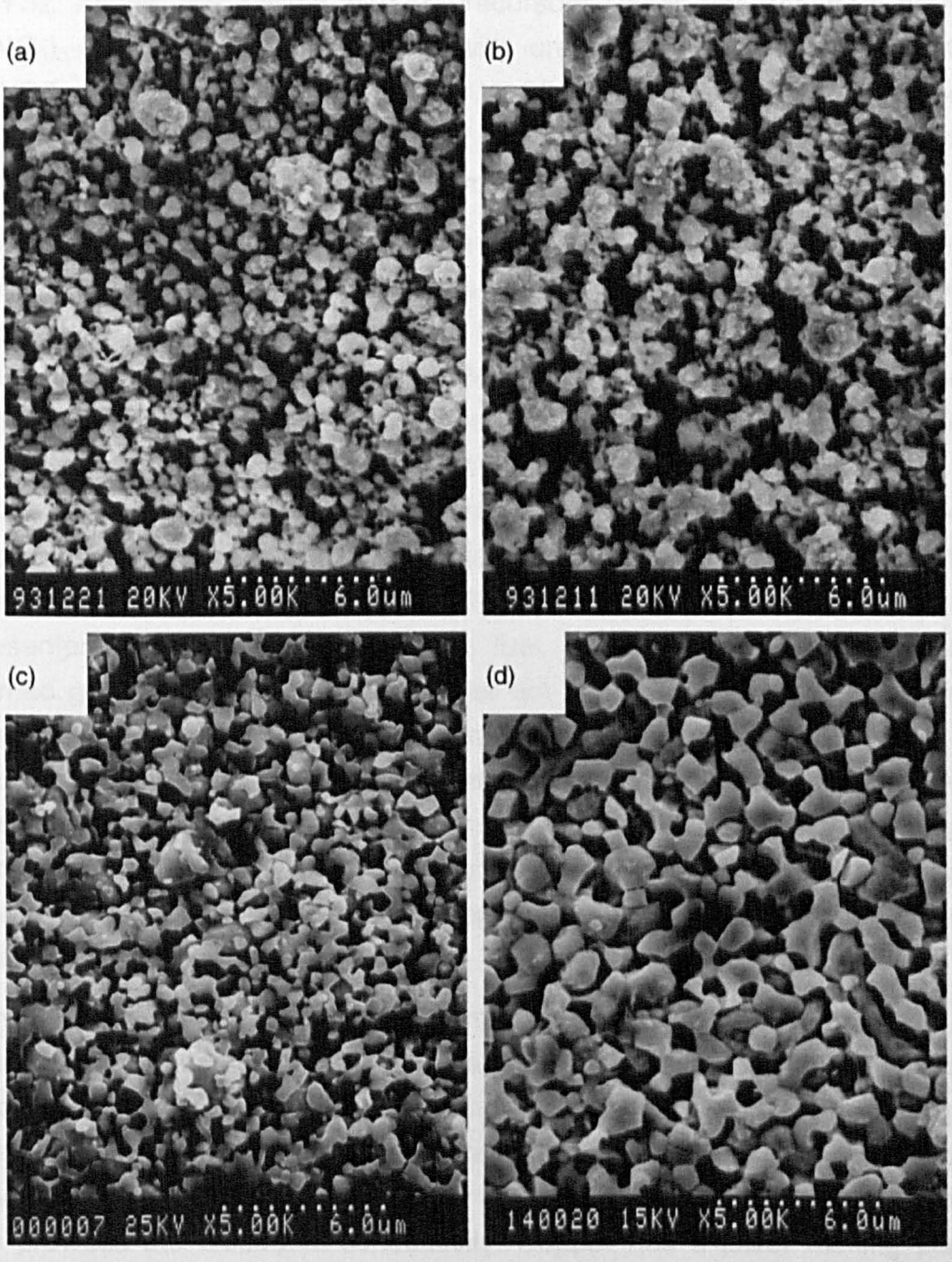

Figure 2.23. SEM of Ni-YSZ cermet anode fabricated at various sintering temperature of (a) 1200 °C, (b) 1300 °C, (c) 1350 °C and (d) 1400 °C from NiO/YSZ cermet, respectively [58].

Furthermore, apart from conventional ceramic mixing process based on commercial NiO and YSZ powders, Aruna *et al.* [59] used nickel nitrate, yttrium nitrate and zirconium nitrate to prepare Ni/YSZ by combustion synthesis method. The as-formed cermet powders were fine with average agglomerated particle size in a range of 0.25−0.8 μm. The best performance was achieved with high electrical conductivity (40 Sm^{-1}) and low thermal expansion coefficient about 11.64 × 10^{-6} K^{-1} with Ni content≤ 30 vol.%. Ringuede *et al.* [60, 61] also used combustion synthesis method to produce Ni/YSZ anode. By mixing nitrate precursors, such as $ZrO(NO_3)_2 \cdot 6H_2O$, $Y(NO_3)_3 \cdot 6H_2O$ and $Ni(NO_3)_2 \cdot 6H_2O$ with urea $CO(NH_2)_2$ on a hot plate, Ni/YSZ was obtained after combustion at 600 °C. The electrode polarization resistance was measured to be 0.2 Ωcm^2 at 1000 °C. This value was comparable to conventional oxide powder cermet.

Although at present Ni/YSZ are the best and most widely used anode materials, there were known problems such as sulfur poisoning and carbon deposition by using hydrocarbon fuels. Under high carbon activity environment Fe, Ni, Co and their related alloys were corroded by a process called metal dusting. Metal dusting involved disintegration of bulk metals and alloys into metal particles at high temperatures, between 300 and 850 °C, in environment that were supersaturated carbon [54]. The operation temperature and gas composition seriously influenced the Ni corrosion rate. The higher the temperature, the higher carbon deposition rate was presented. By using wet methane as fuel, carbon deposited onto Ni and formed graphite. More seriously, it was not possible to burn the deposited graphite by electrochemically permeated oxygen. Furthermore, at temperature below 700 °C, nickel particle converted back to nickel oxide because of high oxygen partial pressure. This resulted as volume change and caused instability of Ni/YSZ anode microstructure. Therefore, Ni/YSZ became un-suitable for IT-SOFC application with operation temperature between 500 and 700 °C.

Several approaches to limit carbon formation on anode materials have been taken. One approach has been to replace the Ni component with Cu. Copper does not catalyze carbon formation and does not play a role in the electro-catalysis but it is effective as a current collector. To achieve reasonable power densities, it is necessary to add cerium oxide as an oxidation catalyst; Cu provides the electronic conductivity. Copper has a lower melting point than nickel, and consequently, Cu-containing anodes have to be used at lower temperature to avoid loss of surface area [62, 63].

One way of enhancing the activity and stability of Cu-based anodes involves alloying the Cu with a second metal such as Ni or Co that have higher catalytic activities [23]. Kim *et al.* [64] examined the use of Cu-Ni alloys as anodes for the direct oxidation of methane in YSZ solid-oxide fuel cells at 800 °C and demonstrated that carbon formation was greatly suppressed on the alloys compared to pure Ni. In a similar way, anodes containing mixtures of Cu and Ni or Cu and Co showed improved performance in H_2 at 700 °C compared to Cu-based anodes and decreased carbon formation in n-butane compared to Ni- or Co-based anodes.

On the other hand, doped ceria materials had been largely investigated as alternative electrodes or electrolytes to replace YSZ for IT-SOFC applications. The major problem with ceria as the anode or electrolyte material was the reduction of Ce^{4+} to Ce^{3+} under the fuel rich conditions, introducing electronic conductivity and lattice expansion. The introduced electronic conductivity under fuel reducing environment had been explored for the anode application as it had been shown that CeO_2 anode could electrochemically oxidize dry methane as the presence of mobile lattice oxygen reduces the rate of carbon deposition. The high electro-catalytic activity of ceria-based materials for methane oxidation was most likely due to the extraordinary ability of ceria to store, release and transport oxygen ions.

Marina *et al.* [65] described the application of $Ce_{0.6}Gd_{0.4}O_{1.8}$ as the anode for both H_2/H_2O and CH_4/H_2O oxidation reactions at 800–1015 °C. In order to improve the adhesion between CGO electrode and YSZ electrolyte, an intermediate layer of coarse grain YSZ was deposited on YSZ electrolyte. An area specific internal resistance of 0.39 Ωcm^2 and a power density of 470 mW/cm^2 was observed at 1000 °C using $H_2/H_2O/N_2$ = 9/1.2/89.8 as fuel. In contrast, an area specific internal resistance of 2 Ωcm^2 and a power density of 80 mW/cm^2 for CH_4 were obtained. No carbon deposition and degradation was found on these specimens after a full redox cycle compared with Ni/YSZ.

Uchida *et al.* [66] studied the electro-catalytic activity of mixed conducing oxides of Sm-doped CeO_2 (SDC) and Y-doped CeO_2 (YDC) for the H_2 oxidation with and without addition of Ru. At 800 °C, a performance of 0.2–0.25 Acm^{-2} was obtained on SDC and YDC anodes. The current increased to 0.4–0.5 Acm^{-2} with addition of fine Ru particles.

Overall, to develop alternative anodes for direct oxidation of hydrocarbon fuels with volume stable, high electronic and ionic conductivity anode for low temperature SOFC became the main targets for materials chemists [54].

2.3.2 Cathode

The SOFC cathode has received extensive attention, as it is the component which contributes significantly to the overall resistance. Large amounts of different materials have been studied in order to reduce the cathodic polarization. Most of the state of art cathode materials consist of active perovskite type oxides with lanthanum based composition substituted with Sr on the A-site to introduce oxygen vacancies to facilitate oxygen transport. In addition, significant level of electronic conductivity is required for this compound and hence transition metal perovskites are also employed. In this report, two different series of cathode materials including $Ln_{1-x}Sr_xFe_{1-y}Co_yO_{3-\delta}$ (Ln = La, Sm, Nd, Gd and Dy) or $Ln_{1-x}A_xM_{1-y}Mn_yO_{3-\delta}$ (Ln = La, Nd and Pr, A = Ca and Sr, M = transitional metal) are discussed in details [24].

$Ln_{1-x}Sr_xFe_{1-y}Co_yO_{3-\delta}$ was a series of materials where Ln = La, Sm, Nd, Gd and Dy. The use of lanthanum cobaltate materials, mainly LSC and LSCF, had been extensively studied as possible cathodes.

The $La_{1-x}Sr_xCoO_{3-\delta}$ (LSC) perovskite materials [48] were proved to have considerable oxide ion conductivity and high electronic conductivity which made them as mixed ionic – electronic conductors. The operating conditions and the choice of electrolyte could seriously influence LSC performance in SOFC. For example, it reacted with zirconia and formed poorly conducting inter-phase (La_2ZrO_7 or $SrZrO_3$) and thus, there was little use with YSZ electrolyte. Hwang *et al.* [67] synthesized LSC using sol-gel method. Mixed La-nitrate, Sr-chloride and Co-nitrate with 2-methoxy ethanol were deposited onto different substrates. The final thickness of LSC films was about 0.7−0.8 μm confirmed by XRD. Fine crystalline LSC was observed by SEM as shown on Figure 2.24.

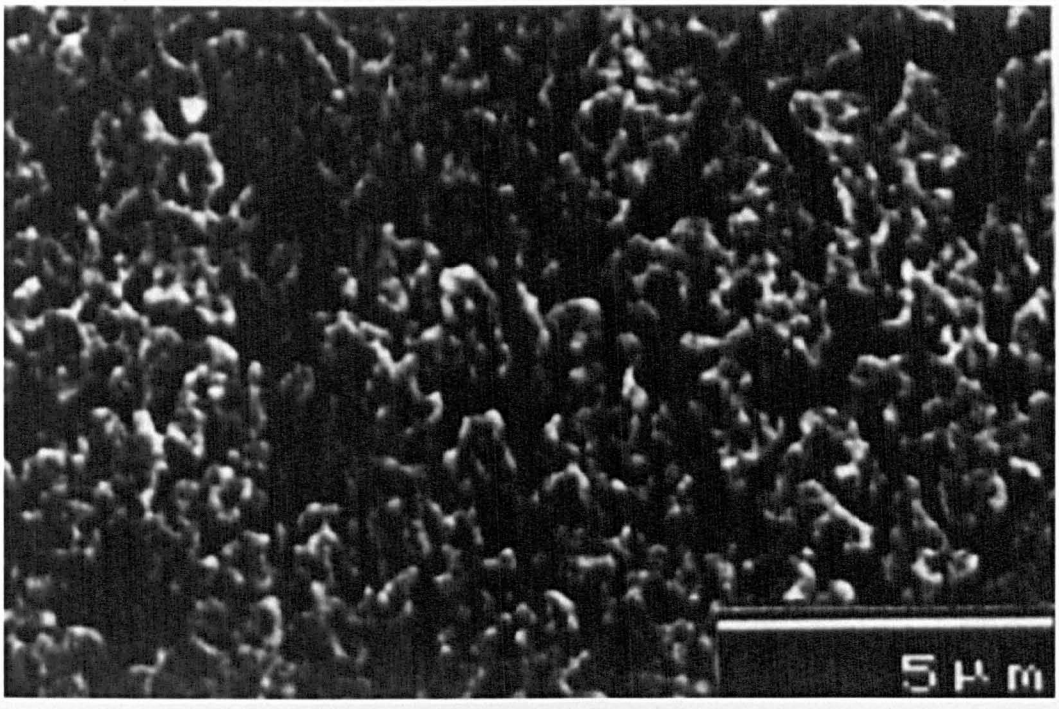

Figure 2.24. SEM of the surface of LSC/MgO annealed at 800 °C [67].

Further development of perovskite cathode was to produce SOFC device thin films using Flame-assisted Vapor Deposition (FAVD) [68]. This technique enabled many layered devices to be constructed enhancing the overall performance of the cell. In this paper, standard LSC/CGO, LSC/YDC/YSZ and LSC/CGO/YSZ had been studied. It was found that the electrode/electrolyte interfacial resistance was reduced significantly, lowest measured values of 0.017 and 0.0036 Ωcm^{-2} at 800 and 900 °C for LSC/CGO/YSZ.

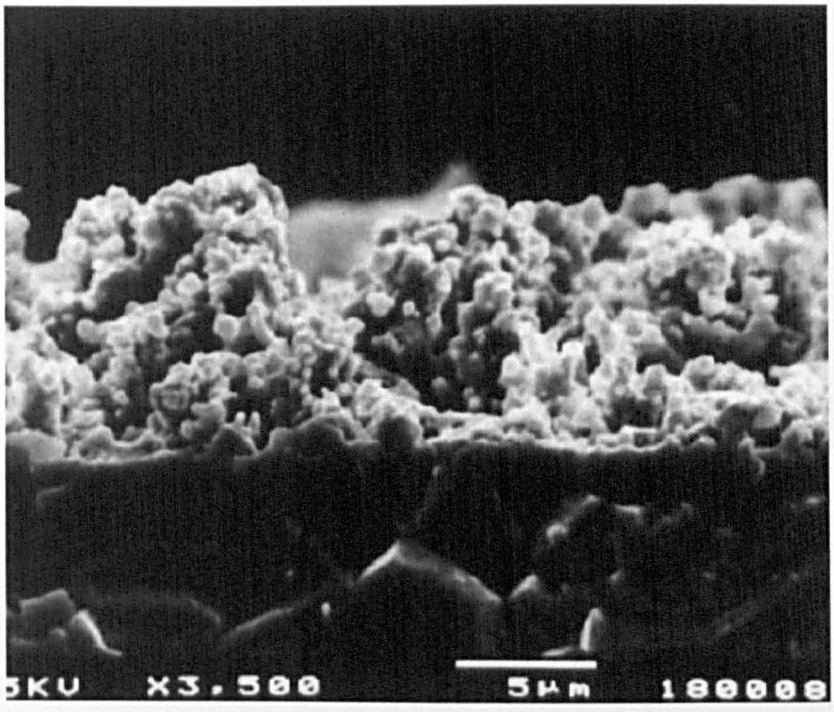

Figure 2.25. Cross-section of LSC/CGO/YSZ [68].

Tai *et al.* [69, 70] carried out some substantial studies of $La_{1-x}Sr_xCo_{1-y}Fe_yO_3$ (LSCF) perovskite materials. The characteristic of these materials structure such as identifying the rhombohedral / orthorhombic transition at y = 0.8 for the x = 0.2 composition and the thermal expansion coefficient (~20.0 × 10^{-6} K^{-1}) had been evaluated. In electrical property measurements, these researchers found out that the conductivity decreased with decrease in Fe content. In addition, the effect of the La:Sr ratio was also involved with remarkable effect on the performance on these materials. The peak conductivity of LSCF was ~350 Scm^{-1} at x = 0.4 composition which compared with ~160 Scm^{-1} for x = 0.2 at 550 °C. In conclusion, they suggested a composition of $La_{0.6}Sr_{0.4}Co_{0.8}Fe_{0.2}O_3$ would be a suitable candidate for cathode material.

Variation of the Fe:Co ratio had been studied in the $La_{0.84}Sr_{0.16}Co_{1-y}Fe_yO_3$ composition and the effect on performance when it was used as cathode on CGO electrolyte by Maguire *et al.* [71]. At the ratio of Fe:Co = 0.3:0.7, a conductivity of 643 Scm^{-1} at 800 °C was reported, which steadily increased over the 200−800 °C temperature range.

Investigation of the effect of LSCF thermal expansion performance was carried out by Kostogloudis *et al.* [72] there was a significant improvement in performance observing with increasing A-site deficiency. Although the electrical conductivity was found to decrease slightly as the Sr content

decreased, the thermal expansion coefficients were found to be lowest for $La_{0.6}Sr_{0.2}Co_{0.2}Fe_{0.8}O_{3-\delta}$ with value 13.8 × 10^{-6} K^{-1} at 700 °C. Furthermore, Tu *et al.* [73] had performed a study of a series of LSCF materials in which the Fe:Co ratio was maintained at 0.8:0.2 but the type of lanthanide ion varied. Their findings indicated that all compositions had a high electrical conductivity with $Nd_{0.6}Sr_{0.4}Co_{0.8}Fe_{0.2}O_{3-\delta}$ having the highest conductivity ~600 Scm^{-1} at 400 °C. However, the thermal expansion coefficients were still high.

Whilst a significant amount of work has been carried out on the $Ln_{1-x}Sr_xFe_{1-y}Co_yO_{3-\delta}$ materials, further research has focused on another significant class of materials which was $Ln_{1-x}A_xM_{1-y}Mn_yO_{3-\delta}$ perovskites. $Ln_{1-x}A_xM_{1-y}Mn_yO_{3-\delta}$ was a range of materials where Ln = La, Nd and Pr, A = Ca and Sr and M = transitional metal.

Strontium-doped lanthanum manganite $La_{0.84}Sr_{0.16}MnO_{3-\delta}$ (LSM) perovskite oxide had for some years been known to be good cathode materials for SOFC applications. In contrast to the LSC materials, the LSM oxides had been shown to be very poor oxide ion conductors [74], but it was the electronic conductivity which was sufficiently high as to make this an attractive cathode material. The thermal expansion coefficient was 12.3 × 10^{-6} K^{-1} between 30 and 1000 °C for LSM. The electronic conductivity (σ_e) and ionic conductivity (σ_i) were 102 and 1.7 × 10^{-4} Scm^{-1}, respectively. However, lanthanum manganites doped with alkaline earth elements had been observed to react with YSZ electrolyte forming a poorly conductive $La_2Zr_2O_7$ phase. On the other hand, by using other electrolyte such as CGO, no reaction of secondary phase was observed.

Furthermore, A-site doping of LaMnO3 had been carried out to establish the relative interfacial reactivity between $La_{1-x}A_xMnO_{3\pm\delta}$ and YSZ for A = Ca and Sr [75-78]. It was found that reactions were observed in both Ca-doped and Sr-doped samples. $CaZrO_3$ and $La_2Zr_2O_7$ phases were formed. Of interest were their findings that the majority of the phase formations occurred during fabrication stage rather than operation. Therefore, these emphasized the need to develop not only new materials, but also a low temperature fabrication route.

Herle *et al.* [79] studied the different cathode performances of porous and dense LSM on YSZ electrolyte. In addition, two-layer cathode design including a thin dense LSM layer (~1 μm) and a thick porous layer (0.3 mm) had been investigated. The author concluded that double layers LSM had better performance compared with single LSM layer design.

2.4 Sol-gel Method

In the past few years, the sol-gel reaction has gained much notoriety in the ceramic synthesis area. The fundamental property of sol-gel is to produce ceramic materials at low temperature. The sol-gel process offers a number of advantages in materials synthesis:

- The temperature for gelation is close to room temperature which saves the energy during processing.
- High purity products can be obtained since no reaction with containers took place.
- Air pollution is minimized.
- Materials with exceptional chemical homogeneity can be obtained since the mixing process of constituent occurred at molecular level during the chemical reaction.

In contrast, there are also some limitations in sol-gel synthesis process:

- The starting materials (e.g. metal alkoxides) are usually expensive which will limit large scale production.
- Long time drying process is required to evaporate the water containing in the gel matrix.

Sol-gel processes are usually distinguished into particulate gel route and polymeric gel route, as shown in Figure 2.26. In the particulate gel route the sol consists of dense colloidal particles with diameter 1 to 1000 nm. In contrast, the polymeric gel route consists of polymer chains without dense particles of diameter greater than 1 nm.

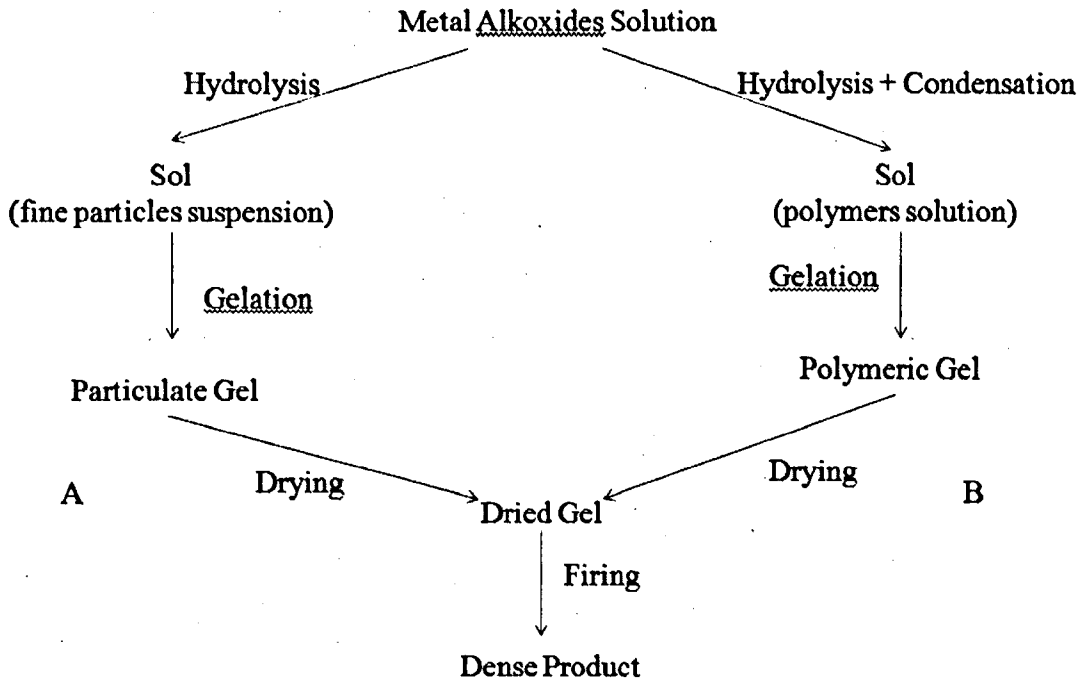

Figure 2.26. Sol-gel flow chart of (A) particulate route and (B) polymeric route.

In the particulate gel route, the precursors followed a number of hydrolysis and polymerization reactions to form a sol. A sol is a solid particles suspension in liquid with a diameter of few hundred nanometers where the Brownian motion suspended the particles. The sol particle preparation depended on their size, temperature and pH of the solution.

In the polymeric gel route, when the sol particles condensed, a new phase named gel was formed. This new phase appeared when a monomer could make at least two bonds with no limit on the size of the formed molecule. The initial gel had a high viscosity and low elasticity and the gel point was the time (or degree of reaction) at which the last bond was formed and completed the giant molecule. Thus, gel contained a continuous solid macro-molecule in a liquid phase. The gel had elasticity due to the continuity of the solid structure. In particulate sol route, gels could be obtained due to the attractive Van der Waals forces that caused the whole structure to stick together to form a network. Drying by evaporation under normal conditions caused shrinkage of the gel network. After this treatment, a porous solid matrix named xerogel was obtained with reduced volume by a factor of 5 to 10 compared to the original wet gel. It was found that xerogel contained many labile sites and thus, offered opportunities for new chemical reactions.

The starting materials used in the sol-gel preparation are usually metal or metalloid element surrounded by various reactive ligands such as metal alkoxides. Metal alkoxides were members of the metal-organic compounds family, which had the general formula $M(OR)_x$ where M was the metal, R was an alkyl group and x was the metal valence state. All metal alkoxides easily reacted with water through hydrolyses process and the corresponding hydroxide or oxide was obtained. The most widely used metal alkoxides were alkoxysilanes, such as tetra-methoxysilane (TMOS) and tetra-ethoxysilane (TEOS), but other materials such as aluminates, titanates and borates were also used. The alkoxides of the group I and II elements were solid, non-volatile and with low solubility in water, thus they were difficult to obtain with high purity. Due to this, the metal salts provide a viable alternative because they were high purity, readily converted to oxide by thermal or oxidative decomposition.

There are three most important chemical methods, Pechini, Co-precipitation and GN method, for obtaining nanopowders. Yamahara *et al.* used all three of these methods to obtain 8YSZ from zirconium ($ZrO(NO_3)\cdot xH_2O$) and yttrium ($Y(NO_3)\cdot 6H_2O$) salts. In the Pechini method, YSZ salts were dissolved in distilled water after which citric acid (CA - $C_6H_8O_7$) and ethylene glycol (EG - $C_2H_6O_2$) were added into the solution resulting in polymer citrate gel formation. In the co-precipitation method a solution of 30% ammonium hydroxide was added drop wise to yttrium and zirconium salts dissolved in water. In the GN method, glycerine $C_3H_8O_3$ and nitric acid were used as medium materials. The author concluded that all these three methods could produce single phase 8YSZ. The calcined GN powders were found to contain small amount of impurities depending on the G/N ratio.

2.4.1 Organic Materials

Suciu *et al.* [13] investigated zirconia nanoparticles synthesis with organic precursors sucrose $C_6H_{12}O_6$ and pectin by using sol-gel method. As shown in Figure 2.27, zirconium nitrate $Zr(NO_3)_4\cdot 5H_2O$ was used as a starting material and dissolved into nitric acid and water with pH 4.5 at room temperature, Solution 1 was formed. Solution 2 was formed by dissolving sucrose and pectin with large quantities of water at ratio of 10:1 up to 15:1. Then solution 1 was dripped into solution 2 under continuous stirring and slowly dried at 90−100 °C to form a brown resin with NO_x gases emitted during the process. The mixture was then sintered at 900 and 1000 °C respectively. In this research, Suciu *et al.* concluded that the concentration of Zr salt should be lower than 20 g/L. The XRD data indicated that the ZrO_2

crystallites were present and the distinct particles had fairly uniform dimensions ranging from 50 to 90 nm.

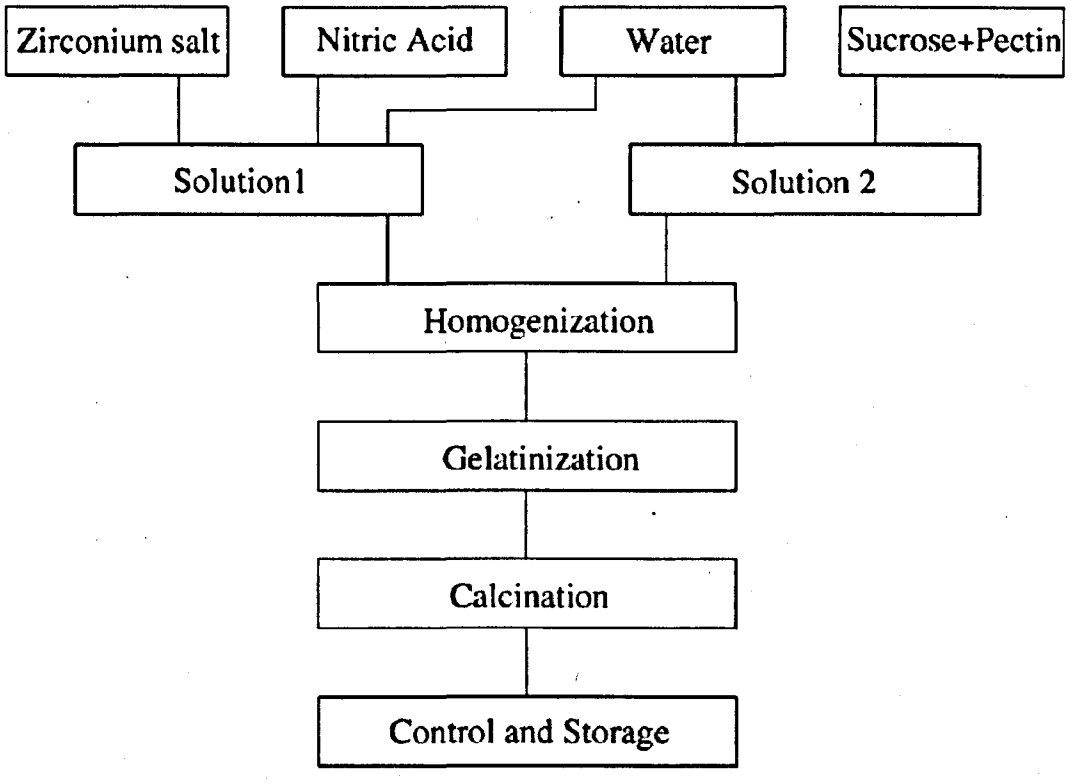

Figure 2.27. Scheme of Operation.

The author also obtained a binary mixture of YSZ particles and NiO particles for the manufacture of SOFC anode using the same method [80]. Thermal analysis indicated the NiO and YSZ phases were completely formed at 800 °C with no other phases observed from XRD. The obtained particles were all smaller than 135 nm and a homogeneous distribution of YSZ and NiO nanoparticles as shown in Figure 2.28.

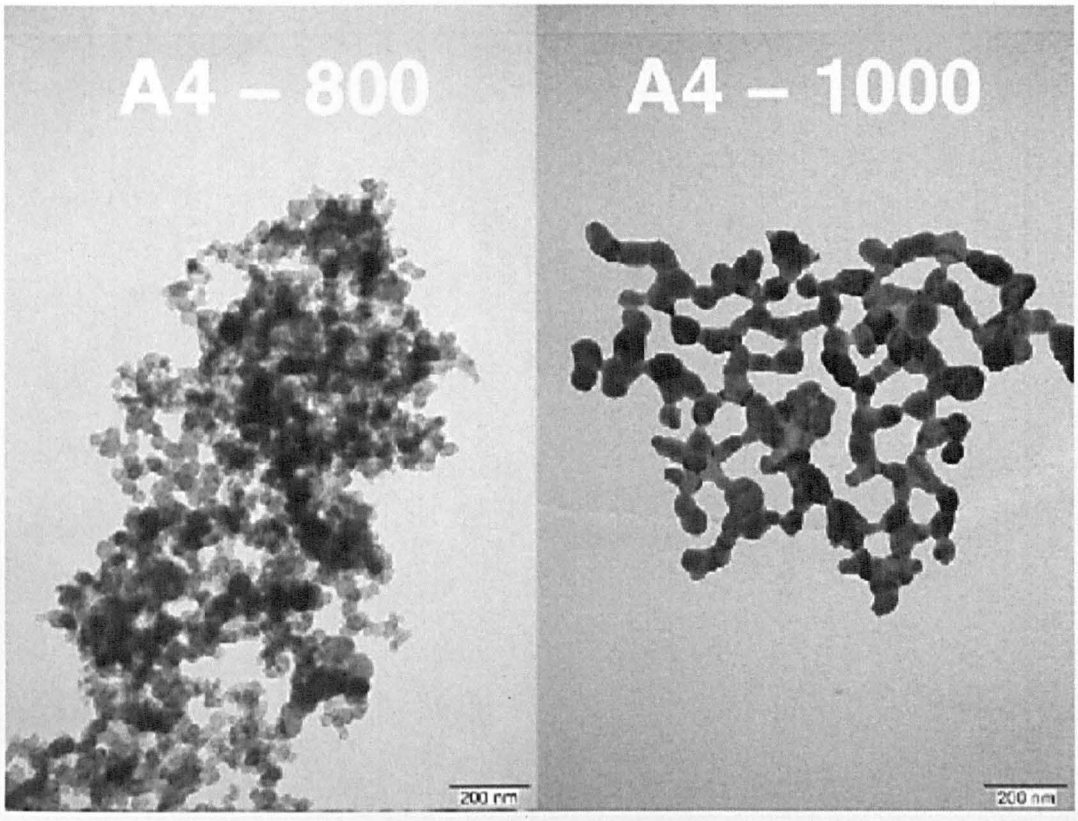

Figure 2.28. TEM images of YSZ-NiO (50-50 wt%) nanopowders calcined at 800 and 1000 °C with sucrose : pectin = 100 : 4 wt% [80].

The advantage of this method using sucrose as chelating and pectin as gelling agent was that these two organic materials are relatively cheap. Nanopowders of ceramic materials could be synthesized at low temperatures which could be used in commercial production. However, a long gelation time is required in this process.

2.4.2 Sodium Alginate

Sodium alginate (Na-ALG, $NaC_6H_7O_6$) is a polymer extracted from brown seaweed. It contains varying amount of 1, 4´-linked β-D-mannuronic acid (M) and α-L-guluronic acid (G) residues covalently linked together in sequence as –GG– or –MM– structures or as –GM– block copolymers as shown in Figure 2.29. Gelation of alginate is due to the interaction of alginate with metal ions [81] in aqueous solution. Once alginate is gelled with metal ions, the metal ion binds preferentially to G blocks. During calcination, the metal ions become immobile and cannot readily get close to each other, hence the possibility of producing small nanoparticles of metal oxides.

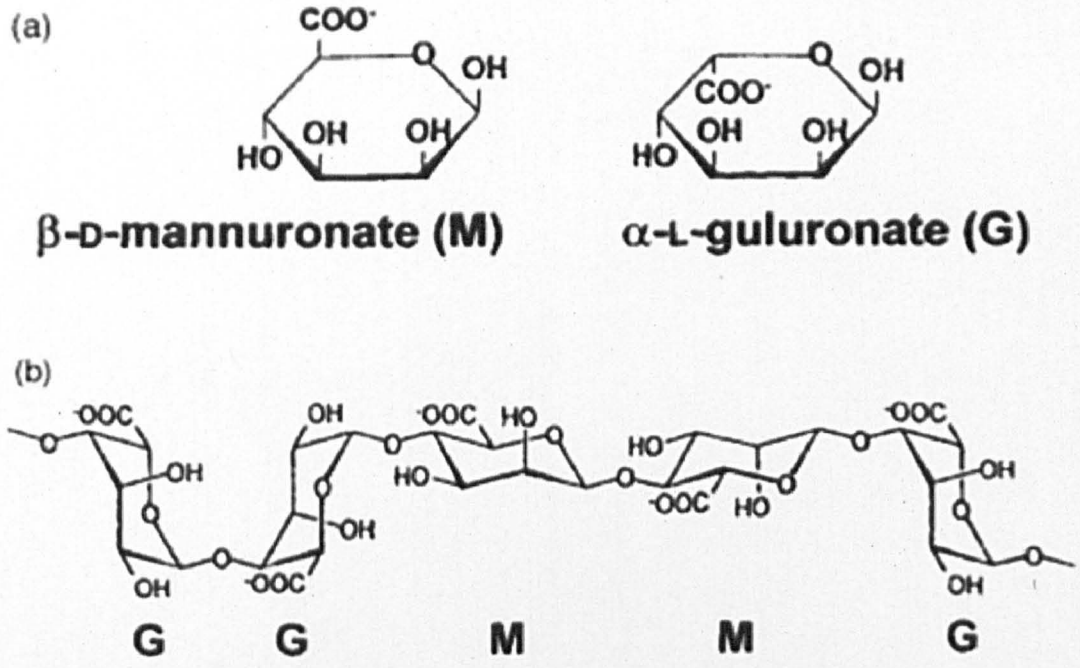

Figure 2.29. Structure of alginate (a) alginate monomers and (b) chain conformation, respectively.

Baskoutas *et al.* [82] investigated zinc oxide nanoparticles based on the thermal decomposition of zinc alginate gels. These gels were produced in the form of beads by ionic gelation between zinc solution and sodium alginate solution. As shown in Figure 2.30, zinc nitrate $Zn(NO_3)_4 \cdot 5H_2O$ or acetate were used as a starting materials and dissolved into ultrapure water at room temperature to form Solution 2. Solution 1 was formed by dissolving sodium alginate with concentration of 1% w/w under magnetic stirring. Then solution 1 was dripped into solution 2 by volume percent 1:2 through a stainless steel needle under continuous stirring. After the gel beads were formed, gentle stirring was continued for 30 mins in the gelling medium. The wet beads were then calcined at 450 °C and 800 °C for 24 hours, respectively. In this research, Baskoutas *et al.* [82] concluded that ZnO nanoparticles could be obtained using this sol-gel synthesis method. At different calcination temperature, uniform particles with size 50−130 nm at 450 °C and 200−400 nm at 800 °C were obtained, respectively. The ability of alginate to absorb metals such as Cu, Cd and Zn could be consider as a potential precursor for the preparation of other technologically important oxides.

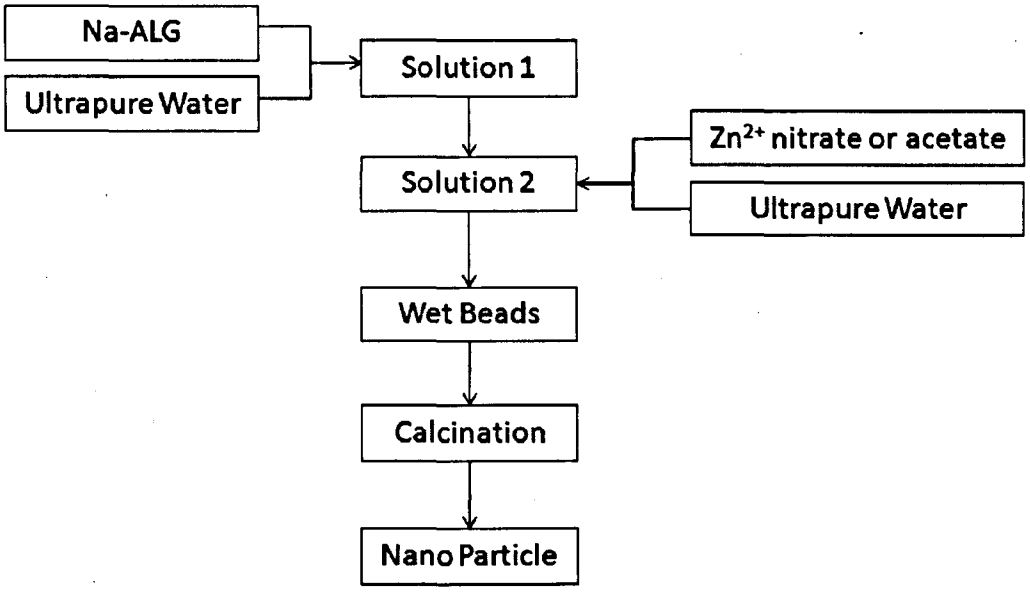

Figure 2.30. Scheme of Operation.

Takada *et at.* [83] synthesized bismuth-based high-T_c superconducting fiber Bi-Pb-Sr-Ca-Cu-O (BPSCCO) using sodium alginate as a media based on ion-exchange property of the alginate. However, even with long annealing time, small amount of impurities were still observed in XRD pattern as shown in Figure 2.31.

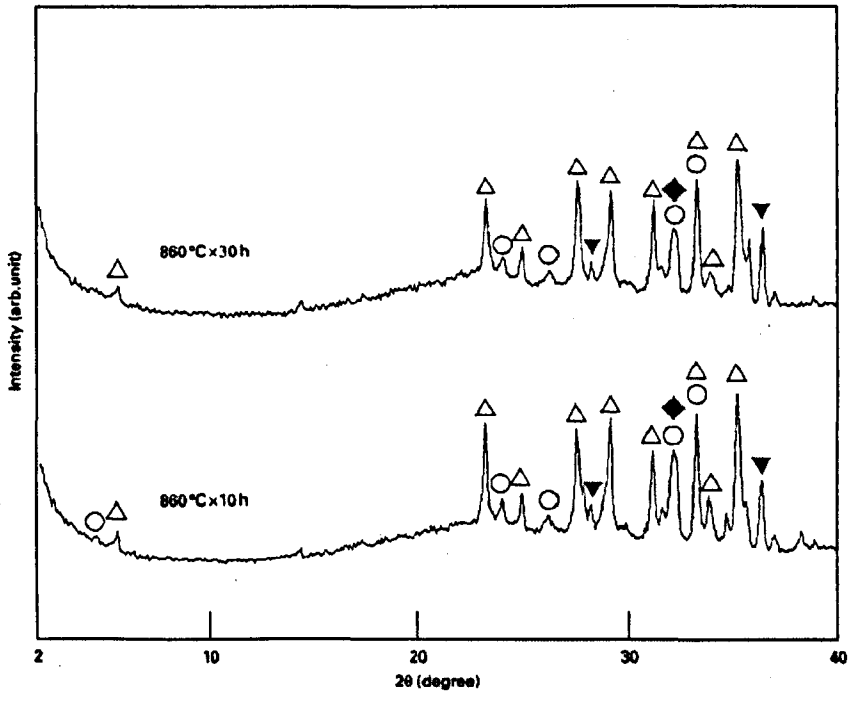

Figure 2.31. XRD patterns for BPSCCO sintered at 860 °C for 10 and 30 hrs. Keys: o (2223) phase, (2212) phase, black inverted triangle Ca_2CuO_3 and black diamond $(Sr, Ca)_3Cu_5O_x$, respectively [83].

Said *et al.* [84] studied thermal decomposition of some divalent metal alginate gel compounds using thermogravimetric (TG) and differential thermal analysis (DTA). The author concluded that the thermal decomposition processes of these complexes proceed via the formation of stable metal oxalates ($M(COO)_2$, M = metal ions) as intermediate fragments.

Sartori *et al.* [85] used Fourier transform infrared spectroscopy (FTIR) to determine the ion-exchange reaction between sodium and calcium ions at different time lengths as shown in Figure 2.32.

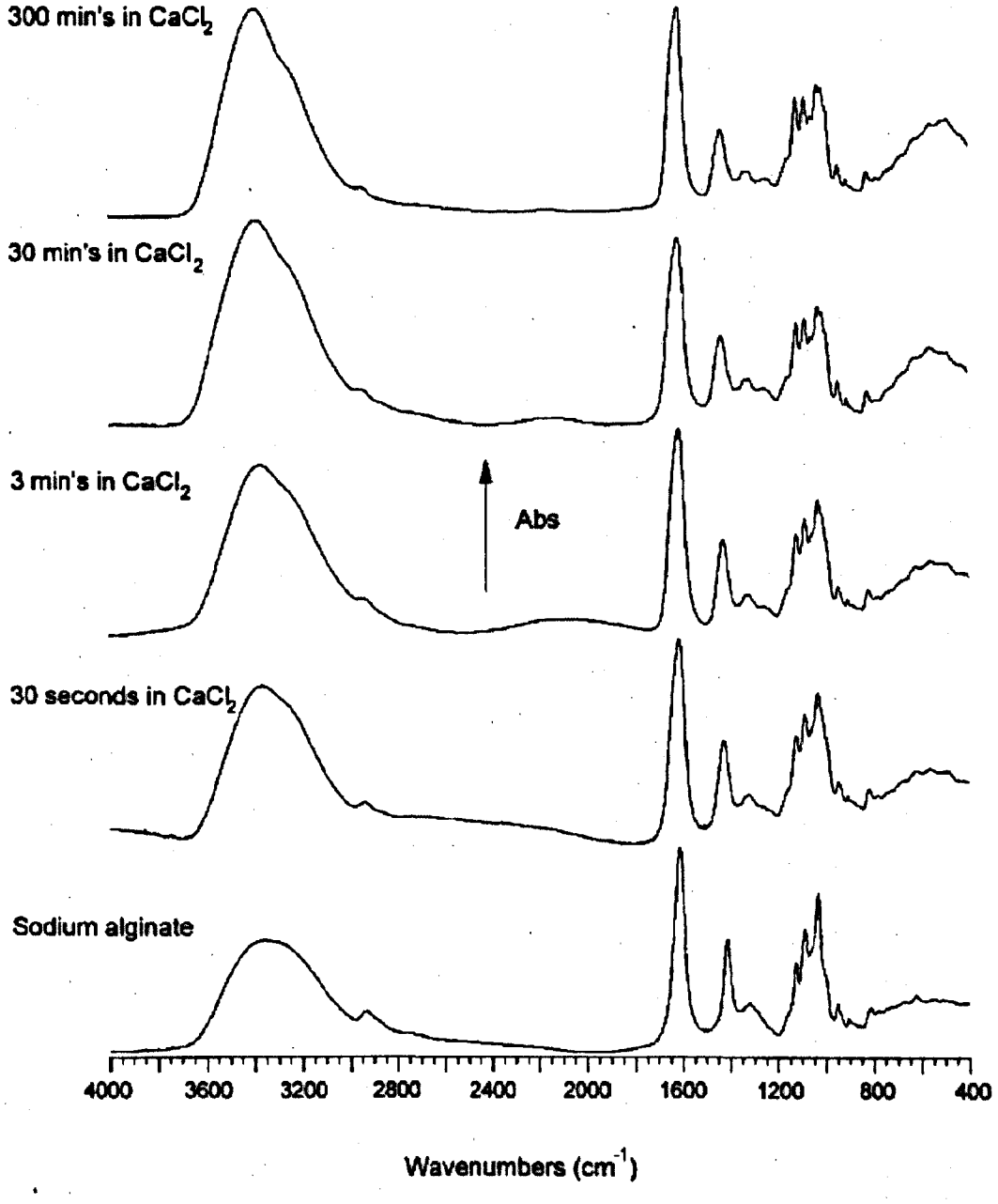

Figure 2.32. FTIR spectra of sodium alginate for different lengths of time in calcium chloride solution [84].

As shown in Figure 2.32, the COO^- peak around 1420 cm^{-1} exhibited a large shift to higher wavenumbers, as well as a decrease in intensity as the reaction time increased. Since calcium ions replaced sodium ions in the alginate blocks, the charge density, the radius and the atomic weight of the cation were changed, creating a new environment around the carbonyl group. Therefore, the author concluded that the ability to quantify ion content from FTIR provided a valuable tool for analyzing unknown Na/Ca contents.

Some researchers also studied the kinetics and mechanism of sol-gel transformation between sodium alginate and some heavy divalent metal ions [86-89].

2.5 Scope of the project

On the basis of literature review, the focus of this investigation is to develop novel sol-gel synthesis method in a cost effective, simple, environmentally friendly and non-toxic route for a large scale production of high purity single phase nanopowders at significantly low temperatures. The following tasks will be implemented during the investigation:

It is very clear from the literature that the selection of SOFC materials and initial particle size are very important for successfully designing a high performance cell. Therefore, electrode material CGO2 ($Ce_{0.8}Gd_{0.2}O_{1.9}$) is selected due to its high conductivity in intermediate or low operating temperature of SOFC. The experimental process of CGO2 nanoparticles obtained by sol-gel method using new organic gelling media: maltose + pectin or sucrose + pectin which are abundant in the world, will be described in the next chapter. The calcination process will be studied by thermal analysis TGA/DSC under different conditions, respectively. The particle size observed by TEM should show good agreement with the calculation from XRD Rietveld refinement. The nominal compositions of CGO2 should be in excellent agreement with that determined by TEM-EDS and ICP-AES. The conductivity of CGO2 materials obtained by this new sol-gel route will be analysed by AC-impedance which will qualify the use of this material for SOFC as solid electrolyte and in the fabrication of composite electrodes.

On the other hand, from the literature review, it is very clearly shown that NiO particles size is crucial in coarsening treatment of starting powder in SOFC anode preparation. A novel genetic sol-gel synthesis method will be investigated based on sodium alginate ion-exchange property. The obtained gels will be heat treated at different temperatures for different time lengths to

determine crystallite growth rate. The particle size observed by TEM should show good agreement with the calculation from XRD Rietveld refinement.

Based on the results so far, it is well known that alginate dissolves in water rapidly but it gels in the presence of multivalent ions, especially divalent ions like Ca, forming the so-called egg-box structure that promotes chemical gelation. To further develop this process, sodium alginate powders will be first compacted into a dried granule form and directly react with metal ions such as Ni^{2+}. This process will significantly reduced the sample preparation time compared with using sodium alginate beads extruded from syringe.

Finally, nanopowders of two different compositions of cerium gadolinium oxides designated as CGO1 ($Ce_{0.9}Gd_{0.1}O_{1.95}$) and CGO2 ($Ce_{0.8}Gd_{0.2}O_{1.9}$) will be synthesized by a sodium alginate (Na-ALG) mediated novel ion-exchange sol-gel process. After calcination at low temperature, TEM-EDS and ICP-AES will be used to determine the chemical composition of the obtained samples. the electrical properties of these two compositions will be studies to qualify the use of SOFC electrolyte. The results will confirm that this novel sol-gel method not only produces simple oxide such as NiO, but also produces complex oxide such as CGO for many applications. The experimental process of sodium alginate sol-gel method are described in Chapter 3.

Since the physical, chemical and electrical properties of the metal oxide nanopowders obtained from different sol-gel methods is crucial in SOFC electrodes and electrolytes applications, it is very important to in deep understand the fundamental working principles of various characterization techniques such as TGA/DSC, XRD, TEM, ICP-AES, etc. This will be described in the next chapter.

Chapter 3 Experimental Methods and Materials

It is necessary to optimize the physical, chemical and electrical properties of various metal oxide materials used in the fabrication of SOFC components. The metal oxide materials have been prepared through three novel developed sol-gel methods using sugar + pectin or sodium alginate as media. The phase transformation, chemical composition, microstructure and electrical properties have been examined by using Fourier transform infrared spectroscopy (FTIR), simultaneous thermo-gravimetric analysis and differential scanning calorimetry (TGA/DSC), high temperature X-ray diffraction (HT-XRD), powder X-ray diffraction (XRD) with Rietveld refinement, X-ray micro-tomography (XMT), scanning electron microscopy (SEM), transmission electron microscopy (TEM), energy dispersive X-ray spectroscopy (EDS), inductively coupled plasma - atomic emission spectrometry analysis (ICP-AES) and AC-impedance spectroscopy. The general knowledge of the above techniques and the aspect of the materials preparation and processing are presented below.

3.1 Organic Sol-gel Synthesis Method

In this experiment, organic materials sucrose ($C_{12}H_{22}O_{11}$ F.W. = 342.30 g mol^{-1}), maltose ($C_{12}H_{22}O_{11}$ F.W. = 360.31 g mol^{-1}) and pectin are used for gel preparation and mixed in a mass ratio sucrose : pectin = maltose : pectin = 20:1. All these materials were purchased from Fisher Scientific Ltd (Loughborough, UK).

In order to prepare the dried gel containing Ce^{3+} and Gd^{3+} metal ions, cerium nitrate hexahydrate ($Ce(NO_3)_3 \cdot 6H_2O$, 99+ % purity) and gadolinium nitrate hexahydrate ($Gd(NO_3)_3 \cdot 6H_2O$, 99.9+ % purity) are used as precursors in this experiment. Pectin and sucrose or maltose is dissolved in 200 mL of distilled water forming a clear solution denoted as Solution 1. Similarly, the starting precursor hexahydrate nitrate salts of Ce^{3+} and Gd^{3+} are then dissolved in 200 mL of distilled water forming also a clear solution labeled as Solution 2. Both the solutions are prepared at ambient temperature. The cationic concentration of Solution 2 is controlled to yield 30 g L^{-1} of the final CGO2 ($Ce_{0.8}Gd_{0.2}O_2$) material. These two solutions are mixed by dripping Solution 1 into Solution 2 while continuously stirring the mixture for 1 hour. The aim of this treatment is to prevent agglomeration of the constituent particles and to avoid their solidification into crystals or raw granular formations during

different stages of processing, all of which has deleterious effects on the final product purity.

The mixed solution is slowly dried in a beaker on a warm plate at ~90 °C for 3 hours. A light yellow gel is gradually formed under constant magnetic stirring. The obtained gel is dried in a convection oven for 24 hours at 90 °C until it became completely gelatinized. The process flow diagram using sugar (sucrose or maltose) and pectin is schematically shown in Figure 3.1.

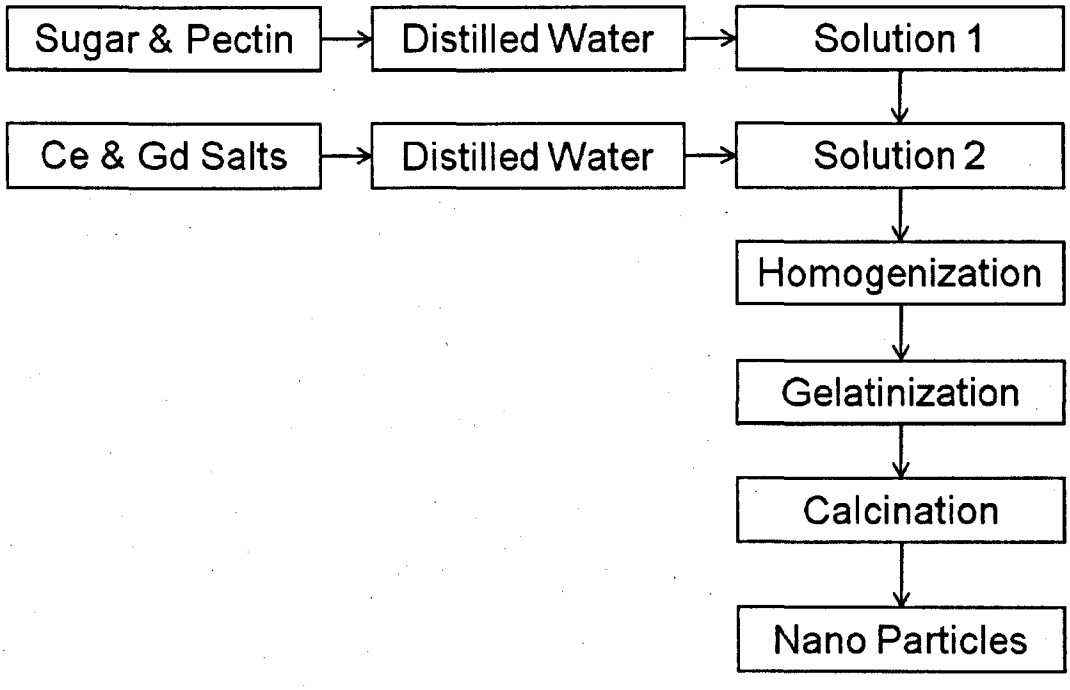

Figure 3.1. Flow diagram of sugar and pectin sol-gel process.

Different samples of dried gel are calcined at 500, 600, 700 and 900 °C (based on TGA/DSC) separately for 2 hours in static air condition in order to transform into CGO nanopowders. The temperature is changed at the rate of 3 °C min^{-1} during the heating and cooling cycles. The physical and chemical properties of these samples are obtained by XRD, TEM and ICP, respectively. For electrical property measurement, the calcined nanopowders are first compacted into approximately a 10 mm diameter disc in a uniaxial die at approximately 14 MPa pressure, and then repressed at 250 MPa pressure in a cold isostatic press for further compaction. The specimens are subsequently sintered at 1500 °C for 2 hours with a programmed heating and cooling rate of 3 °C min^{-1}. The sintered CGO samples are above 95% of the theoretical density. After AC impedance analysis, the microstructure of the sintered pellets are observed by SEM.

3.2 Alginate Sol-gel Synthesis Method

In this experiment, various commercial nitrate or chloride salts and sodium alginate powders are purchased from Fisher Scientific Ltd (Loughborough, UK). Sodium alginate solution at concentration of 4 wt% is prepared by dissolving appropriate amounts of sodium alginate in distilled water under high frequency stirring denoted as Solution 1. Metal solution is prepared by dissolving the respective salts in distilled water named as Solution 2. The cationic concentration of Solution 2 is controlled at 30 g L^{-1} of the final metal oxide. The solutions are both prepared at ambient temperature. The metal alginate beads are prepared by dripping 200 mL sodium alginate Solution 1 into 200 mL Solution 2 through a 16 G (1.194 mm) inner diameter stainless steel needle attached to a hypodermic syringe having a volume of 20 mL. The beads are approximately 4–5 mm in diameter and are spherical in nature (see Figure 3.2). The prepared beads are maintained in the gelling medium for 2 hours under gentle magnetic stirring for ion-exchange reaction between Na^+ and metal cations to complete. These beads are then separated from the solution through a ~2 mm stainless steel sieve. The metal containing beads are washed with distilled water several times and dried in a convection oven for 24 hours at 90 °C so that they become completely dried. The process flow diagram using nickel nitrate as precursor is schematically shown in Figure 3.2. Figure 3.3 shows different metal alginate wet vs. dried beads obtain from different metal salts.

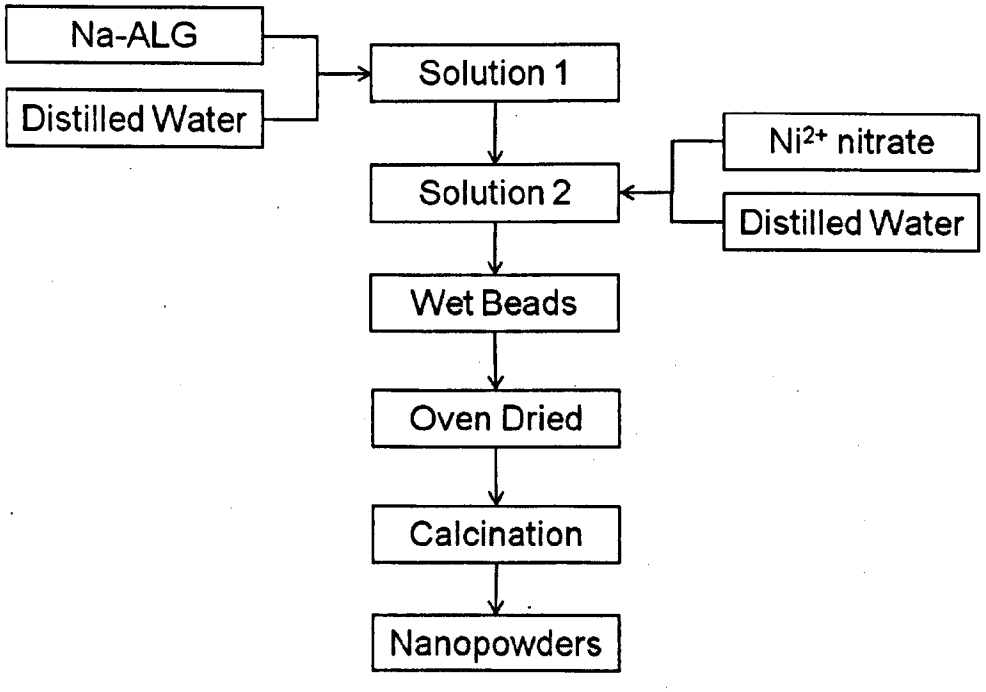

Figure 3.2. Flow diagram of sodium alginate sol-gel process using nickel nitrate as precursor.

Figure 3.3. Different metal alginate wet (top) vs. dried (bottom) beads obtain from different metal salts.

Some of the nickel alginate beads (Ni-ALG) are also dried using a freeze dryer (Scanvac Cool Safe 55-9, Denmark) to compare the effect of this method with convention oven dried beads which is described in Section 4.2.2 and Section 5.2.2. Freeze-drying is achieved in two steps. The first step is to freeze the samples in a -80 °C freezer. The pre-frozen sample is then placed in the equipment at -52 °C for a period of 48 hours until they are completely dried.

Since alginate beads production requires long processing time by dripping sodium alginate solution from a syringe, a novel method using sodium alginate granules is developed to improve the production rate. Sodium alginate granules are prepared, related to Section 4.2.3 and Section 5.2.3, from the powder form of the material, using commercial pan granulator (ERWEKA AR400, USA). Water is used as the binder. The granules are dried and sieved in the sieve range ~2 mm. Metal solution, such as nickel solution, is prepared by dissolving the respective salts in distilled water at ambient temperature with concentration of 0.05 M. The nickel alginate granules are prepared by dropping 10 g sodium alginate granules into 200 mL nickel solution. The granules gel rapidly and do not allow the granules to disintegrate. The granules are maintained in the gelling medium for 1 hour under gentle magnetic stirring in order to ensure that the ion-exchange reaction between Na^+ and Ni^{2+} is completed. These granules are then separated from the solution through a stainless steel sieve. The nickel granules are washed with distilled water and dried in a convection oven for 24 hours at 90 °C until they become completely dried and ready for calcination.

Different samples of dried gel are calcined from 500 to 700 °C (based on TGA/DSC) separately for various hours in static air condition in order to transform into metal oxide nanopowders. The alginate gel structure of Ni-ALG freeze dried sample is observed by XMT. While the chemical structures of Na-ALG and CGO alginate beads are obtained by FTIR. The physical and chemical properties of these nanopowders after calcination are obtained by XRD, TEM and ICP, respectively. For electrical property measurement, the CGO nanopowders are first compacted into approximately a 10 mm diameter disc in a uniaxial die at approximately 14 MPa pressure, and then repressed at 250 MPa pressure in a cold isostatic press for further compaction. The specimens are subsequently sintered at 1300 °C for 2 hours with a programmed heating and cooling rate of 3 °C min^{-1}. The sintered CGO samples are 91% and 93% of the theoretical density, respectively. After AC impedance analysis, the morphologies of the sintered pellets are observed by SEM.

3.3 TGA/DSC

Thermal Gravimetric Analysis (TGA) is a type of testing which determines changes in weight in relation to changes in temperatures. This technique is generally used to determine phase transformations as a function of

temperature and environment. Therefore, highly accurate measurements of weight, temperature and temperature change are required. The analyzer usually consists of a high precision balance with an alumina crucible loaded with specimen. The crucible is located in an electrical furnace with a thermocouple to accurately measure the temperature changed. Gases (air, pure O_2, helium, etc) can be flowed into the furnace for different thermal analysis. In this research, analysis is carried out by raising the temperature gradually from room temperature to high temperatures and plotting weight against temperature. Different annealing times can be also set during the experiment. The weight loss curve indicates material transformation and thus, the calcination temperature can be predicted using this method. Differential Scanning Calorimetry (DSC) is a thermal analytical technique in which the difference in the amount of heat required to increase the temperature of a sample and reference is measured as a function of temperature. Both the sample and reference are maintained at nearly the same temperature throughout the experiment. Generally, the temperature program for a DSC analysis is designed such that the sample holder temperature increases linearly as a function of time. A well-defined reference sample (α-Al_2O_3) over the range of temperatures to be scanned is used in this experiment. The basic principle underlying this technique is that when the sample undergoes a physical transformation such as phase transitions, more or less heat will need to flow to it than the reference to maintain both at the same temperature. Whether less or more heat must flow to the sample depends on whether the process is exothermic or endothermic. The result of a DSC experiment is a curve of heat flux (energy differences in mW between reference and sample material) versus temperature or time. More details can be found elsewhere [90].

In this present study, thermal analysis is carried out employing a Mettler Toledo STAR^e System, UK, which is capable of performing thermogravimetric analysis (TGA) and differential scanning calorimetric (DSC) investigations simultaneously. The TGA and DSC experiments are conducted in controlled atmosphere of air at a flow rate of 50 or 10 mL min^{-1}. The TGA/DSC analyses are carried out from ambient temperature to 1000 °C with heating rate maintained at 3 °C min^{-1} without any holding time. Additional samples are analyzed in flowing helium gas at 50 mL min^{-1} with heating rate of 3 °C min^{-1} from ambient temperature to 500 °C. Once the sample reached 500 °C, helium gas is switched over to air for 1 hour of high temperature annealing. In all the TGA/DSC experiments, the mass of the

sample used is about 15 mg which is kept constant all the time between the scans.

3.4 FTIR

Fourier Transform Infrared Reflection spectroscopy (FTIR) a technique to determine qualitative and quantitative features of IR-active molecules in organic or inorganic solid, liquid or gas samples. It is a rapid and relatively inexpensive method for the analysis of solids that are crystalline, micro-crystalline, amorphous, or films. Samples are analyzed on the scale of microns to the scale of kilometers and new advances make sample preparation, where needed, relatively straight forward. Another advantage of the IR technique is that it also can provide information about the "light elements" (e.g. H and C) in inorganic substances.

In order to obtain the best possible IR spectra of samples it is necessary to choose the appropriate IR source, detection method and accessories. First, the analyst needs to determine the appropriate region of the infrared spectrum, in which the sample under investigation has diagnostic features. For example, C-O is located in the mid-IR, while H_2O and OH^- are found in the mid- to near-IR region. These regions are defined using wavelengths with unit cm^{-1}. Once the IR ranges of interest has been decided, it is also necessary to choose an optimal infrared source, interferometer unit, sample chamber, sample geometry and detector. Finally, the methods for data acquisition and manipulation need to be defined as well. More details about the FTIR working principle can be found elsewhere [91].

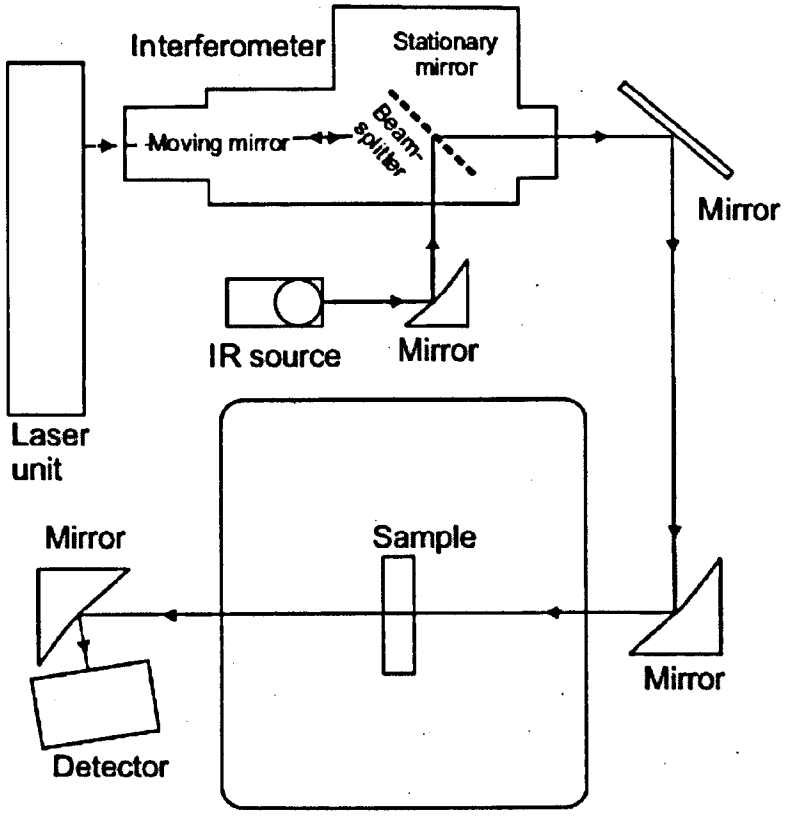

Figure 3.4. Scheme of IR spectrometer with the source, interferometer, sample, and detector [91].

In this present study, the experiment is carried out by FTIR (Thermo Scientific Nicolet iS10 FTIR spectrometer) with a diamond iTR attenuated total reflectance (ATR) sampling accessory. The spectra are taken over the wavenumber range 400−4000 cm^{-1} and 36 scans are used per spectrum.

3.5 XRD

X-rays are electromagnetic radiation with wavelengths in the range 0.5-2.5 Å. Since this is of the same order of magnitude as the inter-atomic distances in solids, X-rays are frequently used to study the crystallite structure of materials. XRD analysis is based on the physical phenomenon of diffraction. When an electromagnetic beam hits the specimen, the ray bends in a certain way creating a diffraction pattern. This pattern is characteristic to the material. Hence, this technique has been used to characterize the phase constitution and crystallite size of the investigated materials. X-rays with wavelength λ of the order of lattice spacing are elastically scatted (i.e. diffracted) from the atomic planes in a crystalline material yielding diffraction

peaks. The condition for diffraction from planes with interplanar spacing d is given by Bragg's law:

$$n\lambda = 2d_{(hkl)} \sin\theta \qquad (3.1)$$

where:

- n is an integer (n = 1, 2, 3.....)
- λ is the wavelength (Cu Kα λ = 1.541 Å)
- $d_{(hkl)}$ is the interplanar spacing
- θ is the angle between the atomic planes and the incident X-ray beam

As shown in Figure 3.5, it is clear that diffraction from a set of planes will only occur if the normal to these planes is bisecting the angle between the incident and the scattered beam. Alternatively, one defines a scattering vector $K = k_e - k_i$ as the difference between the wave vector k_e of the scattered wave, and the wave vector k_i of the incident X-ray, as shown in the inset of Figure 3.5. Diffraction (i.e. constructive interference of the scattered X-rays) will occur if the Bragg condition (eq. 3.1) is fulfilled and of the scattering vector K is parallel to the normal of the hkl-planes.

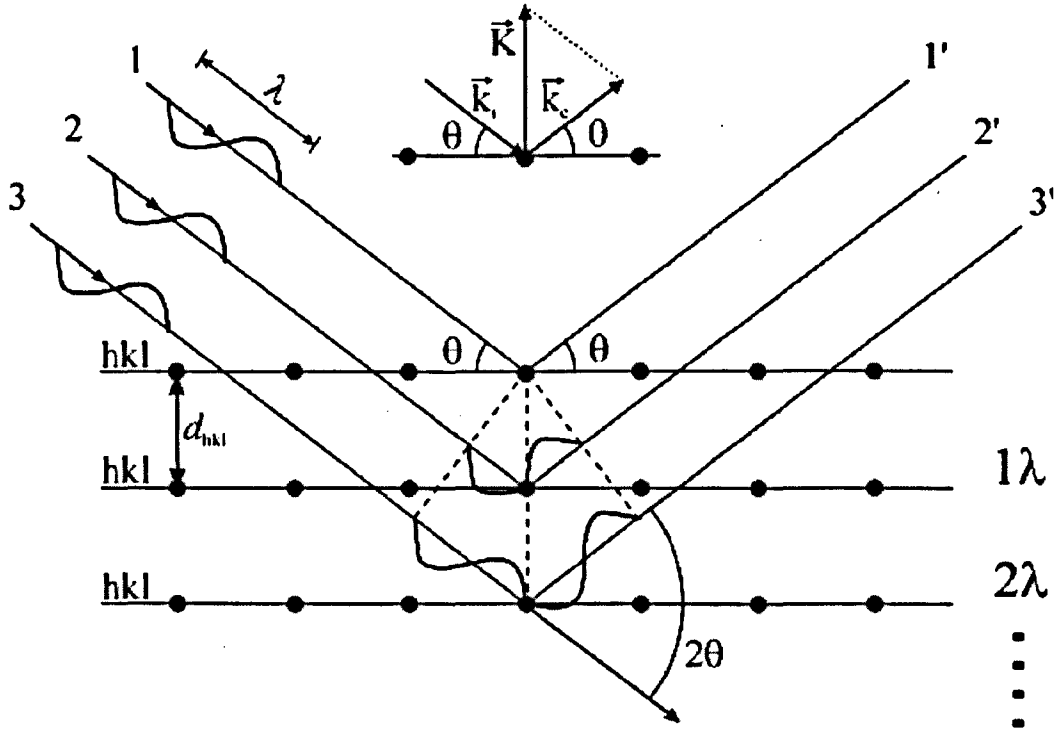

Figure 3.5. Scheme of X-ray diffraction.

The identification of a phase is accomplished determining the d-spacing and the relative intensities of the peaks and comparing the values with the reference data from JCPDS (Joint Committee on Powder Diffraction Standards). Resultant diffraction pattern could be used to obtain the information of phase constitution, lattice constant, crystallite size, residual stress or preferred orientation. If there are two phases coexisting in the composite, the volume fraction of each phase could be easily estimated by comparing the integrated area under the highest intensity peak of each phase. The integration could be performed by using the commercial software based. According to the relationship between the d-spacing and Miller indices assigned to the crystal planes, the lattice parameters could be calculated. For example in a cubic system, the relationship between d and hkl given by:

$$\frac{1}{d^2_{(hkl)}} = \frac{h^2+k^2+l^2}{a^2} \qquad (3.2)$$

where d(hkl) is the inter-planar spacing of the plane (hkl) and "a" is the apparent lattice parameter of the crystalline unit cell. Several methods are used to improve the accuracy of the obtained lattice parameter, such as Rietveld refinement and Nelson and Riley's extrapolation function.

In this present study, most of the XRD analysis is done with solid powders. Since crystals are randomly oriented, it is certain that all reflections will be observed and an average crystallite size will be obtained. Crystallite size is obtained by comparing the broadening of a particular peak in a diffraction pattern associated to a particular reflection plane from within the crystal unit cell. It is inversely to the FWHM (full width of peak at half maximum of the peak) of an intensity peak. The equation that gives crystallite size is the Scherrer equation [92] which assumes all reflections along to the reflection plane.

$$L = \frac{\lambda K}{\beta \cos\theta} \qquad (3.2)$$

where:

- L is mean crystalline dimension in Å

- K is constant (see Table 3.1)
- β is FWHM of the peak in radians of 2θ

Table 3.1. K values given by different researchers [92].

Researchers & Time	K value
Scherrer (1920)	0.94
Bragg (1933)	0.89
Seljakow (1925)	0.92
Laue (1926)	1.42
Stokes (1942)	1.07

For XRD studies, the powders are mounted in a stainless steel spinner sample holder and analyzed using X-ray diffraction (XRD, P'Analytical X'Pert MPD, Netherlands) employing Cu Kα (λ = 1.541 Å) radiation. Scans are usually performed over a range 2θ = 20−100° using a step size of ca. 0.033°, with a total scan time of approximately 30 mins. The surd in step size is due to the X'cellerator multi-detector employed by this system. Programmable divergence and anti-scatter slits are used for producing a constant irradiation length on the sample in order to improve the data collection statistics at high angles, and reduce the effect of air scattering at low angles. A simple trigonometric algorithm is then used to convert the data from automatic to fixed slit, in order to make it suitable for structural analysis.

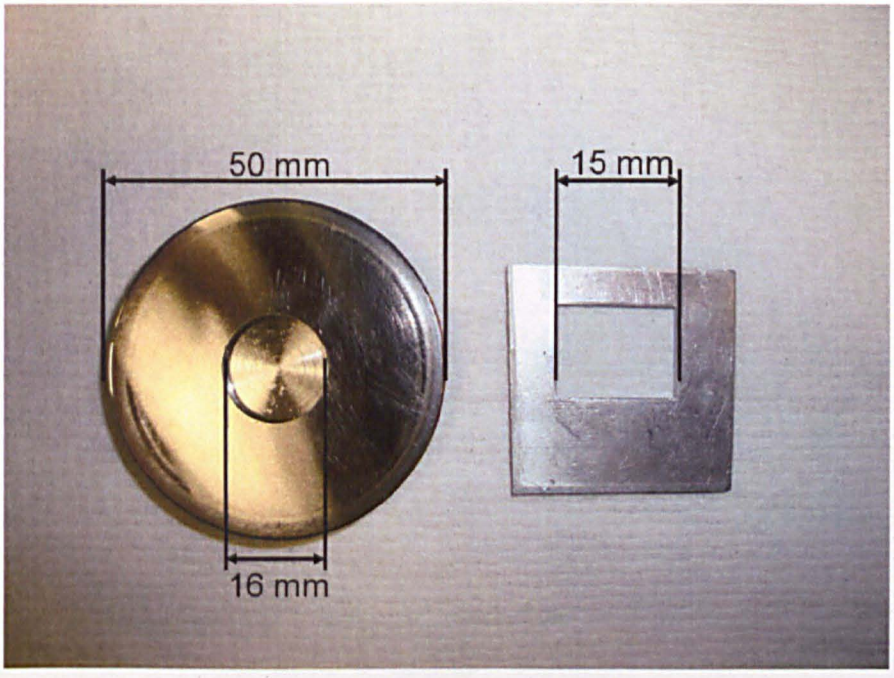

Figure 3.6. Standard Philips spinner (left) and bracket (right) sample holders.

A Rietveld structural refinement is performed using the resultant XRD data (X'Pert HighScore Plus, P'Analytical, Netherlands). Using the software, size/strain analyses is used to most accurately match the modelled structure to the collected data. Diffraction data are collected using an external Si standard (NIST Si standard SRM 640b), under identical conditions, in order to determine the instrumental broadening, a prerequisite of performing a size/strain analysis. Details of the Rietveld refinement method using X'Pert HighScore Plus software package can be found elsewhere [93].

A pseudo-Voigt profile is used for the refinement, comprising a mixture of Gaussian and Lorentzian components and the relative proportion of each component is modified during the refinement routine. Details of the Rietveld method can be found elsewhere [94, 95].

The High Temperature X-ray Diffraction (HT-XRD) measures the phase transformation of samples at tightly controlled temperatures from room temperature to 1200 °C. During the measurement, samples are mounted in a α-Al_2O_3 sample holder with a Pt substrate and analyzed using high temperature X-ray diffraction (HT-XRD, P'Analytical X'Pert MPD attached with Anton Paar HTK-1200, Netherlands) employing Cu Kα radiation. The temperature program is set to increase temperature of sample every 25 °C interval from room temperature to 1000 °C with heating rate maintained at 3 °C min^{-1} in static air condition. At each temperature, 30 mins annealing time is allowed for the sample to equilibrate. HT-XRD scan is performed over a range of 2θ using a step size of ca. 0.033° to obtain the identity of phase at each temperature. Programmable divergence and anti-scatter slits are used for producing a constant irradiation length on the sample in order to improve the data collection statistics at high angles, and reduce the effect of air scattering at low angles. A simple trigonometric algorithm is then used to convert the data from automatic to fixed slit, in order to make it suitable for structural analysis.

3.6 XMT

X-ray Micro-Tomography (XMT) uses X-rays to create cross-sections of a 3D-object for visualizing interior features within solid specimens, and for obtaining digital information on their 3D geometries and properties. This technique combines 2D radiography with a numerical technique known as 3D reconstruction to precisely characterize the internal microstructure of a wide range of materials. The resulting 3D volume is made up a series of slices corresponding to what the object being scanned would look like if it

were sliced along the cross-sectional plane, and correspond to a certain thickness of the object being scanned. So, while a digital image is composed of pixels, a tomographic image is composed of voxels. The gray levels in a tomographic image correspond to X-ray attenuation, which reflects the proportion of X-rays scattered or absorbed as they pass through each voxel. X-ray attenuation is primarily a function of X-ray energy and the density and composition of the material being imaged.

The elements of the X-ray tomography apparatus are an X-ray source, a detector to measure X-ray intensity attenuation, and a rotational geometry with respect to the object being imaged. As shown in the image (Figure 3.7), a sample is placed between the X-ray source and detector, and is step-wise rotated at small angular orientations. At each position, a radiograph is acquired. These radiographs are then reconstructed into a 3D tomographic image. More details can be found elsewhere [96].

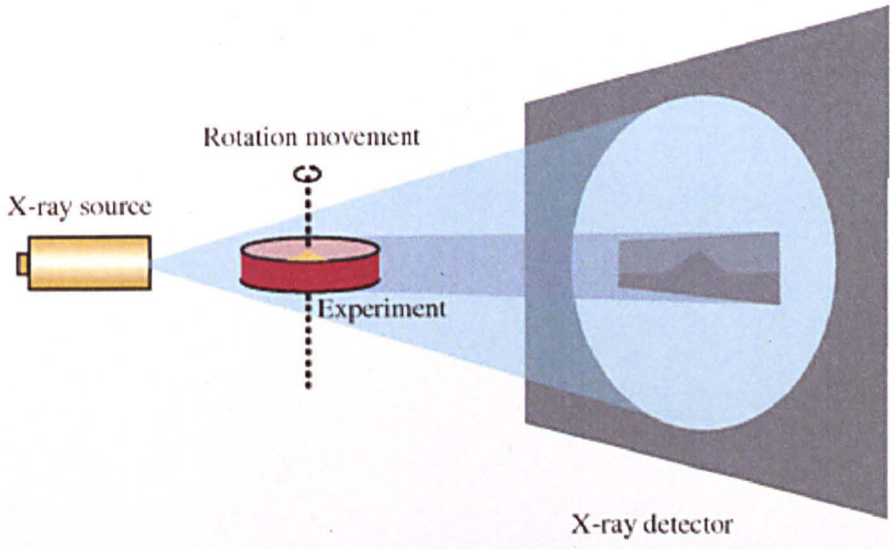

Figure 3.7. Scheme of XMT operation [96].

In this experiment, a Phoenix X-ray Nanotom 160NF (GE Phoenix X-ray, Germany) was used for the X-ray attenuation scan. A constant cone beam of x-ray was generated by a tungsten filament at ~80 kV and 80 µA. The scan was carried out with a rotational sample stage, located between the X-ray source and a detector (2304 × 2304 pixel), at resolutions of 1−3 micron per pixel and a rotation step of 0.25 degree. Projective attenuation images of 1440 were thus obtained for each scan and reconstructed using the reconstruction software of Phoenix for digital volume structures. The volume data were visualized and analyzed using VGStudio (v2.1.1).

3.7 SEM

When primary electrons with high energy strike the specimen, the interactions between the high-energy electrons and the atoms in the specimen result into scattering (elastic and inelastic) of electrons, x-rays or absorption and emission of energy. Among all the effects caused by the different types of interactions, the secondary effects are generally collected and transformed into the useful information to reveal the surface features of the particles or gains in the specimen since they have narrow intensity distribution and therefore capable of giving a better spatial resolution than the other signals such as backscattered electrons. Furthermore, the number of the secondary electrons is independent of the atomic number of the specimen. On the contrary, backscattered electrons have a broader energy spread, which gives a poor spatial resolution, but the number of backscattered electrons has a strong dependence on the atomic number of the specimen. Therefore, they are collected to give the compositional maps. The collection or detection of secondary and backscattered electrons is achieved by using Scanning Electron Microscopy (SEM). SEM (LEO 1530 Gemini field emission SEM) has been employed in this study to obtain the microscopic morphological features of the prepared powders or cross section of the samples.

In addition to its imaging capability by secondary electrons and micro-structural analysis by backscattering electron imaging, the SEM equipped with energy-dispersive X-ray spectrometer (EDS: Oxford Instruments) offers a means of rapidly evaluating the qualitative and semi-quantitative elemental analysis of a sample. A quantitative compositional mapping technique (X-ray mapping) provides a strong link between the microstructure and elemental distribution in the sample under investigation. The X-ray spectrum consists of a series of peaks, the energies of which are representative of the element type and the intensities reflect the relative amounts of each element present in the sample.

For SEM sample powder preparations, the synthesized ceramic powders are dispersed in acetone or methanol and ultrasonically vibrated for several minutes. A droplet of as-obtained suspension is transferred to a clean aluminum metal stub by using a glass rod. Then the sample on the sub is dried for a few minutes. In order to obtained the microstructure of a sintered ceramic pellet fracture surface, the fractured specimen is mounted on a carbon sticker and attached on the aluminum metal stub. Since the ceramic powders or pellets have low electronic conductivity for SEM observation,

coating (e.g. Pt/Pd, Gold or Carbon) must be deposited onto the sample surface with 5-10 nm thickness by commercial sputter coater (Argon Instruments).

3.8 TEM

Transmission Electron Microscopy (TEM) can be used to obtain some useful information on the internal structure of the samples such as phase composition, crystal structure, atomic arrangement and defects by collecting the transmitted or diffracted electrons. TEM (FEI Tecnai TF20 FEG-TEM) has been used in this work to study the as-prepared nano sized ceramic powders to determine the particle size and distribution. The interplanar spacing can be obtained by the bright or dark- field image and electron diffraction pattern. The chemical composition of the sample is obtained using the energy dispersive X-ray spectroscopy (EDS: Oxford Instruments), similar to the EDS in SEM which mentioned earlier. The high-resolution TEM (HR-TEM) has been used to obtain the lattice image and consequently, determine the phase formation at a nanometer scale.

For TEM powder sample preparation, a droplet of ultrasonically vibrated powder in acetone is deposited on a commercial copper grid coated with holy carbon film which is specifically used for TEM. The sample is subsequently dried and stored in a small clean plastic box before conducting the experiment.

3.9 ICP-AES

Inductively coupled plasma - atomic emission spectroscopy (ICP-AES), also referred to as inductively coupled plasma - optical emission spectrometry (ICP-OES), is an analytical technique used for the detection of trace metals. It is a type of emission spectroscopy that uses the inductively coupled plasma to produce excited atoms and ions that emit electromagnetic radiation at wavelengths characteristic of a particular element. The intensity of this emission is indicative of the concentration of the element within the sample.

For ICP analysis sample preparation, about 10 mg dried powders are digested using nitric acid (HNO_3) microwave digestion (Multiwave 3000, Anton Paar Ltd., UK). The obtained solutions are further diluted by 10, 000 times and measured using ICP-AES, PerkinElmer ELAN DRC-e for chemical analysis.

3.10 AC Impedance Spectroscopy

Electrical conductivity has been measured by using an AC impedance spectroscopy (Solartron SI1260, AMETEK Advanced Measurement Technology, UK). Details application of AC impedance spectroscopy and data analysis can be found elsewhere [97]. It has been found that the simultaneous measurement of resistance and capacitance of a cell over a wide range of frequency and the construction of an impedance plot from such data reveals much more information than a DC or single-frequency AC measurement. The impedance allows the electrical properties (i.e. bulk, grain boundary and electrode) to be determined and enables the investigation of the nature of the mobile charge carriers in the bulk or in interfacial regions. The transport of electrons is through the external conductor to the electrodes where reduction and oxidation reactions occur. The flow rate of the charge particles (current) depends on the ohmic resistance of the electrode and the electrolytes.

Electrochemical impedance is usually measured by applying a small AC potential to an electrochemical cell and measuring the current through the cell. Normally a sinusoidal potential excitation is applied onto an electrochemical device. The response to this potential is an AC current signal, containing the excitation frequency and its harmonics. This current signal can be analyzed as a sum of sinusoidal function (a Fourier series). In a linear (or pseudo-linear) system, the current response to a sinusoidal potential will be a sinusoid at the same frequency but shift in phase by $\pi/2$. To obtain the pseudo-linear system, the AC excitation voltage should be less than the thermal activation energy defined as RT/F where R, T and F have their usual physical meanings. Generally, the AC excitation voltage is set to be less than 10 mV.

The results of EIS investigation can be recorded as plot of $Z_{imaginary}$ vs. Z_{real} for which equivalent circuits can be produced by using proprietary software of ZView (Scribner Inc, USA) for a given electrolyte. The peak angular frequency attributed to bulk and grain boundary relaxation processes are denoted by $f_{b(max)}$ and $f_{gb(max)}$ respectively. The values of the resistance R_b, R_{gb} and R_e which represent the bulk, grain boundary and electrode resistance respectively can be obtained from the intercept of semicircles with abscissa (Z_{real}).

Normally, resistance (R), capacitance (C), and conductivity (σ) obey the following equations:

$$RC = \frac{1}{2\pi f_{max}}, \; R = \rho\frac{L}{A} \text{ and then: } \sigma = \frac{1}{\rho} \qquad (3.4)$$

Where:

- R is resistance (Ω)
- C is capacitance (F)
- f_{max} is maximum frequency in one semi-circle (Hz)
- ρ is resistance (Ωcm)
- L is the length of the pellet (cm)
- A is the area of the pellet (cm^2)

The area of the pellet is calculated by using πr^2, where r is the radius of the pellet. The activation energy (E_a), for ionic conduction in solid state electrolytes can be determined by the Arrhenius equations:

$$\sigma_T = \sigma_0 \exp\left(-\frac{E_a}{RT}\right) \qquad (3.5)$$

Where:

- σ_0 is pre-exponential conductivity
- E_a is activation energy ($J\ mol^{-1}$)
- R is gas constant (8.314 $J\ mol^{-1}\ K^{-1}$)

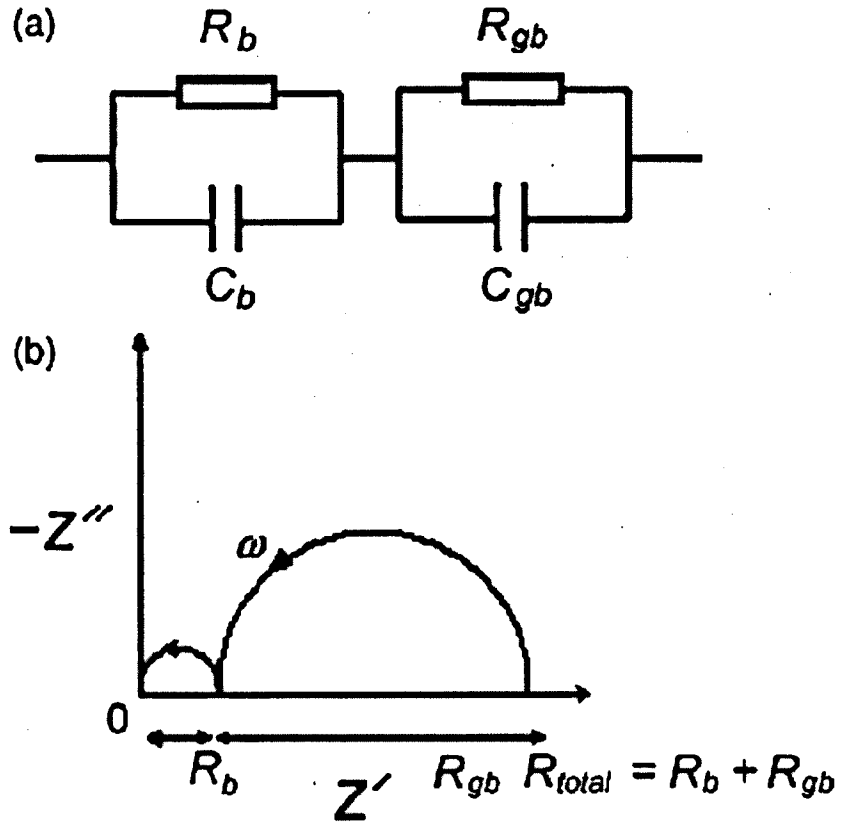

Figure 3.8. Simulated complex impedance response of a polycrystalline ceramic with corresponding equivalent circuit.

Taking "ln" on both sides of the equation, this can be represented in the following equation:

$$\ln \sigma_T = \ln \sigma_0 + \left(-\frac{E_a}{R}\right)\frac{1}{T} \qquad (3.6)$$

Hence, by measuring the conductivity at different temperature and plotting $\ln \sigma_T$ against $\frac{1}{T}$, the value of the activation energy for ionic conduction of the process can be obtained.

The conductivity of the sample is determined by AC impedance spectroscopy in the frequency range from 0.1 Hz to 32 MHz using a computer-controlled Solartron SI1260 frequency response analyzer (Farnborough, UK) at different temperature range in ambient air atmosphere. The sintered sample is in the form of a disk with platinum paste electrodes on both flat surfaces. Before performing the impedance measurement, pellets with platinum paste are fired at 900 °C for 1 hour twice in order to remove the organic binder in the platinum paste, which if present may affect

the results of electrical conductivity. The pellet is mounted in a spring-loaded quartz rig with electrical contact being made by means of Pt gauze (99.9%, 52 meshes, Aldrich Ltd, UK) spot welded to Pt wires (99.99%, 0.127 mm diameter, Aldrich Ltd, UK).

This assembly is then placed in a stainless steel tube located in a horizontal Lenton Tube furnace (Lenton Thermal Designs Ltd, UK). The stainless steel tube is grounded to minimize electrical interference which many arise from the furnace windings and other external electrical sources. The temperature is monitored with a type K thermocouple located adjacent to the rig. At each temperature, the measurements are performed at a DC potential of 10−100 mV after at least 30 minutes stabilization.

Overall, in this present study, various analytical methods such as TGA/DSC, FTIR, XRD, XMT, SEM, TEM and AC impedance spectroscopy have been used for material characterizations. The advantages and disadvantages of these techniques are summarized in Table 3.2.

Table 3.2. Advantages and Disadvantages of various characterization techniques.

Techniques	Advantages	Disadvantage
TGA/DSC	Easy sample preparation. Small test specimens (typically 5–20 mg). Wide range of temperature applicability. Monitor small weight changes.	Difficult to assign T_g value for some materials, either because the wrong thermal transition has been assigned as the T_g or because there may be only a small change in heat flux as the T_g is passed through during the temperature ramp.
FTIR	Fast scanning time. Large wavenumber ranges per scan. Low cost of basic optical equipment.	The interferograms sometimes cannot be visually interpreted, which makes it for an operator to judge quickly whether or not an experiment is satisfactory.
XRD/XMT	Cost efficient. No damage of specimen.	They do not interact very strongly with lighter elements.
SEM	Suitable for almost all kinds of samples, conducting and non-conducting. No requirement of electron-transparent sample.	Usually required surface stain-coating with metals for electron conducting.
TEM	High resolution, as small as 0.2 nm. Direct imaging of crystalline lattice. No metallic stain-coating needed .	To prepare an electron transparent sample from the bulk is difficult (due to the conductivity or electron density and sample thickness).
AC Impedance	Useful on high resistance materials.	Expensive.

Chapter 4. Results

This chapter provides the details of the research works and its findings of various metal oxides. It is being separated into three sections, including 4.1 $Ce_{0.8}Gd_{0.2}O_{1.9}$ production by organic precursors, 4.2 NiO production by Na-ALG (sodium alginate) and 4.3 $Ce_xGd_{1-x}O_{2-\delta}$ production by Na-ALG beads, respectively. More information can be found below.

4.1 $Ce_{0.8}Gd_{0.2}O_{1.9}$ Production by Organic Precursors

The Cerium Gadolinium Oxide ($Ce_{0.8}Gd_{0.2}O_{1.9}$, CGO2) nanopowders were prepared by maltose + pectin or sucrose + pectin routes, respectively. The physical, chemical and electrical property results of CGO were shown below.

4.1.1. $Ce_{0.8}Gd_{0.2}O_{1.9}$ Production using Maltose and Pectin

The thermal analysis (TGA/GSC) of maltose, pectin, maltose + pectin mixed gel and Ce^{3+} + Gd^{3+} incorporated maltose + pectin mixed gel in controlled atmosphere of air at a flow rate of 50 mL min^{-1} from ambient temperature to 1000 °C with heating rate of 3 °C min^{-1} without any holding time have been shown in Figure 4.1.1a, 4.1.1b and 4.1.2, respectively. The negative values observed in the TGA/DSC profiles between 800 and 1000 °C are due to the instrument error.

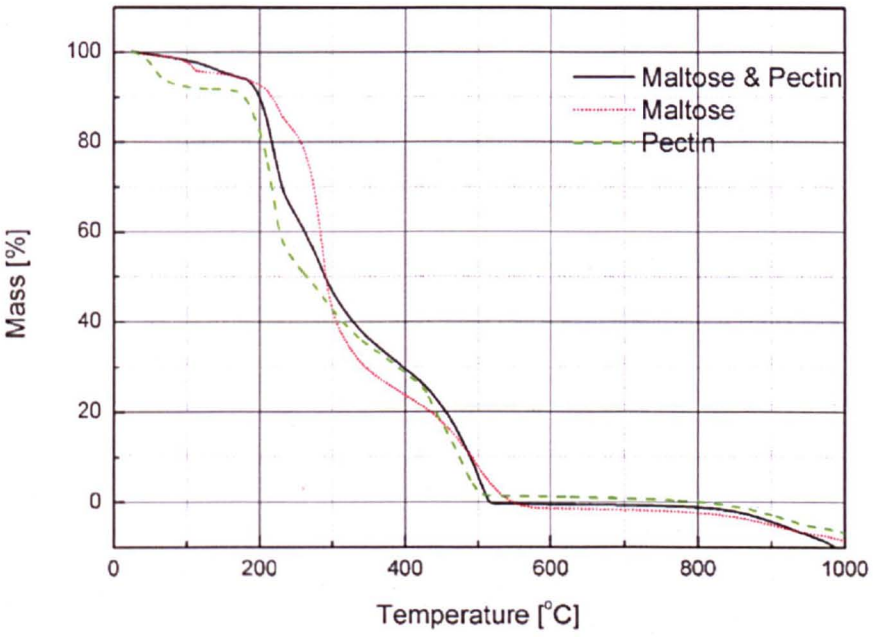

Figure 4.1.1a. TGA of maltose, pectin and, maltose and pectin mixed gel in air.

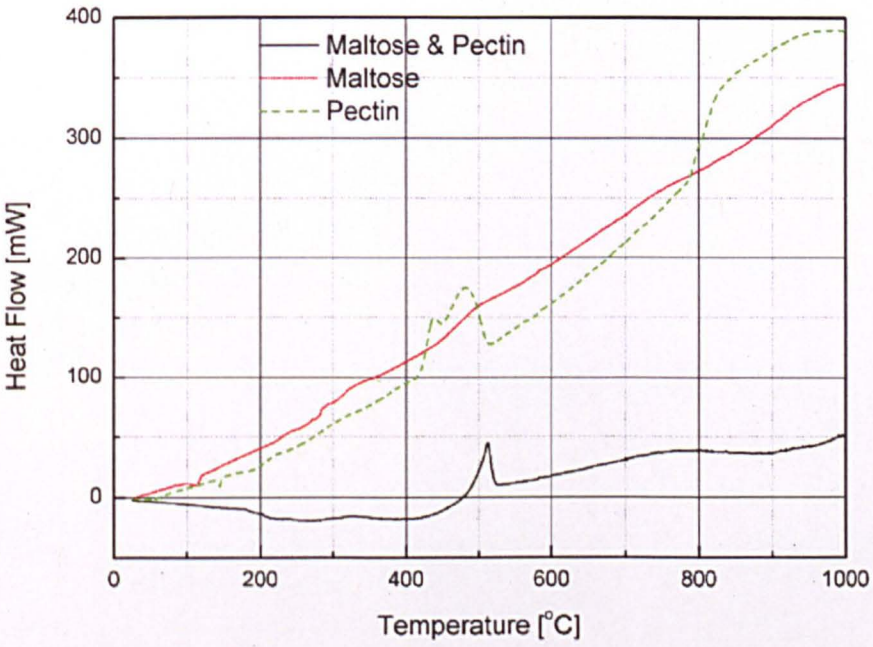

Figure 4.1.1b. DSC of maltose, pectin and, maltose and pectin mixed gel in air.

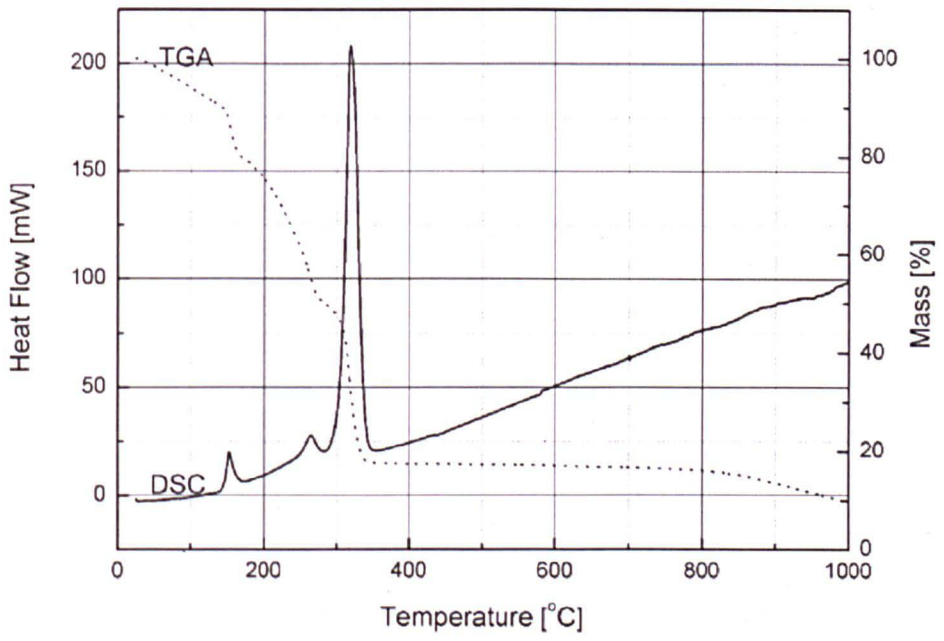

Figure 4.1.2. Thermal analyses of Ce^{3+} and Gd^{3+} incorporated maltose and pectin mixed gel in air.

The Ce^{3+} + Gd^{3+} incorporated maltose + pectin mixed gel sample was also analyzed in flowing helium gas at 50 mL min^{-1} with heating rate of 3 °C min^{-1} from ambient temperature to 500 °C. Once the sample reached 500 °C, helium gas was switched over to air for 1 hour of high temperature annealing. The TGA/DSC graphs are shown in Figure 4.1.3a and 4.1.3b, respectively.

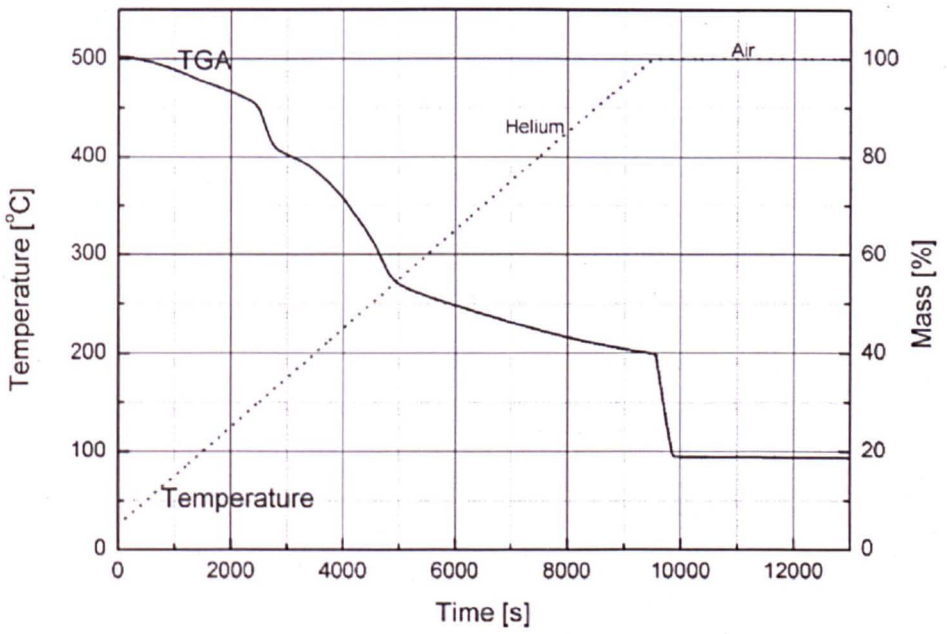

Figure 4.1.3a. TGA of Ce^{3+} and Gd^{3+} incorporated maltose and pectin mixed gel under flowing He and air.

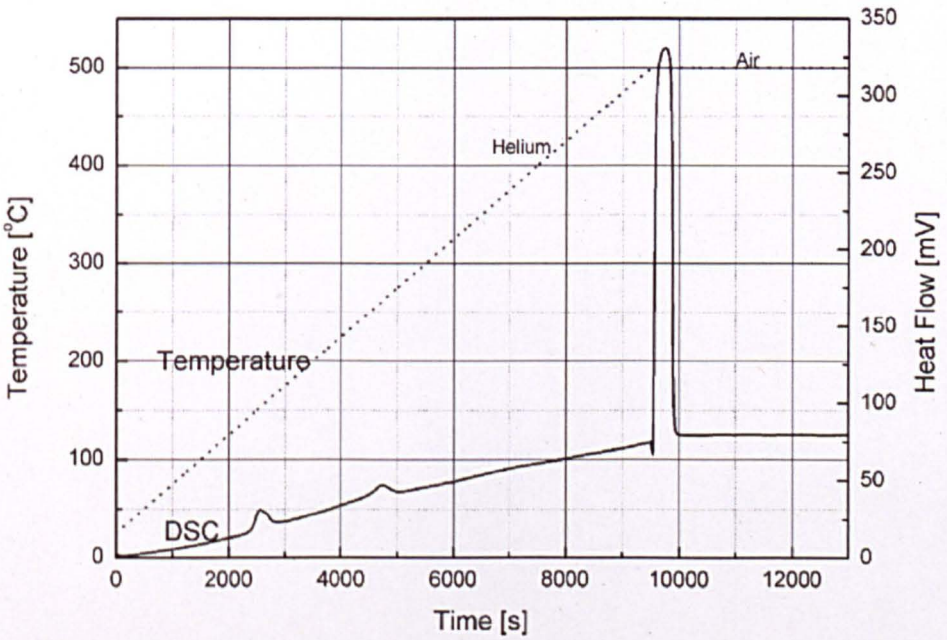

Figure 4.1.3b. DSC of Ce^{3+} and Gd^{3+} incorporated maltose and pectin mixed gel under flowing He and air.

The XRD patterns of as-synthesized CGO2 ($Ce_{0.8}Gd_{0.2}O_{1.9}$) nanopowders after calcination at various temperatures for 2 hours are shown in Figure 4.1.4.

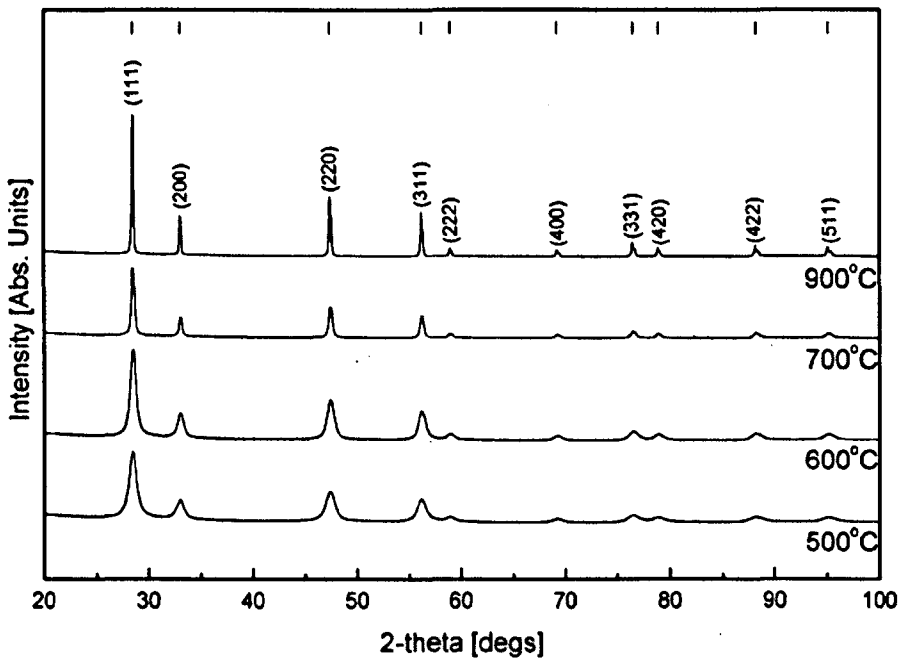

Figure 4.1.4. XRD of CGO2 nanopowders calcined at 500, 600, 700 and 900 °C for 2 hrs. The tick marks of pure $Ce_{0.8}Gd_{0.2}O_{1.9}$, ICDD 04-14-0032, are shown at the top of the figure.

The TEM images for the above CGO2 samples are shown in Figure 4.1.5.

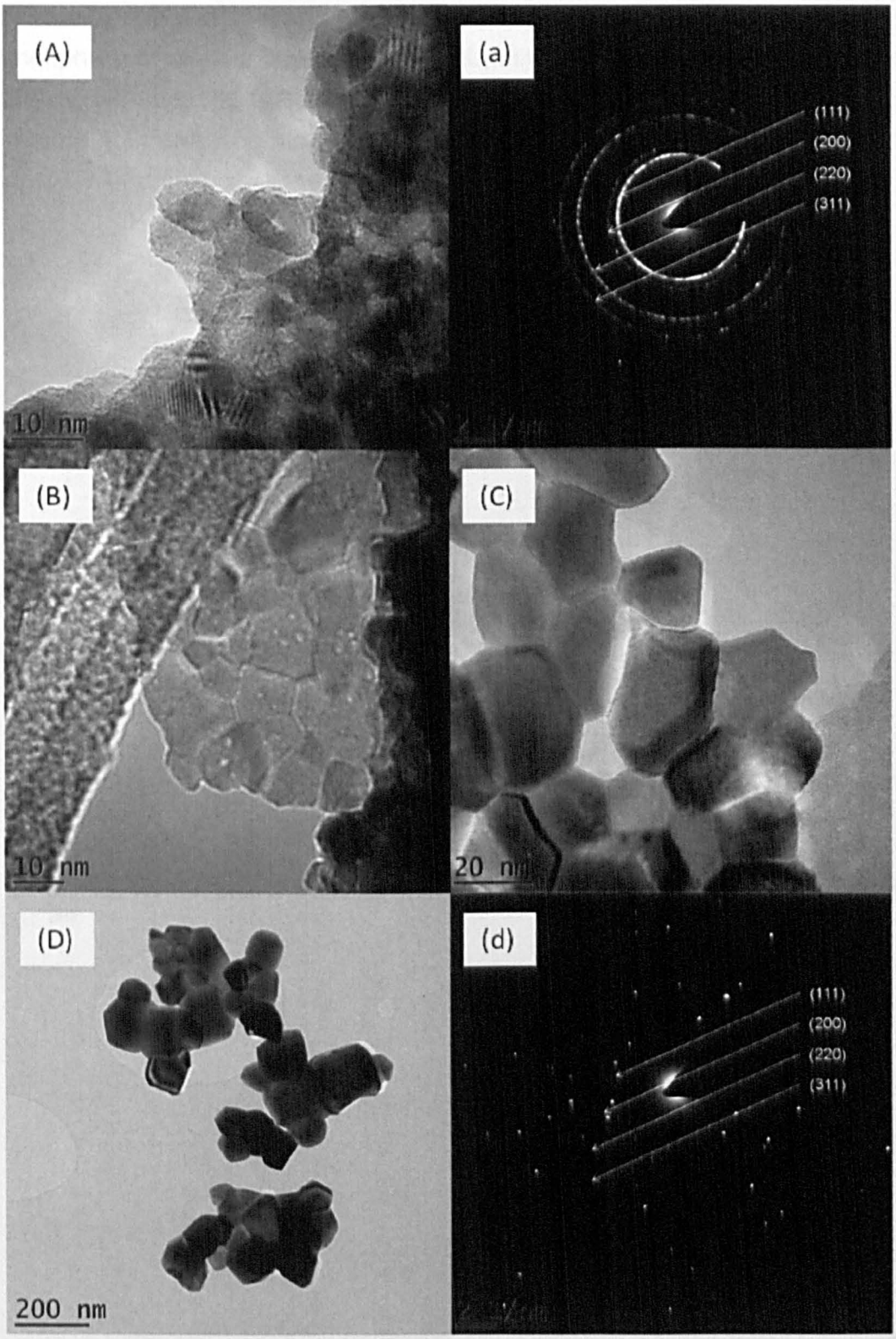

Figure 4.1.5. Samples calcined at different temperatures for 2 hrs: (A) 500 °C, (a) SAED of sample A, (B) 600 °C, (C) 700 °C, (D) 900 °C and (d) SAED of sample D.

4.1.2. $Ce_{0.8}Gd_{0.2}O_{1.9}$ Production using Sucrose and Pectin

The thermal analysis (TGA/GSC) of sucrose, pectin, sucrose + pectin mixed gel and Ce^{3+} + Gd^{3+} incorporated sucrose + pectin mixed gel in controlled atmosphere of air at a flow rate of 50 mL min^{-1} from ambient temperature to 1000 °C with heating rate of 3 °C min^{-1} without any holding time are shown in Figure 4.1.6a, 4.1.6b and 4.1.7, respectively. The negative value observed in the TGA profile between 800 and 1000 °C is due to the instrument error.

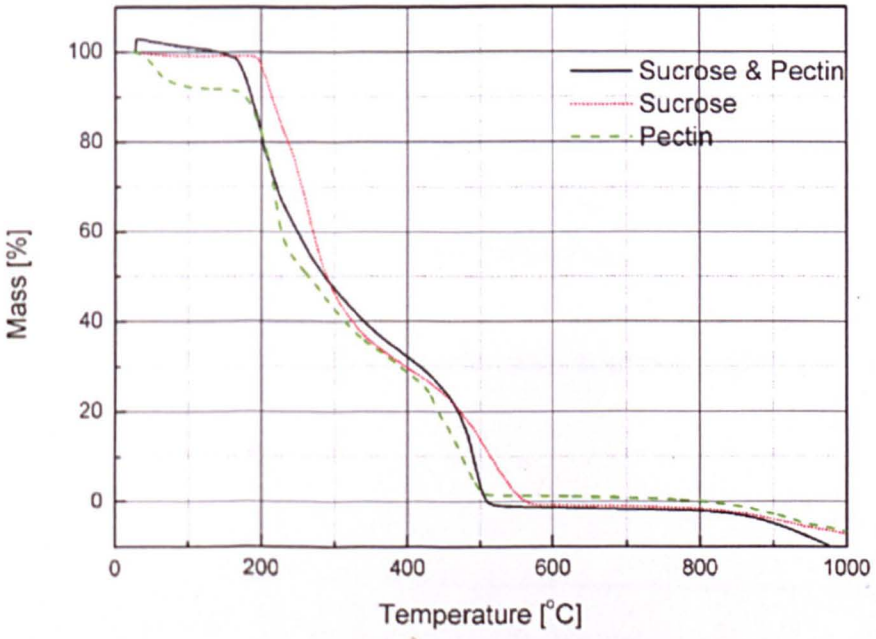

Figure 4.1.6a. TGA of sucrose, pectin and, sucrose and pectin mixed gel in air.

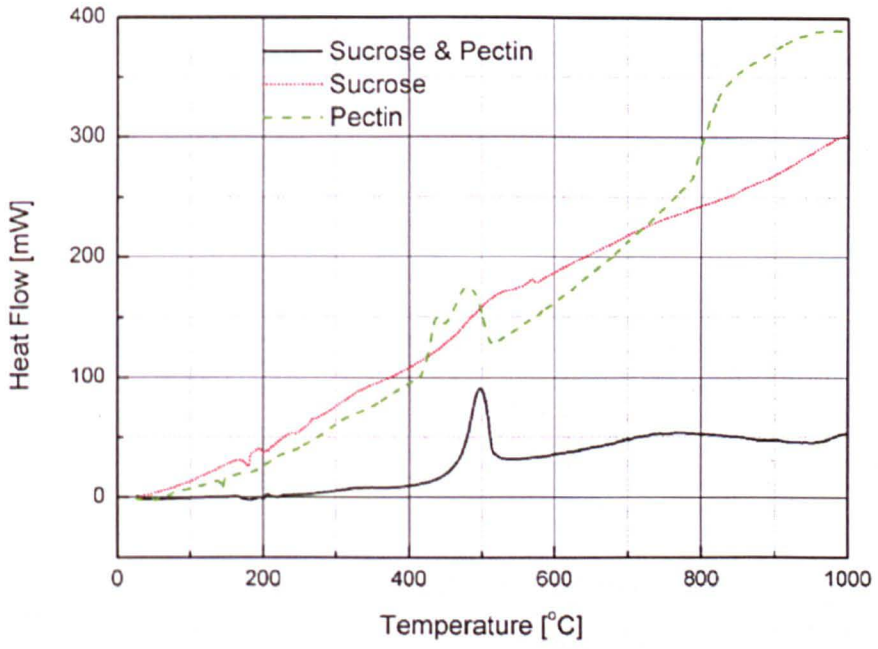

Figure 4.1.6b. DSC of sucrose, pectin and, sucrose and pectin mixed gel in air.

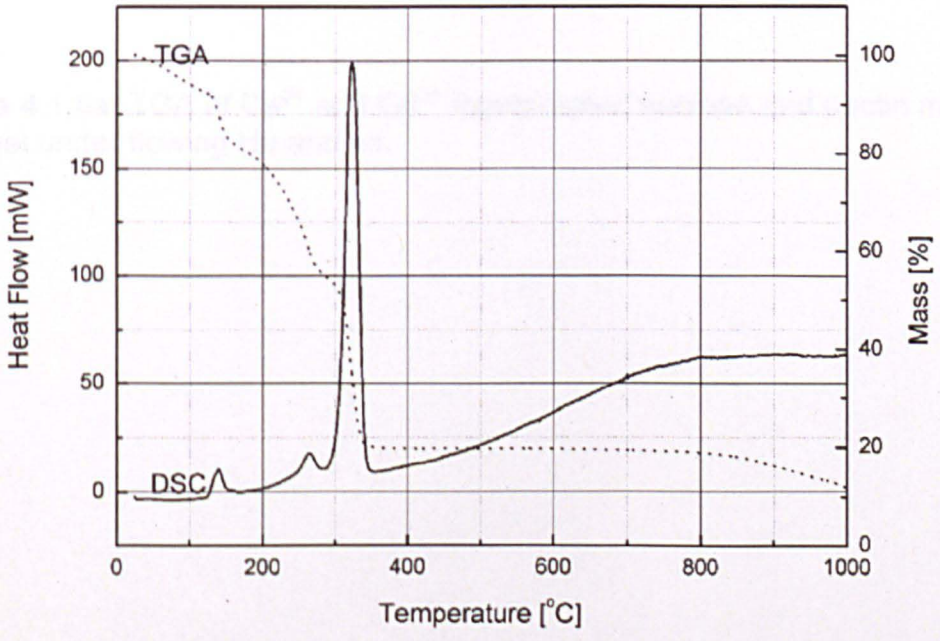

Figure 4.1.7. Thermal analysis of Ce^{3+} and Gd^{3+} incorporated sucrose and pectin mixed gel in air.

The Ce^{3+} + Gd^{3+} incorporated sucrose + pectin mixed gel sample was also analyzed in flowing helium gas at 50 mL min^{-1} with heating rate of 3 °C min^{-1} from ambient temperature to 500 °C. Once the sample reached 500 °C, helium gas was switched over to air for 1 hour of high temperature annealing. The TGA/DSC graphs are shown in Figure 4.1.8a and 4.1.8b, respectively.

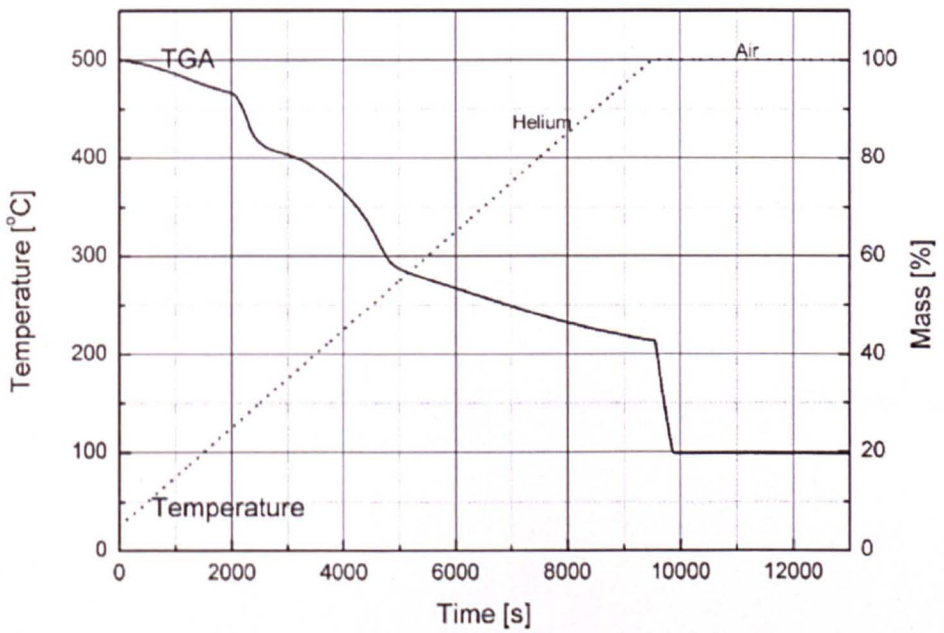

Figure 4.1.8a. TGA of Ce^{3+} and Gd^{3+} incorporated sucrose and pectin mixed gel under flowing He and air.

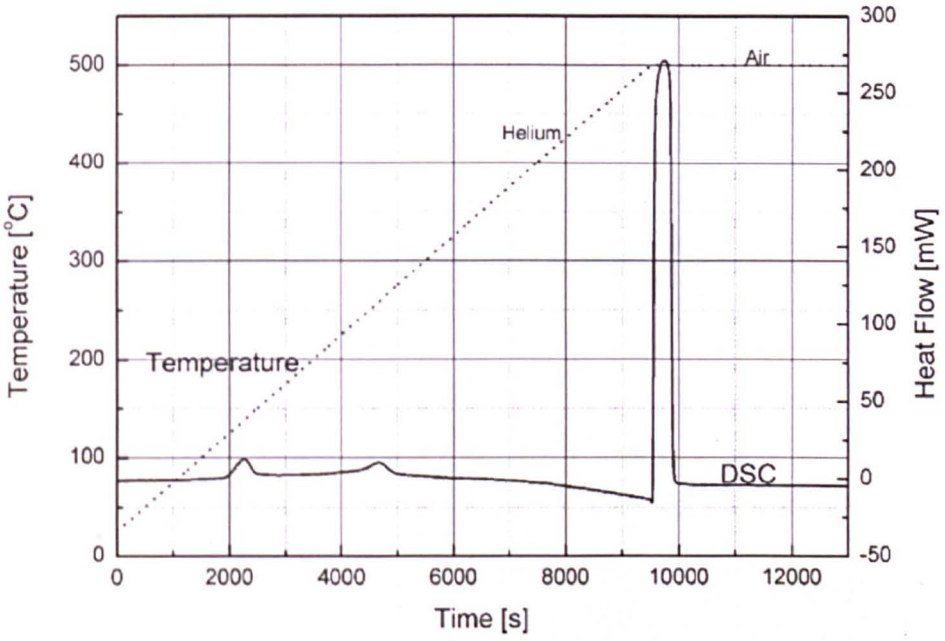

Figure 4.1.8b. DSC of Ce^{3+} and Gd^{3+} incorporated sucrose and pectin mixed gel under flowing He and air.

The XRD patterns of as-synthesized CGO2 ($Ce_{0.8}Gd_{0.2}O_{1.9}$) nanopowders after calcination at various temperatures for 2 hours are shown in Figure 4.1.9.

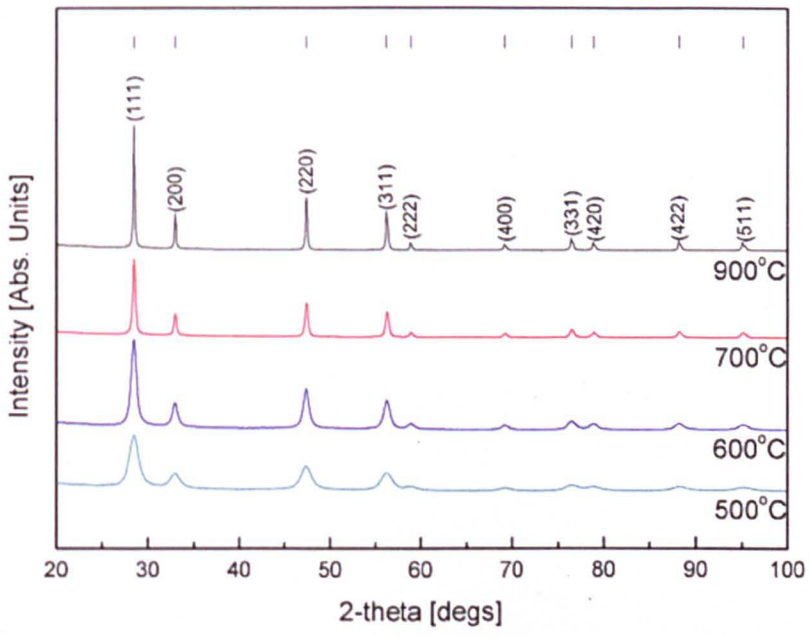

Figure 4.1.9. XRD of CGO2 nanopowders calcined at 500, 600, 700 and 900 °C for 2 hrs. The tick marks of pure $Ce_{0.8}Gd_{0.2}O_{1.9}$, ICDD 04-14-0032, are shown at the top of the figure.

The TEM and SAED images for the above CGO2 samples are shown in Figure 4.1.10 and 4.1.11, respectively.

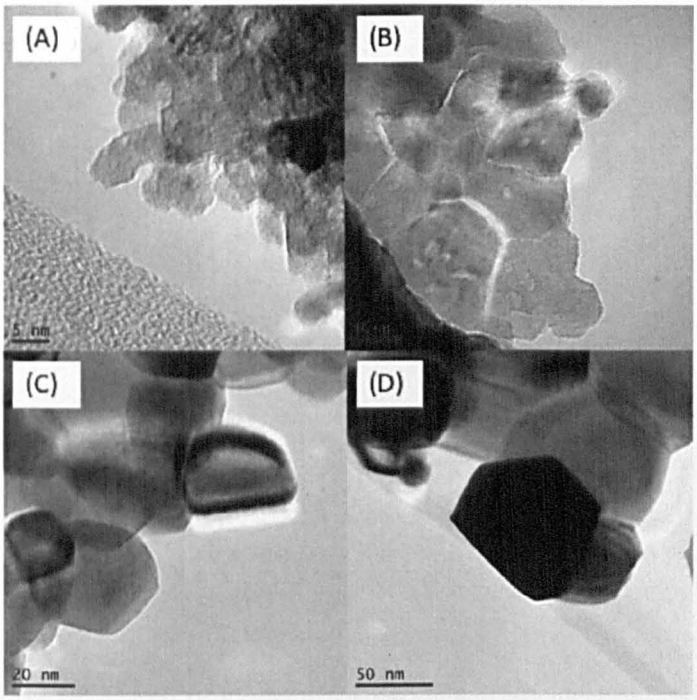

Figure 4.1.10. Samples calcined at different temperatures for 2 hrs: (A) 500 °C, (B) 600 °C, (C) 700 °C and (D) 900 °C, respectively.

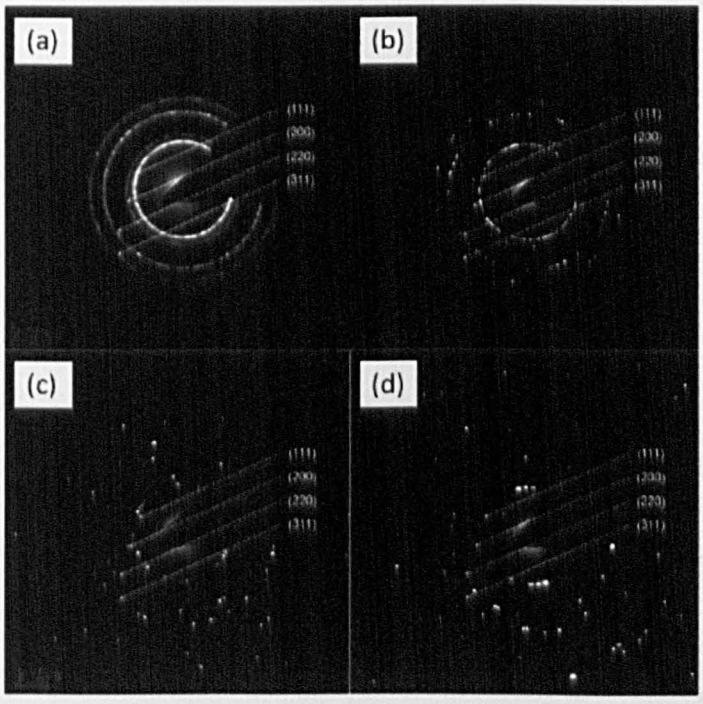

Figure 4.1.11. SAED patterns for samples calcined at different temperatures for 2 hrs: (a) 500 °C, (b) 600 °C, (c) 700 °C and (d) 900 °C, respectively.

4.1.3. Material Conductivity Analysis for SOFC Application

The SEM images of fracture surfaces of CGO2 pellets prepared by maltose + pectin or sucrose + pectin routes are shown in Figure 4.1.12, respectively.

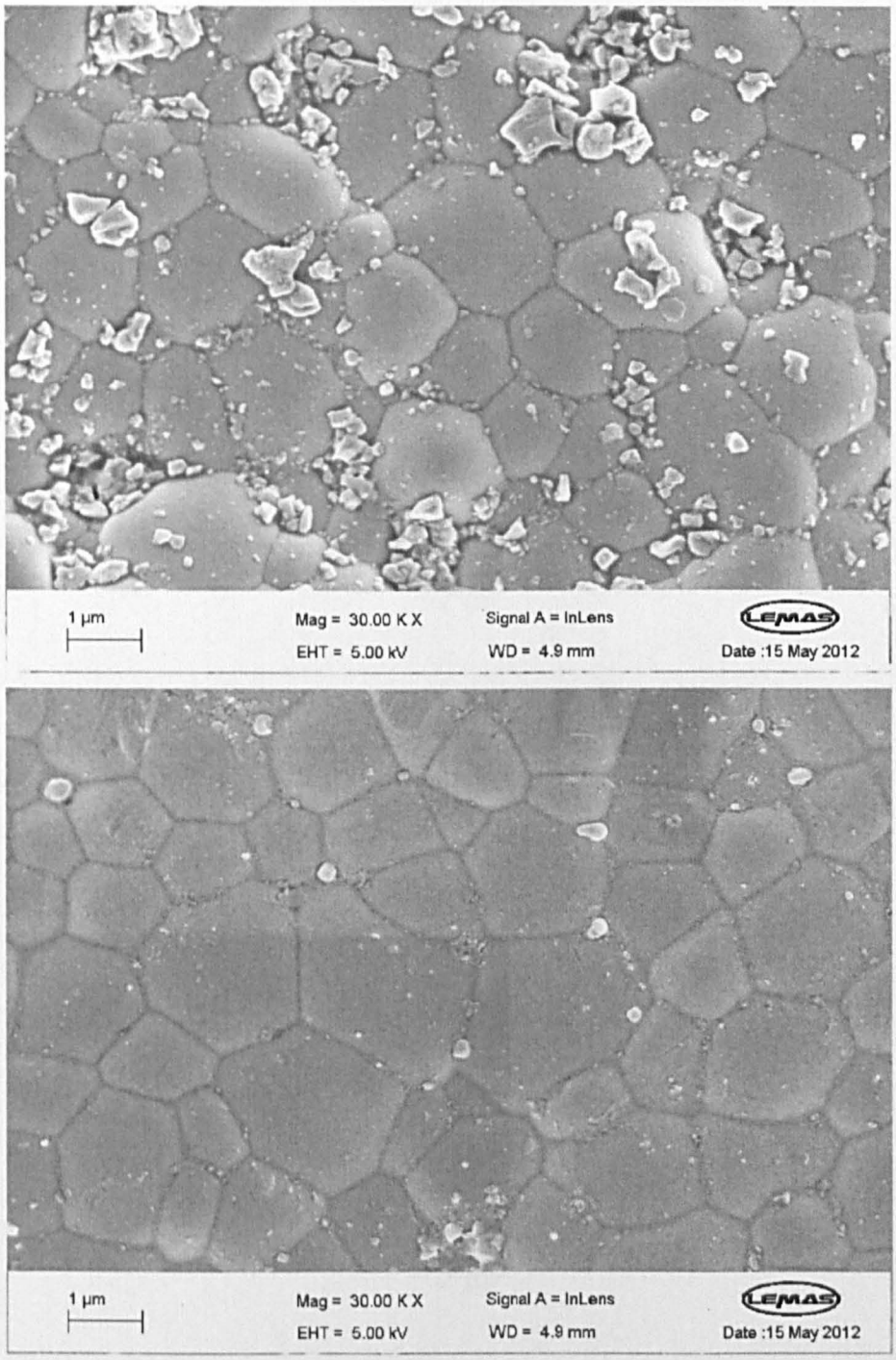

Figure 4.1.12. SEM images of the fracture surface of CGO2 pellets sintered at 1500 °C – 2 hrs. CGO2 produces by maltose + pectin (Top) and sucrose + pectin (Bottom).

The measured impedance spectra for CGO2 prepared by maltose + pectin or sucrose + pectin routes at different temperatures are shown in Figure 4.1.13 – 4.1.16, respectively.

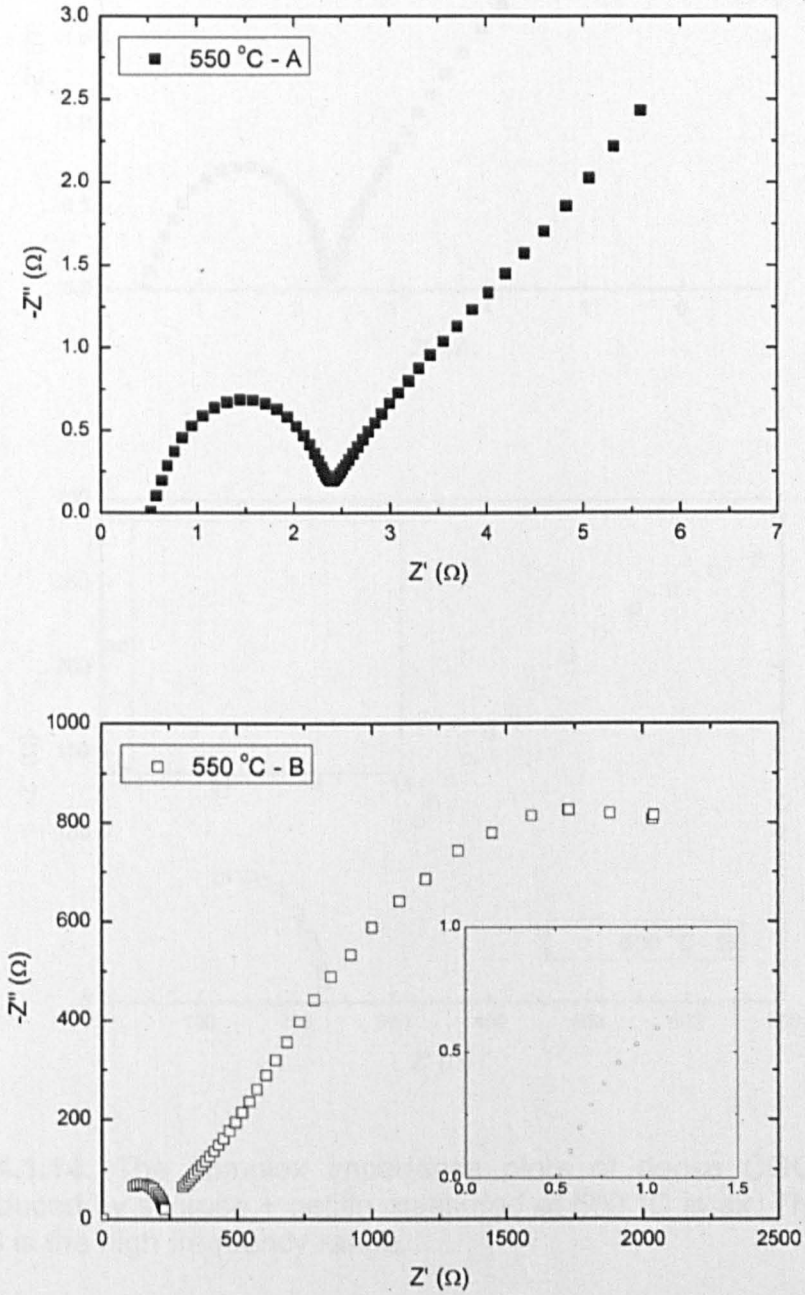

Figure 4.1.13. The complex impedance plots of dense CGO2 ceramic produced by maltose + pectin measured at 550 °C in air. The inset plot in B is the high frequency range.

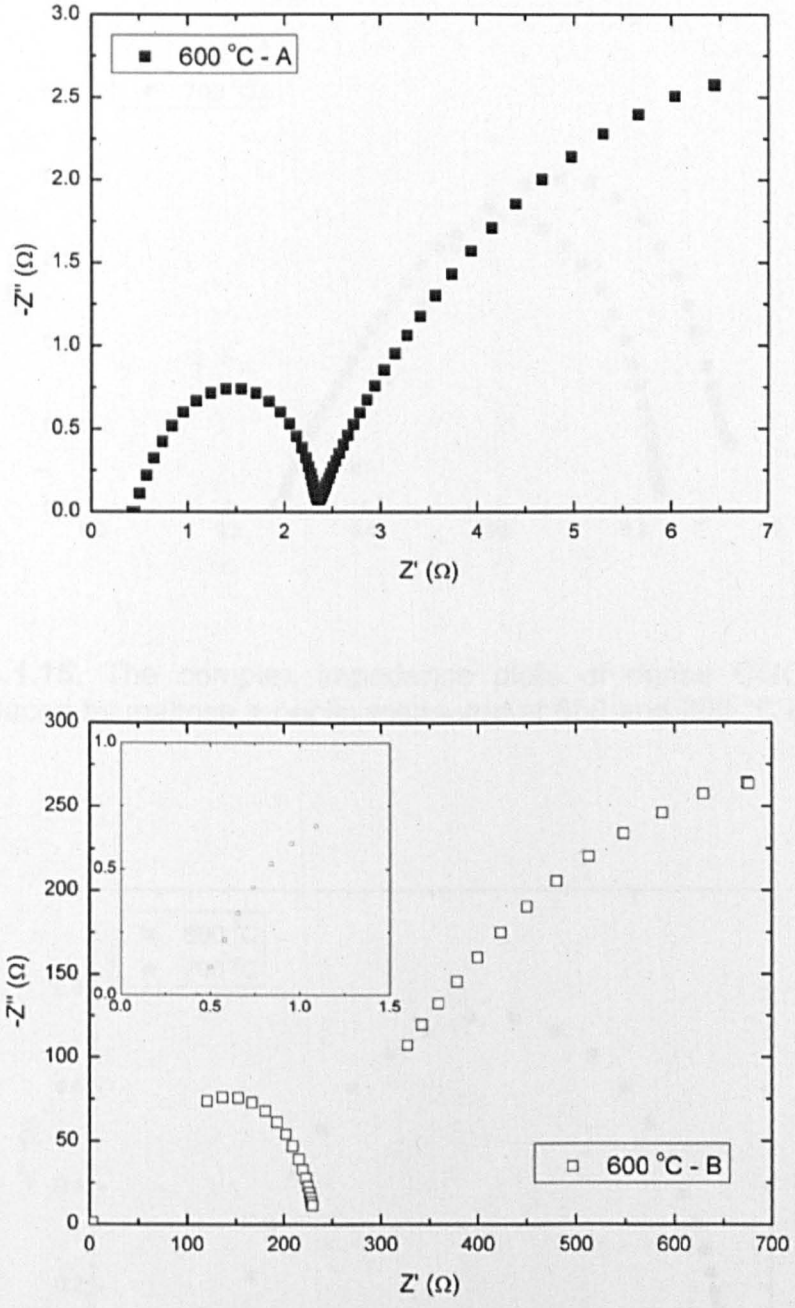

Figure 4.1.14. The complex impedance plots of dense CGO2 ceramic produced by sucrose + pectin measured at 600 °C in air. The inset plot in B is the high frequency range.

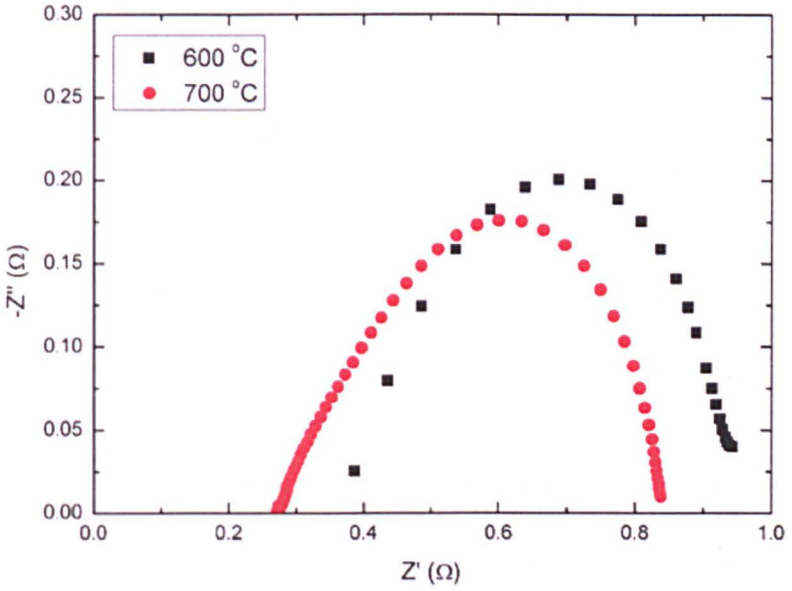

Figure 4.1.15. The complex impedance plots of dense CGO2 ceramic produced by maltose + pectin measured at 600 and 700 °C in air.

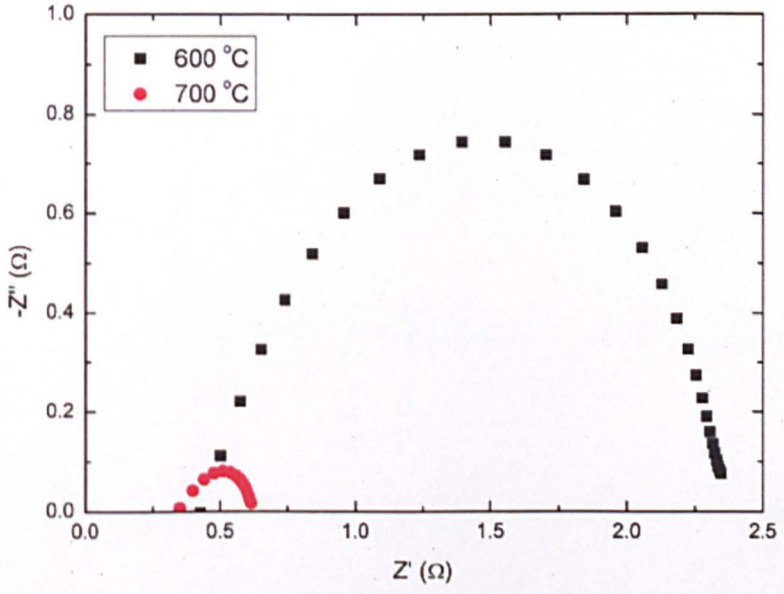

Figure 4.1.16. The complex impedance plots of dense CGO2 ceramic produced by sucrose + pectin measured at 600 and 700 °C in air.

4.2 NiO Production by Na-ALG

The nickel oxide (NiO) nanopowders were syntheses using sodium alginate (Na-ALG) in forms of beads or granules, respectively. The physical and chemical property results of NiO are shown below.

4.2.1. NiO Production by Na-ALG Beads

The images of nickel alginate (Ni-ALG) wet and dried beads after ion-exchanged with 4 wt% sodium alginate solution have been shown in Figure 4.2.1, respectively. The thermal analysis (TGA/DSC) of the dried Ni-ALG beads in controlled atmosphere of air at a flow rate of 10 mL min^{-1} from ambient temperature to 1000 °C with heating rate of 3 °C min^{-1} without any holding time is shown in Figure 4.2.2. The negative value observed in the TGA profile between 800 and 1000 °C is due to the instrument error.

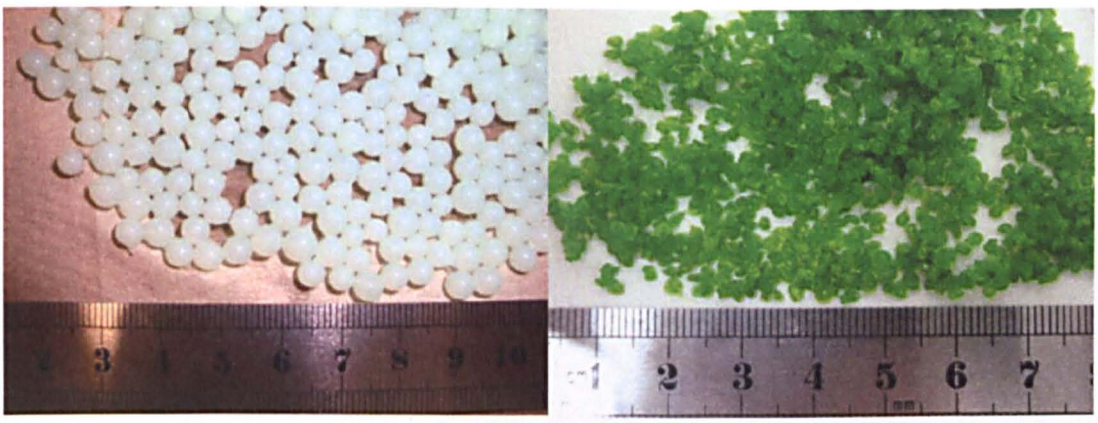

Ni-ALG wet beads

Ni-ALG dried beads

Figure 4.2.1. Ni-ALG Wet vs. Dried Beads, respectively.

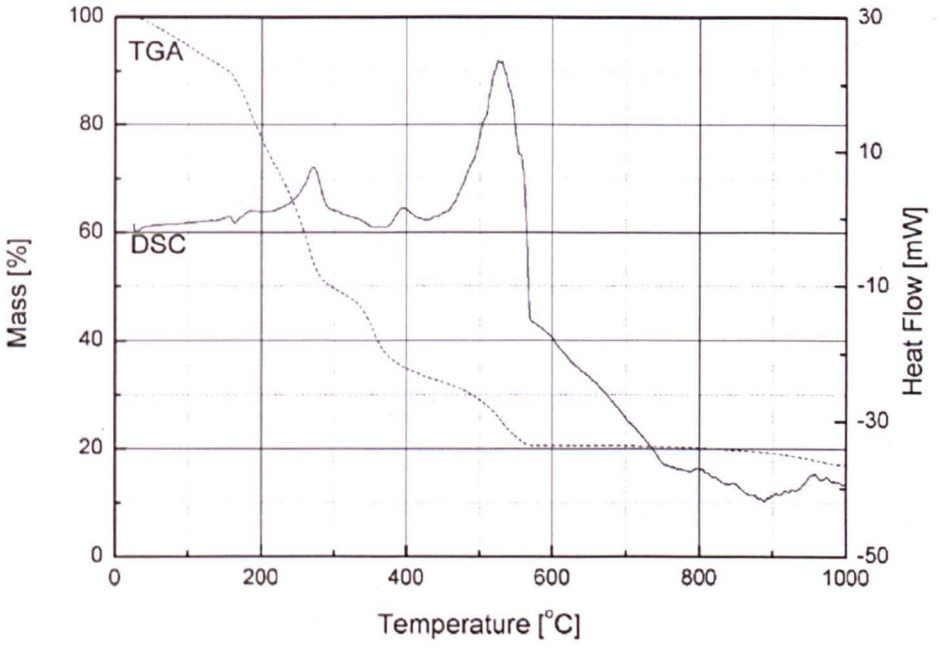

Figure 4.2.2. Thermal analysis of Ni-ALG dried beads in air.

The High Temperature X-ray diffraction (HT-XRD) patterns of dried Ni-ALG beads have been shown in Figure 4.2.3a, 4.2.3b and 4.2.3c, respectively. The temperature program was set every 25 °C interval from room temperature to 600 °C with heating rate maintained at 3 °C min^{-1} in static air condition. At each temperature, 30 mins annealing time was allowed for the sample to equilibrate.

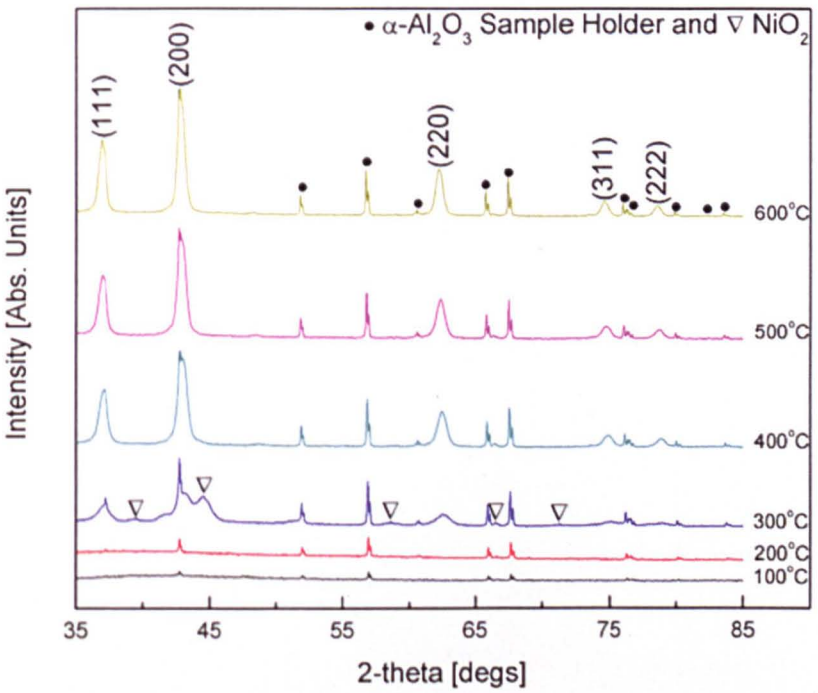

Figure 4.2.3a. HT-XRD of Ni-ALG dried beads at different temperatures. The patterns are indexed by ICDD 04-002-0665 as cubic NiO shown at the top of the peaks. Tick marks "black dot" for reference pattern of α-Al_2O_3 (ICDD 01-076-7777) and tick marks "white triangles" for reference pattern of NiO_2 (01-085-1977) are shown at the top of the peaks, respectively.

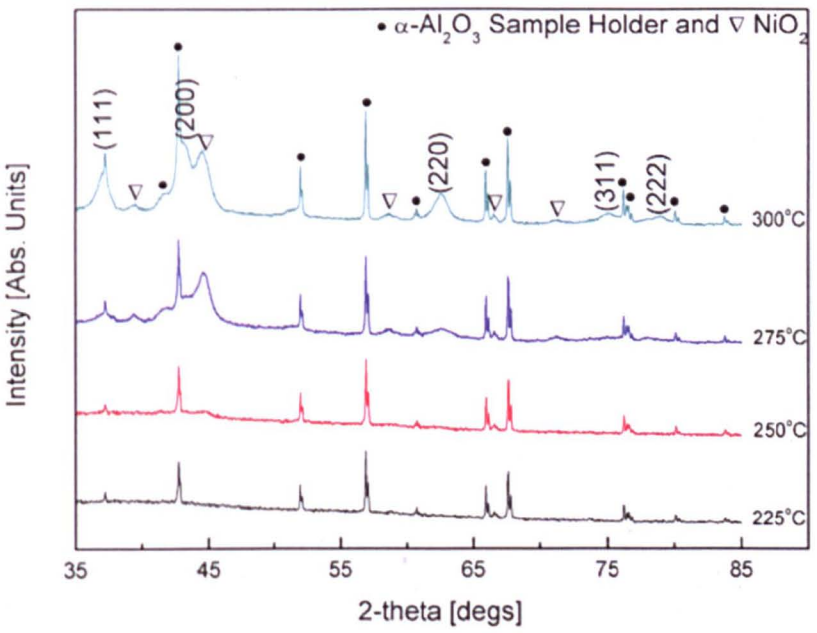

Figure 4.2.3b. HT-XRD of Ni-ALG dried beads heat treated from 225 to 300 °C.

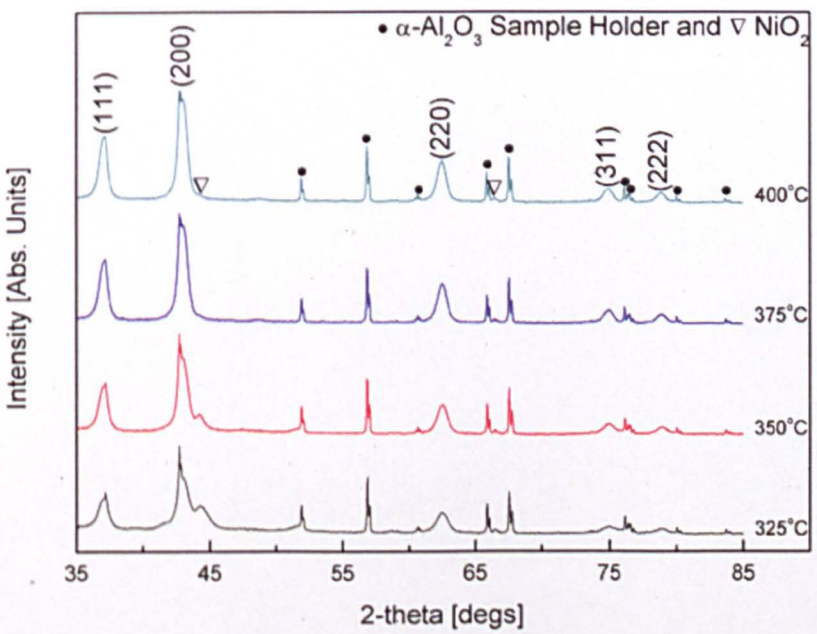

Figure 4.2.3c. HT-XRD of Ni-ALG dried beads heat treated from 325 to 400 °C.

The XRD patterns of as-prepared NiO nanopowders heat treated at different temperatures for various annealing time lengths are shown in Figure 4.2.4a and 4.2.4b, respectively.

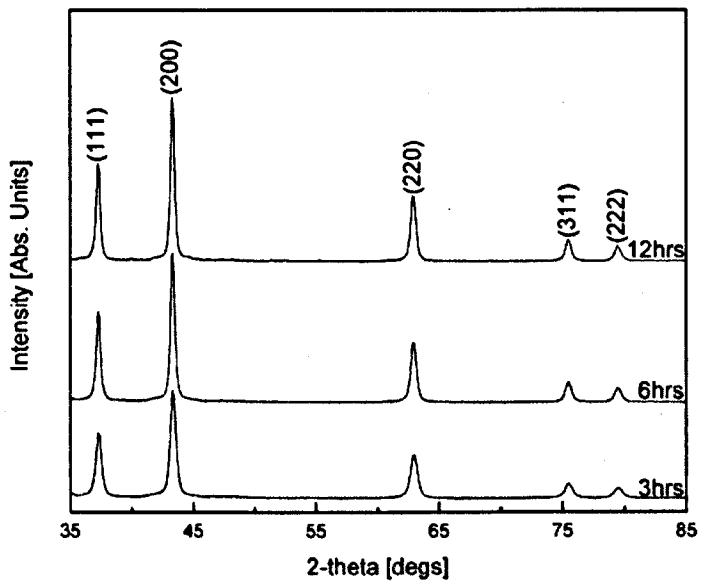

Figure 4.2.4a. XRD of NiO nanopowders calcined at 500 °C for 3, 6 and 12 hrs annealing time. The patterns are indexed by ICDD 04-002-0665 shown at the top of the peaks.

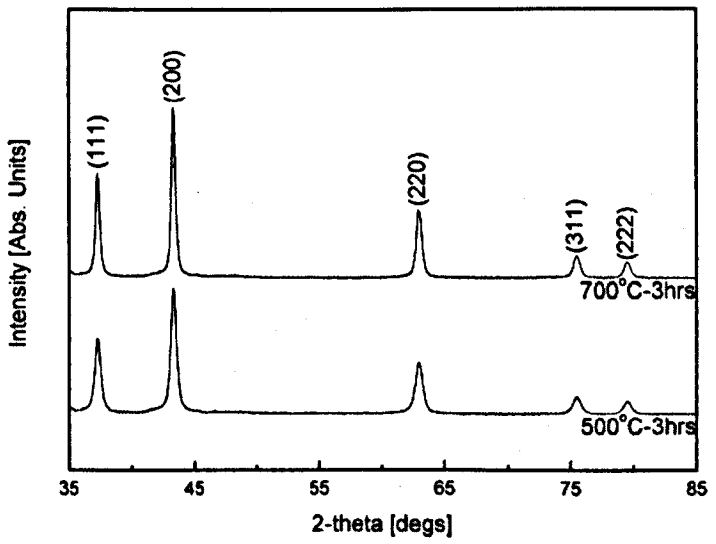

Figure 4.2.4b. XRD of NiO nanopowders calcined at 500 or 700 °C for 3 hrs annealing time.

The TEM and SAED images for the above NiO samples are shown in Figure 4.2.5a and 4.2.5b, respectively.

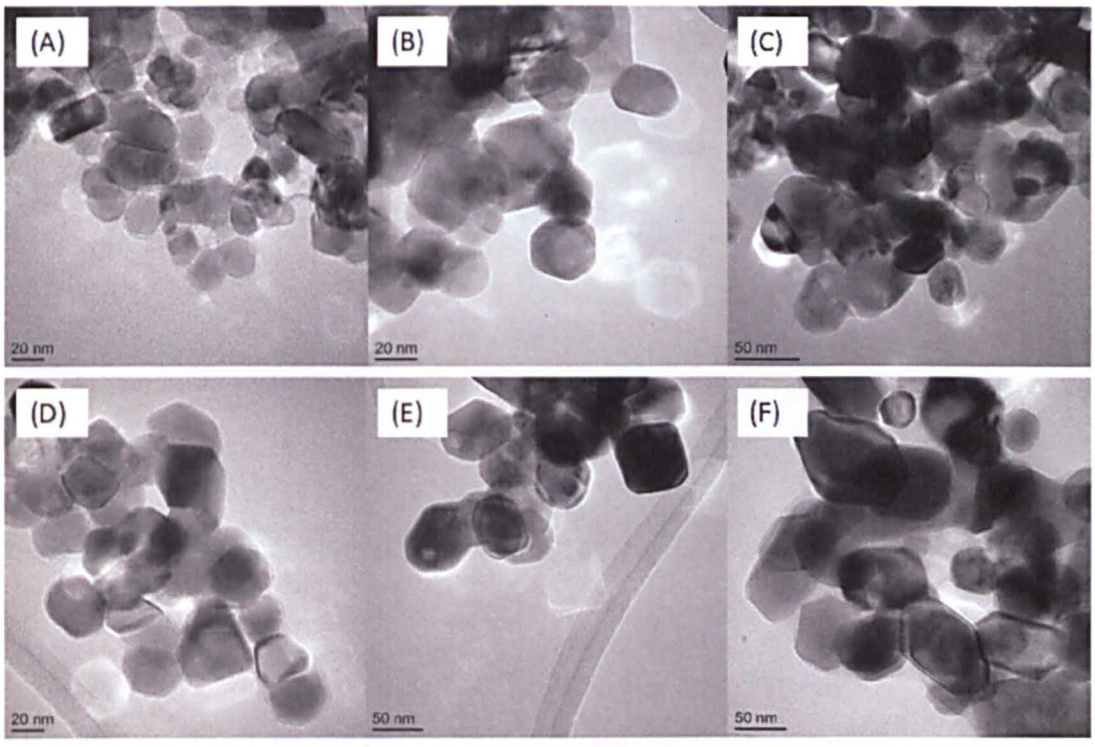

Figure 4.2.5a. TEM images of NiO calcined at different conditions: (A) 500 °C – 3 hrs, (B) 500 °C – 6 hrs, (C) 500 °C – 12 hrs, (D) 700 °C – 3 hrs, (E) 700 °C – 6 hrs and (F) 700 °C – 12 hrs, respectively.

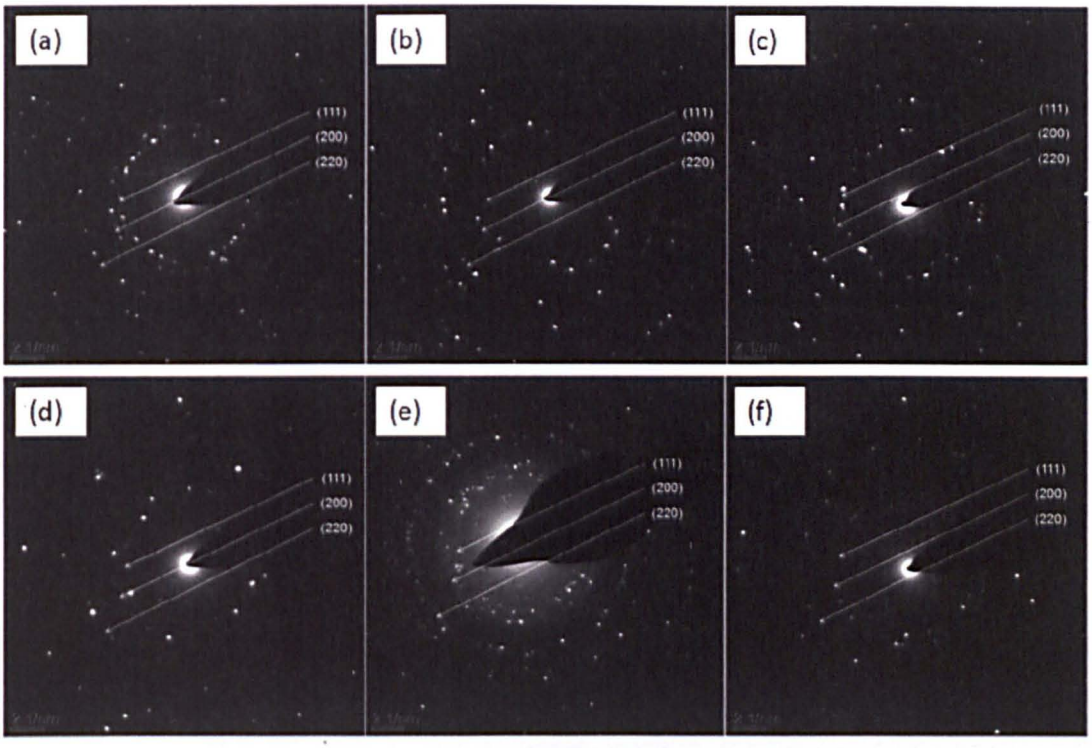

Figure 4.2.5b. SAED images of NiO calcined at different conditions: (a) 500 °C – 3 hrs, (b) 500 °C – 6 hrs, (c) 500 °C – 12 hrs, (d) 700 °C – 3 hrs, (e) 700 °C – 6 hrs and (f) 700 °C – 12 hrs, respectively.

4.2.2. XMT of Freeze Dried Ni-ALG Beads

The images of nickel alginate (Ni-ALG) wet and freeze dried beads after ion-exchanged with 4 wt% sodium alginate solution are shown in Figure 4.2.6, respectively.

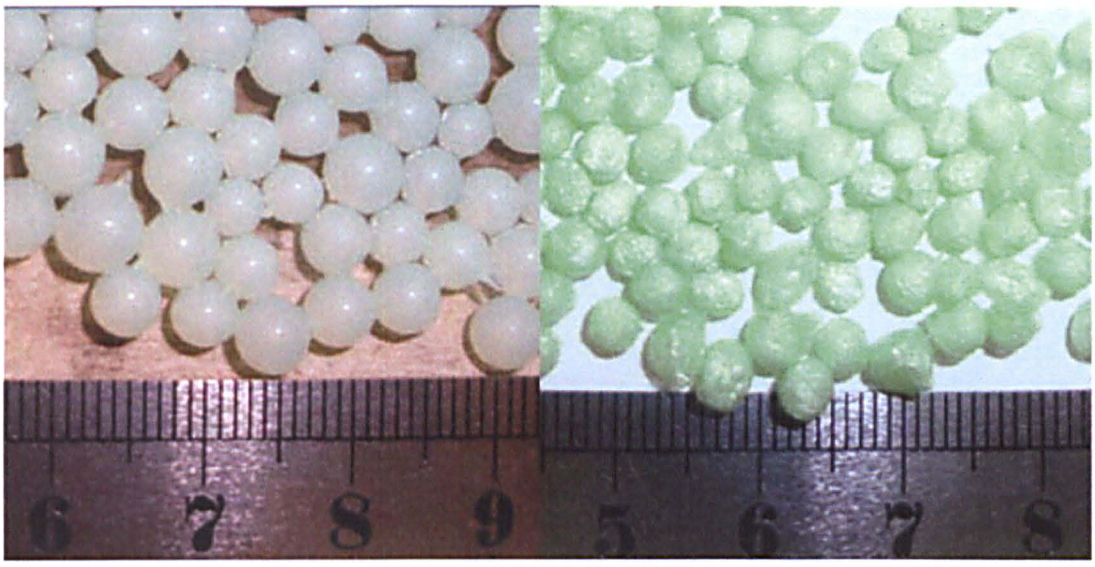

Figure 4.2.6. Nickel alginate wet beads (left) and freeze dried beads (right).

The XMT patterns of freeze dried Ni-ALG beads and NiO beads after calcination are shown in Figure 4.2.7 and 4.2.8, respectively.

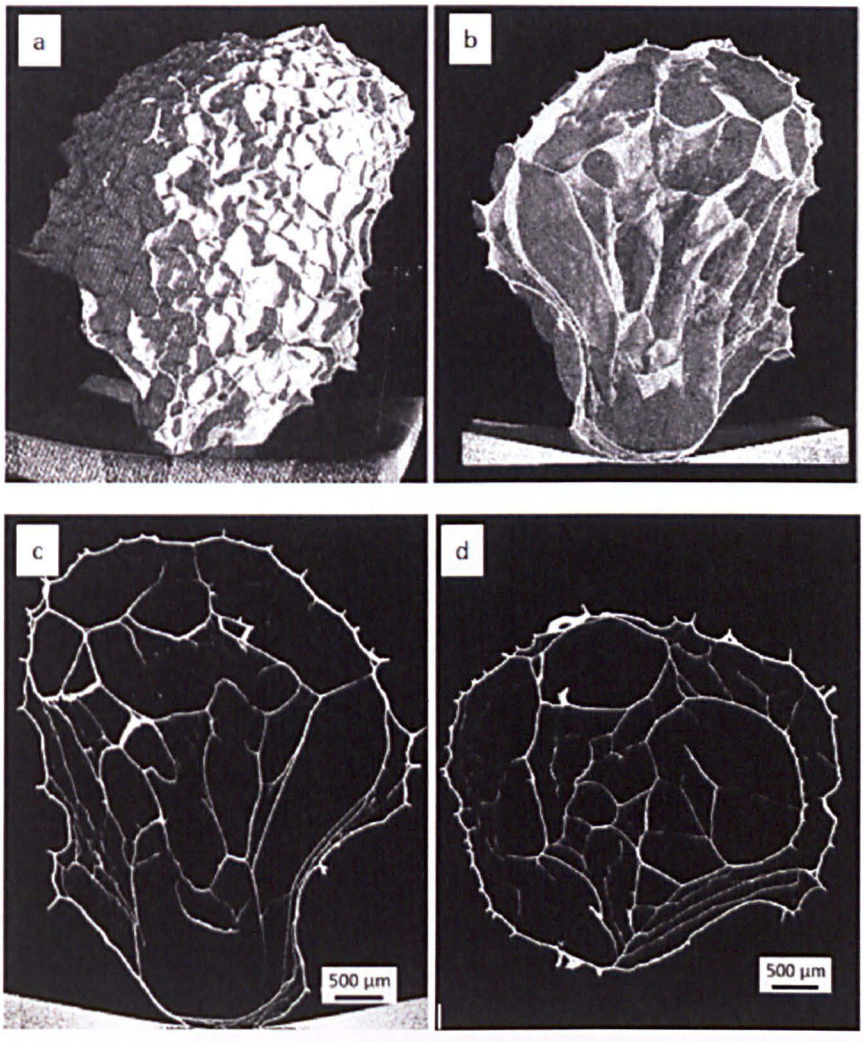

Figure 4.2.7. XMT images of the freeze dried nickel alginate bead: (a and b) 3D structure from outside and inside, (c and d) transverse and cross sections, respectively.

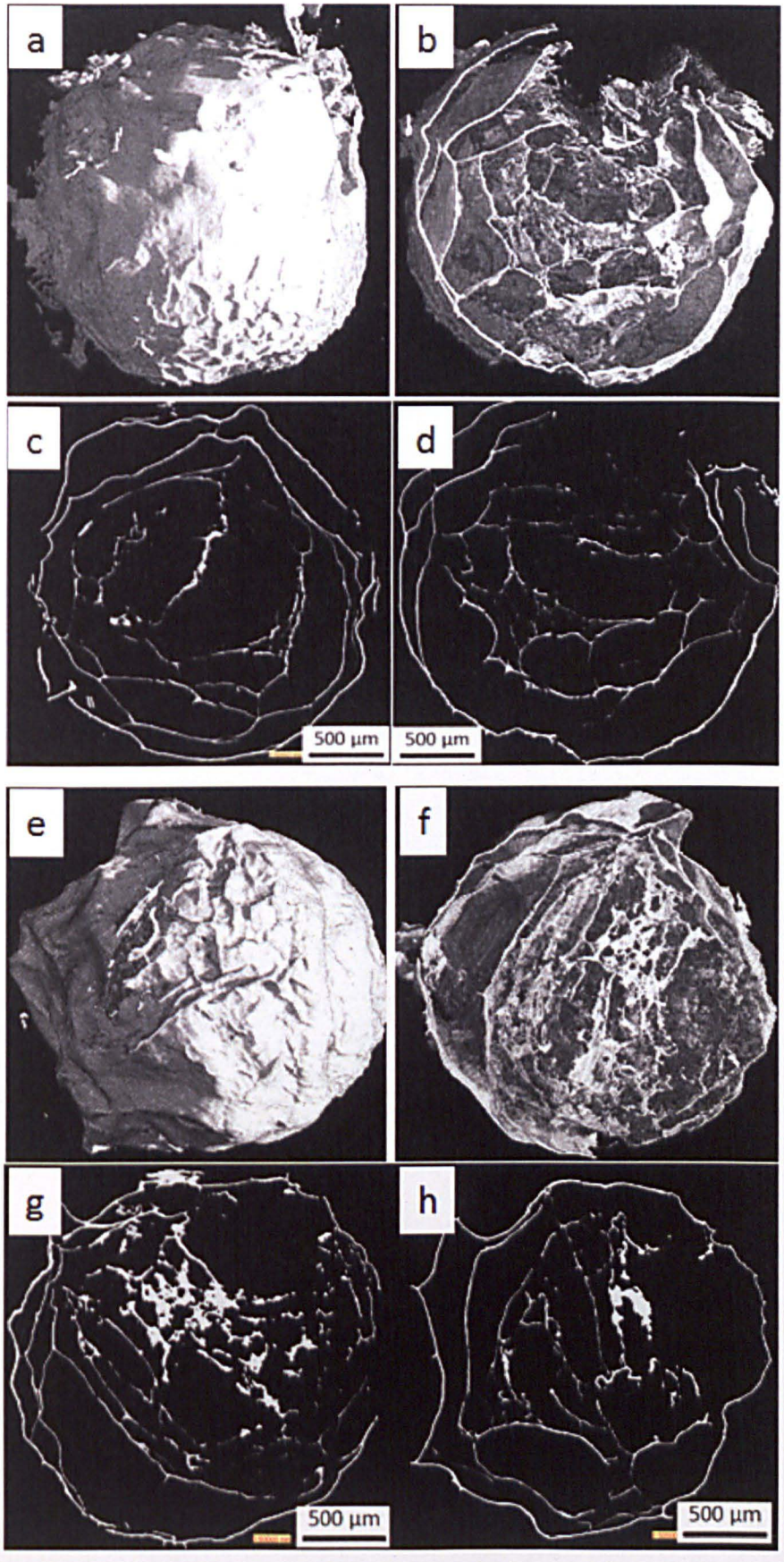

Figure 4.2.8. XMT images of two calcined beads: (a, b, e and f) 3D structure from outside and inside, (c, d, g and h) transverse and cross sections, respectively.

The TEM images and XRD pattern of as-prepared NiO nanopowders after calcination are shown in Figure 4.2.9 and 4.1.10, respectively.

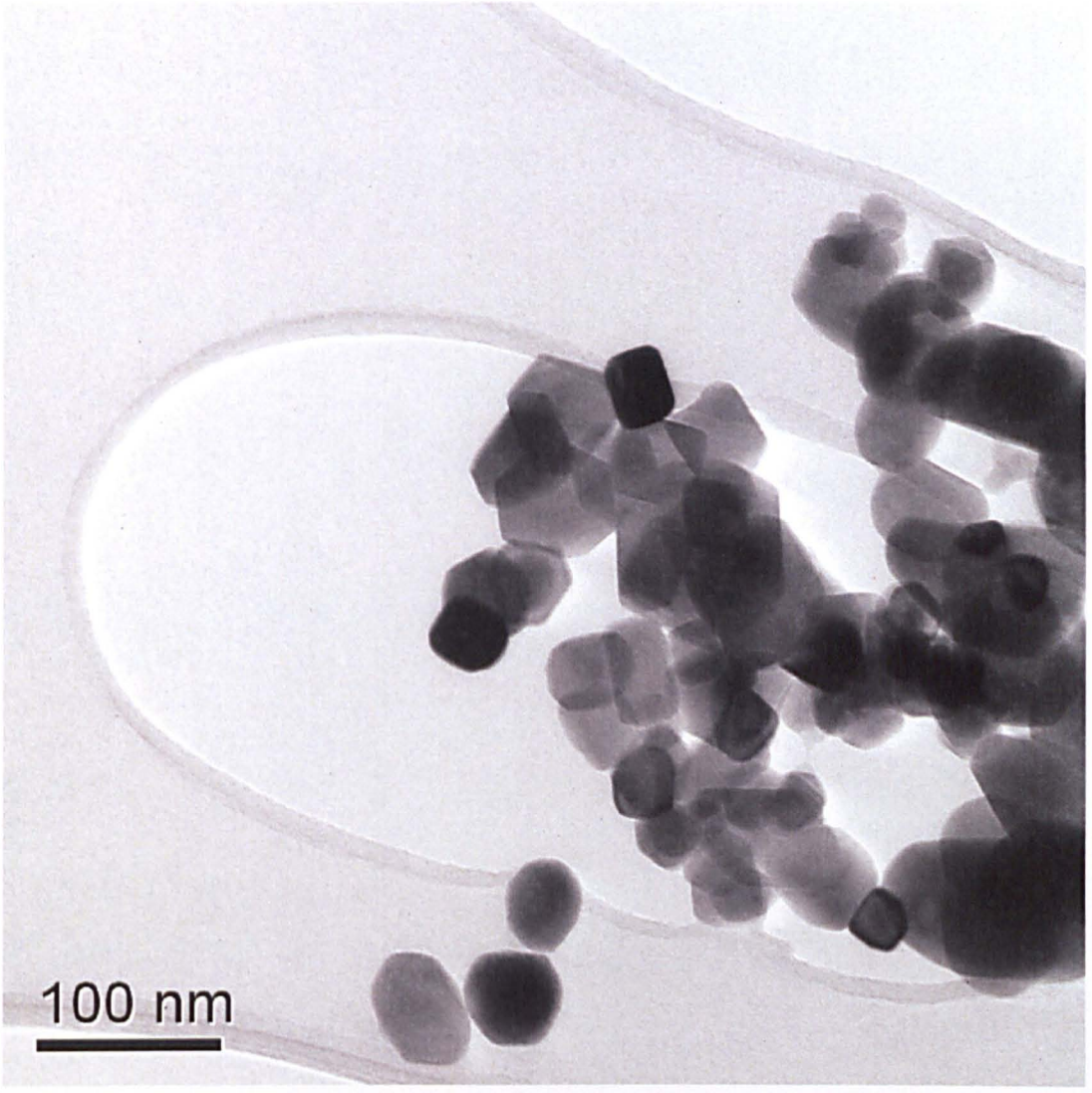

Figure 4.2.9. TEM image of NiO nanoparticles prepared by the calcinations of freeze dried nickel alginate beads at 700 °C.

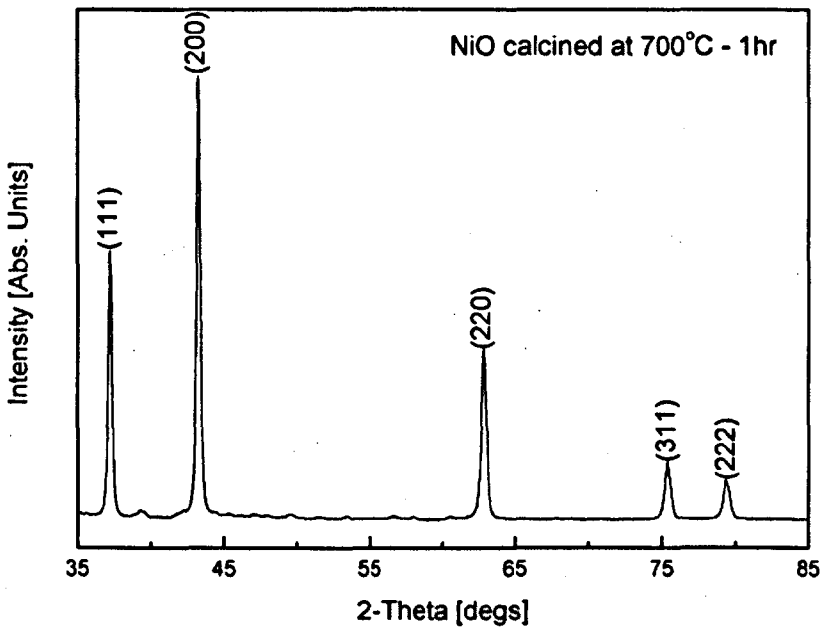

Figure 4.2.10. XRD of NiO nanopowders calcined at 700 °C for 1 hour. The pattern is indexed using the (hkl) values from ICDD 04-002-0665 shown at the top of the peaks.

4.2.3. NiO Production by Na-ALG Granules

The images of Ni-ALG dried granules after ion-exchanged with sodium alginate granules have been shown in Figure 4.2.11. The TGA/DSC of the dried Ni-ALG granules in controlled atmosphere of air at a flow rate of 50 mL min^{-1} from ambient temperature to 1000 °C with heating rate of 3 °C min^{-1} without any holding time are shown in Figure 4.2.12.

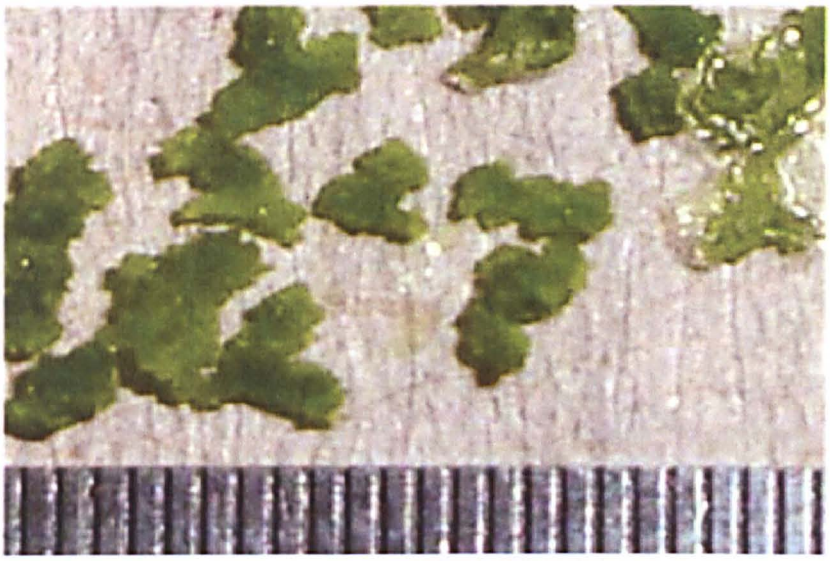

Figure 4.2.11. Nickel alginate dried granules (scale = 1 mm).

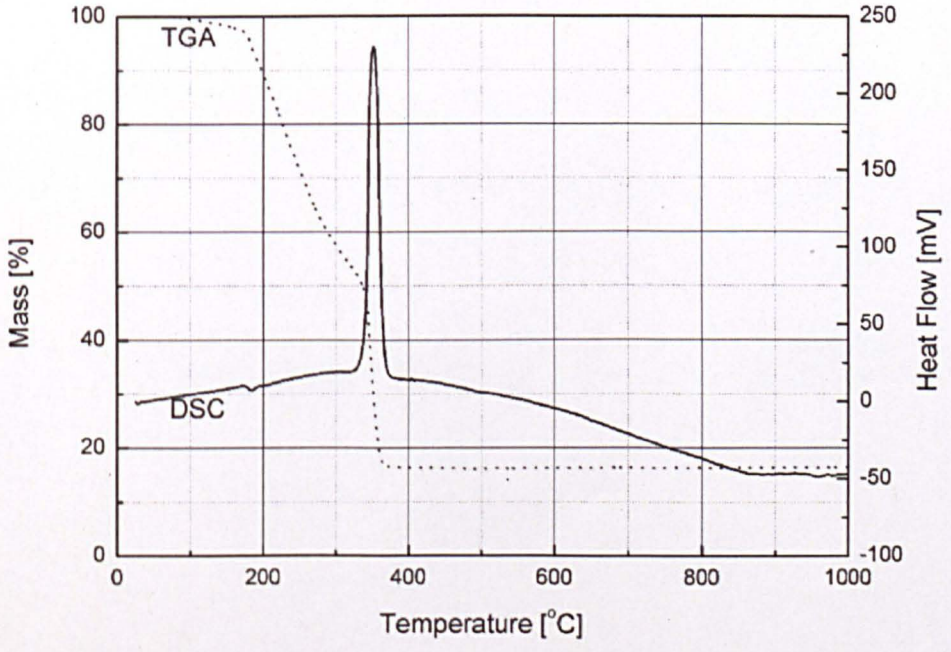

Figure 4.2.12. Thermal analysis of nickel alginate dried granules in air.

The HT-XRD patterns of dried Ni-ALG granules have been shown in Figure 4.2.13a and 4.2.13b, respectively. The temperature program was set every 25 °C interval from room temperature to 600 °C with heating rate maintained at 3 °C min^{-1} in static air condition. At each temperature, 30 mins annealing time was allowed for the sample to equilibrate. The XRD patterns of as-prepared NiO nanopowders after calcination has been shown in Figure 4.1.14. And the TEM and SAED patterns of NiO are shown in Figure 4.1.15.

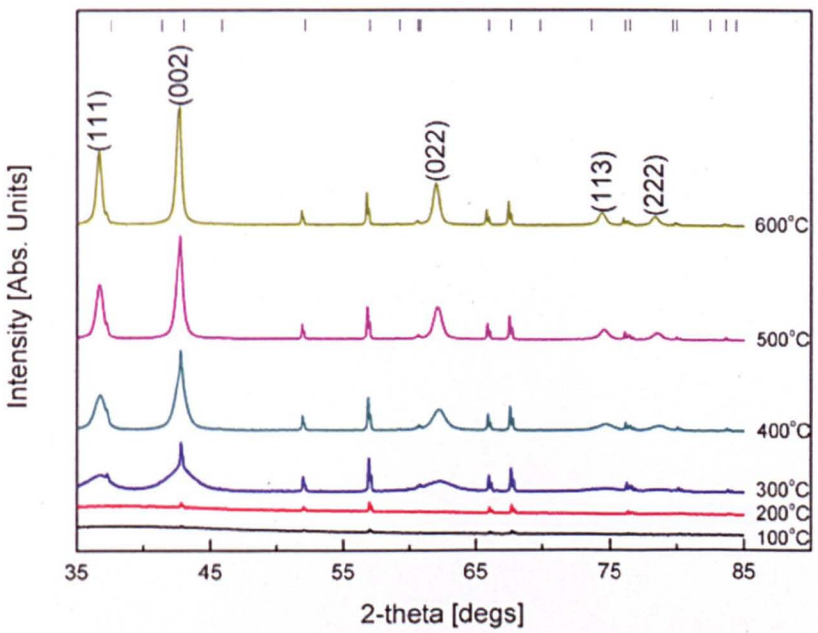

Figure 4.2.13a. HT-XRD of Ni-ALG dried granules at different temperatures. The patterns are indexed by ICDD 04-002-0665 as cubic NiO shown at the top of the pattern. Tick marks for reference pattern of α-Al_2O_3, ICDD 01-076-7777, are shown at the top of the figure.

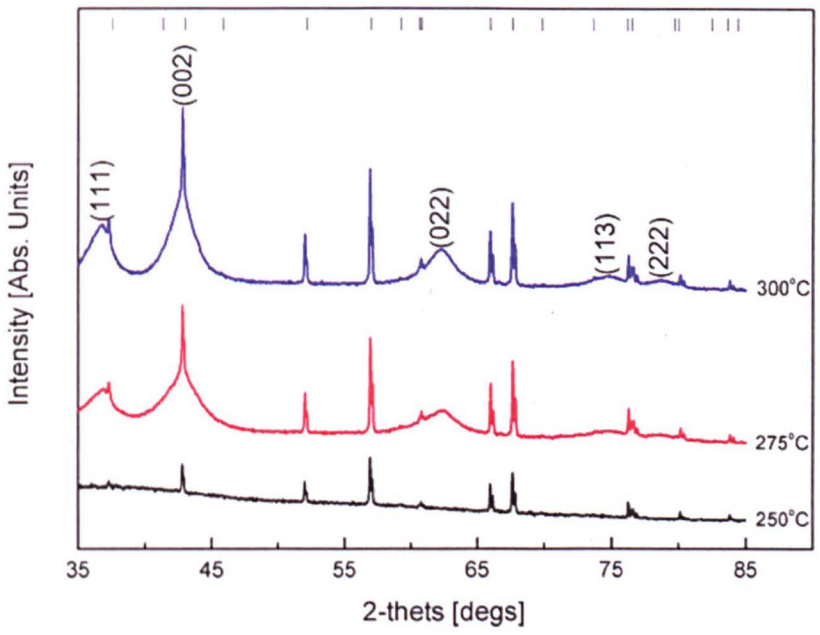

Figure 4.2.13b. HT-XRD of Ni-ALG dried granules heat treated from 250 to 300 °C.

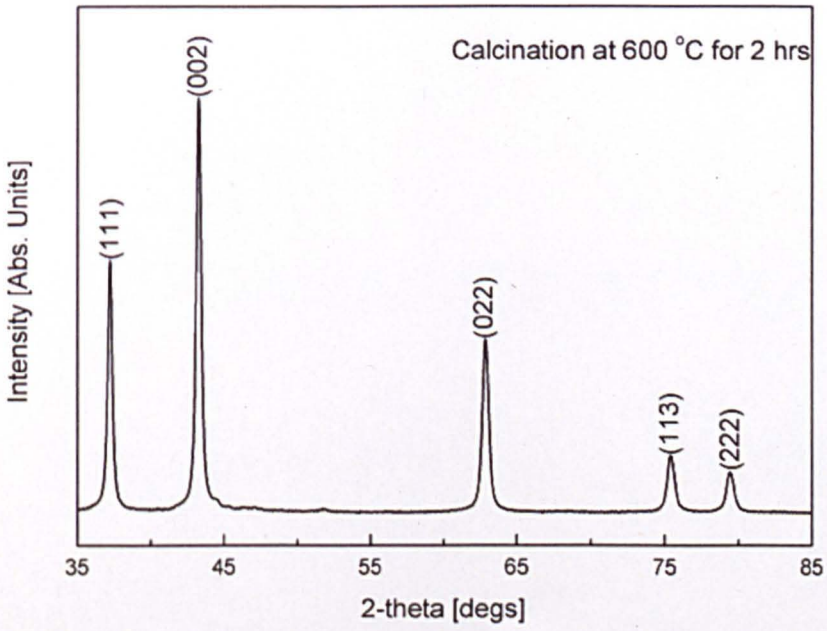

Figure. 4.2.14. XRD of NiO nanopowders calcined at 600 °C for 2 hrs annealing time. The patterns are indexed by ICDD 04-002-0665 shown at the top of the figure.

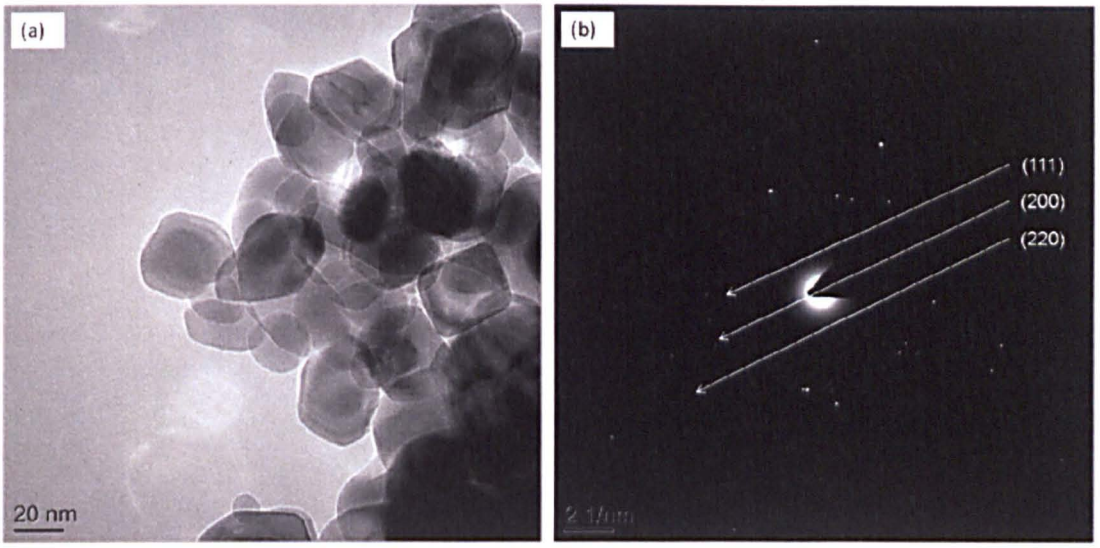

Figure 4.2.15. a, TEM image of NiO calcined at 600 °C for 2 hrs, and b, SAED pattern of the sample.

4.3 $Ce_xGd_{1-x}O_{2-\delta}$ Production by Na-ALG Beads

The Cerium Gadolinium Oxide ($Ce_{0.9}Gd_{0.1}O_{1.95}$, CGO1 and $Ce_{0.8}Gd_{0.2}O_{1.9}$, CGO2) nanopowders were prepared by sodium alginate (Na-ALG) beads. The physical, chemical and electrical property results of CGO1 and CGO2 are shown below.

4.3.1. $Ce_xGd_{1-x}O_{2-\delta}$ Production by Na-ALG Beads

The images of cerium gadolinium alginate (CGO-ALG) wet and dried beads after ion-exchanged with 4 wt% sodium alginate (Na-ALG) solution have been shown in Figure 4.3.1, respectively. The FTIR analysis of CGO-ALG and Na-ALG are shown in Figure 4.3.2.

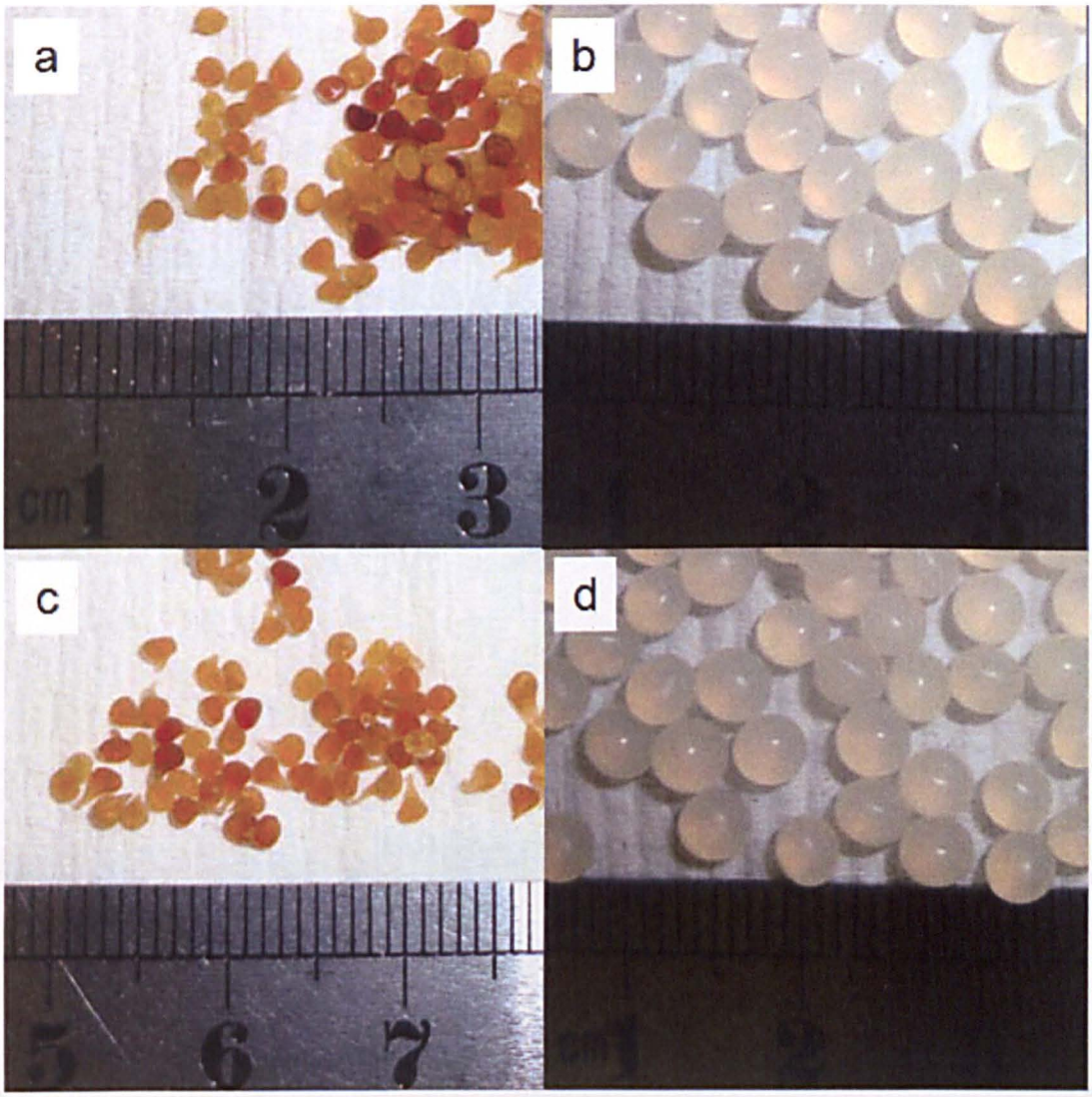

Figure 4.3.1. CGO-ALG dried and wet beads. a CGO1-ALG dried beads, b CGO1-ALG wet beads, c CGO2-ALG dried beads and d CGO2-ALG wet beads, respectively.

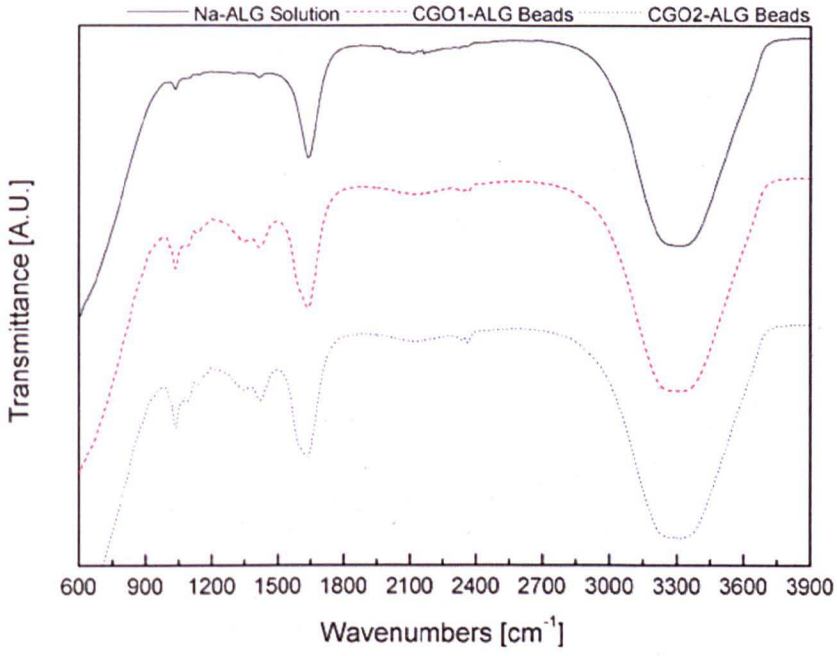

Figure 4.3.2. FTIR full wavenumber scan spectra of 4 wt% Na-ALG solution, CGO1 and CGO2 alginate wet beads, respectively.

The XRD patterns and TEM images of as-prepared CGO nanopowders after calcination are shown in Figure 4.3.3 and 4.3.4, respectively.

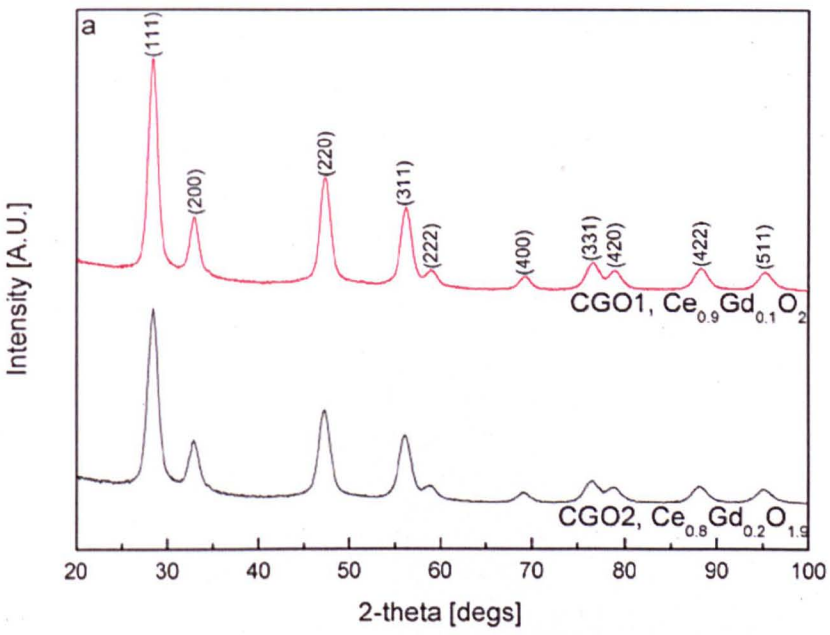

Figure 4.3.3a. XRD patterns of CGO1 and CGO2 nanopowders calcined at 500 °C for 2 hours. The XRD patterns are indexed by ICDD 04-002-6160 as $Ce_{0.9}Gd_{0.1}O_{1.95}$ and ICDD 04-14-0032 as $Ce_{0.8}Gd_{0.2}O_{1.9}$ shown at the top of the peaks.

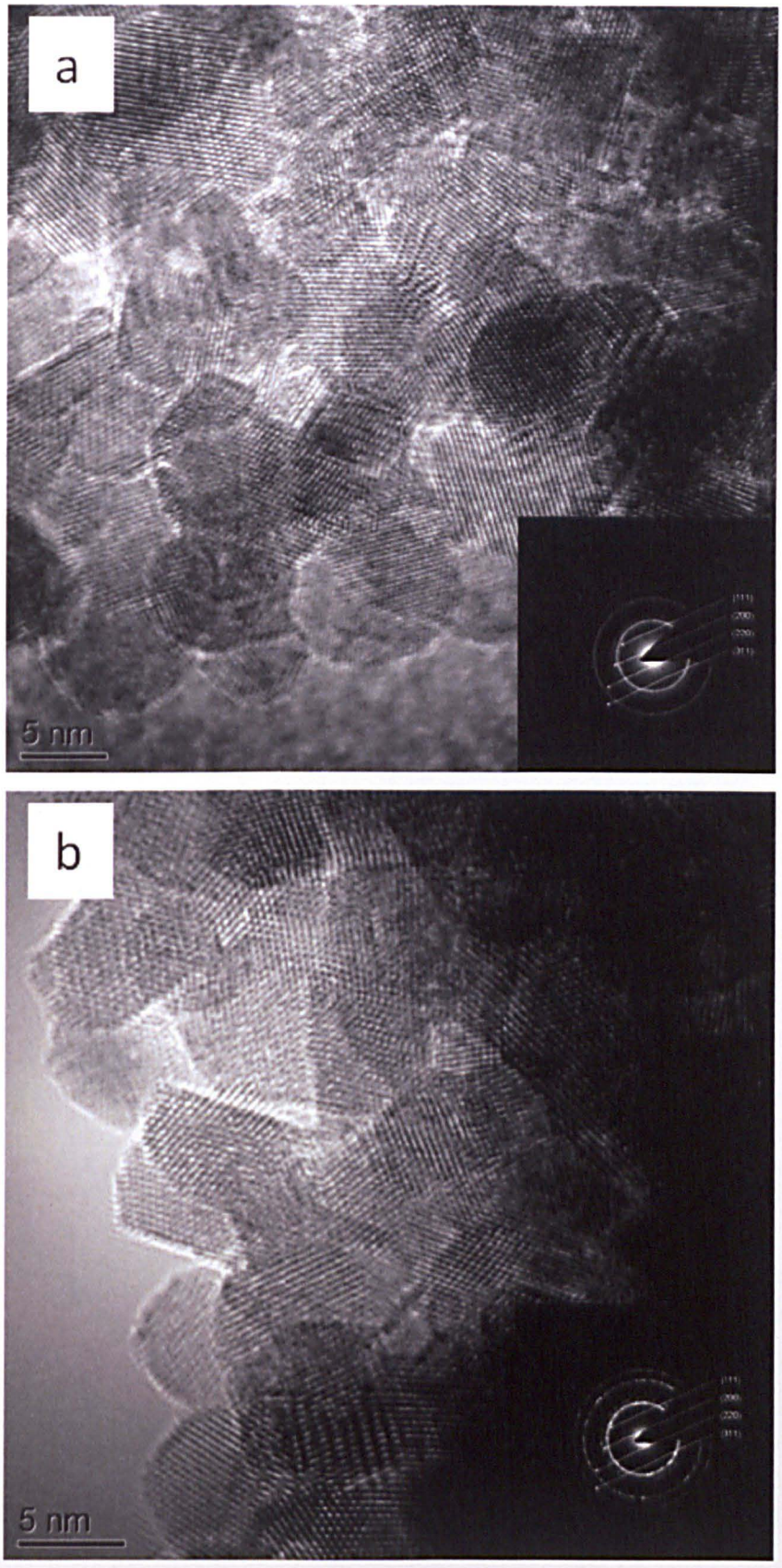

Figure 4.3.4. TEM images of the obtained nanopowders. a CGO1 and b CGO2 samples calcined at 500 °C for 2 hours. The inset images are SAED patterns to the corresponding samples.

4.3.2. Materials Conductivity Analysis for SOFC Application

The SEM images of fracture surfaces of CGO pellets prepared by sodium alginate beads are shown in Figure 4.1.12, respectively.

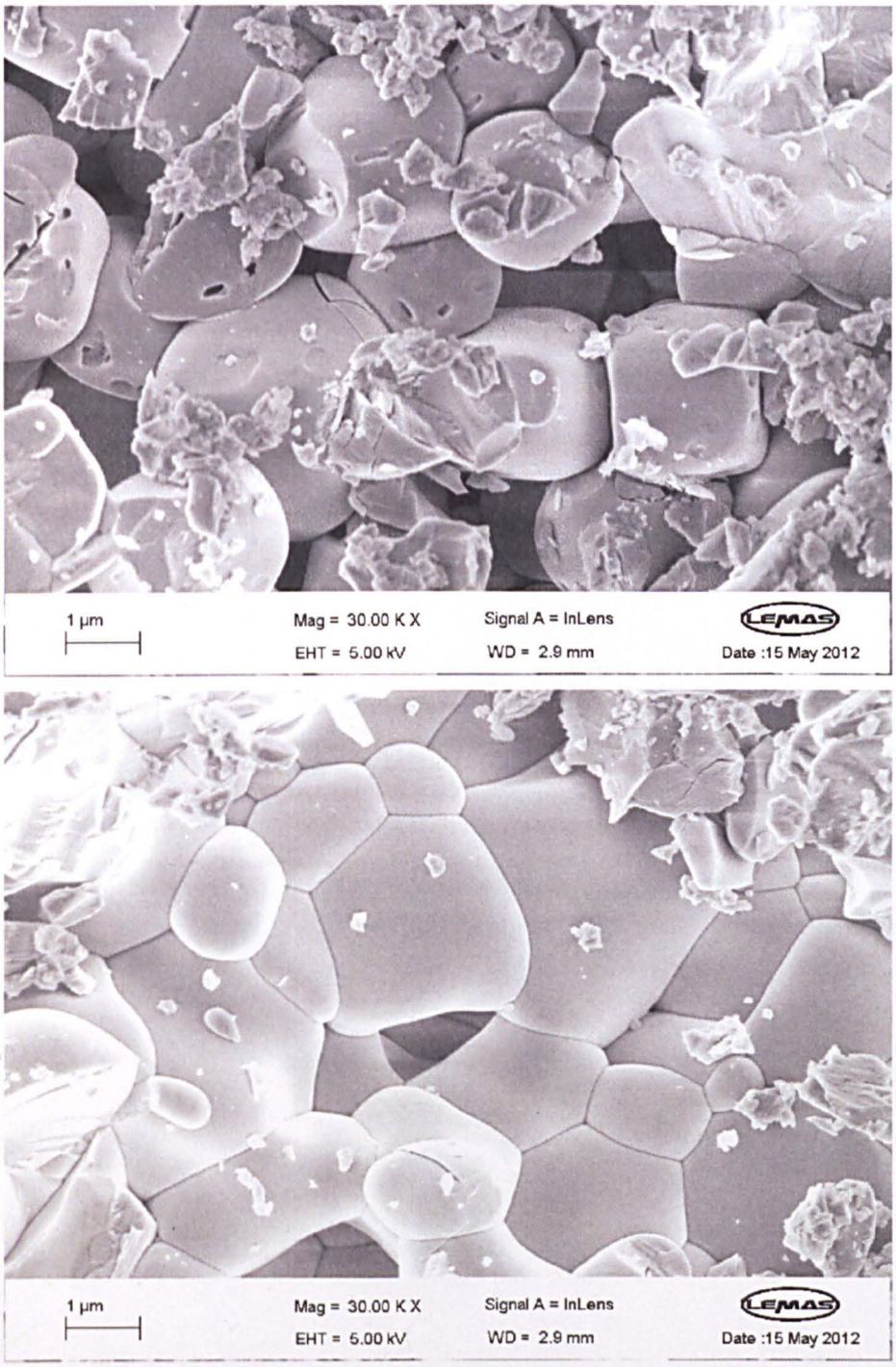

Figure 4.3.5. Grains, grain boundaries and pores interface SEM images of the fracture surface of CGO pellets sintered at 1300 °C – 2 hrs. Top image is CGO1 and bottom image is CGO2.

The measured impedance spectra for CGO prepared at different temperatures are shown in Figure 4.1.6 – 4.1.8, respectively.

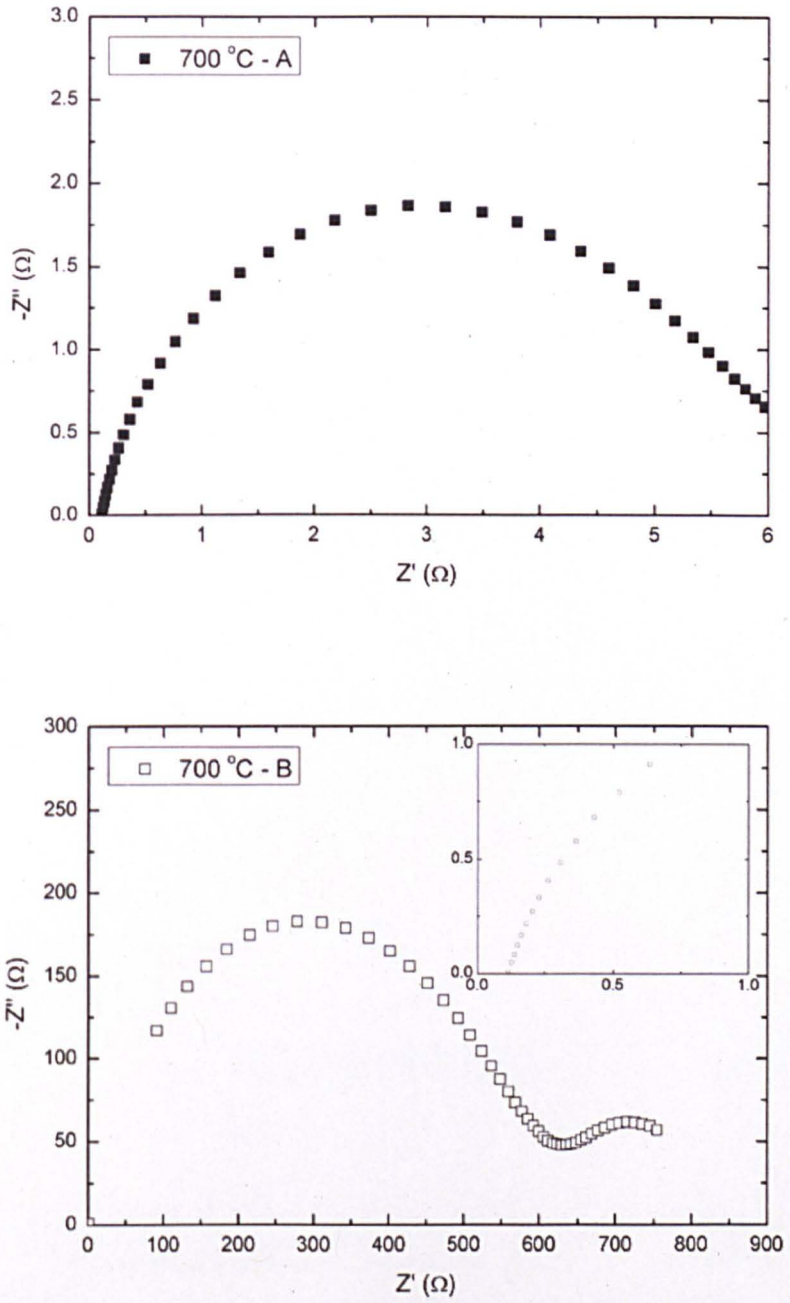

Figure 4.3.6. The complex impedance plots of dense CGO1 ceramic measured at 700 °C in air. The inset plot in B is the high frequency range.

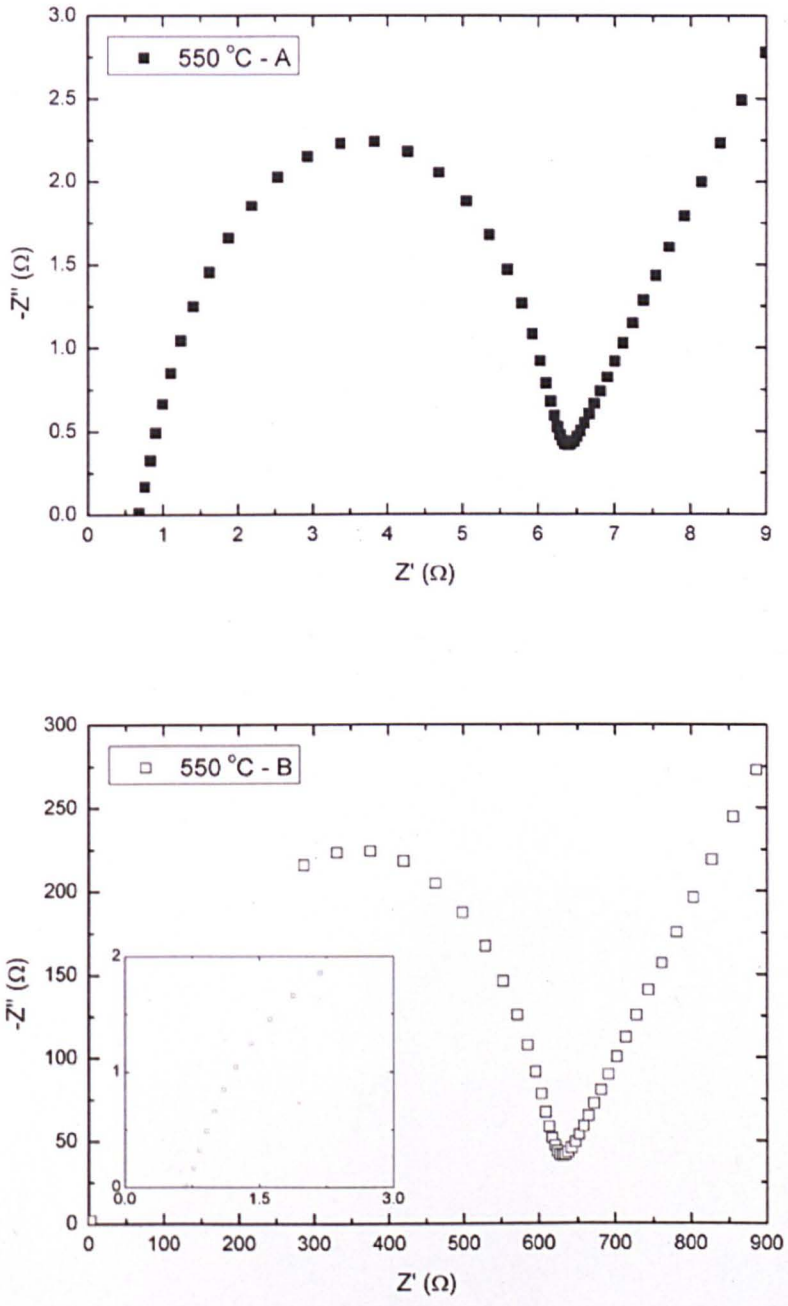

Figure 4.3.7. The complex impedance plots of dense CGO2 ceramic measured at 550 °C in air. The inset plot in B is the high frequency range.

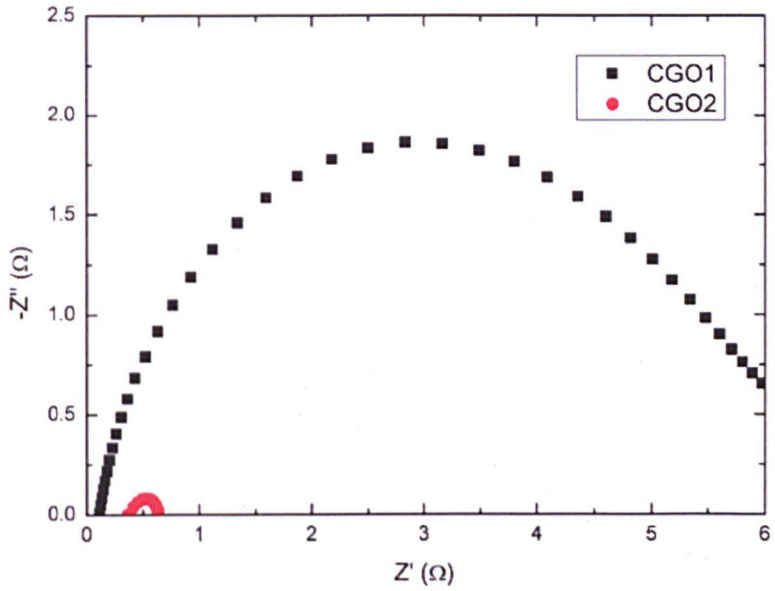

Figure 4.3.8. The complex impedance plots of dense CGO1 and CGO2 ceramic produced measured at 700 °C in air.

Chapter 5 Discussion

This chapter provides the in-depth discussion and analysis of the research findings (shown in Chapter 4 Results) of various metal oxides. It is separated into three sections, including 5.1 $Ce_{0.8}Gd_{0.2}O_{1.9}$ production by organic precursors, 5.2 NiO production by Na-ALG and 5.3 $Ce_xGd_{1-x}O_{2-\delta}$ production by Na-ALG beads, respectively. Full details can be found below.

5.1 $Ce_{0.8}Gd_{0.2}O_{1.9}$ production by Organic Precursors

In this section, Cerium Gadolinium Oxide ($Ce_{0.8}Gd_{0.2}O_{1.9}$, CGO2) nanopowders prepared by maltose + pectin or sucrose + pectin routes are discussed, respectively. Sucrose is made from one unit of α-glucose and one unit of β-fructose, and is probably one of the most abundant naturally occurring organic chemicals in the world. These two unit in chains are linked by a β-glycosidic bond which is a covalent bond between two monosaccharides that involves carbon C_1 (anomeric) of the glucose and carbon C_2 of the fructose. Maltose is a disaccharide containing two α-glucose units linked by α-glycosidic bond. This covalent bond connects two monosaccharide at the carbon C_1 (anomeric) of the first unit of glucose to carbon C_4 of the second unit of glucose. Pectin is naturally present in ripe fruits and some vegetables. Pectin is a linear polysaccharide containing between 300 and 1000 monosaccharide units. Pectin is widely used in the food industry as a gelling agent. Structural formulae of sucrose, maltose and pectin are shown in the figure below.

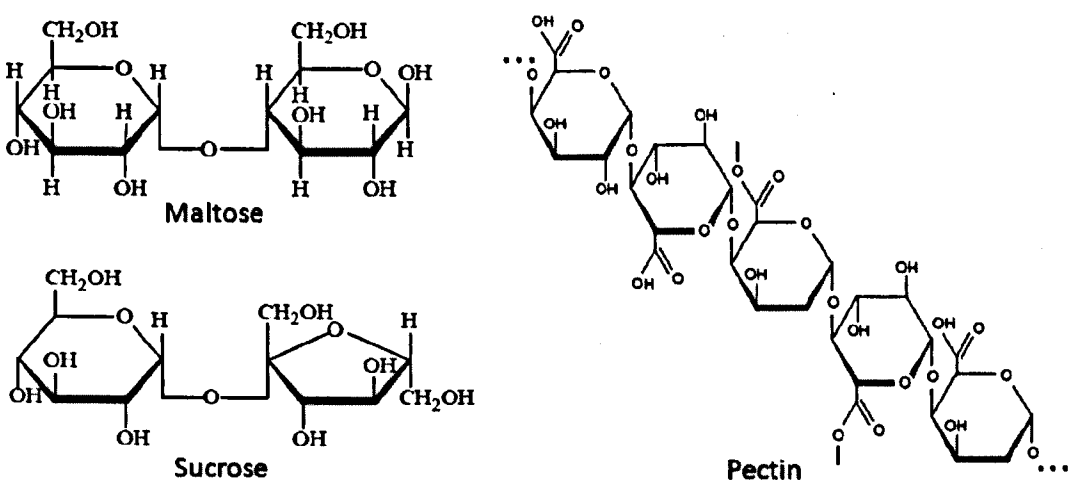

Figure 5.1.1. Structural formula for Sucrose, Maltose and Pectin.

It is believed that the electronegative O atom present in each of the two glucose ring structure between C_1 and C_5 carbon atoms and in the $C_1 - C_4$ α-glycosidic link per unit formula of maltose or in the C_1 - C_4 β-glycosidic link per unit formula of sucrose gains a partial negative charge. This enables the Ce^{3+} and Gd^{3+} cations from the precursor solutions to chelate with the partially negatively charged O atoms. These cations are kept at a distance by the large pectin molecule consisting of 300 to 1000 monosaccharide units that forms gelatinous matrix structure hosting the Ce^{3+} and Gd^{3+} cations. This is important for the prevention of the formation of large crystals during the subsequent calcination stage which is essential for the formation of nano crystalline CGO2 solid solution.

The CGO2 nanopowders obtained in this study have been characterized by simultaneous TGA/DSC, Powder XRD with Rietveld structural refinement, ICP-AES and TEM. The sinterability, electrical conductivity and microstructure of CGO are also studied. Details of the research work and its findings are discussed below.

5.1.1. $Ce_{0.8}Gd_{0.2}O_{1.9}$ Production using Maltose and Pectin

This section describes a sol-gel production of $Ce_{0.8}Gd_{0.2}O_{1.9}$ (CGO2) nanopowders using maltose and pectin. The experimental details of sol-gel experimental process can be found in Section 3.8. The results of this investigation can be found in Section 4.1.1.

The progress of calcination of the dried CGO2 gels and the organic components of the gel was studied by simultaneous TGA/DSC. The results of thermal analysis are shown in Figures 4.1.1–4.1.3, respectively.

As shown in Figure 4.1.1a, the organic materials in the dried gel decomposed in three steps for mixed maltose + pectin gel, whereas the decomposition occurred in four steps for individual components, maltose and pectin. The first three steps appeared to be mildly endothermic, whereas the final step was considerably exothermic as shown in Figure 4.1.1b. The first decomposition step occurred at around 100 °C. The second and third step was observed in a temperature range of 180–350 °C and the final step between 420–520 °C. The decomposition steps in the TGA trace of maltose, pectin and maltose + pectin were in good agreement with the DSC profiles shown in Figure 4.1.1b. An endothermic decomposition peak for maltose was observed at about 100 °C and for pectin observed at 150 °C, as seen in Figure 4.1.1b. The same trend was not seen clearly for the dried maltose and pectin mixed gel. Instead, a small and very broad endothermic peak

occurred over a wider temperature range from 150 to 240 °C. It could be seen in Figure 4.1.1b that the decomposition peak of maltose was simpler than that of pectin probably because of the simple molecular structure of maltose, as compared with the complex-branched heavy molecular weight structure of pectin. Further, it appeared that the formation of mixed maltose and pectin gel stabilized the structure of maltose by cross-linking with pectin resulting into the shift of decomposition peak to higher temperature, at approximately 500 °C, as shown in Figure 4.1.1b.

The decomposition of cerium and gadolinium ions (Ce^{3+} and Gd^{3+}) incorporated maltose and pectin mixed gel was found to be a three step process as shown in Figure 4.1.2. These three decomposition processes were observed in the temperature range of 140–180 °C, 250–280 °C and 290–350 °C, respectively. They were all exothermic in nature unlike those observed in Figure 4.1.1b. These exothermic decomposition processes were most likely due to the oxidative decomposition of Ce^{3+} and Gd^{3+} incorporated gel. The final decomposition step was highly exothermic compared to the first and second stages. In order to understand the excessive evolution of heat during the third stage of the decomposition, further thermal analysis was carried out between ambient temperature and 500 °C in flowing helium gas condition as a function of time.

TGA/DSC of Ce^{3+} and Gd^{3+} incorporated gel in flowing helium gas between ambient temperature and 500 °C is shown in Figures 4.1.3a and 4.1.3b. Once the temperature was attained, helium gas was substituted with air for 1 hour without further increase in temperature for high temperature annealing of the sample. The weak exothermic peaks due to the first two stages of decompositions in helium suggested that oxygen presented in the molecular structure of Ce^{3+} and Gd^{3+} incorporated maltose and pectin mixed gel was probably responsible for the oxidative decomposition. Once the loosely bonded oxygen was exhausted from the structure, no further exothermic peaks were observed up to 500 °C. Following this, when air was allowed to bleed in, the action instantly resulted into a significant reduction in mass of the sample and corresponding highly exothermic peak was observed. Here, it should be noted that in flowing air, the final decomposition step occurred between 290 and 350 °C as seen in Figure 4.1.2. However, it was found to be absent in helium gas up to 500 °C (Figures 4.1.3a and b). This led us to believe that oxygen was necessary for the final oxidative decomposition step of Ce^{3+} and Gd^{3+} incorporated maltose and pectin mixed gel to yield single phase CGO as shown later.

Based on the results shown in Figures 4.1.1–4.1.3, it could be concluded that at temperatures below 250 °C oxygen present in air did not play an active role in oxidative decomposition of Ce^{3+} and Gd^{3+} incorporated maltose and pectin mixed gels. Whereas at temperature higher than 300 °C, oxygen present in air was crucial for the thermal decomposition process of the cationic gel.

XRD patterns of the product of decomposition process carried out at different temperatures from 500 °C to 900 °C for 2 hours duration are shown in Figure 4.1.4. The peaks could be indexed successfully for the formation of single phase $Ce_{0.8}Gd_{0.2}O_{1.9}$. This suggested that the highly exothermic peak in the temperature range of 290–340 °C seen in Figure 4.1.2 was mainly due to the oxidation of Ce^{3+} and Gd^{3+} cations incorporated in maltose and pectin mixed gels to form single phase CGO.

XRD analysis of the cationic gel processed at different temperatures showed that all the obtained samples were single phase, cubic, $Ce_{0.8}Gd_{0.2}O_{1.9}$ powders as seen in Figure 4.1.4. The XRD patterns could be entirely indexed with the reference pattern available in the literature (ICDD 04-14-0032) marked at the top of Figure 4.1.4. It was found that the XRD pattern of CGO became sharper, and the peaks became progressively narrower due to increase in the crystallite size, as the calcinations temperature was increased from 500 °C to 900 °C.

Clearly, there were a number of factors which could contribute to profile broadening in diffraction data, namely coherence length, micro-strain, compositional homogeneity or a combination thereof. However, it should be noted that the effects of compositional homogeneity and micro-strain result in a similar effect on the observed profile. The effects of utilizing size, strain and a combination of size and strain are shown in Figure 5.1.2 and broadening due to the these effects manifested most strongly at high values of 2-theta, hence this range was shown in order to make a visual comparison.

In Figure 5.1.2, it can be seen that the strain broadening provided a poor description of the observed profile. There was considerable disparity between the model and raw data as highlighted by the residual below the data. Particle size effects provided a far better description of the broadening, but clearly a combination of size and strain provided the best model as shown at the top of Figure 5.1.2. It is not unreasonable to assume that as particles became extremely small, as was observed here, an element of

strain would be apparent. Note that a size/strain analysis was used in both Figure 5.1.3 and Table 5.1.1.

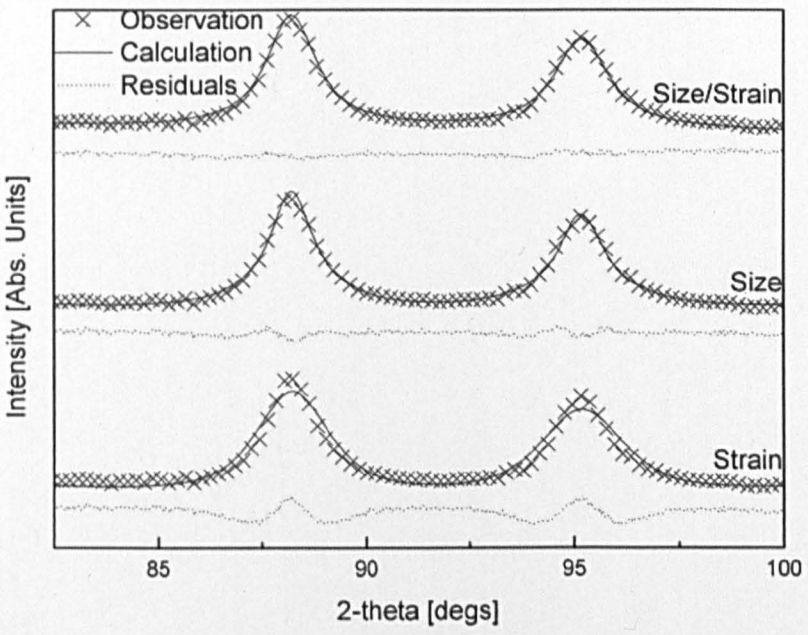

Figure 5.1.2. Rietveld refinement of CGO2 calcined at 500 °C for 2 hrs using strain, size and strain/size models. The raw data are shown as crosses, the model as a solid line and the residual below.

Figure 5.1.3 shows a comparison between the calculated and the observed XRD patterns obtained experimentally of the nanopowders of CGO2 calcined at 500 °C for 2 hrs employing a size/strain Rietveld structural refinement. It is clear from the figure that the agreement between the experimental data and the calculated pattern is excellent showing negligible residual pattern.

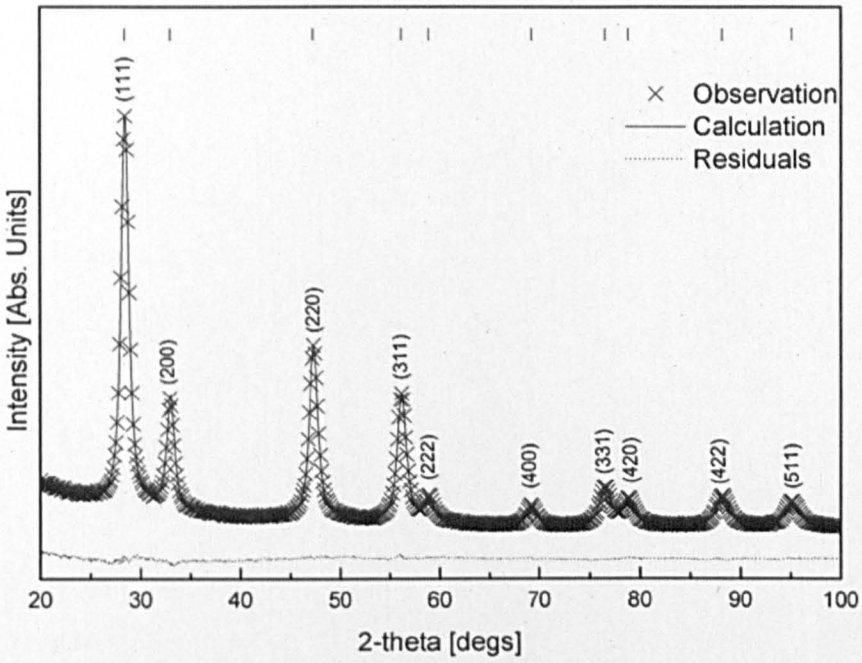

Figure 5.1.3. Size/strain Rietveld structural refinement analysis of CGO2 sample calcined at 500 °C for 2 hrs. The raw data are shown as crosses, the model as a solid line, and the residual shown below. Tick marks for reference pattern of $Ce_{0.8}Gd_{0.2}O_{1.9}$, ICDD 04-14-0032, are shown at the top of the figure.

During the refinement, a number of parameters were modified; the unit cell lattice parameter, isotropic temperature factors for each species (Ce, Gd and O) and profile parameters describing the peak shapes. Note that neither the occupancy factors (concentration of each atom per site) nor the fractional coordinates were altered. The refined parameters are shown in Table 5.1.1 alongside that of the initial values obtained from the reference XRD pattern ICDD 04-14-0032 of CGO2. In the absence of more suitable values from the literature (no refined figures are reported for cubic $Ce_{0.8}Gd_{0.2}O_{1.9}$, $Fm\bar{3}m$), the temperature factor, B_{ISO}, was set to 0.5 $Å^2$ for each of the atoms, as an initial value for the refinement procedure.

The refined value for the lattice parameter is similar to that reported in ICDD 04-14-0032. The temperature factors generated for each species seem plausible; in the host material, CeO_2 ($Fm\bar{3}m$), a range of temperature factors are reported in the literature; $B_{ISO}Ce$ = 0.28–2.19 $Å^2$ and $B_{ISO}O$ = 0.51–4.056 $Å^2$ [98-101]. Clearly, the refined values reported in Table 5.1.1 fall within this range. For Gd_2O_3 (Cubic, $Ia\bar{3}$), a range $B_{ISO}Gd$ = 0.21–0.35 $Å^2$ is reported

[102-104]; our refined values $B_{ISO}Gd$ = 0.12 $Å^2$ is somewhat lower than this, which may result from the use of a different crystal structure.

Table 5.1.1. Structural parameters of CGO2 calcined at 500 °C for 2 hrs sample obtained by size/strain Rietveld structural refinement analysis.

Parameter	ICDD 04-14-0032	Refinement
Lattice parameter (Å)	5.430	5.424(1)
$B_{ISO}Ce$ ($Å^2$)	0.5	0.53(1)
$B_{ISO}Gd$ ($Å^2$)	0.5	0.12(4)
$B_{ISO}O$ ($Å^2$)	0.5	0.64(5)

The results of size/strain analysis are shown in Table 5.1.2 as a function of calcination temperature. As the processing temperature increases, a gradual coarsening in particle size, and a reduction in micro-strain was observed. As expected, the weighted residual from the refinement, R_{wp}, range from 2.46–4.13 %, providing evidence of excellent agreement between the data and the refined model. Note that the errors presented in Table 5.1.2 are the statistical standard deviation from the refinement.

Table 5.1.2. Structural parameters of CGO2 samples obtained using Size/Strain Rietveld structural refinements.

Sample	Rietveld Size-Strain Analysis				
	Size (nm)	Micro Strain	R_{wp} (%)	R_{exp} (%)	GOF
A. 500°C-2hrs	10.64(2)	0.3(4)	2.46	1.30	1.89
B. 600°C-2hrs	13.61(1)	0.2(3)	2.23	1.30	1.72
C. 700°C-2hrs	27.18(1)	0.1(2)	3.68	2.00	1.84
D. 900°C-2hrs	76.3(3)	0(0)	4.13	2.02	2.04

The morphology of the obtained powders was investigated using Transmission Electron Microscopy (FEI Tecnai TF20 FEG-TEM). As shown on Figure 4.1.5, the CGO2 nanoparticles had shown relatively uniform shapes with narrow size distribution which matched with the calculations using XRD Rietveld refinements. The d-spacing values obtained from SAED

patterns in Figures 4.1.5a and 4.1.5d were compared with the XRD results. All these values were in good agreements with the reference data (04-014-0032) as shown in Table 5.1.3. Sample compositions were also confirmed using EDS.

Table 5.1.3. Comparison of CGO2 d-spacing values obtained by TEM and XRD Rietveld refinement with (04-014-0032) reference data.

h	k	l	Ref. *d*/ (Å)	TEM *d*/ (Å)		XRD *d*/ (Å)	
				A	D	A	D
1	1	1	3.135	3.135	3.138	3.136	3.135
2	0	0	2.715	2.715	2.716	2.715	2.714
2	2	0	1.919	1.921	1.917	1.919	1.918
3	1	1	1.637	1.644	1.636	1.636	1.636

Table 5.1.4 shows the results of chemical analysis of the final products obtained after different heat treatment conditions determined by ICP-AES analysis. All samples were confirmed as $Ce_{0.8}Gd_{0.2}O_{1.9}$. These findings of ICP-AES analysis are in excellent agreement with the nominal composition of the starting materials and the results obtained from XRD and TEM-EDS.

Table 5.1.4. ICP-AES and TEM-EDS analysis of the obtained CGO2 samples.

Sample	Ce Conz. (ppb)	Gd Conz. (ppb)	Molar Ratio Ce:Gd	EDS Ce:Gd
A	1.45(2)	0.34(0)	83 : 17	80 : 20
D	1.47(2)	0.33(2)	83 : 17	81 : 19

A novel sol-gel method has been developed for the production of high purity nanopowders of cerium gadolinium oxide (CGO2, $Ce_{0.8}Gd_{0.2}O_{1.9}$) solid solution using maltose as an organic chelating agent and pectin for gelation. The results of this investigation indicate that the final particle size of approximately 10 nm can be obtained after calcination of the predried gel at 500 °C for 2 hours in ambient air. An insight in to the calcination process has been obtained by using thermo-gravimetric analysis and differential scanning

calorimetry. Powder X-ray diffraction confirms that all samples are single phase cubic CGO2 powders with no trace of impurity. The mean crystallite sizes calculated from XRD analysis using Rietveld refinement method agree with the morphological features observed by transmission electron microscopy. The nanopowders produced in this study exhibit negligible strain as indicated by Rietveld refinement procedure. The nominal composition of CGO2 has been found to be in excellent agreement with that determined by energy dispersive X-ray spectroscopy and inductively coupled plasma - atomic emission spectrometry analysis. The XRD and TEM analyses indicate that there is a significant influence of calcination temperature on the particle size which increases with increasing temperature for a fixed annealing time. This new sol-gel method is a cost effective, simple, environmentally friendly and non-toxic route for a large scale production of high purity single phase nanopowders of complex oxide functional ceramic materials at significantly low temperatures.

5.1.2. $Ce_{0.8}Gd_{0.2}O_{1.9}$ Production using Sucrose and Pectin

This section describes a sol-gel production of $Ce_{0.8}Gd_{0.2}O_{1.9}$ (CGO2) nanopowders using sucrose and pectin. The experimental details of sol-gel experimental process can be found in Section 3.8. The results of this investigation can be found in Section 4.1.2.

The progress of calcination of the dried CGO2 gels and the oxidation/combustion of the organic components of the gel was studied by simultaneous TGA/DSC. The results of thermal analyses are shown in Figures 4.1.6 - 4.1.8, respectively.

As shown on Figure 4.1.6a, the organic materials in the dried gel decomposed in four steps as expected of pectin. On the other hand, sucrose or sucrose + pectin mixed gel decomposed in three steps. The first step of decomposition of sucrose and sucrose + pectin gel occurs between 180 and 240 °C, the second step occurs at 300–420 °C and the third step occurs 470–520 °C. Amongst these decomposition steps, the first and last steps are rapid, whereas the second step is sluggish. It can be seen in Figure 4.1.6b that the decomposition of sucrose, pectin and sucrose + pectin gel is endothermic below 400 °C, whereas above 420 °C it is considerably exothermic. This could be mainly due to the oxidation of organic compounds at higher temperature aided by the presence of oxygen in flowing air atmosphere. Further, it can be seen in Figure 4.1.6b that the decomposition peak of sucrose was simpler compared to that of pectin probably because of the simple molecular structure of sucrose relative to the complex-branched heavy molecular weight structure of pectin. The formation of mixed sucrose and pectin gel appears to stabilize the structure of sucrose by cross-linking with pectin resulting into the shift of decomposition peak to higher temperature as seen in Figure 4.1.6b.

Following the incorporation of Ce^{3+} and Gd^{3+} ions in sucrose and pectin mixed gel, the decomposition of newly formed gel had been found to be a three step process. These three decomposition processes were observed in temperature range 130–150 °C, 250–280 °C and 290–350 °C, respectively (see Figure. 4.1.7). They were all exothermic in nature and occurred at lower temperature compared to those observed in Figure 4.1.6b prior to incorporation of cations in the sucrose + pectin gel. The exothermic decomposition processes were probably due to the oxidative decompositions of Ce^{3+} and Gd^{3+} ions incorporated gel and in part due to the formation of $Ce_{0.8}Gd_{0.2}O_{1.9}$ solid solution step. The final decomposition was highly exothermic compared to the first and second stages. In order to

understand the excessive evolution of heat during the third stage of the decomposition, further thermal analysis was carried out between room temperature and 500 °C in flowing helium gas condition.

Figure 4.1.8a and 4.1.8b show the TGA/DSC trace of Ce^{3+} and Gd^{3+} ions incorporated gel in flowing helium gas between room temperature to 500 °C. Once the maximum temperature was reached, helium gas was substituted with air for 1 hour high temperature annealing. The weak exothermic peaks due to the first two stages decompositions in He suggested that the oxygen present in the molecular structure of Ce^{3+} and Gd^{3+} ions incorporated sucrose and pectin mixed gel could be causing the oxidative decompositions. Once the loosely bonded oxygen was exhausted from the structure, no further exothermic peaks were observed up to 500 °C. Following this, air was allowed to bleed in which instantly resulted into a significant reduction in mass of the sample and a corresponding highly exothermic peak was observed as seen in Figure 4.1.8b. It should be noted that in flowing air final decomposition step occurred between 290 and 350 °C in Figure 4.1.7. However, it was found to be absent in helium gas up to 500 °C (Figure 4.1.8a and 4.1.8b). This indicated that an excess of oxygen was necessary for the final decomposition step of Ce^{3+} and Gd^{3+} ions incorporated sucrose and pectin mixed gel that led to the formation of $Ce_{0.8}Gd_{0.2}O_{1.9}$ solid solution.

XRD analysis of the cationic gel processed at different temperatures showed that all the obtained samples were single phase cubic $Ce_{0.8}Gd_{0.2}O_{1.9}$ (ICDD 04-014-0032) powders as seen in Figure 4.1.9. The XRD patterns could be entirely indexed with the reference pattern available in the literature (ICDD 04-14-0032) marked at the top of Figure 4.1.9. It was found that the XRD pattern of CGO2 became sharper and the peaks became progressively narrower as the calcination temperature increased from 500 °C to 900 °C mainly because of the growth of the crystallite size.

Figure 5.1.4 shows a comparison between the calculated and the observed XRD patterns obtained experimentally of the nanopowders of CGO2 calcined at 500 °C for 2 hrs employing a size/strain Rietveld structural refinement. It is clear from the figure that the agreement between the experimental data and the calculated pattern is excellent showing negligible residual pattern.

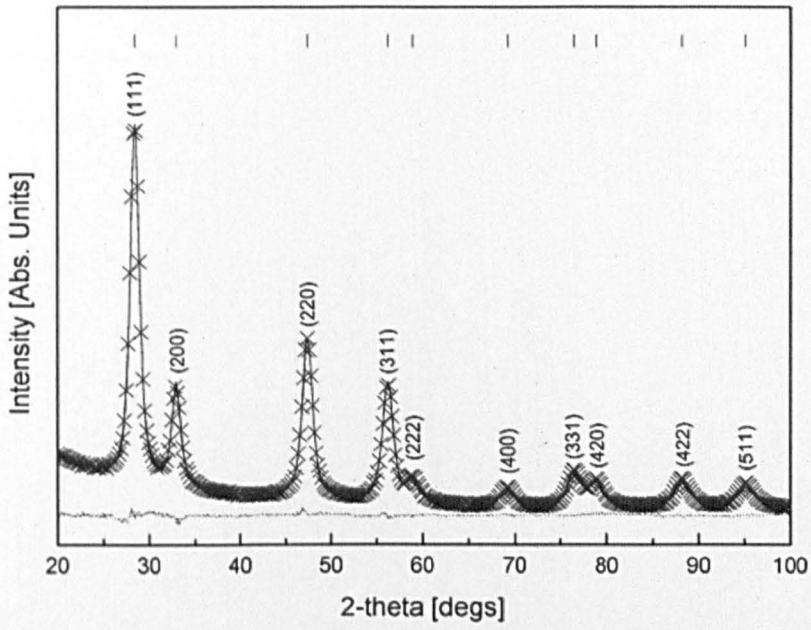

Figure 5.1.4. Size/strain Rietveld structural refinement analysis of CGO2 sample calcined at 500 °C for 2 hrs. The raw data are shown as crosses, the model as a solid line, and the residual shown below. Tick marks for reference pattern of $Ce_{0.8}Gd_{0.2}O_{1.9}$, ICDD 04-14-0032, are shown at the top of the figure.

During the refinement, a number of parameters were modified; the unit cell lattice parameter, isotropic temperature factors for each species (Ce, Gd and O) and profile parameters describing the peak shapes. Note, that neither the occupancy factors (concentration of each atom per site) nor the fractional coordinates were altered. The refined parameters are shown in Table 5.1.5 alongside those of the initial values obtained from the reference XRD pattern ICDD 04-14-0032 of CGO2. In the absence of more suitable values from the literature (no refined figures are reported for cubic $Ce_{0.8}Gd_{0.2}O_{1.9}$, $Fm\bar{3}m$), the temperature factor, B_{ISO}, was set to 0.5 $Å^2$ for each of the atoms, as an initial value for the refinement procedure.

The refined value for the lattice parameter is similar to that reported in ICDD 04-14-0032. The temperature factors generated for each species seem plausible; for the host material, CeO_2 ($Fm\bar{3}m$), a range of temperature factors are reported in the literature; $B_{ISO}Ce$ = 0.28–2.19 $Å^2$ and $B_{ISO}O$ = 0.51–4.056 $Å^2$ [98-101]. Clearly, the refined values reported here fall within this range. For Gd_2O_3 (Cubic, $Ia\bar{3}$), a range $B_{ISO}Gd$ = 0.21–0.35 $Å^2$ is

reported [102-104]; our refined values $B_{ISO}Gd$ = 0.19 Å^2 is somewhat lower than this, which may be because of the use of a different crystal structure.

Table 5.1.5. Structural parameters of $Ce_{0.8}Gd_{0.2}O_{1.9}$ calcined at 500 °C for 2 hrs sample obtained by size/strain Rietveld structural refinement analysis.

Parameter	ICDD 04-14-0032	CGO
Lattice parameter (Å)	5.430	5.424(3)
$B_{ISO}Ce$ (Å^2)	0.5	0.60(2)
$B_{ISO}Gd$ (Å^2)	0.5	0.19(5)
$B_{ISO}O$ (Å^2)	0.5	0.66(8)

The results of size/strain analysis are shown in Table 5.1.6 as a function of calcination temperature. As the processing temperature increases, a gradual coarsening in particle size and a reduction in micro-strain was observed. As expected, the weighted residual from the refinement, R_{wp}, range from 1.91−3.60 %, providing evidence of excellent agreement between the data and the refined model. Note that the errors presented are the statistical standard deviation from the refinement.

Table 5.1.6. Structural parameters of CGO2 samples obtained using Size/Strain Rietveld structural refinements.

Sample	Size/Strain Rietveld structural refinement				
	Size (nm)	Micro Strain	R_{wp} (%)	R_{exp} (%)	GOF
A	8.04(1)	0.4(5)	1.91	1.31	2.14
B	14.10(6)	0.2(3)	2.39	1.31	3.34
C	29.10(4)	0.0(7)	3.26	1.98	2.70
D	61.1(2)	0(0)	3.60	2.01	3.23

Samples heat treated at different temperatures: (A) 500 °C, (B) 600 °C, (C) 700 °C and (D) 900 °C for 2 hours, respectively.

The morphology of the obtained powders was investigated using Transmission Electron Microscopy (FEI Tecnai TF20 FEG-TEM). As shown

in Figure 4.1.10, the CGO2 nanoparticles had shown relatively uniform shapes with narrow size distribution which matched with the calculations using XRD Rietveld refinements. The XRD patterns shown in Figure 5.1.4 and SAED patterns shown in Figure 4.1.11 clearly indicated that the CGO2 nanopowders were single phase and fully crystalline. Furthermore, the changing nature of ring patterns in Figure 4.1.11 also indicated the growth of crystallite size with increasing temperature. The d-spacing values obtained from SAED patterns in Figure 4.1.11 were compared with the XRD results. All these values were in good agreements with the reference data (04-014-0032) as shown in Table 5.1.7. Sample compositions were also confirmed using EDS.

Table 5.1.7. Comparison of CGO2 d-spacing values obtained by TEM and XRD Rietveld refinement with (04-014-0032) reference data.

h	k	l	Ref. *d*/ (Å)	TEM *d*/ (Å)				XRD *d*/ (Å)			
				A	B	C	D	A	B	C	D
1	1	1	3.135	3.134	3.135	3.136	3.134	3.137	3.137	3.136	3.136
2	0	0	2.715	2.714	2.717	2.713	2.715	2.716	2.716	2.716	2.715
2	2	0	1.920	1.922	1.918	1.917	1.919	1.919	1.920	1.919	1.919
3	1	1	1.637	1.637	1.631	1.635	1.636	1.637	1.637	1.637	1.637

Samples heat treated at different temperatures: (A) 500 °C, (B) 600 °C, (C) 700 °C and (D) 900 °C for 2 hours, respectively.

Table 5.1.8 shows the chemical analysis results of the final products obtained at different heat treatment conditions determined by ICP-AES analysis. All samples were confirmed as $Ce_{0.8}Gd_{0.2}O_{1.9}$. These findings were in good agreement with the expected composition of the starting materials and the results obtained from XRD and TEM-EDS.

Table 5.1.8. ICP-AES and TEM-EDS analysis of the obtained CGO2 samples.

Sample	Ce : Gd ratio	
	ICP-AES	TEM-EDS
A	81 : 19	80 : 20
B	83 : 17	80 : 20
C	83 : 17	81 : 19
D	83 : 17	81 : 19

Samples heat treated at different temperatures: (A) 500 °C, (B) 600 °C, (C) 700 °C and (D) 900 °C for 2 hours, respectively.

In the present investigation, high purity nanopowders of cerium gadolinium oxide (CGO2, $Ce_{0.8}Gd_{0.2}O_{1.9}$) is synthesized by sol-gel method using sucrose as an organic chelating agent and pectin for gelation. The results of this investigation indicate that the final particle size of approximately 8 nm can be obtained after calcination of the predried gel at 500 °C for 2 hours in ambient air. An insight in to the calcination process has been obtained by using simultaneous TGA/DSC. Powder XRD confirms that all samples crystallized as single phase cubic CGO2 powders with no trace of impurity. The mean crystallite sizes calculated from XRD analysis using Rietveld refinement method agree with the morphological features observed by TEM. The nanopowders produced in this study exhibit negligible strain as indicated by Rietveld refinement procedure. The nominal composition of CGO2 has been found to be in excellent agreement with that determined independently by EDS and ICP-AES. The XRD and TEM analyses indicate that there is a significant influence of calcination temperature on the crystal size which increases with increasing temperature for a fixed annealing time.

5.1.3. Materials Conductivity Analysis for SOFC Application

This section describes microstructure and electrical conductivity of the obtained $Ce_{0.8}Gd_{0.2}O_{1.9}$ (CGO2) produced by maltose + pectin (MP) or sucrose + pectin (SP) sol-gel routes. The sample sintering process and a.c. impedance spectroscopy measurement technique can be found in Section 3.8 and 3.9. The results of this investigation can be found in Section 4.1.3.

The relative densities of CGO2-MP and CGO2-SP calculated by Archimedes principle are above 95% of the theoretical density. The microstructure observed from SEM images in Figure 4.1.12 of the fracture samples of CGO2 sintered at 1500 °C indicates relatively small particles of uniform size ~1 μm and high density.

Impedance spectroscopy normally resolves the bulk, grain boundary and electrode conduction processes in ceramic samples by exhibiting successive semicircles (with some distortion) in the complex plane. In the case of $Ce_{0.8}Gd_{0.2}O_{1.9}$ produced by maltose + pectin (MP) or sucrose + pectin (SP), the grain boundary and bulk processes remain distinguishable to 800 °C. Figure 5.1.5–5.1.8 shows the plot of log σ vs. 1/T measured in air, where σ is the conductivity. It also compares the total conductivity, including bulk and grain boundary contributions with only the ionic (bulk) conductivity.

The Arrhenius plots of total conductivities of dense CGO2-MP and CGO2-SP (see Figure 5.1.7) indicate two activation energies, respectively. For the CGO2-MP sample, the different starts at 550 °C with E_a = 1.04 eV at high temperature range and E_a = 1.02 eV at low temperature range. The total conductivities at 550 °C are calculated as 3.47×10^{-2} S cm^{-1} as shown in Figure 4.1.13a and 2.79×10^{-4} S cm^{-1} as shown in Figure 4.1.13b, respectively. More or less the same results are obtained from CGO2-SP sample. The total conductivities at 600 °C are calculated as 5.31×10^{-2} S cm^{-1} as shown in Figure 4.1.14a and 4.93×10^{-4} S cm^{-1} as shown in Figure 4.1.14b, respectively. This may due to a glassy phase formed at the CGO grain surface and lead to conductivity increment at certain temperature range. However, further research is required for clarification.

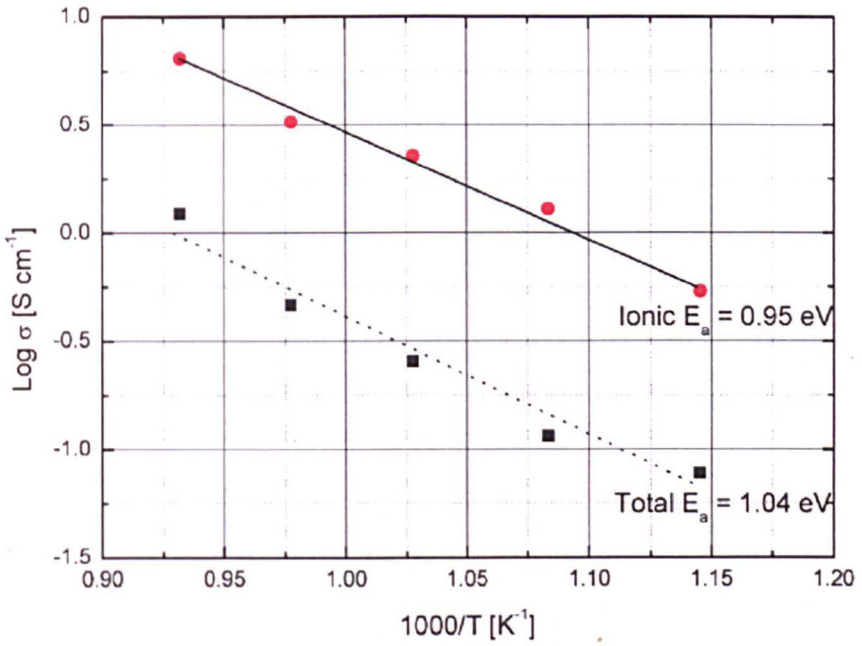

Figure 5.1.5. Arrhenius plot of total and ionic conductivity of the dense $Ce_{0.8}Gd_{0.2}O_{1.9}$ ceramic produced by maltose + pectin (MP) measured from 600 to 800 °C in air.

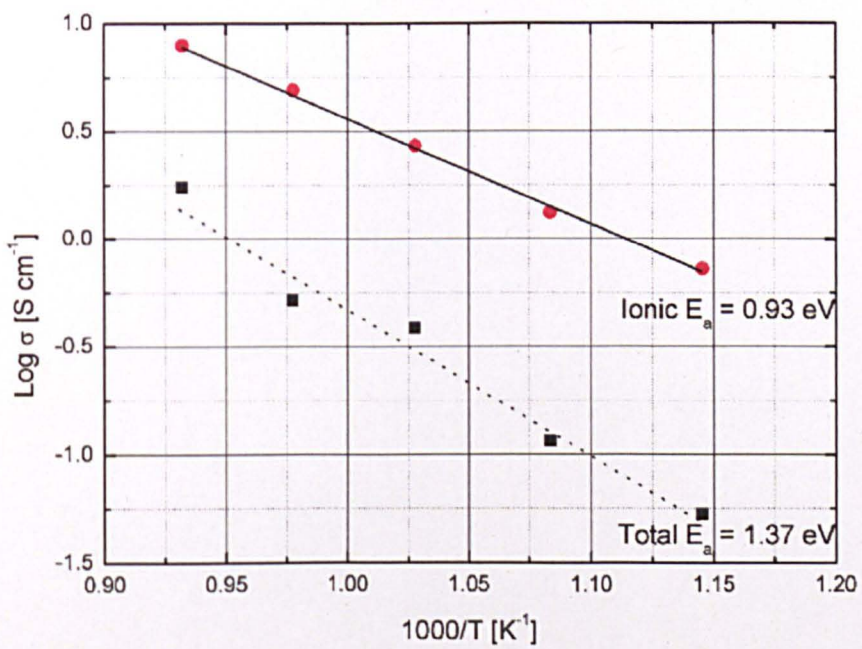

Figure 5.1.6. Arrhenius plot of total and ionic conductivity of the dense $Ce_{0.8}Gd_{0.2}O_{1.9}$ ceramic produced by sucrose + pectin (SP) measured from 600 to 800 °C in air.

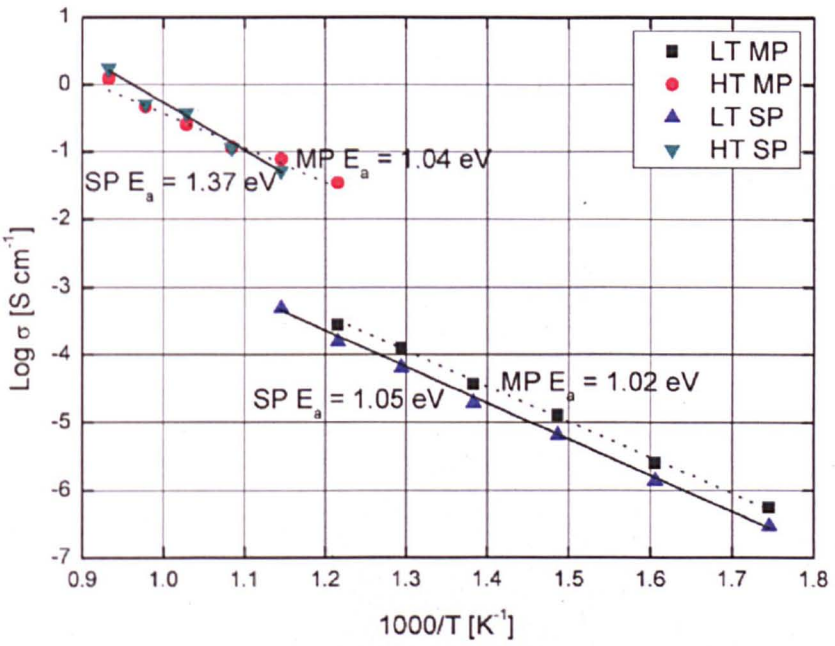

Figure 5.1.7. Arrhenius plot of total conductivity of the dense $Ce_{0.8}Gd_{0.2}O_{1.9}$ ceramic produced by SP and MP measured from 300 to 800 °C in air. LT is low temperature measurements and HT is high temperature measurements, respectively.

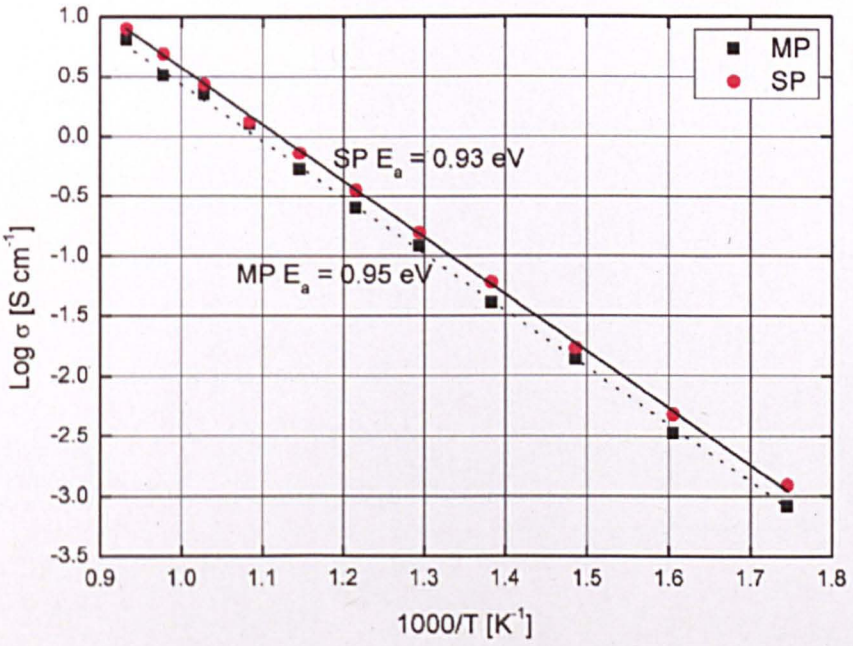

Figure 5.1.8. Arrhenius plot of ionic conductivity of the dense $Ce_{0.8}Gd_{0.2}O_{1.9}$ ceramic produced by both SP and MP measured from 300 to 800 °C in air.

Table 5.1.9 shows the conductivity and activation energy for conduction of $Ce_{0.8}Gd_{0.2}O_{1.9}$ produced by MP or SP, respectively. The total conductivity at high temperature range and ionic conductivity of both CGO2-MP and CGO2-SP samples measured in this investigation are in reasonable agreement with the data reported by Dikmen *et al.* [32] and Steele [105]. The ionic conductivities of this investigation at 600 °C are much higher than the one obtained by Steele $\sigma_{600\,°C}$ = 0.018 S cm^{-1} [105].

Table 5.1.9. Conductivity and activation energy of $Ce_{0.8}Gd_{0.2}O_{1.9}$ solid solutions.

Parameters		CGO-MP	CGO-SP
Total Activation energy E_a (eV)	Low Temp.	1.02	1.05
	High Temp.	1.04	1.37
Total conductivity $\sigma_{600\,°C}$ (S cm^{-1})		0.08	0.05
Total conductivity $\sigma_{700\,°C}$ (S cm^{-1})		0.26	0.38
Ionic Activation energy E_a (eV)		0.95	0.93
Ionic conductivity $\sigma_{600\,°C}$ (S cm^{-1})		0.54	0.73
Ionic conductivity $\sigma_{700\,°C}$ (S cm^{-1})		2.27	2.72

5.2 NiO Production by Na-ALG

In this section, NiO nanopowders produced by sodium alginate were investigated. Sodium alginate (Na-ALG, $NaC_6H_7O_6$) is a polymer extracted from brown seaweed. It contains varying amount of 1, 4′-linked β-D-mannuronic acid (M) and α-L-guluronic acid (G) residues. Gelation of alginate is due to the interaction of carboxylate groups with metal ions [81], such as Ni^{2+}, in aqueous solution. During calcination, the nickel ions become immobile and cannot readily get close to each other, hence the possibility of producing small nanoparticles.

In this study, novel methods for NiO nanopowders synthesis based on thermal decomposition of nickel alginate are presented. The obtained samples have been characterized by TGA/DSC, HT-XRD, XRD with Rietveld size/strain structural refinement, XMT and TEM. Details of the research work and its findings are discussed below.

5.2.1. NiO Production by Na-ALG Beads

This section describes a sol-gel production of NiO nanopowders using sodium alginate beads. The experimental details of sol-gel experimental process can be found in Section 3.9. The results of this investigation can be found in Section 4.2.1.

The progress of calcination of the dried Ni-ALG beads was studied by simultaneous TGA/DSC. The results of thermal analysis are shown in Figures 4.2.2.

The decomposition of nickel alginate (Ni-ALG) dried beads was found to be a four step process. These four decomposition processes were observed in the temperature range of ambient–200 °C, 200–300 °C, 300–450 °C and 450–575 °C, respectively. The decomposition steps in the TGA profile were found to be in good agreement with the DSC profile also shown in Figure 4.2.2. A small endothermic decomposition peak observed at temperature between ambient and 200 °C corresponding to about 10% weight loss as shown in the TGA profile. This was possibly due to evaporation of water during heat treatment. After this, all decomposition peaks were exothermic in nature. These exothermic peaks were due to the progressive oxidative decomposition of nickel alginate dried beads. At a temperature range of 200–300 °C, about 40% weight loss was observed in the TGA profile. This is probably due to the cleavage of G-G, G-M and M-M weaker linkages in the alginate polysaccharide molecule leading to significant evolution of oxygen

and hence the corresponding weight loss. This simultaneously promotes the oxidation of Ni^{2+} ions chelated in alginate structure to form coexisting NiO and NiO_2 as seen in Figure 4.2.3. The net result of the above two simultaneous endothermic and exothermic processes led to the formation of a mildly exothermic peak as seen in the DSC trace of Figure 4.2.2. As temperature increased to 450 °C, further decomposition occurred and resulted in about 10% weight loss in the TGA profile. This can be inferred to the decomposition of thus metastable-NiO_2 to thermodynamically more stable NiO phase (see Figure 4.2.3) which is manifested as a small exothermic peak in Figure 4.2.2. Finally, the β-D-mannuronic acid (M) and α-L-guluronic acid (G) residues were completely oxidized at high temperature leading to the large exothermic peak in the DSC profile. No further weight loss was observed which indicated that the decomposition process was complete at ~500 °C. It can be inferred from Figure 4.2.2 that the process described in this study can yield 200 kg of NiO nanopowders per ton of dried Ni-ALG beads.

HT-XRD was performed every 25 °C interval from room temperature to 600 °C with heating rate maintained at 3 °C/min in static air condition on a α-Al_2O_3 sample holder. Clean cubic NiO HT-XRD pattern observed at temperature 400–500 °C confirms that high purity single phase NiO is formed completely during the thermal decomposition process of Ni-ALG which is consistent with the TGA/DSC analysis trace shown in Figure 4.2.2. Extra peaks from α-Al_2O_3 sample holder were also observed since a small amount of x-rays penetrate through the Ni-ALG sample up to the surface of the sample holder.

No XRD peaks (apart from α-Al_2O_3 sample holder) were observed at temperature below 225 °C indicating that Ni-ALG dried beads did not form NiO below this temperature. HT-XRD pattern indicated that multiple phases of nickel oxide namely NiO and NiO_2 were found to coexist at temperature ~250 °C as shown in Figure 4.2.3b. As the temperature increased from 225 to 300 °C, more and more NiO and NiO_2 nanoparticles were formed and resulted in increase in the corresponding peak intensity.

As temperature further increased from 325 to 350 °C, the fraction of NiO_2 phase decreased as peak intensity reduced and finally became NiO at 375 °C as shown in Figure 4.2.3c. No further phase change was observed indicating that NiO nanocrystals were obtained even after partial decomposition Ni-ALG structure for which the onset of decomposition occurred at 400 ± 10 °C (Figure 4.2.2). Note the small temperature shift

observed for various reaction steps between TGA/DSC and HT-XRD was because of the dynamic nature of TGA/DSC experiments compared with the static HT-XRD experiments.

According to the results of TGA/DSC (Figure 4.2.2) and HT-XRD (Figure 4.2.3), it can be concluded that the thermal decomposition of Ni-ALG complexes proceed in four stages. A possible general decomposition mechanism in flowing oxygen atmosphere can be suggested as follow:

$$Ni^{2+} - ALG \cdot xH_2O \xrightarrow{<200\ ^{\circ}C} Ni^{2+} - ALG + xH_2O \quad (5.1)$$

$$Ni^{2+} - ALG \xrightarrow{200-300\ ^{\circ}C} NiO + NiO_2 + G - residue + M - Residue \quad (5.2)$$

$$NiO + NiO_2 \xrightarrow{300-400\ ^{\circ}C} 2NiO + \frac{1}{2}O_2 \quad (5.3)$$

$$G - residue + M - Residue \xrightarrow{>400\ ^{\circ}C} yCO_2(g) + zH_2O \quad (5.4)$$

where Ni^{2+}-ALG and G/M-residue refers to nickel alginate and guluronic acid or mannuronic acid residue, respectively.

XRD analysis of the nickel alginate dried beads processed at 500 °C with 3, 6 and 12 hours annealing time showed that all the obtained samples were single phase cubic NiO (04-002-0665) powders as seen in Figure 4.2.4a. Same results were also obtained from the samples calcined at 700 °C for 3, 6 and 12 hours. The XRD patterns could be entirely indexed with the reference pattern available in the literature marked at the top of figures. It was found that the XRD pattern of NiO became sharper and the peaks became progressively narrower as the calcination temperature increased from 500 to 700 °C (see Figure 4.2.4b) and as annealing time increased mainly because of the growth of the crystal size.

Rietveld size/strain structural analysis of NiO nano powders obtained after calcination of Ni-ALG beads at 500 °C for 3 hours was carried out to determine structural parameters and micro-strain in obtained NiO by XRD method. Figure 5.2.1 shows a comparison between the calculated and the observed XRD patterns obtained experimentally of the nanopowders of NiO calcined at 500 °C for 3 hours employing a size/strain Rietveld structural refinement. It is clear from the figure that the agreement between the experimental data and the calculated pattern is excellent showing negligible residual strain. The same analysis was also performed at the other samples, the size and lattice parameter values are shown in Table 5.2.1.

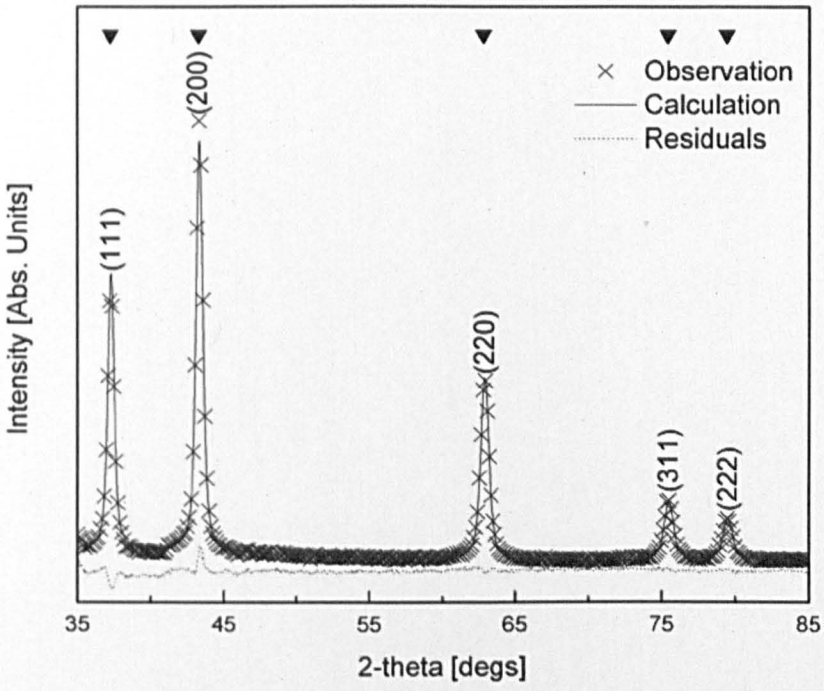

Figure 5.2.1. Size/Strain Rietveld structural refinement analysis of NiO sample calcined at 500 °C for 3 hrs. A number of raw data, observation points are omitted for clarity. Tick marks "black triangles" for reference pattern of NiO, ICDD 04-002-0665, are shown at the top of the peaks.

Table 5.2.1. Structural parameters of NiO samples obtained using Size/Strain Rietveld structural refinements.

Sample	Heat Treatment	Size/Strain analysis				
		Size (nm)	Micro Strain	R_{wp} (%)	R_{exp} (%)	Lattice parameter (Å)
A	500 °C - 3 hrs	20.2(8)	0.1(8)	1.35	0.54	4.1772
B	500 °C - 6 hrs	29.1(4)	0.1(5)	1.20	0.53	4.1780
C	500 °C - 12 hrs	30.5(7)	0.1(3)	1.28	0.53	4.1779
D	700 °C - 3 hrs	30.9(3)	0.2(6)	1.44	0.53	4.1774
E	700 °C - 6 hrs	45.5(1)	0.1(9)	1.40	0.53	4.1780
F	700 °C - 12 hrs	52.7(8)	0.1(6)	1.43	0.54	4.1777

The results of size/strain analysis are shown in Table 5.2.1 as a function of calcination time at 500 and 700 °C. As expected, the weighted residual from the refinement, R_{wp}, is in the range from 1.20−1.44%, providing evidence of excellent agreement between the data and the refined model. Note that the errors presented are the statistical standard deviation from the refinement and are given in the brackets. As the processing temperature increases, a gradual coarsening in particle size and a reduction in micro-strain was observed. In addition, as the annealing time increases from 3 to 12 hours, particle coarsening was also observed, although the influence of time on crystal size is not as strong as temperature shown in Table 5.2.1. During the refinement, unit cell lattice parameters were modified which were comparable to ICDD (04-002-0665) with a = 4.1780 Å.

The morphology of the obtained powders was investigated using Transmission Electron Microscopy (FEI Tecnai TF20 FEG-TEM). As shown in Figure 4.2.5a, the crystallite size of NiO nanoparticles are good agreement with the calculated values using XRD Rietveld refinements presented in Table 5.2.1. This clearly indicated that the XRD peak broadening in especially due to crystallite size effect and has negligible contribution from strain or instrumental broadening effect. This is also confirmed from the values of micro-strain in NiO nanoparticles presented in Table 5.2.1. The d-spacing values obtained from SAED patterns in Figure 4.2.5b have been compared with the XRD results. The d-values of the samples shown in Figure 4.2.5b for (111), (200) and (220) are in reasonable agreement with the reference data (04-002-0665) as shown in Table 5.2.2.

Table 5.2.2. Comparison of NiO d-spacing values obtained by TEM and XRD Rietveld refinement with (04-002-0665) reference data.

	Peak or Ring No.	h	k	l	Sample A	Sample B	Sample C	Sample D	Sample E	Sample F	Aver. *d*/(Å)	Ref. *d*/(Å)
TEM *d*/(Å)	1	1	1	1	2.47	2.50	2.50	2.41	2.30	2.47	2.44	2.41
	2	2	0	0	2.17	2.09	2.16	2.08	2.11	2.03	2.11	2.09
	3	2	2	0	1.55	1.48	1.54	1.50	1.51	1.48	1.51	1.48
XRD Rietveld Refinement *d*/(Å)	1	1	1	1	2.41	2.41	2.41	2.41	2.41	2.41	2.41	2.41
	2	2	0	0	2.09	2.09	2.09	2.09	2.09	2.09	2.09	2.09
	3	2	2	0	1.48	1.48	1.48	1.48	1.48	1.48	1.48	1.48

In this present investigation, a novel and generic sol-gel method has been developed for the production of high purity metal oxide nanopowders using sodium alginate. This has been demonstrated successfully employing nickel oxide (NiO) as a model material in this instance. The results of this investigation indicate that the final particle size of ~20 nm can be obtained after calcination of the predried beads at 500 °C for 3 hours in ambient air. An insight into the calcination process has been obtained by using simultaneous thermo-gravimetric analysis and differential scanning calorimetry and high temperature X-ray diffraction. Powder X-ray diffraction confirms that the obtained samples are single phase cubic NiO powders with no trace of impurity. During the phase transformation, NiO + NiO_2 have been found to co-exist between 250–350 °C and a reaction scheme is proposed to account for this. The mean crystallite sizes calculated from XRD analysis using Rietveld refinement method agree with the morphological features observed by transmission electron microscopy. The NiO nanopowders produced in this study exhibit negligible strain as indicated by Rietveld refinement procedure. The XRD and TEM analyses indicate that there is a significant influence of calcination temperature and time on the particle size which increases with increasing temperature and annealing time. The process described in this study can yield 200 kg of NiO nanopowders per ton of dried Ni-ALG beads according to the TGA/DSC analysis.

5.2.2. XMT of Freeze Dried Na-ALG Beads

This section describes a sol-gel production of NiO nanopowders using sodium alginate beads via freeze dried. The experimental details of sol-gel experimental process can be found in Section 3.9. The results of this investigation can be found in Section 4.2.2.

Figure 4.2.6 shows ion-exchanged nickel alginate beads in wet state and after freeze drying. The wet beads appear as spherical light green in color having a diameter of ~5 mm. It can be seen that the beads changed their color to bright green, characteristic color of nickel compounds, and nearly maintained their shape and size after freeze drying. The freeze dried nickel alginate beads were then calcined at 700 °C for 1 hour in ambient air giving rise to black spherical beads with sizes in the range of ~2 mm. The calcined samples are very fragile due to high degree of porosity.

Freeze dried nickel alginate beads and calcined samples were individually scanned using XMT. Figures 4.2.7 and 4.2.8 show their reconstructed 3D images from outside, inside, transverse and cross sections, respectively. It can be seen that both the freeze dried and calcined samples have foam-like structures composed of a dominant proportion of voids and thin films as the wall of the foam structure. The outside walls have out-pointed wrinkles, which have very similar thickness to the adjacent wall. These wrinkle structure formed during freeze drying can be remained after calcinations (comparing Figure 4.2.7a with Figures 4.2.8a and e). The inside walls in the freeze dried sample are relatively thinner than its outside wall, in the range of ~20 μm and ~30 μm, respectively, and occasionally shows smaller wrinkles at the side towards outside. Both the outside and inside films showed good continuity at the scale examined.

The calcined bead samples show similar structures to their precursors, although they are obviously smaller in size (being shrunk from ~5 mm to ~2 mm). Their outside walls are ~20 μm thick, generally thinner than that of the freeze dried sample, while their inside walls varies from less than 5 μm to more than 25 μm in thickness. The formation of the thicker inside wall could suggest a certain degree of aggregation during the fast calcinations process so that some pores formed in the film (Figures 4.2.8b and 4.2.8f). The aggregation and pore formation results in a less continuity of the calcined inside film than the freeze one.

Figure 5.2.2 presents the volume distribution of the freeze dried and calcined samples at different linear attenuation coefficients. The X-ray attenuation is a

function of product of the linear attenuation coefficient μ (cm^{-1}) of the compound and the voxel length (x), following the Beer's law.

$$I = I_0 e^{-\mu x} \qquad (5.5)$$

where I_0 and I are the X-ray intensity before and after it penetrates the voxel. In the tomography reconstruction a μ value is assigned to each voxel. When the voxel is completely filled by a pure component, the μ value will be the linear attenuation coefficient of the component at the X-ray wavelength. If the voxel is filled by a mixture of different components (including air or free space), the corresponding μ value is an apparent value weighted from all the components in the voxel.

For the highly porous materials, such as the samples studied here, a low value close to zero refers to empty space with air, and a higher apparent linear attenuation coefficient refers to the wall materials composed of components with solid materials, a larger population of nickel atoms or a larger proportion of the voxel packed by the nickel compounds.

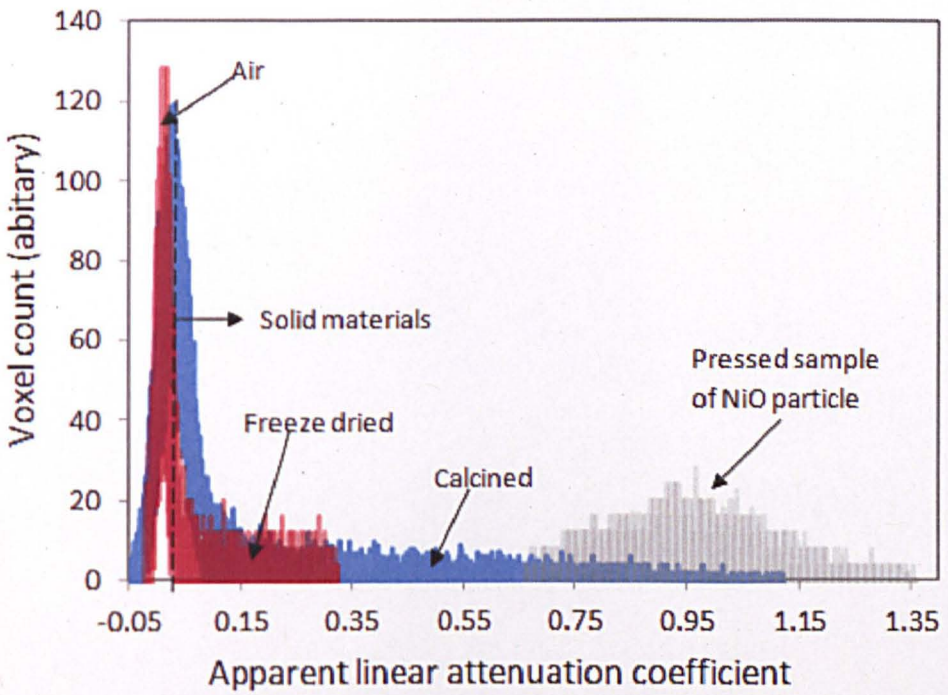

Figure 5.2.2. Comparison of the grey scale histogram of x-ray attenuation of the freeze dried and calcined samples.

Figure 5.2.2 also shows that the freeze dried and calcined structures are mostly composed of air, and only a small fraction of the total volume are composed of solid wall materials. The apparent linear attenuation coefficient spreads in the range of 0.05−0.43 for the freeze dried sample, 0.05−1.27 for the calcined sample. The figure also gives the apparent linear attenuation coefficient of a sample pressed from pure NiO nano powder. It is in the range of 0.65−1.43 with a peak at 0.95.

The distribution of the apparent linear attenuation coefficient demonstrates the effect of nickel concentration and spatial structure of the highly porous samples. The freeze dried sample contains ~14% of nickel, while the calcined sample contains ~78% of nickel. It explains that the highest apparent linear attenuation coefficient for the freeze dried sample is less than 0.34, because the linear attenuation coefficient of nickel is a few thousand times that of carbon, hydrogen and oxygen. The contribution of alginate to the apparent attenuation coefficient is relatively small. In contrast, the apparent linear attenuation coefficient of the calcined sample extends to 1.43.

The thin film structure results in the wider distribution of the histogram, because the voxel size (2 or 3 μm for the scan, 4 or 6 μm for the reconstructed structures is large compared to the thickness of the films (5−30 μm). It can be imagined that the large amount of voxels at the film surface are partially packed by the film and partially packed by the empty space, resulting in lower and scattered values of apparent linear attenuation coefficient. For the calcined sample, the apparent linear attenuation coefficient occurs in a wide range, but only a very small proportion reached the range of that for the compressed NiO sample (0.65−1.47), suggesting a possibility of the existence of free fissures between the nanoparticles in the size range of ~50 nm (Figure 4.2.9). The free space makes the calcined foam very fragile and easily to be pulverized. Both structural and x-ray attenuation analysis clearly suggest that the foam-like structure and well separated thin film walls of the nickel alginate beads are beneficial for the formation of nickel oxide nanoparticles in a nanostructured dimension during calcination stage.

The morphology of the NiO nanopowders obtained by breaking the calcined sample has been investigated using TEM. As shown in Figure 4.2.9, the nanoparticles have cubic morphology and are approximately ~50 nm. This is in good agreement with that calculated using XRD Rietveld refinements shown in Figure 4.2.10 and 5.2.3.

Figure 4.2.10 shows the XRD diffraction pattern of the NiO nanoparticles formed during the calcination of nickel alginate freeze dried beads at 700 °C for 1 hour. It shows a perfect single phase cubic NiO powders. The XRD pattern could be entirely indexed with the reference pattern (ICDD 04-002-0665) available in the literature.

Figure 5.2.3 shows a comparison between the calculated and the observed XRD patterns obtained experimentally of the nanopowders of NiO employing a Rietveld size/strain structural refinement. It is clearly seen from the figure that the agreement between the experimental data and the calculated XRD pattern is excellent ($R_{exp} \approx 0.50\%$, $R_{wp} \approx 2.18\%$) showing negligible residual pattern. This suggests that the nanoparticles of NiO are free of any strain. The mean crystallite size calculated from XRD Rietveld refinement is 49.1 ± 4 nm which is in excellent agreement with the average size of 50 nm obtained from TEM analysis (Figure 4.2.9). The lattice parameter and d-spacing values for various crystal planes obtained from XRD Rietveld refinement analysis are compared with the ICDD 04-002-0665 reference data in Table 5.2.3. The results obtained in the present investigation are in good agreement with the reference data.

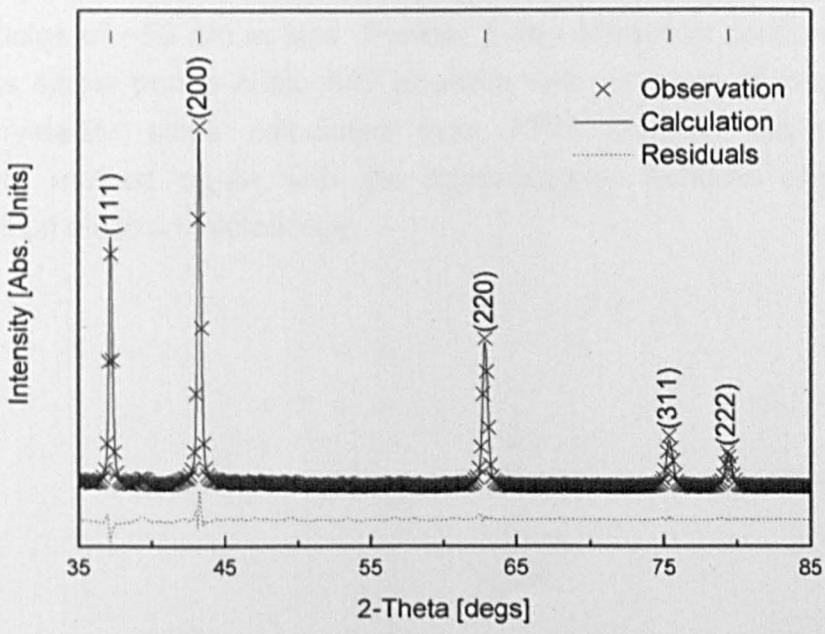

Figure 5.2.3. Size/Strain Rietveld structural refinement analysis of NiO sample calcined at 700 °C – 1 hour. Tick marks for reference pattern of NiO, ICDD 04-002-0665, are shown at the top of the figure.

Table 5.2.3. Structural parameters of NiO 700 °C – 1 hour samples obtained using Size/Strain Rietveld structural refinements.

h	k	l	Rietveld Refinement	ICDD 04-002-0665
1	1	1	2.42	2.41
0	0	2	2.09	2.09
0	2	2	1.48	1.48
1	1	3	1.26	1.26
2	2	2	1.21	1.21
Lattice parameter a (Å)			4.1794	4.1780

In this section, a generic novel ion-exchange mediated sol-gel method has been developed for the production of high purity nickel and other metal oxide nanopowders using sodium alginate or alginic acid precursor. X-ray micro-tomography shows that nickel ions have been uniformly cross-linked in the alginate structure and remained stable after freeze drying evidenced by the bright green color of the freeze dried beads. The freeze dried nickel alginate beads exhibit porous foam-like structure composing of thin nickel alginate film and a dominant fraction of voids. The porous nickel alginate beads when calcined at 700 °C for 1 hour in ambient air yielded spherical nickel oxide nanoparticles of ~50 nm in size. Powder X-ray diffraction confirms that the sample is single phase cubic NiO powders with no trace of impurity. The mean crystallite sizes calculated from XRD analysis using Rietveld refinement method agree with the morphological features observed by transmission electron microscopy.

5.2.3. NiO Production by Na-ALG Granules

This section describes a sol-gel production of NiO nanopowders using sodium alginate granules. The sol-gel experimental process can be found in Section 3.9. The results of this investigation can be found in Section 4.2.3.

The progress of calcination of the dried Ni-ALG granules was studied by simultaneous TGA/DSC. The results of thermal analysis are shown in Figures 4.2.12.

The decomposition of nickel alginate (Ni-ALG) dried granules was found to be a four step process. These four decomposition processes were observed in the temperature range of ambient temperature–200 °C, 200–275 °C, 275–350 °C and 350–375 °C, respectively, as shown in the TGA profile in Figure 4.2.12. An endothermic decomposition peak observed in the corresponding DSC profile at temperature between ambient temperature and 200 °C is associated with about 5% weight loss as shown in the TGA profile. This was possibly due to water evaporation during the heat treatment process. No significant heat effects were seen in the second (200–275 °C) and third (275–350 °C) decomposition processes in the DSC profile in Figure 4.2.12. However, in the second decomposition process, about 35% weight loss was observed in the TGA profile. This is probably due to the cleavage of G-G, G-M and M-M weaker linkages in the alginate polysaccharide molecule leading to significant evolution of oxygen and hence the corresponding weight loss. As temperature further increased to 350 °C, about 10% weight loss was observed in the TGA profile.

According to the previous investigation of thermal decomposition of Ni-ALG beads (see Section 5.2.1), coexisting NiO and NiO_2 phases were observed at temperatures between 200 and 450 °C. However, neither DSC peak (Figure 4.2.12) nor a signature of the NiO_2 phase (Figure 4.2.13) was observed in this study involving granulated Ni-alginate. This might be due to the net results of competing processes such as thermal decomposition of alginate structure (exothermic) and phase transformation between NiO and NiO_2 phases (endothermic) processes that led to undetectable heat change as seen in the DSC trace in Figure 4.2.12. Therefore, we believe that the energy requirement for phase transformations is fully provided by heat of combustion of the nickel alginate granules. Finally, a strong exothermic peak was observed at temperatures between 350 and 375 °C due to the complete oxidative decomposition of β-D-mannuronic acid and α-L-guluronic acid residues at high temperatures. No further weight loss was observed beyond 400 °C which indicated that the decomposition process was complete at

400 °C. Furthermore, it was noted that the temperature for complete decomposition using highly compact alginate granules was 100 ± 50 °C lower compared to that using alginate beads. This might be in part due to higher energy evolved during the combustion of highly compact alginate granules.

HT-XRD was performed every 25 °C interval from room temperature to 600 °C with heating rate maintained at 3 °C min^{-1} in static air condition on a α-Al_2O_3 sample holder. Clean cubic NiO HT-XRD pattern was observed at 400 °C, indicating that thermal decomposition process was complete. This corroborates with the thermal analysis results shown in Figure 4.2.12. Extra peaks from α-Al_2O_3 sample holder are also seen in the diffraction patterns due to the interactions of X-rays with the sample holder.

No NiO peaks were observed at a temperature below 250 °C indicating that Ni-ALG dried granules had amorphous structure (see Figure 4.2.13a and 4.2.13b). HT-XRD pattern indicated that cubic NiO was formed at ~275 °C, as seen in Figure 4.2.13b. No further phase change was observed, indicating that NiO nanocrystals were obtained even after partial decomposition Ni-ALG structure for which the onset of decomposition occurred at 275 ± 10 °C (Figure 4.2.13). Note the small temperature shift observed for various reaction steps between TGA/DSC and HT-XRD was because of the dynamic nature of TGA/DSC experiments compared with the static HT-XRD experiments.

XRD analysis of the nickel oxide obtained from the combustion of dried alginate granules processed at 600 °C with 2 hours annealing time showed that the obtained sample was single phase cubic NiO (04-002-0665) powders as seen in Figure 4.2.14. The XRD pattern could be entirely indexed with the reference pattern available in the literature which is indexed at the top of each peak.

Figure 5.2.4 shows a comparison between the calculated and observed XRD patterns of NiO after calcination at 600 °C for 2 hrs employing a size-strain Rietveld structural refinement. The agreement between the experimental data and the calculated pattern is excellent, showing negligible residual pattern. The crystallite size and lattice parameter of the obtained NiO nanopowders are shown in Table 5.2.4.

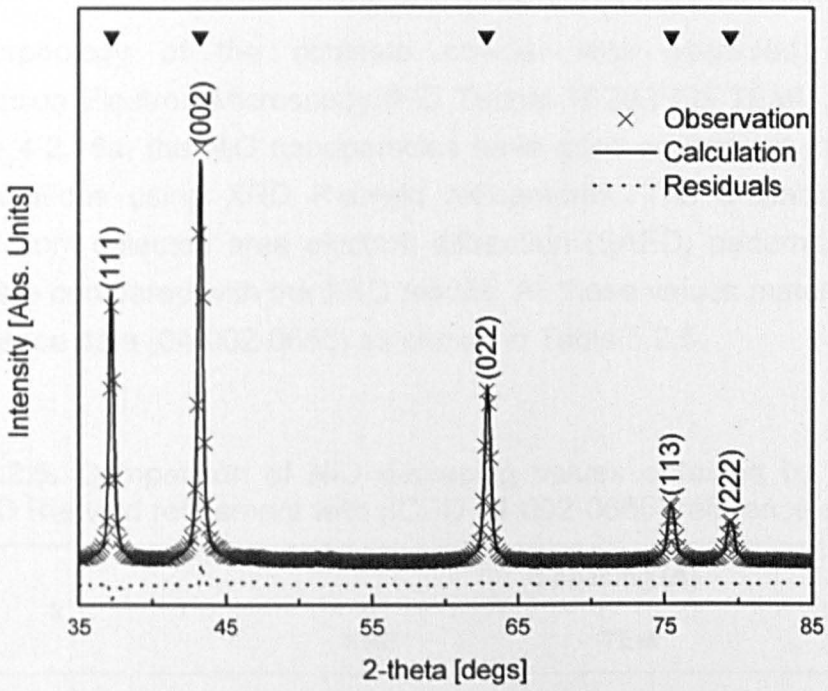

Figure 5.2.4. XRD of NiO nanopowders calcined at 600 °C for 2 hrs annealing time. The patterns are indexed by ICDD 04-002-0665 shown at the top of the figure.

Table 5.2.4. Structural parameters of NiO calcined at 600 °C for 2 hrs using Size/Strain Rietveld structural refinements.

Parameters	Size/Strain Analysis
Lattice parameter a (Å)	4.1772
Size (nm)	29.3(1)
Micro Strain	0.1(1)
R_{wp} (%)	1.27
R_{exp} (%)	0.48

The results of size/strain analysis of NiO sample are shown in Table 5.2.4. As expected, the weighted residual from the refinement (R_{wp} = 1.27%) provides evidence of excellent agreement between the data and the refined model. Note that the errors presented are the statistical standard deviation from the refinement. The mean crystallite size calculated from XRD analysis using Rietveld refinement method is ~30 nm with negligible strain. During the

refinement, unit cell lattice parameter was modified which were comparable to reference (ICDD 04-002-0665) a = 4.1780 Å.

The morphology of the obtained powder was observed by using Transmission Electron Microscopy (FEI Tecnai TF20 FEG-TEM). As shown in Figure 4.2.15a, the NiO nanoparticles have good agreement in size with the calculations using XRD Rietveld refinements. The d-spacing values obtained from selected area electron diffraction (SAED) patterns in Figure 4.2.15b are compared with the XRD results. All these values match well with the reference data (04-002-0665) as shown in Table 5.2.5.

Table 5.2.5. Comparison of NiO d-spacing values obtained by TEM and XRD Rietveld refinement with (ICDD 04-002-0665) reference data.

h	k	l	d-spacing (Å)		
			XRD	TEM	Ref.
1	1	1	2.42	2.45	2.41
0	0	2	2.09	2.11	2.09
0	2	2	1.48	1.49	1.48
1	1	3	1.26	1.27	1.26
2	2	2	1.21	1.22	1.21

In this section, a novel and generic sol-gel method has been developed for the production of high purity nickel oxide (NiO) nanopowders using metal ion-exchange with the Na^+ ion of granulated sodium alginate. The results of this investigation indicate that the final particle size of ~30 nm can be obtained after calcination of the pre-dried granules at 600 °C for 2 hours in ambient air. An insight into the calcination process has been obtained by using simultaneous thermo-gravimetric analysis and differential scanning calorimetry and high temperature X-ray diffraction. Powder X-ray diffraction confirms that the sample is single phase cubic NiO powders with no trace of impurity. The mean crystallite size calculated from XRD analysis using Rietveld refinement method agrees with the morphological feature observed by transmission electron microscopy. The nanopowders produced in this study exhibit negligible strain as indicated by Rietveld refinement procedure.

5.3 $Ce_xGd_{1-x}O_{2-\delta}$ Production by Na-ALG Beads

A novel and generic sol-gel method has been developed for the production of high purity nanopowders of metal oxides and their solid state solutions using organic powders such as sodium alginate (Na-ALG) which can function as ion-exchange medium. Sodium alginate dissolves readily in water, and it forms a gel if it is brought into contact with an aqueous solution of metal ions, whereby the sodium ion in the polymer structure is replaced by the metal ion. By virtue of the gel structure, the metal ions become immobile and cannot readily get close to each other, hence the possibility of producing small nanoparticles. Moreover, the energy requirement for calcinations is partially provided by heat of combustion of the alginate. Therefore, metal oxides can be produced after calcination at a temperature range that is much lower than the conventional methods. This method is simple, quick and environmental friendly which not only produces simple oxide such as NiO, CuO, CoO, Y_2O_3, ZrO_2 or Fe_2O_3, but also produces complex oxide such as gadolinium doped ceria (CGO) for many applications.

In order to obtain nano crystalline pure CGO powders, various sol-gel techniques have been explored, including the use of maltose (see Section 5.1.1) and sucrose (see Section 5.1.2) with pectin as precursors, akin to jam making process employed in food industry. However, from a commercial perspective, it is important to synthesize large quantities of CGO nanopowders rapidly in an environmentally friendly and cost effective manner. Alginate is an anionic polysaccharide that is naturally found in abundance in the cell walls of brown algae and it has 200 ~ 300 times more water absorbing capacity compared to its own weight. In this study, a novel environmentally friendly generic method for low temperature synthesis of two compositions of CGO, CGO1 ($Ce_{0.9}Gd_{0.1}O_{1.95}$) and CGO2 ($Ce_{0.8}Gd_{0.2}O_{1.9}$), nanopowders, involving sodium alginate mediated ion-exchange process, has been developed. The chemical structure of the Na-ALG solution and the obtained CGO beads are analyzed by FTIR. The obtained samples of nanopowders have been characterized employing XRD coupled with Rietveld refinement, TEM and ICP-AES. The sinterability, electronic conductivity and microstructure of CGO are also investigated. Details of the research work and its findings are described below.

5.3.1. $Ce_xGd_{1-x}O_{2-\delta}$ Production by Na-ALG Beads

This section describes a sol-gel production of CGO nanopowders using sodium alginate beads. The experimental details of sol-gel process can be found in Section 3.9 where metal nitrate salts are cerium nitrate and gadolinium nitrate. The results of this investigation can be found in Section 4.3.1.

Alginate contains varying amount of 1, 4′-linked β-D-mannuronic acid (M) and α-L-guluronic acid (G) residues covalently linked together in sequence as –GG– or –MM– structures or as –GM– block copolymers. Once alginate is gelled with metal ions, the metal ion binds preferentially to G blocks. FTIR spectra of 4 wt% Na-ALG solution, CGO1-ALG (90 mol% Ce & 10 mol% Gd) and CGO2-ALG (80 mol% Ce & 20 mol% Gd) wet beads are shown in Figure 4.3.2 with a weak peak at wavenumber range 1375−1450 cm^{-1}, a medium peak at 1600−1675 cm^{-1} corresponding to O=C–O- stretching [85] and a strong broad peak at wavenumber range 3000−3600 cm^{-1} corresponding to O–H stretching [85], respectively.

In Figure 4.3.2, a shoulder peak is observed at wavenumber ~1580 cm^{-1} in CGO-ALG profiles. This is due to M–O bonds formed after ion-exchange reaction between Ce^{3+}/Gd^{3+} and Na^+ in alginate [106]. A very strong peak is also present at wavenumber region 1625−1650 cm^{-1} probably related to $(O=C–O^-)Na$ or $(O=C–O^-)_3Gd$ and $(O=C–O^-)_4Ce$ stretching vibration in the three samples, respectively [85]. However, the peak width becomes more pronounced in CGO-ALG spectra because of increase in the charge density, since the radius and atomic weight of trivalent $Ce^{3+}$and Gd^{3+} cations is higher than monovalent Na^+ around the carbonyl groups. A minor peak shift is noted corresponding to M–O bonds in CGO1-ALG and CGO2-ALG because of the change in Ce^{3+}/Gd^{3+} ratio in the samples.

Based on the charge balance, three Na^+ ions are required for bonding with trivalent Ce^{3+}/Gd^{3+} cations. This would lead to formation of egg-box structure during the ion-exchange process. This process leads to instantaneous gelling of the alginate. Hence beads are formed when Na-ALG solution is dripped into an aqueous solution of Ce^{3+}/Gd^{3+}. Similar phenomenon is observed when Na-ALG solution is made to come in contact with aqueous solutions containing Ni^{2+}, Fe^{2+}, Cu^{2+}, Co^{2+}, Fe^{3+}, Y^{3+} and Zr^{4+} cations as seen in Figure 3.3. Since the higher molecular weight ketones are known to be less soluble in water compared to lower molecular weight ketones, we are led to believe that the surface of beads is likely to be hydrophobic and the core of the beads to be hydrophilic. This is in agreement with the

evidence that the beads after ion-exchange are always filled with aqueous solution (see Figure 5.3.1a and 5.3.1b).

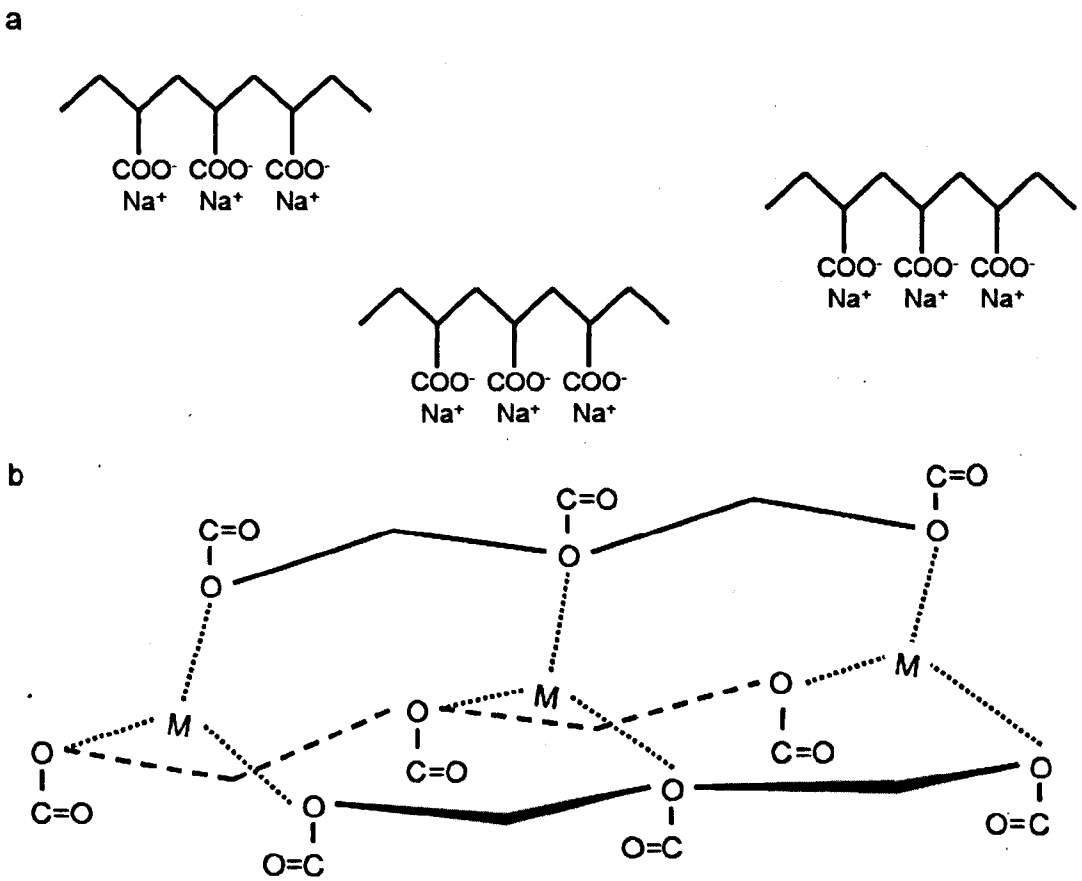

Figure 5.3.1. Scheme of alginate beads formation with Ce^{3+} and Gd^{3+} cations. a, viscous Na-ALG solution before ion-exchange with Ce^{3+} and Gd^{3+} cations and b, cross-linked structure after ion-exchange with Ce^{3+} and Gd^{3+} cations. M represents Ce^{3+} and Gd^{3+}.

XRD analysis of the CGO1 and CGO2 show that both samples crystallized in single phase cubic form of $Ce_{0.9}Gd_{0.1}O_{1.95}$ (04-002-6160) and $Ce_{0.8}Gd_{0.2}O_{1.9}$ (ICDD 04-014-0032) powders as shown in Figure 4.3.3a. The XRD patterns can be entirely indexed with the reference pattern available in the literature marked at the top of peaks.

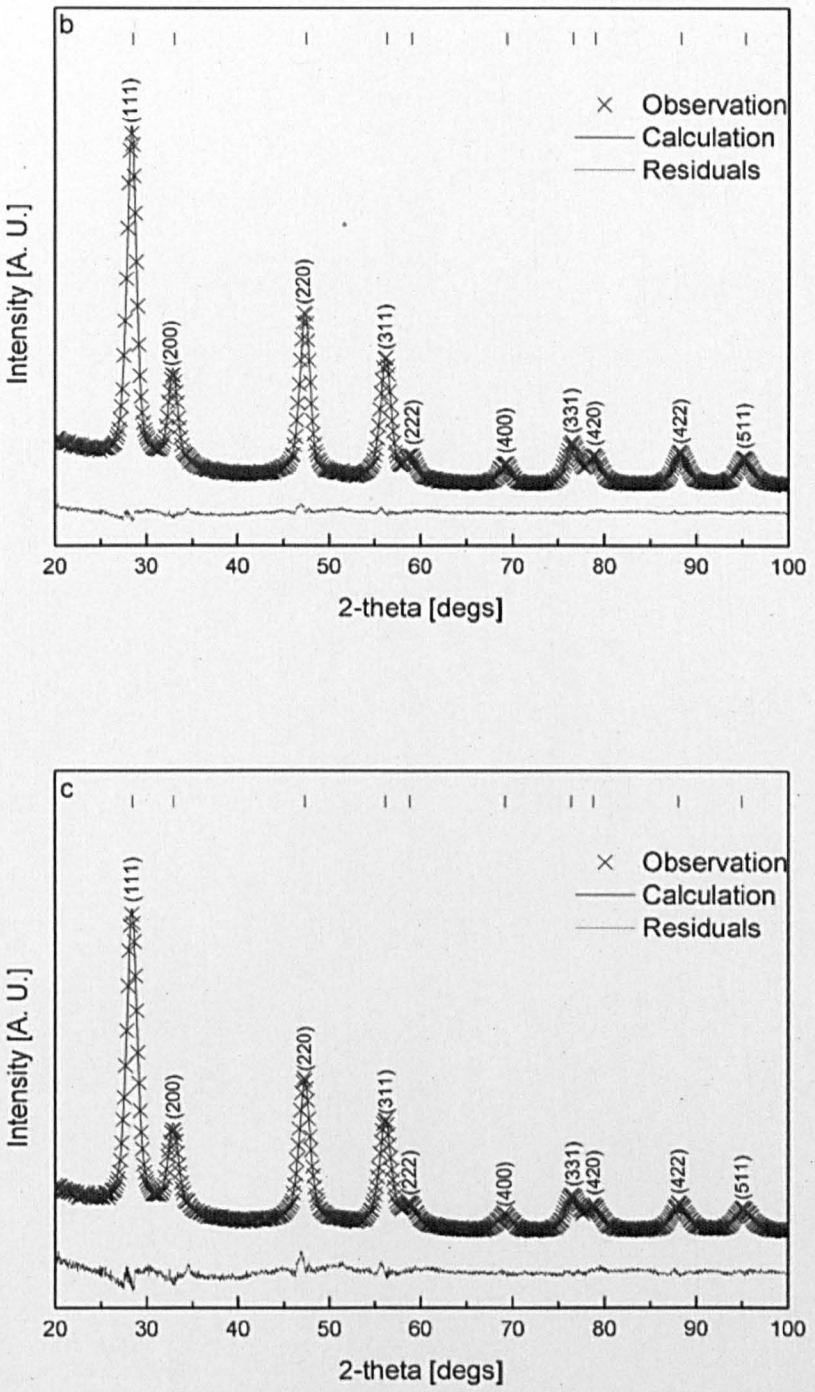

Figure 5.3.2. XRD patterns of CGO1 and CGO2 nanopowders calcined at 500 °C for 2 hours. b, Size/Strain Rietveld structural refinement analysis of CGO1 sample. c, Size/Strain Rietveld structural refinement analysis of CGO2 sample. A number of raw data, observation points are omitted for clarity. Tick marks corresponding to the peaks in the reference pattern of $Ce_{0.9}Gd_{0.1}O_{1.95}$, ICDD 04-002-6160 and $Ce_{0.8}Gd_{0.2}O_{1.9}$, ICDD 04-14-0032 are shown at the top of figures.

Figures 5.3.2b and 5.3.2c show a comparison between the observed XRD patterns obtained experimentally of the nanopowders of CGO calcined at 500 °C for 2 hours and the calculated patterns employing a size/strain Rietveld structural refinement, respectively. It is clear from the figures that the agreement between the experimental data and the calculated pattern is excellent showing negligible residual pattern.

The results of Rietveld size/strain refinement analysis (see Table 5.3.1) suggests that the crystallite size of CGO nanopowders is ~8 nm for CGO1 and ~7 nm for CGO2, respectively. The calculated lattice parameters of CGO1 and CGO2 presented in Table 5.3.1 are in good agreement with reference data as given in Table 5.3.1. The nanopowders produced in this study exhibit negligible strain as indicated by Rietveld refinement procedure. The small weighted residual (R_{wp}) and Goodness of Fit (GOF) values from the refinement in Table 5.3.1 give strong evidence of an excellent agreement between the measured data and the refinement model.

Table 5.3.1. Structural parameters of CGO1 and CGO2 calcined at 500 °C for 2 hours calculated by size/strain Rietveld structural refinement analysis. Note that the errors presented are the statistical standard deviation from the refinement and are given in the parenthesis.

Parameters	CGO1	CGO2
Lattice parameter (Å)	5.4170	5.4240
Reference lattice parameter (Å)	5.4170 [107]	5.4300 [108]
Size (nm)	7.88(8)	7.02(7)
Micro Strain	0.3(6)	0.3(5)
R_{wp} (%)	2.86	2.39
R_{exp} (%)	1.53	1.41
GOF	3.48	2.87

It can be clearly seen in Figure 4.3.4 that the CGO nanoparticles have relatively uniform hexagonal shape and narrow size distribution that closely matches with the calculated values using XRD Rietveld refinements. The hexagonal morphology of crystallites seen in Figure 4.3.4 further confirms the earlier results of XRD (Figure 4.3.3a, 5.3.2b and 5.3.2c) that the crystal structure of CGO1 and CGO2 is cubic. The values of interplanar spacing (d-

spacing) calculated from the SAED patterns (see Figure 4.3.4 insets) are compared with those calculated from the XRD results in Table 5.3.2. All these values (d_{hkl}) are in excellent agreements with the reference data as shown in Table 5.3.2. Compositions of CGO1 and CGO2 also have been confirmed using EDS (see Table 5.3.3).

Table 5.3.2. Comparison of d-spacing values of CGO1 and CGO2 obtained from TEM and XRD Rietveld refinement with 04-002-6160 and 04-014-0032 reference data.

(hkl)	Ref.[a] *d*/ (Å)	CGO1	
		TEM d (Å)	XRD d (Å)
(111)	3.13	3.19	3.15
(200)	2.71	2.75	2.72
(220)	1.92	1.96	1.92
(311)	1.63	1.68	1.64

(hkl)	Ref.[b] *d*/ (Å)	CGO2	
		TEM d (Å)	XRD d (Å)
(111)	3.14	3.15	3.15
(200)	2.72	2.75	2.72
(220)	1.92	1.93	1.92
(311)	1.64	1.64	1.64

[a] Reference pattern of $Ce_{0.9}Gd_{0.1}O_{1.95}$ (ICDD 04-002-6160).

[b] Reference pattern of $Ce_{0.8}Gd_{0.2}O_{1.9}$ (ICDD 04-14-0032).

Table 5.3.3 shows the results of chemical analysis of the CGO1 and CGO2 nanoparticles determined by ICP-AES analysis. The residual amount of sodium present in the sample is 7.2 ppb and 7.7 ppb, respectively. This is insignificant and therefore does not show any signature of its presence in the XRD data of CGO1 and CGO2 presented in Figure 4.3.3a. The results of EDS and ICP-AES analysis confirm that the stoichiometry of the CGO1 and CGO2 is $Ce_{0.9}Gd_{0.1}O_{1.95}$ and $Ce_{0.8}Gd_{0.2}O_{1.9}$, respectively. These findings are in excellent agreement with the nominal composition of the starting material.

Table 5.3.3. ICP-AES and TEM-EDS analysis of the CGO1 and CGO2 samples.

Analytical Method	Ce : Gd ratio	
	CGO1	CGO2
ICP-AES	91.93 : 8.07	83.72 :16.28
TEM-EDS	89.33 : 10.66	79.59 : 20.40

Table 5.3.4 shows the total conductivity and activation energy for conduction of CGO1 and CGO2 at 600 and 700 °C, respectively. It can be seen from Table 5.3.4 that the total conductivity of CGO1 and CGO2 samples measured in this investigation is in reasonable agreement with the data reported by Dikmen *et al.* [32] and Steele [105]. The higher activation energy obtained for CGO1 and CGO2 may in part be due to marginally lower density (91–93%) of the samples investigated in this study compared to 95–97% dense samples used by Dikmen *et al.* [32] and possibly by Steele [105] too which is not explicitly stated in their article.

Table 5.3.4. Total conductivity of CGO1, $Ce_{0.9}Gd_{0.1}O_{1.95}$ and CGO2, $Ce_{0.8}Gd_{0.2}O_{1.9}$ solid solutions.

		CGO1	CGO2
Conductivity σ, 600 °C ($S\ cm^{-1}$)	This study	2.65×10^{-3}	5.23×10^{-2}
	Dikmen *et al.* [32]	3.31×10^{-4}	5.09×10^{-3}
	Steele [105]	2.53×10^{-2}	1.80×10^{-2}
Conductivity σ, 700 °C ($S\ cm^{-1}$)	This study	1.75×10^{-2}	4.28×10^{-1}
	Dikmen *et al.* [32]	1.43×10^{-3}	1.63×10^{-2}
	Steele [105]	5.44×10^{-2}	4.70×10^{-2}
Activation Energy E_a (eV)	This study	1.33	1.27
	Dikmen *et al.* [32]	0.99	0.83
	Steele [105]	0.64	0.78

In this present investigation, nanopowders of two different compositions of cerium gadolinium oxides designated as CGO1 ($Ce_{0.9}Gd_{0.1}O_{1.95}$) and CGO2 ($Ce_{0.8}Gd_{0.2}O_{1.9}$) have been synthesized by a sodium alginate (Na-ALG) mediated novel ion-exchange process. The results indicate that the nanopowders having a final particle size of ~7 nm can be obtained after calcination of ion-exchanged alginate precursor at 500 °C for 2 hours in ambient air. The chemical structures of Na-ALG solution and CGO beads are analyzed by Fourier transform infrared spectroscopy. X-ray diffraction confirms that nanopowders of CGO1 and CGO2 are high purity single phase without any trace of un-reacted impurities. The mean crystallite size calculated using XRD Rietveld refinement agrees well with that estimated value from the morphologies observed by transmission electron microscopy. The nominal compositions of CGO1 and CGO2 have been found to be in excellent agreement with that determined by energy dispersive x-ray spectroscopy and inductively coupled plasma - atomic emission spectrometry analysis. The activation energies (E_a = 1.33 and 1.27 eV) and conductivities at 600 and 700 °C for CGO1 and CGO2 are also measured.

5.3.2. Materials Conductivity Analysis for SOFC Application

This section describes microstructure and electrical conductivity of the obtained CGO1 ($Ce_{0.9}Gd_{0.1}O_{1.95}$) and CGO2 ($Ce_{0.8}Gd_{0.2}O_{1.9}$) produced by sodium alginate sol-gel rout. The sample sintering process and a.c. impedance spectroscopy measurement technique can be found in Section 3.8 and 3.9. The results of this investigation can be found in Section 4.3.2.

The relative densities of CGO1 and CGO2 calculated by Archimedes principle are 91–93% of the theoretical density, respectively. The microstructure observed from SEM images in Figure 4.3.5 of the fracture samples of CGO sintered at 1300 °C indicates relatively small particles of uniform size 2–5 μm. During sample preparation, the fracture surface is also polished using sand paper, hence small amount of dust is also observed in the microstructure.

Impedance spectroscopy normally resolves the bulk, grain boundary and electrode conduction processes in ceramic samples by exhibiting successive semicircles (with some distortion) in the complex plane. In the case of CGO1 and CGO2, the grain boundary and bulk processes remain distinguishable to 800 °C. Figures below show the plot of log σ vs. 1/T measured in air, where σ is the conductivity. It also compares the total conductivity, including bulk and grain boundary contributions with only the ionic (bulk) conductivity.

The Arrhenius plots of total conductivities of CGO1 and CGO2 (see Figure 5.3.5) indicate two activation energies, respectively. For CGO1 sample, the different starts at 700 °C with E_a = 1.33 eV at high temperature range and E_a = 0.77 eV at low temperature range. The total conductivities at 700 °C are calculated as 1.75×10^{-2} S cm^{-1} as shown in Figure 4.3.6a and 1.57×10^{-4} S cm^{-1} as shown in Figure 4.3.6b, respectively. More or less the same results are obtained from CGO2 sample. The total conductivities at 550 °C are calculated as 2.01×10^{-2} S cm^{-1} as shown in Figure 4.3.7a and 1.69×10^{-4} S cm^{-1} as shown in Figure 4.3.7b, respectively. This may due to a glassy phase formed at the CGO1 and CGO2 grain surface and lead to conductivity increment at certain temperature range. However, further research is required for clarification.

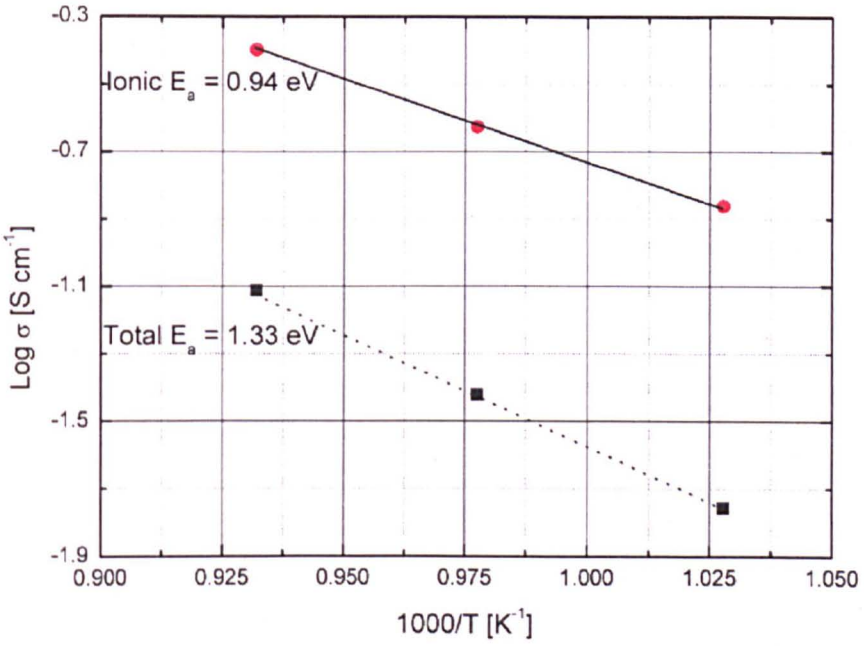

Figure 5.3.3. Arrhenius plot of total and ionic conductivity of the dense CGO1 ceramic measured from 700 to 800 °C in air.

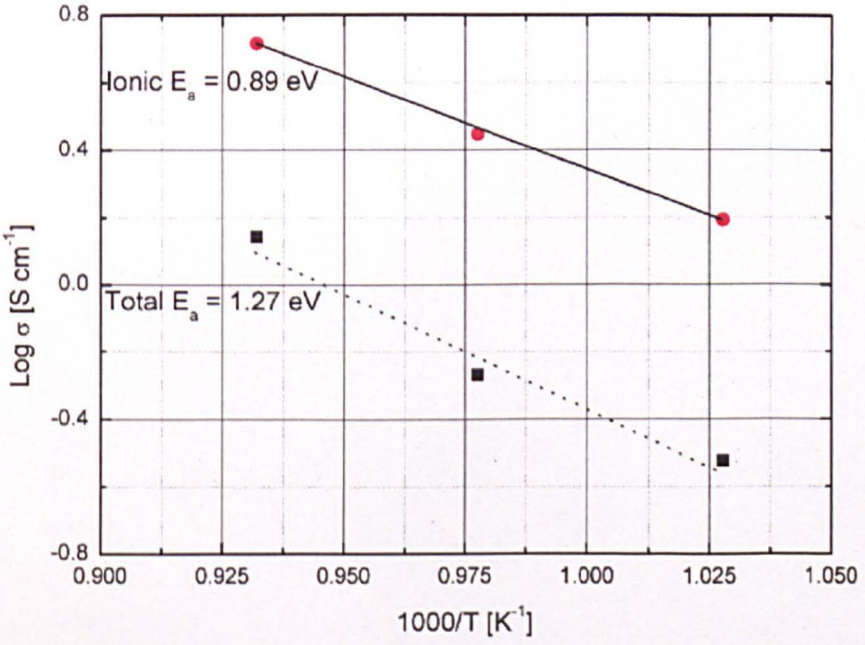

Figure 5.3.4. Arrhenius plot of total and ionic conductivity of the dense CGO2 ceramic measured from 700 to 800 °C in air.

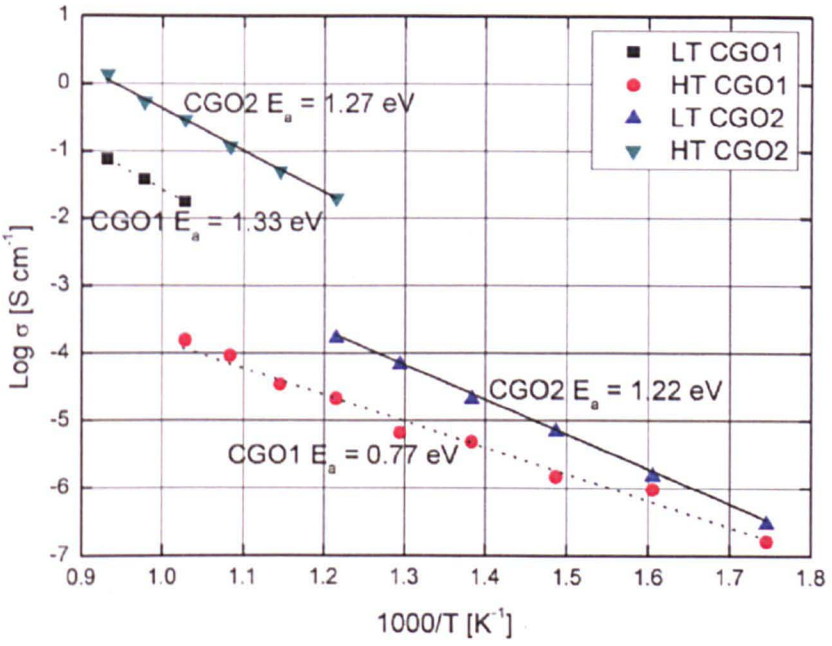

Figure 5.3.5. Arrhenius plot of total conductivity of the dense CGO1 and CGO2 ceramic measured from 300 to 800 °C in air. LT is low temperature measurements and HT is high temperature measurements, respectively.

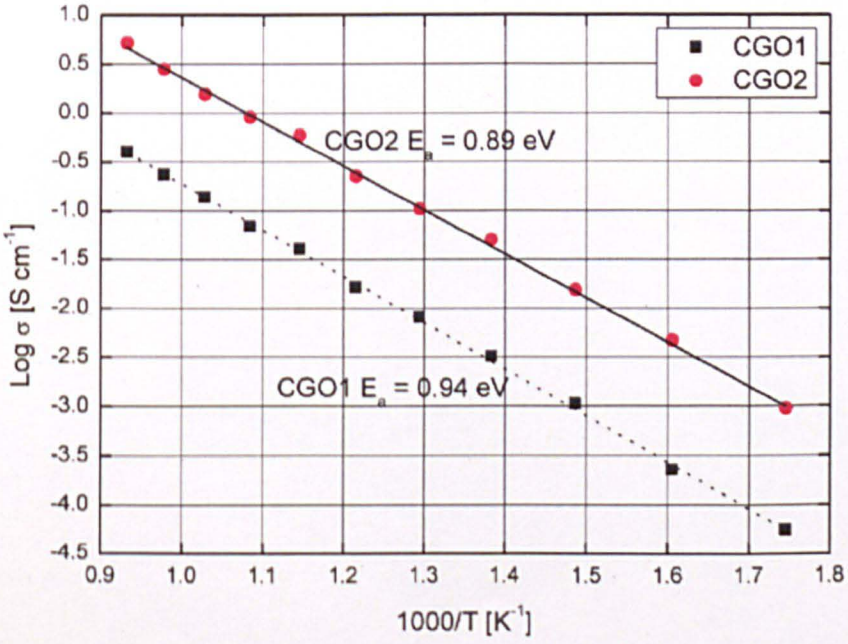

Figure 5.3.6. Arrhenius plot of ionic conductivity of the dense CGO1 and CGO2 ceramic measured from 300 to 800 °C in air.

Table 5.3.5 shows the conductivity and activation energy for conduction of CGO1 and CGO2, respectively. It can be seen that the ionic conductivity of both samples measured in this investigation are in reasonable agreement with the data reported by Dikmen *et al.* [32] and Steele [105]. The ionic conductivities of this investigation at 700 °C, as shown in Figure 4.3.8, are much higher than the one obtained by Steele $\sigma_{700\,^{\circ}C}$ = 0.054 and 0.047 S cm^{-1} [105] for CGO1 and CGO2, respectively.

Table 5.3.5. Conductivity and activation energy of CGO1 and CGO2 solid solutions.

Parameters		CGO1	CGO2
Total Activation energy E_a (eV)	Low Temp.	0.77	1.22
	High Temp.	1.33	1.27
Total conductivity $\sigma_{700\,^{\circ}C}$ (S cm^{-1})		0.02	0.43
Ionic Activation energy E_a (eV)		0.94	0.89
Ionic conductivity $\sigma_{700\,^{\circ}C}$ (S cm^{-1})		0.14	1.56

Chapter 6 Conclusions

In recent years a growing need for nano sized ceramic powders has been shown. Very often these advanced ceramic powders are specially made to suit specific applications. Chemical synthesis methods play an important role in designing such products. The use of chemistry in the preparation of nano materials can mitigate at least three major problems, namely diffusion, impurity and agglomeration.

In the past few years, sol-gel reaction has gained more and more attentions in the ceramic synthesis area. The fine powders prepared by sol-gel methods allow for shorter diffusion distances and improve homogeneity; the gelation media used can easily be refined to increase the purity; and careful control of solutions obtained from the precursors will lead to production of fluffy agglomerates easily to crush. However, since the gelling media is usually very expensive and acidic, it is important to synthesis bulk ceramic nanopowders more rapidly in an environmentally friendly and cost effective manner.

It is well known that sugar is a chelating agent as it contacts with metal ions. And sodium alginate will ion-exchange with metal ions and form an egg-like structure. Both of these materials are abundant in the world. In this research, new chemical sol-gel techniques proposed using sugar + pectin, sodium alginate beads and sodium alginate granules as gelation media have been investigated. These medias seek to form an amorphous solid intermediate phase from the liquid metal solution. the intermediate phase in subsequently decomposed and thermal reaction take place to form metal oxide phases such as gadolinium doped cerium oxide (CGO) or nickel oxide (NiO).

First of all, the preparation of CGO nanopowders by a modified sol-gel methods using sugar (maltose or sucrose) and pectin is reported in this research. The present study indicates that it is possible to produce single cubic phase $Ce_{0.8}Gd_{0.2}O_{1.9}$ (CGO2) nanoparticles using maltose or sucrose as an organic chelating agent and pectin for gelation in a relatively simple condition. In this sol-gel production method, homogeneous distribution of metal ions and slow collapse of the carbohydrate structure during calcination prevent the rapid agglomeration of metal ions, which ensures small particle size of the product and high purity single phase material is formed at temperature as low as 500 °C. The TGA/DSC results obtained in different environmental conditions indicate that at temperatures below 250 °C oxygen

is not crucial in oxidative decomposition of the mixed gel. However, at temperature, higher than 300 °C, oxygen present in air plays an active role in the thermal decomposition process and formation of product phase (CGO2). The XRD data indicate that single phase cubic CGO2 is formed after calcined at 500 °C for 2 hours, confirming that the solid solution formation is complete. The crystalline size determined by Rietveld structural refinement based on size/strain model varied between 8–10 nm at 500 °C and 60–80 nm at 900 °C by using maltose or sucrose precursors. These also show excellent agreement with data obtained from the TEM images. The d-spacing values obtained by Rietveld refinement and SAED are very similar for all samples. ICP-AES and EDS analysis of powder samples confirm that the final chemical composition of the product phase is $Ce_{0.8}Gd_{0.2}O_{1.9}$. The microstructure of both CGO2-MP and CGO2-SP after sintering with average size ~1 μm were obtained. The conductivity of this material was investigated which qualified the use for solid oxide fuel cells as solid electrolyte and in the fabrication of composite electrodes.

On the other hand, a simple method to produce single cubic phase nickel oxide (NiO) nanoparticles by ion-exchange with sodium alginate and subsequent thermal decomposition of the alginate beads has been developed. The process of ion-exchange produces a homogeneous distribution of metal ions; the slow collapse of the alginate structure during thermal decomposition and calcination prevent the rapid agglomeration of metal ions, which ensures small particle size of the product and high purity single phase material at temperature as low as 500 °C. The TGA/DSC and HT-XRD results indicate that thermal decomposition process is complete at 500 °C and leads to formation of product phase (NiO). During the phase transformation, NiO + NiO_2 have been found to co-exist between 250–350 °C and a reaction scheme is proposed to account for this. The process described in this study can yield 200 kg of NiO nanopowders from 1 ton of dried Ni-ALG beads according to the TGA/DSC analysis. The phase transformations during heat treatment, analyzed by HT-XRD indicate that single phase cubic NiO is formed after calcined at 500 °C for 3 hours, confirming that the solid solution formation is complete. The crystallite size determined by Rietveld structural refinement based on size/strain model shows that the calcination temperature and time control the final particle size. This varies between ~20 nm at 500 °C for 3 hours and ~50 nm at 700 °C for 12 hours. These measurements also show excellent agreement with data obtained from TEM images. The d-spacing values obtained by Rietveld refinement and SAED are comparable for all samples.

In addition, an insight into internal physical structures of freeze dried beads of nickel alginate before and after calcination are determined using XMT. The XMT analysis shows that nickel ions have been uniformly cross-linked in the alginate structure and remained stable after freeze drying. After calcination, due to the slow collapse of the carbohydrate structure during thermal decomposition of the alginate prevent the rapid agglomeration of metal ions, NiO nano particles are obtained. The XRD data indicates that single phase cubic NiO is formed after calcined at 700 °C for 1 hour, confirming that the NiO phase formation is complete. The crystalline size determined by Rietveld structural refinement is ~50 nm which shows excellent agreement with data obtained from TEM image.

Moreover, single cubic phase nickel oxide (NiO) nanoparticles can be synthesized using sodium alginate granules. It is well known that sodium alginate powders dissolve readily in water, but it forms a gel if it is brought into contact with an aqueous solution of metal ions, whereby the sodium ion in the polymer structure is replaced by the metal ion. In this research, the sodium alginate powder is first granulated by a pan granulator, where a dense granule can be produced. These granules are immersed in the aqueous solution of the metal ions, where the metal ions diffuse to the structure of the alginate and replace the sodium ion. The gel formation of granules is so rapid that it does not allow the granules to disintegrate. The TGA/DSC and HT-XRD results indicate that the thermal oxidation process is completed at 400 °C and leads to the formation of product phase (NiO). The powder XRD data indicate that single phase cubic NiO is formed after calcination at 600 °C for 2 hours, confirming that the solid solution formation is complete. The crystallite size determined by Rietveld structural refinement based on size/strain model shows that the final particle size is ~30 nm after calcination. These also show excellent agreement with data obtained from TEM images. The d-spacing values obtained by Rietveld refinement and SAED are comparable. The advantages of using sodium alginate granules instead of beads are that the granules can be much easier to produce and dry and higher density, giving higher enthalpy of combustion per unit volume of granules used. The energy requirement for calcinations and phase transformations is partially provided by heat of combustion, hence making the use of granules more attractive.

Finally, the present investigation reported that it is possible to produce single phase cubic gadolinium doped cerium oxide CGO1 ($Ce_{0.9}Gd_{0.1}O_{1.95}$) and CGO2 ($Ce_{0.8}Gd_{0.2}O_{1.9}$) nanoparticles by the novel sodium alginate beads

mediated ion-exchange process in a relatively simple process condition, at low temperature (500 °C) and in an environmentally friendly manner. After calcination, high purity nanopowders with uniform particle size ~7 nm are obtained. The crystallite size determined by Rietveld structural refinement shows excellent agreement with data obtained from the TEM images. The d-spacing values obtained by Rietveld refinement and SAED are in excellent agreement with the reference data for both samples. ICP-AES and EDS analyses of powder samples confirm that the final chemical compositions of the product phases are $Ce_{0.9}Gd_{0.1}O_{1.95}$ and $Ce_{0.8}Gd_{0.2}O_{1.9}$, respectively. The microstructure both CGO1 and CGO2 after sintering with average size 5–2 μm were obtained. The ionic conductivities of these materials were investigated by AC impedance spectroscopy with better property obtained from CGO2 material. These materials produced by alginate sol-gel route should qualify the use for solid oxide fuel cells as solid electrolyte and in the fabrication of composite electrodes.

The ability of sodium alginate to ion-exchange with other metal ions, such as Fe, Co, Ni and Cu, and produce not only simple oxide (NiO), but also complex oxides (CGO), can be considered as a low cost, simple, environmentally friendly and non-toxic route for a large scale production of high purity single phase nanopowders at significantly low temperatures for other technical applications. In addition, for large scale high throughput process, the exothermic combustion of the alginate can contribute to the energy requirement for calcination.

In conclusion, this project has fulfilled the main objectives. Hence, it provides three new methods of obtaining nano particles for SOFC industry. Furthermore, other industries can benefit by using these methods because of their simplicity, low cost and efficiency.

Chapter 7 Future Work

The present work has investigated in details the influence of the factors such as calcination temperatures and annealing time of crystallization of different metal oxide synthesized using two novel sol-gel methods. Although sinterability, electrical conductivity and microstructure of gadolinium doped ceria materials in different compositions have been studied in this work, more detailed investigation needs to be conducted to further investigate various sintering methods to avoid thermal stock on the electrode and electrolyte layers of solid oxide fuel cells using CGO materials at 500 ~ 800 °C. In order to assess the thermal shock resistance of the ceramic layers, a Two Steps Sintering method can be applied which resulted in small grain size as long as maintained high theoretical density. Further work is also needed to use these nanopowders to fabricate an entire solid oxide fuel cell for real world application.

Moreover, although the present investigation shows that nanopowders of various metal oxide materials can be successfully obtained using sodium alginate as a media, the ion-exchange rates for different metal ions still remain as un-known. This is very important to clearly identify the ion-exchange rate for different metal ions which will certainly benefit the production rate during manufacturing process. As shown in the study, sodium alginate gel formation is rapid on the surface and the metal ions will gradually ion-exchange through the surface and reach to the center. Therefore, by using a fixed amount of sodium alginate granules or alginic acid beads to react with various metal ions at different time lengths, the concentrations of the remaining solutions will vary. This allows the ion-exchange rate for different metal ions to be determined.

List of References

1. R. Doshi, V.L. Richards, J.D. Carter, X.P. Wang and M. Krumpelt, *Development of solid-oxide fuel cells that operate at 500 degrees C.* Journal of the Electrochemical Society, 1999. **146**(4): p. 1273-1278.
2. Steele, B.C.H., *Materials for IT-SOFC stacks 35 years R&D: the inevitability of gradualness?* Solid State Ionics, 2000. **134**(1-2): p. 3-20.
3. Y.J. Leng, S.H. Chan, S.P. Jiang and K.A. Khor, *Low-temperature SOFC with thin film GDC electrolyte prepared in situ by solid-state reaction.* Solid State Ionics, 2004. **170**(1-2): p. 9-15.
4. F. Tietz, F.J. Dias, D. Simwonis and D. Stover, *Evaluation of commercial nickel oxide powders for components in solid oxide fuel cells.* Journal of the European Ceramic Society, 2000. **20**(8): p. 1023-1034.
5. Q.A. Zhen, G.M. Kale, G. Shi, R. Li, W.M. He and J.Q. Liu, *Processing of dense nanocrystalline Bi_2O_3-Y_2O_3 solid electolyte.* Solid State Ionics, 2005. **176**(37-38): p. 2727-2733.
6. Q. Zhen, G.M. Kale, W.M. He and J.Q. Liu, *Microwave plasma sintered nanocrystalline Bi_2O_3-HfO_2-Y_2O_3 composite solid electrolyte.* Chemistry of Materials, 2007. **19**(2): p. 203-210.
7. H.Y. Lee and G.M. Kale, *Hydrothermal Synthesis and Characterization of Nano-TiO_2.* International Journal of Applied Ceramic Technology, 2008. **5**(6): p. 657-665.
8. X.T. Wang and G.M. Kale, *Microwave sintering of YSZ electrolyte materials for SOFC.* High-Performance Ceramics V, Pts 1 and 2, 2008. **368-372**: p. 238-240.
9. C. Suciu, A.C. Hoffmann, A. Vik and F. Goga, *Effect of calcination conditions and precursor proportions on the properties of YSZ nanoparticles obtained by modified sol-gel route.* Chemical Engineering Journal, 2008. **138**(1-3): p. 608-615.
10. K.Q. Huang, M. Feng and J.B. Goodenough, *Synthesis and electrical properties of dense $Ce_{0.9}Cd_{0.1}O_{1.95}$ ceramics.* Journal of the American Ceramic Society, 1998. **81**(2): p. 357-362.
11. T.S. Zhang, J. Ma, L.H. Luo and S.H. Chan, *Preparation and properties of dense $Ce_{0.9}Gd_{0.1}O_{2-delta}$ ceramics for use as electrolytes in IT-SOFCs.* Journal of Alloys and Compounds, 2006. **422**(1-2): p. 46-52.
12. E.L. Daniel, *The Organic Chemistry of Sugar.* 2001.
13. C. Suciu, L. Gagea, A.C. Hoffmann and M. Mocean, *Sol-gel production of zirconia nanoparticles with a new organic precursor.* Chemical Engineering Science, 2006. **61**(24): p. 7831-7835.
14. P. Singh and N.Q. Minh, *Solid oxide fuel cells: Technology status.* International Journal of Applied Ceramic Technology, 2004. **1**(1): p. 5-15.
15. L.J. Gauckler, D. Beckel, B.E. Buergler, E. Jud, U.R. Muecke, M. Prestat, J.L.M. Rupp and J. Richter, *Solid oxide fuel cells: Systems and materials.* Chimia, 2004. **58**(12): p. 837-850.

16. H. Yahiro, K. Eguchi and H. Arai, *Electrical-Properties and Reducibilities of Ceria Rare Earth Oxide Systems and Their Application to Solid Oxide Fuel-Cell.* Solid State Ionics, 1989. **36**(1-2): p. 71-75.
17. T. Inoue, T. Setoguchi, K. Eguchi and H. Arai, *Study of a Solid Oxide Fuel-Cell with a Ceria-Based Solid Electrolyte.* Solid State Ionics, 1989. **35**(3-4): p. 285-291.
18. K. Eguchi, T. Setoguchi, T. Inoue and H. Arai, *Electrical-Properties of Ceria-Based Oxides and Their Application to Solid Oxide Fuel-Cells.* Solid State Ionics, 1992. **52**(1-3): p. 165-172.
19. S.W. Zha, C.R. Xia and G.Y. Meng, *Effect of Gd (Sm) doping on properties of ceria electrolyte for solid oxide fuel cells.* Journal of Power Sources, 2003. **115**(1): p. 44-48.
20. T.S. Zhang, P. Hing, H.T. Huang and J. Kilner, *Ionic conductivity in the CeO_2-Gd_2O_3 system (0.05 <= Gd/Ce <= 0.4) prepared by oxalate coprecipitation.* Solid State Ionics, 2002. **148**(3-4): p. 567-573.
21. J. Weitkamp and H.D. Wiemhofer, *Electronic conduction and stability of solid electrolytes based on lanthanum gallates.* Solid State Ionics, 2002. **154**: p. 597-604.
22. N.P. Brandon, S. Skinner and B.C.H. Steele, *Recent advances in materials for fuel cells.* Annual Review of Materials Research, 2003. **33**: p. 183-213.
23. A.J. Jacobson, *Materials for Solid Oxide Fuel Cells.* Chemistry of Materials, 2010. **22**(3): p. 660-674.
24. A. Lashtabeg and S.J. Skinner, *Solid oxide fuel cells - a challenge for materials chemists?* Journal of Materials Chemistry, 2006. **16**(31): p. 3161-3170.
25. M. Gaudon, E. Djurado and N.H. Menzler, *Morphology and sintering behaviour of yttria stabilised zirconia (8-YSZ) powders synthesised by spray pyrolysis.* Ceramics International, 2004. **30**(8): p. 2295-2303.
26. X.J. Chen, K.A. Khor, S.H. Chan and L.G. Yu, *Influence of microstructure on the ionic conductivity of yttria-stabilized zirconia electrolyte.* Materials Science and Engineering a-Structural Materials Properties Microstructure and Processing, 2002. **335**(1-2): p. 246-252.
27. M. Mazaheri, M. Valefi, Z.R. Hesabi and S.K. Sadrnezhaad, *Two-step sintering of nanocrystalline $8Y_2O_3$ stabilized ZrO_2 synthesized by glycine nitrate process.* Ceramics International, 2009. **35**(1): p. 13-20.
28. I.W. Chen and X.H. Wang, *Sintering dense nanocrystalline ceramics without final-stage grain growth.* Nature, 2000. **404**(6774): p. 168-171.
29. A. Tarancon, G. Dezanneau, J. Arbiol, F. Peiro and J.R. Morante, *Synthesis of nanocrystalline materials for SOFC applications by acrylamide polymerisation.* Journal of Power Sources, 2003. **118**(1-2): p. 256-264.
30. J. Ma, T.S. Zhang, L.B. Kong, P. Hing and S.H. Chan, *$Ce_{0.8}Gd_{0.2}O_{2-delta}$ ceramics derived from commercial submicron-sized CeO_2 and Gd2O3 powders for use as electrolytes in solid oxide fuel cells.* Journal of Power Sources, 2004. **132**(1-2): p. 71-76.
31. I.A. Castillo and R.J. Munz, *Inductively coupled plasma synthesis of CeO2-based powders from liquid solutions for SOFC electrolytes.* Plasma Chemistry and Plasma Processing, 2005. **25**(2): p. 87-107.

32. S. Dikmen, P. Shuk, M. Greenblatt and H. Gocmez, *Hydrothermal synthesis and properties of $Ce_{1-x}Gd_xO_{2-delta}$ solid solutions.* Solid State Sciences, 2002. **4**(5): p. 585-590.
33. Y. Tao, J. Shao, J.X. Wang and W.G. Wang, *Morphology control of $Ce_{0.9}Gd_{0.1}O_{1.95}$ nanopowder synthesized by sol-gel method using PVP as a surfactant.* Journal of Alloys and Compounds, 2009. **484**(1-2): p. 729-733.
34. S. Pinol, M. Najib, D.M. Bastidas, A. Calleja, X.G. Capdevila, M. Segarra, F. Espiell, J.C. Ruiz-Morales, D. Marrero-Lopez and P. Nunez, *Microstructure-conductivity relationship in Gd- and Sm-doped ceria-based electrolytes prepared by the acrylamide sol-gel-related method.* Journal of Solid State Electrochemistry, 2004. **8**(9): p. 650-654.
35. T.S. Zhang, J. Ma, Y.J. Leng, S.H. Chan, P. Hing and J.A. Kilner, *Effect of transition metal oxides on densification and electrical properties of Si-containing $Ce_{0.8}Gd_{0.2}O_{2-delta}$ ceramics.* Solid State Ionics, 2004. **168**(1-2): p. 187-195.
36. C.R. Xia and M.L. Liu, *Low-temperature SOFCs based on $Gd_{0.1}Ce_{0.9}O_{1.95}$ fabricated by dry pressing.* Solid State Ionics, 2001. **144**(3-4): p. 249-255.
37. N.M. Sammes and Z.H. Cai, *Ionic conductivity of ceria/yttria stabilized zirconia electrolyte materials.* Solid State Ionics, 1997. **100**(1-2): p. 39-44.
38. G.S. Lewis, A. Atkinson, B.C.H. Steele and J. Drennan, *Effect of Co addition on the lattice parameter, electrical conductivity and sintering of gadolinia-doped ceria.* Solid State Ionics, 2002. **152**: p. 567-573.
39. V.V. Kharton, F.M.B. Marques and A. Atkinson, *Transport properties of solid oxide electrolyte ceramics: a brief review.* Solid State Ionics, 2004. **174**(1-4): p. 135-149.
40. H.S Kang, J.R. Sohn, Y.C. Kang, K.Y. Jung and S.B. Park, *The characteristics of nano-sized Gd-doped CeO_2 particles prepared by spray pyrolysis.* Journal of Alloys and Compounds, 2005. **398**(1-2): p. 240-244.
41. R.T. Leah, N.P. Brandon and P. Aguiar, *Modelling of cells, stacks and systems based around metal-supported planar IT-SOFC cells with CGO electrolytes operating at 500-600 degrees C.* Journal of Power Sources, 2005. **145**(2): p. 336-352.
42. T. Ishihara, Y. Hiei and Y. Takita, *Oxidative Reforming of Methane Using Solid Oxide Fuel-Cell with $LaGaO_3$-Based Electrolyte.* Solid State Ionics, 1995. **79**: p. 371-375.
43. O. Yamamoto, *Solid oxide fuel cells: fundamental aspects and prospects.* Electrochimica Acta, 2000. **45**(15-16): p. 2423-2435.
44. M. Shi, N. Liu, Y.D. Xu, Y.P. Yuan, P. Majewski and F. Aldinger, *Synthesis and characterization of Sr- and Mg-doped $LaGaO_3$ by using glycine-nitrate combustion method.* Journal of Alloys and Compounds, 2006. **425**(1-2): p. 348-352.
45. K.Q. Huang, R.S. Tichy and J.B. Goodenough, *Superior perovskite oxide-ion conductor; strontium- and magnesium-doped $LaGaO_3$: I, phase relationships and electrical properties.* Journal of the American Ceramic Society, 1998. **81**(10): p. 2565-2575.

46. B. Rambabu, S. Ghosh, W.C. Zhao and H. Jena, *Innovative processing of dense LSGM electrolytes for IT-SOFC's.* Journal of Power Sources, 2006. **159**(1): p. 21-28.
47. R. Polini, A. Falsetti and E. Traversa, *Sol-gel synthesis, X-ray photoelectron spectroscopy and electrical conductivity of Co-doped (La, Sr)(Ga, Mg)O3-delta perovskites.* Journal of the European Ceramic Society, 2007. **27**(13-15): p. 4291-4296.
48. N.Q. Minh, *Ceramic Fuel-Cells.* Journal of the American Ceramic Society, 1993. **76**(3): p. 563-588.
49. Y.M. Park and G.M. Choi, *Microstructure and electrical properties of YSZ-NiO composites.* Solid State Ionics, 1999. **120**(1-4): p. 265-274.
50. H. Koide, Y. Someya, T. Yoshida and T. Maruyama, *Properties of Ni/YSZ cermet as anode for SOFC.* Solid State Ionics, 2000. **132**(3-4): p. 253-260.
51. S. Primdahl, B.F. Sorensen and M. Mogensen, *Effect of nickel oxide/yttria-stabilized zirconia anode precursor sintering temperature on the properties of solid oxide fuel cells.* Journal of the American Ceramic Society, 2000. **83**(3): p. 489-494.
52. F.T. Ciacchi, K.M. Crane and S.P.S. Badwal, *Evaluation of Commercial Zirconia Powders for Solid Oxide Fuel-Cells.* Solid State Ionics, 1994. **73**(1-2): p. 49-61.
53. S.P. Jiang, P.J. Callus and S.P.S. Badwal, *Fabrication and performance of Ni/3 mol% Y_2O_3-ZrO_2 cermet anodes for solid oxide fuel cells.* Solid State Ionics, 2000. **132**(1-2): p. 1-14.
54. S.P. Jiang and S.H. Chan, *A review of anode materials development in solid oxide fuel cells.* Journal of Materials Science, 2004. **39**(14): p. 4405-4439.
55. S.P. Jiang, *A comparative study of fabrication and performance of Ni/3 mol % Y_2O_3-ZrO_2 and Ni/8 mol% Y_2O_3-ZrO_2 cermet electrodes.* Journal of the Electrochemical Society, 2003. **150**(11): p. E548-E559.
56. T. Matsushima, H. Ohrui and T. Hirai, *Effects of sinterability of YSZ powder and NiO content on characteristics of Ni-YSZ cermets.* Solid State Ionics, 1998. **111**(3-4): p. 315-321.
57. F.F. Lange, *Powder Processing Science and Technology for Increased Reliability.* Journal of the American Ceramic Society, 1989. **72**(1): p. 3-15.
58. T. Fukui, K. Murata, S. Ohara, H. Abe, M. Naito and K. Nogi, *Morphology control of Ni-YSZ cermet anode for lower temperature operation of SOFCs.* Journal of Power Sources, 2004. **125**(1): p. 17-21.
59. S.T. Aruna, M. Muthuraman and K.C. Patil, *Synthesis and properties of Ni-YSZ cermet: anode material for solid oxide fuel cells.* Solid State Ionics, 1998. **111**(1-2): p. 45-51.
60. A. Ringuede, J.A. Labrincha and J.R. Frade, *A combustion synthesis method to obtain alternative cermet materials for SOFC anodes.* Solid State Ionics, 2001. **141**: p. 549-557.
61. A. Ringuede, D. Bronine and J.R. Frade, *Assessment of Ni/YSZ anodes prepared by combustion synthesis.* Solid State Ionics, 2002. **146**(3-4): p. 219-224.
62. S.D. Park, J.M. Vohs and R.J. Gorte, *Direct oxidation of hydrocarbons in a solid-oxide fuel cell.* Nature, 2000. **404**(6775): p. 265-267.

63. R.J. Gorte, S. Park, J.M. Vohs and C.H. Wang, *Anodes for direct oxidation of dry hydrocarbons in a solid-oxide fuel cell.* Advanced Materials, 2000. **12**(19): p. 1465-1469.
64. H. Kim, C. Lu, W.L. Worrell, J.M. Vohs and R.J. Gorte, *Cu-Ni cermet anodes for direct oxidation of methane in solid-oxide fuel cells.* Journal of the Electrochemical Society, 2002. **149**(3): p. A247-A250.
65. O.A. Marina, C. Bagger, S. Primdahl and M. Mogensen, *A solid oxide fuel cell with a gadolinia-doped ceria anode: preparation and performance.* Solid State Ionics, 1999. **123**(1-4): p. 199-208.
66. H. Uchida, T. Osuga and M. Watanabe, *High-performance electrode for medium-temperature solid oxide fuel cells - Control of microstructure of ceria-based anodes with highly dispersed ruthenium electrocatalysts.* Journal of the Electrochemical Society, 1999. **146**(5): p. 1677-1682.
67. K.S. Hwang, H.M. Lee, S.S. Min and B.A. Kang, *Epitaxially grown $LaSrCoO_3$ thin films on various substrates by the sol-gel method.* Journal of Sol-Gel Science and Technology, 2000. **18**(2): p. 175-180.
68. S. Charojrochkul, K.L. Choy and B.C.H. Steele, *Cathode electrolyte systems for solid oxide fuel cells fabricated using flame assisted vapour deposition technique.* Solid State Ionics, 1999. **121**(1-4): p. 107-113.
69. L.W. Tai, M.N. Nasrallah, H.U. Anderson, D.M. Sparlin and S.R. Sehlin, *Structure and Electrical-Properties of $La_{1-X}Sr_xCo_{1-Y}Fe_yO_3$ .1. the System $La_{0.8}Sr_{0.2}Co_{1-Y}Fe_yO_3$.* Solid State Ionics, 1995. **76**(3-4): p. 259-271.
70. L.W. Tai, M.N. Nasrallah, H.U. Anderson, D.M. Sparlin and S.R. Sehlin, *Structure and Electrical-Properties of $La_{1-X}Sr_xCo_{1-Y}Fe_yO_3$ .2. the System $La_{1-X}Sr_xCo_{0.2}Fe_{0.8}O_3$.* Solid State Ionics, 1995. **76**(3-4): p. 273-283.
71. E. Maguire, B. Gharbage, F.M.B. Marques and J.A. Labrincha, *Cathode materials for intermediate temperature SOFCs.* Solid State Ionics, 2000. **127**(3-4): p. 329-335.
72. G.C. Kostogloudis and C. Ftikos, *Properties of A-site-deficient $La_{0.6}Sr_{0.4}Co_{0.2}Fe_{0.8}O_{3-delta}$-based perovskite oxides.* Solid State Ionics, 1999. **126**(1-2): p. 143-151.
73. H.Y. Tu, Y. Takeda, N. Imanishi and O. Yamamoto, *$Ln_{0.4}Sr_{0.6}Co_{0.8}Fe_{0.2}O_{3-delta}$ (Ln = La, Pr, Nd, Sm, Gd) for the electrode in solid oxide fuel cells.* Solid State Ionics, 1999. **117**(3-4): p. 277-281.
74. A.V. Berenov, J.L. MacManus-Driscoll and J.A. Kilner, *Oxygen tracer diffusion in undoped lanthanum manganites.* Solid State Ionics, 1999. **122**(1-4): p. 41-49.
75. Brugnoni, C., U. Ducati, and M. Scagliotti, *Sofc Cathode/Electrolyte Interfaces .2. Study of $NdAlO_3$, Diffusion-Barriers.* Solid State Ionics, 1995. **76**(3-4): p. 183-188.
76. Brugnoni, C., U. Ducati, and M. Scagliotti, *Sofc Cathode/Electrolyte Interface .1. Reactivity between $La_{0.85}Sr_{0.15}MnO_3$ and ZrO_2-Y_2O_3.* Solid State Ionics, 1995. **76**(3-4): p. 177-182.
77. R.A. De Souza, M.S. Islam and E. Ivers-Tiffee, *Formation add migration of cation defects in the perovskite oxide $LaMnO_3$.* Journal of Materials Chemistry, 1999. **9**(7): p. 1621-1627.

78. Y. Takeda, Y. Sakaki, T. Ichikawa, N. Imanishi, O. Yamamoto, M. Mori, N. Mori and T. Abe, *Stability of $La_{1-X}a_XMnO_{3-Z}$ (a=Ca, Sr) as Cathode Materials for Solid Oxide Fuel-Cells.* Solid State Ionics, 1994. **72**: p. 257-264.
79. J. VanHerle, A.J. McEvoy and K.R. Thampi, *A study on the $La_{1-x}Sr_xMnO_3$ oxygen cathode.* Electrochimica Acta, 1996. **41**(9): p. 1447-1454.
80. C. Suciu, A.C. Hoffmann, E. Dorolti and R. Tetean, *NiO/YSZ nanoparticles obtained by new sol-gel route.* Chemical Engineering Journal, 2008. **140**(1-3): p. 586-592.
81. W.R. Gombotz and S.F. Wee, *Protein release from alginate matrices.* Advanced Drug Delivery Reviews, 1998. **31**(3): p. 267-285.
82. S. Baskoutas, P. Giabouranis, S.N. Yannopoulos, V. Dracopoulos, L. Toth, A. Chrissanthopoulos and N. Bouropoulos, *Preparation of ZnO nanoparticles by thermal decomposition of zinc alginate.* Thin Solid Films, 2007. **515**(24): p. 8461-8464.
83. A. Takada and T. Shimizu, *Synthesis of bismuth-based high-T-c superconducting fibres by using sodium alginate as a polyelectrolyte.* Journal of Materials Science, 1997. **32**(10): p. 2699-2705.
84. A.A. Said and R.M. Hassan, *Thermal-Decomposition of Some Divalent Metal Alginate Gel Compounds.* Polymer Degradation and Stability, 1993. **39**(3): p. 393-397.
85. C. Sartori, D.S. Finch, B. Ralph and K. Gilding, *Determination of the cation content of alginate thin films by FTir spectroscopy.* Polymer, 1997. **38**(1): p. 43-51.
86. R.M. Hassan, S.A. Elshatoury, M.A. Mousa and A. Hassan, *Kinetics and Mechanism of Sol-Gel Transformation for Poly-Electrolytes of Capillary Copper Alginate Ionotropic Membranes.* European Polymer Journal, 1988. **24**(12): p. 1173-1175.
87. R.M. Hassan, M.H. Wahdan and A. Hassan, *Kinetics and Mechanism of Sol-Gel Transformation on Poly-Electrolytes of Nickel Alginate Ionotropic Membranes.* European Polymer Journal, 1988. **24**(3): p. 281-283.
88. R.M. Hassan, A.M. Summan, M.K. Hassan and S.A. Elshatoury, *Kinetics and Mechanism of Sol-Gel Transformation on Poly-Electrolytes of Some Transition-Metal Ions, Especially Cobalt Alginate Ionotropic Membranes.* European Polymer Journal, 1989. **25**(12): p. 1209-1212.
89. K.S. Khairou, W.M. Al-Gethami and R.M. Hassan, *Kinetics and mechanism of sol-gel transformation between sodium alginate polyelectrolyte and some heavy divalent metal ions with formation of capillary structure polymembranes ionotropic gels.* Journal of Membrane Science, 2002. **209**(2): p. 445-456.
90. W.J. Boettinger, U.R. Kattner, K.W. Moon and J.H. Perepezko, *DTA and Heat-flux DSC Measurements of Ally Melting and Freezing.* 2006.
91. P.L. King, M.S. Ramsey, P.F. McMillan and G. Swayze, *Laboratory Fourier Transform Infrared Spectroscopy Methods for Geologic Samples.*
92. N.F.M. Henry, H. Lipson and W.A. Wooster, *The Interpretation of X-ray diffraction photographs.* 1962: p. 212-220.

93. N. Meethong, H.Y.S. Huang, S.A. Speakman, W.C. Carter and Y.M. Chiang, *Strain accommodation during phase transformations in olivine-based cathodes as a materials selection criterion for high-power rechargeable batteries.* Advanced Functional Materials, 2007. **17**(7): p. 1115-1123.
94. H.M. Rietveld, *A Profile Refinement Method for Nuclear and Magnetic Structures.* Journal of Applied Crystallography, 1969. **2**: p. 65-&.
95. R.A. Young, *The Rietveld Method.* Oxford University Press, New York, 1993.
96. S.R. Stock, *Developments in X-Ray Tomography VII* 2010.
97. J.R. Macdonald, *Impedance Spectroscopy-Emphasizing Solid Materials and Systems.* John Wiley & Sons, New York, 1987.
98. E.A. Kummerle and G. Heger, *The structures of C-$Ce_2O_{3+delta}$, Ce_7O_{12}, and $Ce_{11}O_{20}$.* Journal of Solid State Chemistry, 1999. **147**(2): p. 485-500.
99. M. Yashima, S. Kobayashi and T. Yasui, *Crystal structure and the structural disorder of ceria from 40 to 1497 degrees C.* Solid State Ionics, 2006. **177**(3-4): p. 211-215.
100. T. Wakita and M. Yashima, *Structural disorder in the cubic $Ce_{0.5}Zr_{0.5}O_2$ catalyst: A possible factor of the high catalytic activity.* Applied Physics Letters, 2008. **92**(10).
101. S. Hull, S.T. Norberg, I. Ahmed, S.G. Eriksson, D. Marrocchelli and P.A. Madden, *Oxygen vacancy ordering within anion-deficient Ceria.* Journal of Solid State Chemistry, 2009. **182**(10): p. 2815-2821.
102. A. Saiki, N. Ishizawa, N. Mizutani and M. Kato, *Structural change of C-type rare earth oxides, ytterbium oxide and erbium oxide at high temperatures.* Journal of the Ceramic Society of Japan, 1985. **93**: p. 649-654.
103. Z. Heiba, H. Okuyucu and Y.S. Hascicek, *X-ray structure determination of the rare earth oxides ($Er_{1-u}Gd_u)_2O_3$ applying the Rietveld method.* Journal of Applied Crystallography, 2002. **35**: p. 577-580.
104. A.M. Pires, M.R. Davolos, C.O. Paiva-Santos, E.B. Stucchi and J. Flor, *New X-ray powder diffraction data and Rietveld refinement for Gd_2O_3 monodispersed fine spherical particles.* Journal of Solid State Chemistry, 2003. **171**(1-2): p. 420-423.
105. B.C.H. Steele, *Appraisal of $Ce_{1-y}Gd_yO_{2-y/2}$ electrolytes for IT-SOFC operation at 500 degrees C.* Solid State Ionics, 2000. **129**(1-4): p. 95-110.
106. C. Shen and L.L. Shaw, *FTIR analysis of the hydrolysis rate in the sol-gel formation of gadolinia-doped ceria with acetylacetonate precursors.* Journal of Sol-Gel Science and Technology. **53**(3): p. 571-577.
107. A.V. Kovalevskii, V.V. Kharton and E.N. Naumovich, *Ionic and electronic conductivity of $Ce(Gd,Co)O_{2-delta}$ ceramics.* Inorganic Materials, 1996. **32**(11): p. 1230-1233.
108. R.Q. Liu, Y.H. Xie, J.D. Wang, Z.J. Li and B.H. Wang, *Synthesis of ammonia at atmospheric pressure with $Ce_{0.8}M_{0.2}O_{2-delta}$ (M=La, Y, Gd, Sm) and their proton conduction at intermediate temperature.* Solid State Ionics, 2006. **177**(1-2): p. 73-76.